TOMOGRAPHIC CHARACTERIZATION OF AQUIFER HETEROGENEITY

BY

Shane A. Lyle
B.S. Kansas State University, 1993

Submitted to the Department of Geology and the Graduate Faculty of the University of Kansas in partial fulfillment of the requirements for the degree of
Master of Science

Co-Chairman Dr. Carl McElwee

Co-Chairman Dr. David Fowle

Dr. John F. Devlin

Date Defended: February 4, 2011

Acceptance Page

The Thesis Committee for Shane A. Lyle certifies
that this is the approved version of the following thesis:

TOMOGRAPHIC CHARACTERIZATION OF AQUIFER HETEROGENEITY

Advisory Committee:

____
Dr. Carl McElwee, Co-Chairman

____
Dr. David Fowle, Co-Chairman

____
Dr. John F. Devlin

Date approved: ________________________________

Abstract

The Darcy's Law proportionality constant, hydraulic conductivity, describes the relative ease or rate at which water can move through a permeable medium and its fine-scale heterogeneity determines preferential flow rates and pathways. Traditional aquifer tests, such as slug and pumping tests, predict hydraulic conductivity values without detailed information about aquifer heterogeneity. The multiple source and receiver signals of a hydraulic tomography aquifer test can estimate interwell heterogeneity, but it requires extensive time to collect and then invert large amounts of tomographic data. An innovative adaptation of an oscillatory pressure signal was used to reduce the data collection and processing time associated with a tomography test. The phase shift of the sinusoidal pressure signal is related to the hydraulic conductivity. Multiple offset gathers (MOG) ray paths were estimated with a spatially weighted straight ray approximation method and analyzed with data processing programs that extend the 3D homogenous spherical radial equation to the heterogeneous case. A numerical model was used to check the heterogeneous extension for accuracy. High quality zero-offset profile ray paths (ZOP) were used to determine hydraulic conductivity, K, at a relatively fine scale and interpreted into representative aquifer models between different tomographic well pairs. The aquifer models were used with MOG data to evaluate the anisotropy ratio and lateral heterogeneity of the aquifer. Two different oscillatory periods, 3 and 30-sec, were evaluated and compared to previous work at the site. Analysis indicates that the 3-sec period data were more sensitive to different anisotropy ratios and both periods are capable of resolving K zones of about one meter.

Acknowledgements

I would like to thank Dr. Carl McElwee for being my advisor on this project along with his patience and the opportunity to pursue this degree, I’m very grateful.

I would like to thank Dr. Rick Devlin and Dr. David Fowle for serving on my thesis committee.

I would like to thank the Kansas Geological Survey for their support as I juggled family, work and school commitments.

I would like to thank Rebecca Smedlund for field assistance.

I would like to thank Bill Wilson and Kenny Doane with PSA Environmental for their field assistance and providing the Geoprobe equipment for this research.

I would like to thank my family for their support throughout this project. I would like to especially thank my wife, Mary, without her support, this would not have been possible.

This research is funded in part through the Strategic Environmental Research and Development Program (SERDP).

Table of Contents

Introduction

The focus of much environmental work associated with groundwater contamination involves site characterization in support of engineered remediation solutions, such as the injection of electron-donor amendments (e.g., vegetable oil) to stimulate reductive dechlorination of halogenated hydrocarbons (Lane et al., 2006; Lane et al., 2007). Engineered remedial measures such as these require a thorough characterization of an aquifer's hydrogeologic framework to be both effective and economic, (Ricciardi, 2009). Of primary importance to groundwater contamination research is the heterogeneity of the Darcy's Law proportionality constant, hydraulic conductivity, which characterizes preferential flow and the capacity of a medium to transmit water (Domenico and Schwartz, 1998).

Accurate prediction of groundwater flow and solute transport requires a thorough understanding of how hydraulic conductivity changes spatially. However, most well hydraulic equations assume that aquifers are homogeneous and isotropic even though well-studied and relatively ideal aquifers exhibit at least mild heterogeneity with broad spatial hydraulic conductivity variations that result in irregular subsurface flow paths (Sudicky, 1986). Therefore, an aquifer test that evaluates heterogeneity could improve fate and transport characterization and by extension improve the effectiveness of engineered remedial solutions.

Traditional aquifer tests, such as slug and pumping tests, predict average hydraulic conductivity values without much detailed information about aquifer heterogeneity. Slug tests are frequently used due to their relative ease of implementation and data collection (Hvorslev, 1951; Cooper et al., 1967; Butler Jr., 2007). Slug test results are generally limited to the vertical average of the aquifer surrounding the well screen, although discrete interval slugging can increase vertical resolution (Zemansky and McElwee, 2005). The pumping testis another common method that measures water level change near a constant-rate pumping well to estimate approximate transmissivity and storage characteristics. Pumping tests represent large volumetric aquifer averages of transmissivity without detailed characterization of heterogeneity (Cooper et al., 1967; Theis, 1989; Kruseman and de Ridder, 1991; Schad and Teutsch, 1994).

Other aquifer test methods, derived from petroleum exploration techniques, monitor oscillatory pressure waves to describe formation properties between well pairs (Johnson, 1968; Lee, 1982). Like slug testing, vertical resolution increases over smaller, packed-off intervals (Black and Kipp Jr, 1981). Because it’s a cross-well application, continuous pulse test (CPT) methods have the potential to evaluate heterogeneity without the limitations associated with near-well or bulk volumetric hydraulic conductivity values determined from slug or pumping tests, respectively. The variances and applications of slug, pumping, and hydraulic tomography tests are further reviewed by Yeh et al. (2007) and Butler (2008).

Hydraulic tomography is a relatively new hydraulic test method adapted from computerized axial tomography (CAT) scan medical technology, which can directly evaluate aquifer heterogeneity (Yeh and Liu, 2000; Brauchler et al., 2003). The test includes a sequential, cross-hole test followed by data inversion to obtain the hydraulic conductivity distribution between a source and receiver well. The hydraulic tomography method typically uses fully screened wells that are isolated over a discrete interval by packers. Water is pumped from or injected into the aquifer through the discrete interval at a constant rate. Steady-state head data are sequentially recorded in a near-by well at multiple packed-off locations or multilevel sampling wells (Bohling et al., 2002) to collect many source-receiver response data sets. The process can be repeated by moving the pumping or injection interval so that many different aquifer response data points are collected (Yeh and Liu, 2000). The large number of data sets help reduce the non-uniqueness of the inverse problem (Oldenburg and Li, 2005). Data inversion is necessary because the observed response of the test, while related to the physical property of the aquifer, does not directly correspond to hydraulic conductivity.

The methodology for this research combines the oscillatory signal of a CPT with the many discrete interval data points and data inversion of the hydraulic tomography test. The oscillating sinusoidal signal coupled with hydraulic tomography is a unique technique first developed for this research (Engard, 2006; Wachter, 2008). An energy source, an aquifer model, and an energy response typify the tomographic CPT test. The energy source for this research was either a hydraulic pumping or pneumatically-driven sinusoidal excitation point-source. Source and receiver signals of pressure head oscillations were monitored with transducers at discrete intervals. The aquifer model for this research consists of a finite element/finite difference model grid along with a straight-ray approximation method to simulate the ray path of the sinusoidal signal through the aquifer between the source and receiver location. The aquifer model grid between the different well pairs was interpolated from the vertical profile of K values determined from high-quality ZOP data. The phase shift and amplitude decay of the sinusoidal signal is the energy response of the CPT test and is related to the aquifer's physical characteristics. Temporary storage of water due to the compressibility of the aquifer matrix creates time lag or phase shift of the pressure wave. K is a measure of an aquifer’s ability to transmit water and reflects how fast or easily a formation transmits pressure changes. By definition phase shift values vary inversely with K; in high K zones pressure waves propagate more quickly leading to smaller phase shift values and vice versa.

The signal variation of the energy source between the source and receiver (i.e., amplitude and phase shift) is directly related to a quantitative aquifer property, diffusivity, which is the ratio of hydraulic conductivity to specific storage (Brauchler et al., 2003). But, while diffusivity actually gives rise to the signal variation, the amplitude and phase shift are the measured responses of a CPT test and an inverse is required to recover the diffusivity distribution between the source and receiver. Because the straight ray method of tomography, like other geophysical methods such as gravity, magnetics, and induced polarization, are linear (Oldenburg and Li, 2005), it is easier to solve and many results are also available analytically. Therefore, a singular value decomposition (SVD) method implementing a least squares statistical method was used to find the inverse solution for the finite element/fine difference model grid of the aquifer. The method is advantageous because it doesn’t require the computing power needed to solve a numerical model. The data fit to the model can be inspected both visually, by plotting, and statistically from the resulting chi squared and standard deviation values.

Objectives

Previous research indicates that CPT methods agree well with hydraulic conductivity characterization at the University of Kansas Geohydrologic Experimental and Monitoring Site (GEMS) (Ross, 1997; Engard, 2006; Wachter, 2008). The objective of this project is to develop field equipment to efficiently measure high-resolution hydraulic conductivity by hydraulic tomography using CPT and to develop a model for processing, inverting and interpreting the field data.

Two different CPT mechanisms, hydraulic and pneumatic, were evaluated. Data for the hydraulic CPT were collected from five source wells paired to a central receiver well. A single source sensor and a 5-channel receiver array were used to collect the data. Data for the pneumatic CPT were collected from a Geoprobe-deployed source paired with two receiver wells. A single source sensor and two 5-channel receivers were used to collect the data. Source and receiver data were collected on 0.305 m (1 ft) centers over the screened interval of the tomography wells, which span the lower, coarser half of the alluvial aquifer. New research adaptations include: evaluating the well pairs with a hydraulic pumping source in lieu of a pneumatic source (Wachter, 2008); and, a new direct-push pneumatic source was constructed to evaluate tomographic applications deployed with a Geoprobe. A new, multilevel receiver was constructed and deployed along with an existing receiver to increase the rate of data collection by simultaneously collecting data sets between the Geoprobe source and two receiver wells.

The radial coordinate system used in this research allows rays to emanate in any direction from the CPT and these rays are modeled using a straight ray approximation. Conventional theory, which usually assumes homogenous conditions, is transformed to the heterogeneous case by the straight ray approximation along with spatial averages of K along the ray path. Numerical modeling was used to check the accuracy of the approximate heterogeneous extension.

Theory

Pulse data response is similar to tidal effects on groundwater levels; tidal signals decay exponentially and a phase shift occurs in proportion to the distance from shore (Ferris, 1952; Hantush, 1960).

Tidal equations can be generalized for a one-dimensional transient pressure head signal with a sinusoidal boundary condition (Engard, 2006).

$$h\left(r,t\right)=h_o e^d \sin\left(\Phi_0-\Phi_r\right) \qquad (1)$$

where $h(r,t)$ is the head signal received at a radius, r, between the receiver and source well at time, t. h_o is the amplitude of the initial pressure head fluctuation; e^d is an amplitude decay term; Φ_0 is the source reference phase; and Φ_r is the phase shift.

The one-dimensional equation (1) can be adapted to a point source, such as a CPT, that spreads out in all directions. The aquifer response in a homogenous, spherical, radial system is given by the following approximation (Engard, 2006):

$$h\left(r,t\right)=h_o \frac{e^{-\sqrt{\frac{\pi f S_S}{K}}r}}{r}\sin\left(2\pi ft-\sqrt{\frac{\pi fS_S}{K}}r\right) \qquad (2)$$

The one-dimensional transient pressure head signal (1) can also be considered in terms of amplitude, AMP_r, source phase, Φ_0, and phase shift, Φ_r, for the 3D radial system.

$$AMP_r=h_0\frac{e^{-\sqrt{\frac{\pi fS_s}{K}}r}}{r} \qquad (3)$$

$$\Phi_0=\left(2\pi ft\right) \qquad (4)$$

$$\Phi_r = -\sqrt{\frac{\pi f S_s}{K}}r = d \qquad (5)$$

where f is the frequency, S_S is the specific storage, and K is hydraulic conductivity. Frequency, f, is sometimes considered in terms of its inverse, period, P ($P = 1/f$). Both amplitude and phase shift incorporate a common factor, $-\sqrt{\frac{\pi f S_S}{K}}r$, equal to the factor d in the exponential decay term. The amplitude and phase shift depend upon the physical characteristic of the aquifer to facilitate flow in terms of the ratio of hydraulic conductivity to specific storage, which is the hydraulic diffusivity, D. If an Ss value is assumed, K values can be calculated and compared to other hydraulic testing methods such as slug testing. The CPT introduces cyclic stresses within a geologic medium. The soil behavior under cyclic loading is complex and may not always have a linear elastic response. For this research, it is assumed that Ss is constant and stresses from the pressure wave are oscillating relatively faster than hysteretic material (e.g., clay) in the aquifer can develop a full stress/strain path and diffuse excess pore pressure. Therefore, the behavior of the aquifer's physical properties and storage should be somewhat uniform and not influence these cyclic tests (Engard, 2006)

Algebraic relationships within the theory here indicates that the phase shift and exponential amplitude decay should vary linearly with $\sqrt{S_S/K}$ and radial distance, r, from the well. Therefore, average parameters between well pairs may be linearly estimated along a straight ray between the location of an initial pressure head fluctuation to some receiver location along its travel path. Analysis of multiple rays from different locations of pressure head variation is the basis of hydraulic tomography (Yeh and Liu, 2000). While both the amplitude decay and phase shift arise from the diffusivity distribution, Engard (2006) determined that the amplitude requires correction to account for the exponential decay with distance and complicates the data analysis, therefore phase shift, Φ_r, is used in this research to solve for *K* using equation (5).

The spherical, radial system (2) is transformed to the heterogeneous case by using the assumption of a distance weighted average for the hydraulic conductivity with the following substitution (Wachter, 2008):

$$\sqrt{\frac{\pi f S_S}{K}}r \Rightarrow \sum_{i=1}^{I}\sqrt{\frac{\pi f S_S}{K_i}}\left(r_i - r_{i-1}\right) \qquad (6)$$

The index *i* indicate zones of differing hydraulic conductivity encountered along the path; so, the summation continues up to the present location of *r* (e.g., the receiver well) and terminates at that point. The heterogeneous case does not have analytical solutions, therefore numerical methods were used to validate the spatially weighted approximation. The spherical coordinate system allows rays to emanate in any direction from the point source, so diagonal ray paths emanating from the source can be modeled with numerical methods employed by Wachter (2008) and compared to the distance weighted average. Numerical modeling results were in close agreement with the spatially weighted approximation presented above and seem to indicate that the heterogeneous transformation works well. Additional numerical modeling studies were conducted as a component of this research and are further discussed in the numerical modeling section of this report.

Field Site

Tomographic research was completed at the University of Kansas GEMS location. GEMS is located in the alluvial floodplain of the Kansas River north of

Lawrence, Kansas (Fig. 1). The pumped hydraulic source wells are HT-1, HT-2, HT-4, HT-5, and HT-6. The receiver well is HT-3. The pneumatic source, HT-GP, was advanced with a Geoprobe between HT-2 and 7-1. The Geoprobe receiver wells are HT-2 and HT-3 (Fig. 1).

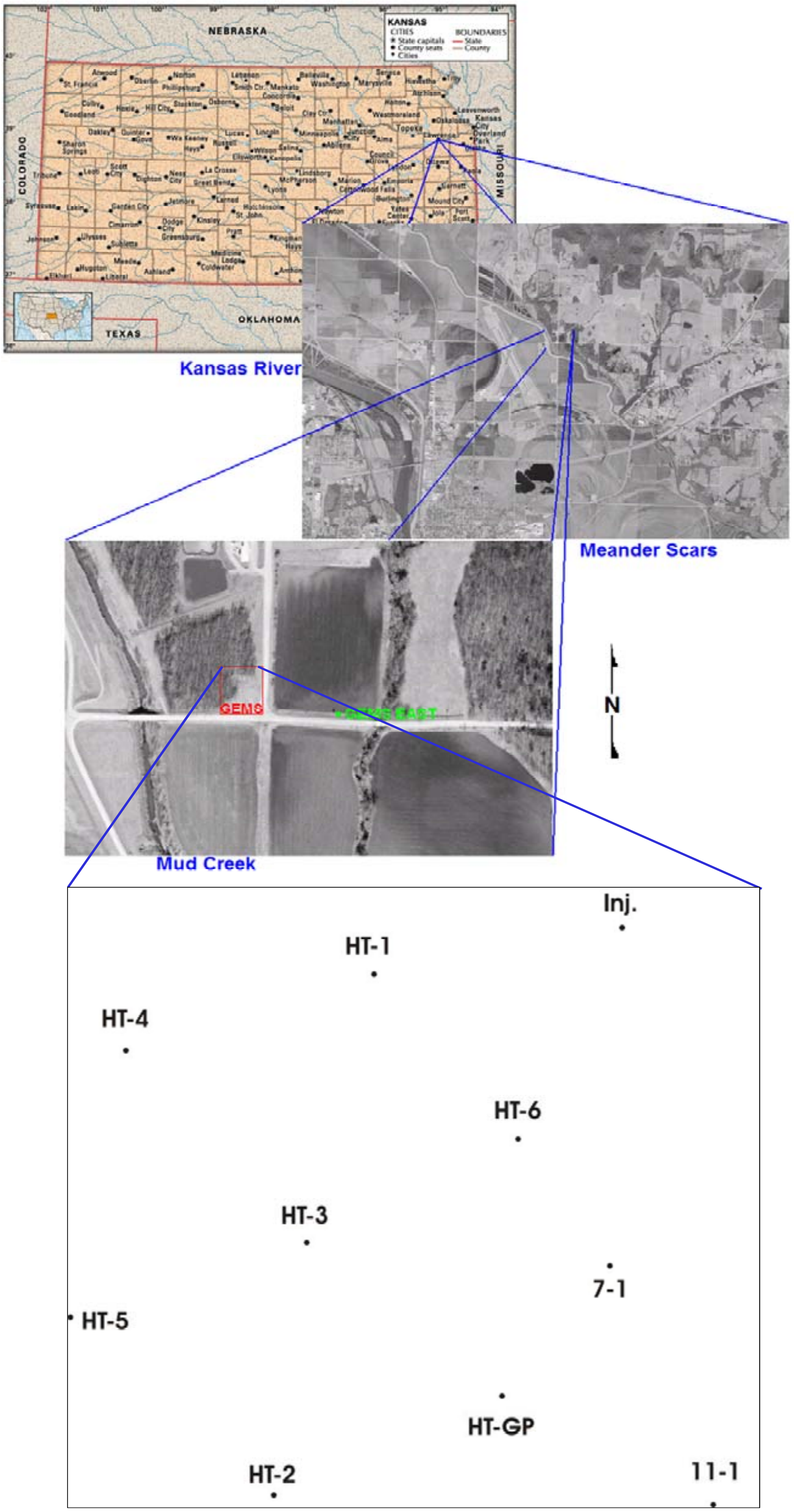

Figure 1 – Map of GEMS and layout of the hydraulic tomography radial well array. Figure modified from Engard (2006) and Wachter (2008).

Drilling and electric conductivity logging at the site indicate that alluvial deposits are approximately 22 meters (m) thick and consist of approximately 10.7 m (35 ft) of confining clay and silt that overlie 10.7 m (35 ft) of basal coarse sand and gravel (Fig. 2) (Butler et al., 2000). The site is a relatively heterogeneous fining upward alluvial depositional sequence, with clay lenses up to 1 m (3.28 ft) in the coarser sand and gravel unit (Healy et al., 2004). GEMS is considered semi-confined due to the overlying clay and silt deposits belonging to the Neogene Newman Terrace deposits. The aquifer is underlain by Pennsylvanian shale and limestone bedrock (O'Conner, 1960)

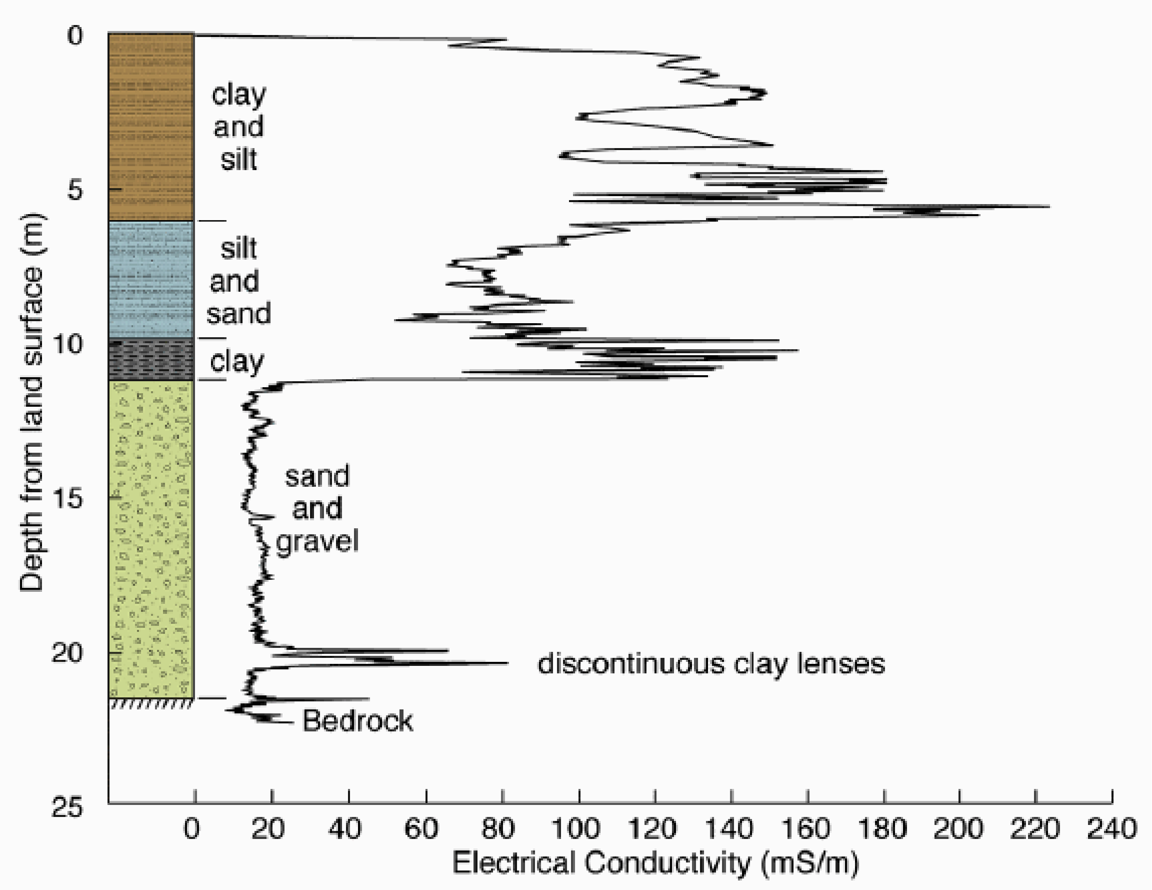

Figure 2 – GEMS general alluvial stratigraphy correlated to an electrical conductivity log. Figure modified from (Butler et al., 2000).

GEMS has been the site of extensive research of groundwater flow in heterogeneous formations, which affords a relatively high degree of control for a field research site. The alluvial profile was sampled and correlated by both physical soil sample and analysis (McElwee et al., 1995) as well as hydraulic conductivity (Butler Jr et al., 1999; Zemansky and McElwee, 2005; Ross and McElwee, 2007). K estimates were derived from a single-well injection test with an electrolyte solution (Huettl, 1992) and a multi-level sampling induced gradient tracer test (Bohling, 1999).

Ten wells at the site were tested by high resolution slug test (HRST) methods to develop hydraulic conductivity profiles at GEMS (Ross, 1997; Ross and McElwee, 2007). A slug test can be initiated by insertion of a solid object or known volume of water. Slug tests can also be initiated by a known vacuum or pressure “slug” (Prosser, 1981) and over a discrete interval with straddle packers to increase the vertical resolution of the method (Zemansky and McElwee, 2005). This high resolution pneumatic method was completed on 0.46 m (1.5 ft) centers to create an extensive spatial distribution of the K at GEMS. The tomographic wells were also slugged by HRST methods and served 5 baseline K for this research along with the earlier work at GEMS (Engard, 2006; Wachter, 2008).

Conceptual Model

The hydraulic tomography conceptual model for this research consists of an energy source, an earth model and a measured energy response followed by an inversion to recover the aquifer physical property, diffusivity, which is used to solve for K (Fig. 3). The energy input is either an oscillating, hydraulic or pneumatic excitation source which stimulates the aquifer. The earth model is the lower sand and gravel portion of the aquifer at GEMS and is represented by a layered model grid consisting of nodes, elements and zones. The aquifer response or forward problem gives rise to the observed output, the phase shift of the sinusoidal signal between the source and receiver. The phase shift is the measured response of the aquifer's physical property, diffusivity. Propagation of the oscillating energy source through the aquifer depends on the diffusivity distribution, and is simulated by data processing with a straight ray approximation method through the model grid of the aquifer. But because there is no direct correspondence between the recorded phase shift values and diffusivity, an inversion or reverse problem is required to recover diffusivity from the phase shift data set by fitting experimental response to an assumed model grid with a least squares statistical method. Using a Ss value adjusted to baseline HRST K to simulate site-specific storage behavior of the aquifer, diffusivity was solved for K. The heterogeneity of the aquifer is represented by the K distribution through the aquifer model grid. The model grid was developed from an interpretation of vertical K calculated from relatively high quality ZOP data on 0.305 m (1 ft) centers. The 0.305 m (1 ft) centers are greater than the expected resolution of the heterogeneity, so the vertical K data were used to develop model grids with thicker hydrostratigraphic layers to simulate and analyze the full MOG data sets.

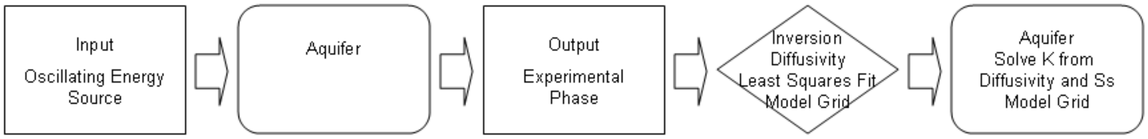

Figure 3 – Hydraulic tomography conceptual model. Adapted from Oldenburg and Li (2005).

Field Methods

Hydraulic tomography data were collected between source and receiver well pairs in the form of a shot gather or multi-offset gather (MOG) data set. A MOG consists of head data between a CPT location and, typically, 28 receiver locations. The intersecting ray paths for various locations of the oscillating head provides the basis of tomographic imaging (Fig. 4). The objective of the tomographic data set is to measure a large number of different ray paths through the aquifer between the source and receiver. Overlapping MOG data sets from different source locations increase the ray path density within the test interval of the aquifer and improve the resolution of the method. Phase shift and amplitude attenuation of the oscillating pressure wave were recorded with pressure transducers in the source and a vertical, five-channel receiver. To complete a single MOG, the receiver was moved using a steel tape and chain vice grips to six different positions within the well screen to obtain ray path coverage on 0.305 m (1 ft) centers. After the MOG data set was completed, the CPT source was moved 0.305 m (1 ft) and the CPT was repeated. The well pair test was complete after the CPT source had completely traversed its well screen interval (Fig. 4).

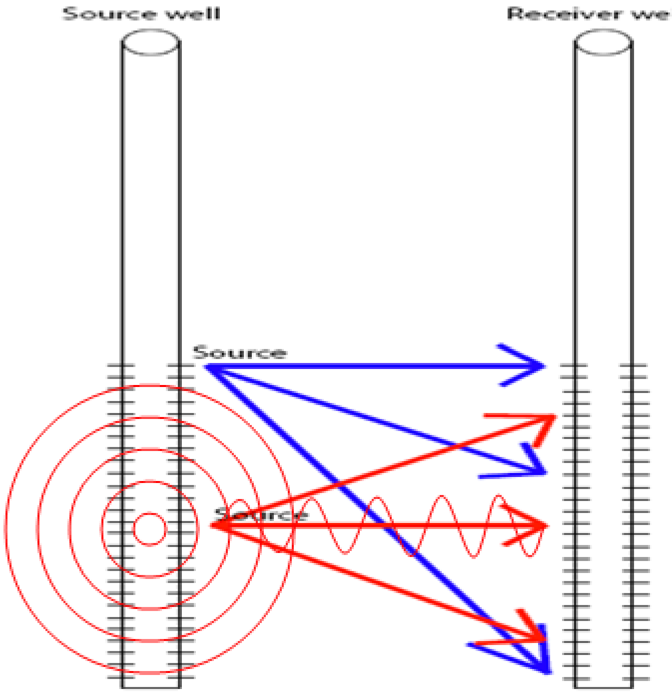

Figure 4 – Conceptual model of a CPT point source and two MOG data sets that depicts the straight ray paths of an oscillating sinusoidal signal. Figure modified from Wachter (2008).

The hydraulic pumping source was deployed in existing PVC monitoring wells and the pneumatic source was deployed using direct-push technology and a Geoprobe (Fig. 2). The CPT locations for each MOG were spaced on 0.305 m (1 ft) centers although the injection interval of the hydraulic and pneumatic source are different lengths. The pressure transducers, receiver design, and the hydraulic and pneumatic sources are further discussed in detail below.

Pressure Transducers

Head data during tomographic testing were collected with submersible pressure transducers. The transducer sensed changes in pressure exerted by the water environment on an internal strain gauge in the transducer. The receiver transducers were connected to a vented data cable that was connected to a data logger at the ground surface. A vented cable excluded the atmospheric pressure component, leaving only the water environment to exert pressure on the strain gauge and is therefore not subject to barometric fluctuations associated with changing weather patterns. Due to design constraints, the source transducer could not be vented and was, therefore, an absolute pressure gauge. Because the CPT tests were conducted over relatively short intervals, barometric pressure should not have had any effect on the recorded pressure head displacement. The pressure signal from the transducers was transmitted as an electronic signal to a data logger. Transducer and software calibration coefficients unique to each transducer enable the data logger to convert the pressure signal to equivalent feet of head above the transducer.

Receiver Array

The multi-level receiver consisted of five pressure transducers isolated by straddle packers (Fig. 5). Previous research demonstrated that isolating straddle packers improves the quality of the receiver signal; data sets have greater amplitude and the sine wave shape more closely matches the source signal (Engard, 2006).

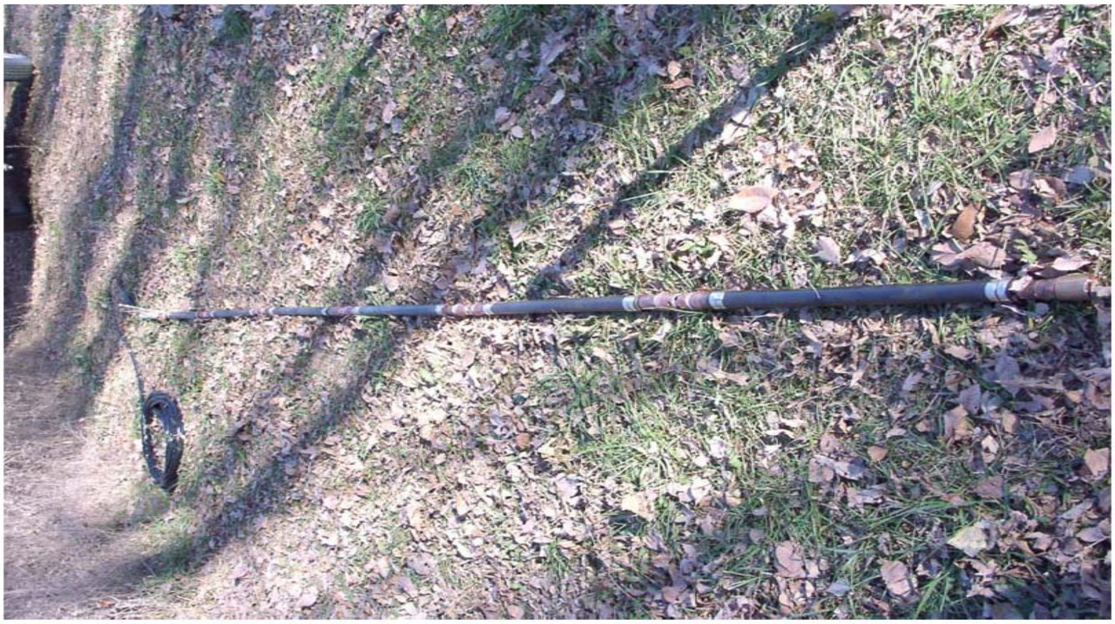

Figure 5 – A 5-channel receiver consisting of 5 transducers on 0.914 m (3 ft) centers isolated by 6 packers. Figure modified from Wachter (2008).

Each transducer is inside the hollow axis of the straddle packers and situated next to a port open to the aquifer. The ports are equidistance between the straddle packers on 0.914 m (3 ft) centers (Fig. 6 and Fig. 7). The new receiver has only a single sample port for each transducer to both facilitate transducer installation and to refine the discrete interval over which the signal is recorded (Fig. 6). The receiver was oriented with the transducer port facing towards the Geoprobe source to ensure that the CPT signal was not artificially attenuated by its well orientation, although previous tests indicated that orientation did not seem to significantly affect the received signal (Wachter, 2008).

Figure 6 – Transducer port located between the straddle packers of the new receiver.

Figure 7 – Transducer port located between the straddle packers of the old receiver.

Before installation of the vertical receiver in the well, a steel measuring tape was attached to the riser pipe near the top of the receiver assembly to record the depth below top of casing (BTOC). The lowest transducer was 4.5 m (14.9 ft) below the attachment point. This correction factor was added to the steel tape reading to obtain the lowest receiver location BTOC. The well casing(s) were surveyed and ties the sample locations to a common datum (ft msl) across the site (Table 1).

Tomography Survey Data		
Location	Elevation (ft msl)	Elevation (m msl)
Corps BM	827.56	252.24
HT-1	830.01	252.99
HT-2	829.66	252.88
HT-3	829.71	252.89
HT-4	830.13	253.02
HT-5	829.65	252.88
HT-6	830.27	253.07
7-1	828.34	252.48
11-1	828.36	252.48
Inj Well	829.79	252.92
Geoprobe BM	828.82	252.62

Well	Radius (m)	Radius (ft)
HT-3 to HT-1	4.77	15.65
HT-3 to HT-2	4.36	14.31
HT-3 to HT-4	4.46	14.62
HT-3 to HT-5	4.21	13.81
HT-3 to HT-6	3.99	13.10
HT-GP to HT-2	4.23	13.88
HT-GP to HT-3	4.25	13.94

Table 1 – Survey elevation and radial distances between wells.

The receiver is attached to a 3.18 cm (1¼-in) inside diameter (ID) PVC riser pipe string. The hollow axis of the PVC riser pipe conveys the transducer cables and a packer inflation line to the surface. Prior to initiating a CPT, the straddle packers are inflated with a nitrogen gas cylinder to isolate the test intervals.

Data processing programs for this study use the top-of-casing elevation, steel tape depth BTOC, and the lowest transducer elevation correction factor to calculate all the receiver transducer locations relative to the survey datum.

One multi-level receiver was used to record the pumped hydraulic source signal. The receiver was installed in the hollow axis of a 2-in ID receiver well (HT-3). A circular array of five, 2-in ID PVC source wells (i.e., HT-1, HT-2, HT-4, HT-5, or HT-6) surround the receiver well.

Two multi-level receivers were used to simultaneously record the pneumatic source signal generated in the Geoprobe drill string. The receivers were installed in two, 2-in ID receiver wells (i.e., HT-2 and HT-3).

CPT Sources

Two different types of oscillating sources were investigated for this research, a pumped hydraulic source with a 30-sec period and a pneumatic source with a 3-sec period. The pumped hydraulic source is mechanically constrained to the longer 30-second injection period, so it could not be matched to the 3 to 4-sec period of the pneumatic source used by Wachter (2008) and the 3-sec period of the Geoprobe pneumatic source used for this research. The basic phase shift equation (5) and radial point source equation (2) when considered in terms of the frequency inverse, period (i.e., $P = 1/f$), and the hydraulic conductivity predicts performance differences between the two CPT sources. In general, phase shift values obtained with a long period (i.e., low frequency) are smaller (i.e., less resolution) than a short period source. While the 30-sec period data set might have less resolution, its signal should propagate further through the aquifer, possibly increasing the effective ray path coverage. If the stimulation frequency is high then, in theory, the pneumatic signal along the longest MOG ray paths could attenuate such that the signal-to-noise ratio prevents meaningful assessment of the phase shift at the ends of the tomogram, possibly decreasing the effective ray path coverage. Also, because the exponential decay term includes 1/K, low hydraulic conductivity materials would tend to further exacerbate the signal attenuation of the 3-sec period data sets.

The hydraulic pumping source injects water through a 0.503 m (1.65 ft) interval between a pair of straddle packers. The pneumatic source injects water over a 0.305 m (1 ft) interval; so, it has less surface area to input energy. If energy delivered by the pneumatic source is significantly less, it could also attenuate the propagation distance of the ray, further modifying the range of the effective ray paths. Data interpretation relative to frequency stimulation is further discussed in the results section of the report.

Pumped Hydraulic Source – Monitoring Wells

The hydraulic source sensor used in this research consists of one pressure transducer isolated by two straddle packers (Fig. 8). A transducer was situated next to a port inside the hollow axis between the straddle packers.

Before installation, a steel measuring tape was attached to the riser pipe near the top of the source to record the depth BTOC. The transducer is 0.95 m (3.1 ft) below the attachment point. This correction factor was added to the steel tape reading to obtain the source location BTOC.

Figure 8 – Pumped hydraulic source assembly consisting of an injection interval straddled between two packers.

The pumped hydraulic source was attached to a 3.18 cm (1¼ -in) inside diameter (ID) PVC riser pipe string. The transducer cable and packer inflation line are conveyed to the surface on the outside of the riser pipe and are intermittently taped to the PVC string of riser pipes which extend to the surface. Prior to initiating a CPT, the straddle packers are inflated with a compressed nitrogen gas cylinder to isolate the aquifer test interval.

After packer inflation, the 3.18 cm (1¼ -in) ID string was connected to a pressurized water source (Fig. 9). Water from a stock tank was delivered to the excitation source with an approximate 70 gpm Grunfos pump and in-line pressure tank. Hoses conveyed the pressurized water to the riser pipe string and the packed-off interval of the source. The injection frequency of the pressurized water was regulated by a computer-controlled proportional valve, which created the sinusoidal, oscillating 30-sec period signal. As the injection continued, the stock tank was periodically filled with water from the discharge well located at GEMS. In Figure 9, the delivery hose continues out of the picture to the left where it is attached to the source assembly in HT-1. HT-3, with the riser pipe of the receiver array, transducer cables, inflation line and nitrogen tank, is visible in front of the stock tank. As water from the injection was pushed out of the well screen into the aquifer, the transducer in the PVC string monitors the injection pressure or head within the source. The inflated packers on either side of the injection interval isolate the source signal to a small interval relative to the rest of the well screen.

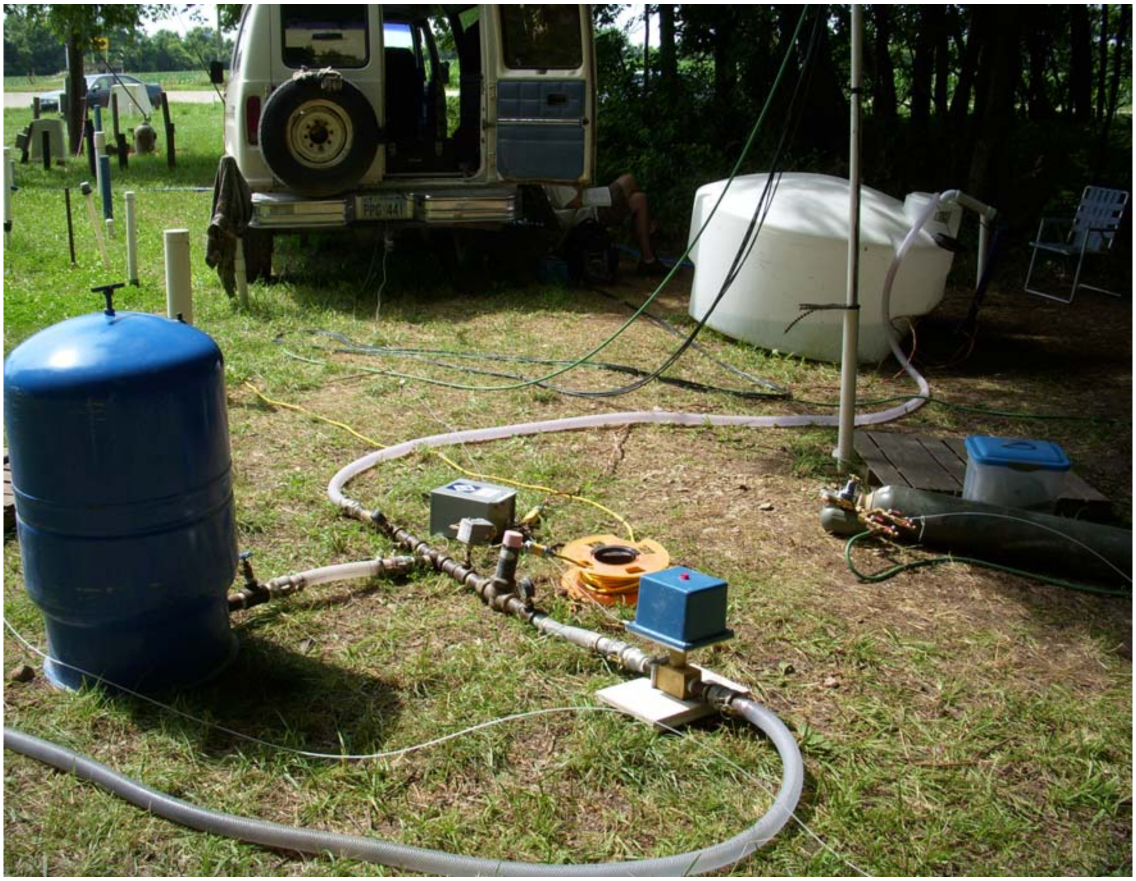

Figure 9 – Pumped hydraulic injection apparatus for the CPT.

Pneumatic Source – Geoprobe

The pneumatic source assembly consists of a 0.305 m (1 ft) long, 5.25 cm (2.07 in) ID well screen with 0.01 milled slots and an inflatable packer and rubber wafer packer above the screen (Fig. 10). A transducer is located in the center of the well screen interval.

Figure 10 – Pneumatic source assembly consisting of a PVC screen interval, PVC blank, wafer packer and inflation packer.

Before installation, a steel measuring tape is attached to the riser pipe near the top of the assembly to record the depth BTOC. The transducer is 0.899 m (2.95 ft) below the steel tape attachment point, but an older steel tape was modified to directly read the depth of the source location BTOC. The pneumatic source assembly is attached to a 3.18 cm (1¼ -in) ID PVC riser pipe string and assembled within the hollow axis of 6.67 cm (2.625 in) ID Geoprobe casing. The steel tape, transducer cable and packer inflation line is conveyed to the surface on the outside of the riser pipe and are intermittently taped to the PVC string (Fig. 11). In Figure 11, an air hose for the excitation source is attached to the manifold on the top of the PVC string. The receivers are in HT-3 (left) and HT-2 (right) located in the foreground of the picture. Transducer cables stretch from the receiver wells and Geoprobe casing to the data logger and computer controls in the van. An air hose stretches out of the picture to left to an air compressor which was used to supply the driving force for the pneumatic CPT.

Figure 11 – Pneumatic injection apparatus for the CPT with Geoprobe. The receivers are in HT-3 (left) and HT-2 (right) located in the foreground of the picture.

Air pressure to the well column was delivered through the air line to the manifold connected to the top of the PVC string (Fig. 12). In Figure 12, the computer controls both the pressure vent valve on the left and the pressure input valve on the right. The electrical wire carries a signal which turns them on and off at regular, 3-sec intervals. The signal is controlled by a computer driven signal generator. The nitrogen inflation hose and transducer cable are attached to the PVC string with electricians tape.

Figure 12 – Pneumatic air manifold.

Prior to initiating a CPT, the Geoprobe casing was retracted one foot to expose the pneumatic source. The PVC injection string was secured with chain vice grips that rested on the top of the Geoprobe casing. Both the injection string and the Geoprobe casing were pulled up in one-foot increments by the rig hydraulics. The wafer packers seal the casing and prevent sand heave in the casing due to the pressure differential between the aquifer and water column in the riser pipe string. The single packer was inflated with a nitrogen gas cylinder to further isolate the source interval. Upon initial inflation, the packer burst. Data collection proceeded with only the wafer packer to provide a seal between the casing and source. The fit was tested by attempting to move the string assembly within the Geoprobe string. The wafer packers tested relatively tight and were judged sufficient for the purposes of the test. In some cases, as the source was pulled with the Geoprobe casing, the source was somewhat loose and could be moved freely within the Geoprobe casing, which indicated that the formation may not have collapsed completely around the well screen or that the fit of the wafer packer varied. Without direct contact of the well screen to the formation, the application of energy may have been reduced, or, perhaps, some stimulating energy was lost up the Geoprobe casing.

The frequency-controlled pneumatic pressure source depressed the water column in the PVC riser pipe. The periodic pressurization and depressurization oscillates the water column in a sinusoidal pattern with a 3-sec period. Two, 5-channel receivers simultaneously recorded MOG data sets in HT-2 and HT-3 (Fig. 10). The two receivers were moved during the CPT to obtain MOG ray path coverage on 0.305 m (1 ft) centers, as previously described in the introduction to the Field Methods section. The CPT was repeated in one-foot increments and completed after the Geoprobe source traversed the aquifer segment which corresponds to the well screen interval at HT-2 and HT-3.

Data Collection

CPT data were collected from source-receiver well pairs during the Summer and Fall of 2009 at GEMS. For this study, the area of interest corresponds to the mill-slotted well screen interval of the hydraulic tomography wells that monitor the lower, coarser-grained alluvial section from bedrock to the semi-confining fine-grained silt and clay units (Fig. 2). The well screen intervals are approximately 232.0 m msl (761 ft msl) to

240.2 m msl (788 ft msl) and source and receiver data were collected on 0.305 m (1 ft) intervals, which is about the smallest practical data collection interval. Phase shift will increase with travel distance. The phase shift values between the wells in an offset profile should plot as a parabola for homogeneous K due to the different travel lengths of the rays within a MOG. The horizontal zero-offset profile (ZOP) rays correspond to the location with the least travel distance between the source and receiver. The remaining rays in the MOG are diagonal and correspond to locations with greater travel distance as the receiver moves up or down in its well (Fig. 13). Hydraulic conductivity variations cause deviations from the expected parabola of the homogenous case; higher hydraulic conductivity material results in a lower than expected phase shift and lower hydraulic conductivity material results in a higher than expected phase shift.

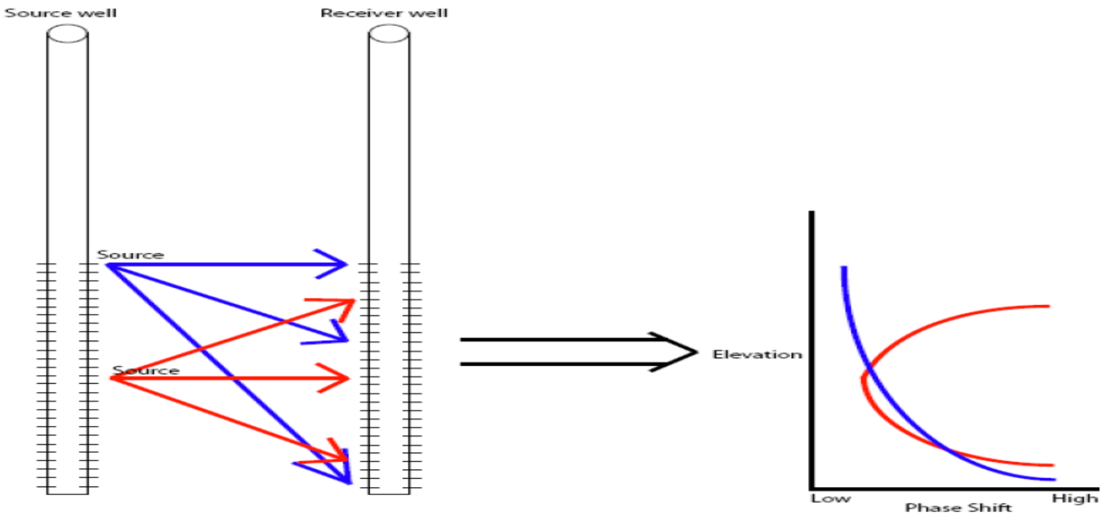

Figure 13 – Hydraulic tomography well pair with two conceptual MOG source locations. Modified from Wachter (2008).

Pumped hydraulic source data were generated from HT-1, HT-2, HT-4, HT-5, and HT-6. Hydraulic receiver data were collected in HT-3 (Fig. 1). Pneumatic source data were generated in HT-GP. Pneumatic receiver data were collected in HT-2 and HT-3 (Fig. 1). Field data collection sheets were used to record the serial numbers of the different transducers, well locations, source type (i.e., pumped or pneumatic), signal period (i.e., 30 or 3-sec), BTOC steel tape readings as well as the data record file names. The field data collection sheets are essential to subsequent data analysis because they correlate the different data records to the source and receiver positions as indicated by the steel tape and the correction factors.

The source and receiver signals were recorded with a data logger and saved to a laptop computer. A grounding rod connected to the data logger minimizes interference from ambient electrical noise. The sine wave signals were viewed real time on the laptop display screen. Data records were sequentially named with a unique identification that included the test number and date. Each individual data record has head data from the oscillating source and five receiver signals (Fig. 14).

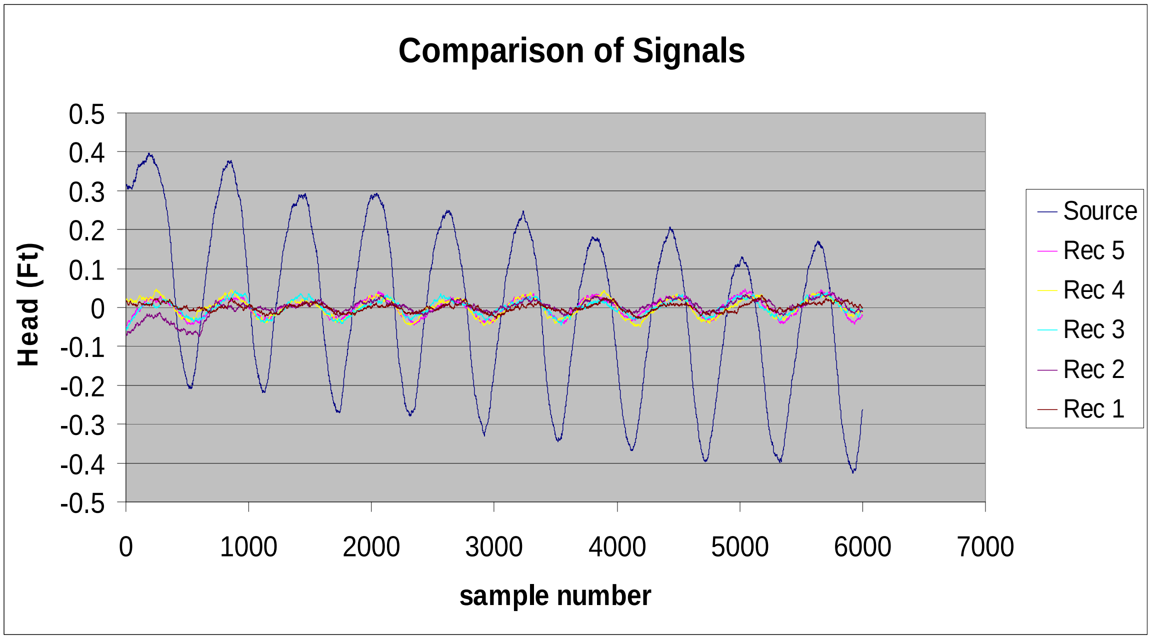

Figure 14 – One data record for a hydraulic CPT source and five receiver channels.

Six data records were collected at each source location and correspond to the different receiver locations necessary to complete the MOG (i.e., 30 locations). The two highest receiver transducers [240.5 m msl (789 ft msl) and 240.8 m msl (790 ft msl)] extend out of the well screen interval and up into the well casing, so valid pulse data could not be collected at these locations. At one well pair, HT-GP to HT-2, the highest three receiver transducers [i.e., 240.2 m msl (788 ft msl), 240.5 m msl (789 ft msl) and 240.8 m msl (790 ft msl)] extend out of the well screen and into the well casing, so valid pulse data were not collected at these locations.

The six data records were compiled by source location into an Excel file with the head data from the source and the 27 or 28 receiver locations (Fig. 15). In Figure 15, the receiver locations within the well casing are highlighted in red and are not used for further data processing. This MOG has 28 usable ray paths and the ZOP ray is highlighted in blue. Phase shift calculation and processing is further discussed in the Data Processing section of the report.

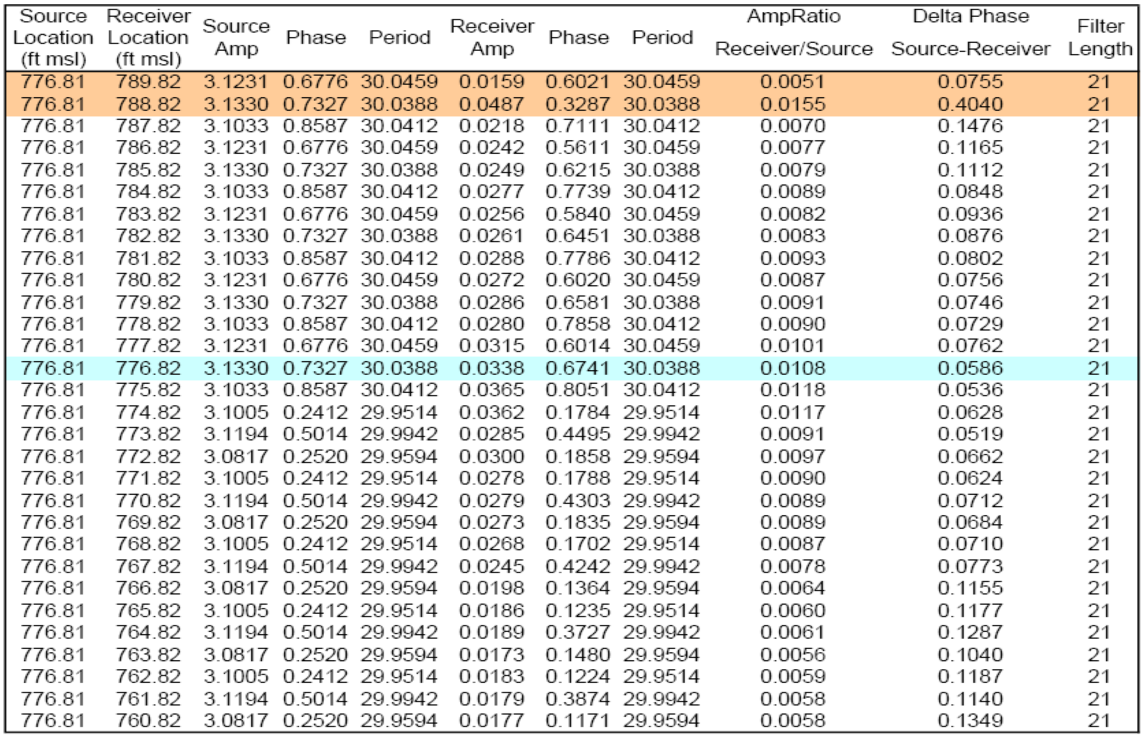

Source Location (ft msl)	Receiver Location (ft msl)	Source Amp	Phase	Period	Receiver Amp	Phase	Period	AmpRatio Receiver/Source	Delta Phase Source-Receiver	Filter Length
776.81	789.82	3.1231	0.6776	30.0459	0.0159	0.6021	30.0459	0.0051	0.0755	21
776.81	788.82	3.1330	0.7327	30.0388	0.0487	0.3287	30.0388	0.0155	0.4040	21
776.81	787.82	3.1033	0.8587	30.0412	0.0218	0.7111	30.0412	0.0070	0.1476	21
776.81	786.82	3.1231	0.6776	30.0459	0.0242	0.5611	30.0459	0.0077	0.1165	21
776.81	785.82	3.1330	0.7327	30.0388	0.0249	0.6215	30.0388	0.0079	0.1112	21
776.81	784.82	3.1033	0.8587	30.0412	0.0277	0.7739	30.0412	0.0089	0.0848	21
776.81	783.82	3.1231	0.6776	30.0459	0.0256	0.5840	30.0459	0.0082	0.0936	21
776.81	782.82	3.1330	0.7327	30.0388	0.0261	0.6451	30.0388	0.0083	0.0876	21
776.81	781.82	3.1033	0.8587	30.0412	0.0288	0.7786	30.0412	0.0093	0.0802	21
776.81	780.82	3.1231	0.6776	30.0459	0.0272	0.6020	30.0459	0.0087	0.0756	21
776.81	779.82	3.1330	0.7327	30.0388	0.0286	0.6581	30.0388	0.0091	0.0746	21
776.81	778.82	3.1033	0.8587	30.0412	0.0280	0.7858	30.0412	0.0090	0.0729	21
776.81	777.82	3.1231	0.6776	30.0459	0.0315	0.6014	30.0459	0.0101	0.0762	21
776.81	776.82	3.1330	0.7327	30.0388	0.0338	0.6741	30.0388	0.0108	0.0586	21
776.81	775.82	3.1033	0.8587	30.0412	0.0365	0.8051	30.0412	0.0118	0.0536	21
776.81	774.82	3.1005	0.2412	29.9514	0.0362	0.1784	29.9514	0.0117	0.0628	21
776.81	773.82	3.1194	0.5014	29.9942	0.0285	0.4495	29.9942	0.0091	0.0519	21
776.81	772.82	3.0817	0.2520	29.9594	0.0300	0.1858	29.9594	0.0097	0.0662	21
776.81	771.82	3.1005	0.2412	29.9514	0.0278	0.1788	29.9514	0.0090	0.0624	21
776.81	770.82	3.1194	0.5014	29.9942	0.0279	0.4303	29.9942	0.0089	0.0712	21
776.81	769.82	3.0817	0.2520	29.9594	0.0273	0.1835	29.9594	0.0089	0.0684	21
776.81	768.82	3.1005	0.2412	29.9514	0.0268	0.1702	29.9514	0.0087	0.0710	21
776.81	767.82	3.1194	0.5014	29.9942	0.0245	0.4242	29.9942	0.0078	0.0773	21
776.81	766.82	3.0817	0.2520	29.9594	0.0198	0.1364	29.9594	0.0064	0.1155	21
776.81	765.82	3.1005	0.2412	29.9514	0.0186	0.1235	29.9514	0.0060	0.1177	21
776.81	764.82	3.1194	0.5014	29.9942	0.0189	0.3727	29.9942	0.0061	0.1287	21
776.81	763.82	3.0817	0.2520	29.9594	0.0173	0.1480	29.9594	0.0056	0.1040	21
776.81	762.82	3.1005	0.2412	29.9514	0.0183	0.1224	29.9514	0.0059	0.1187	21
776.81	761.82	3.1194	0.5014	29.9942	0.0179	0.3874	29.9942	0.0058	0.1140	21
776.81	760.82	3.0817	0.2520	29.9594	0.0177	0.1171	29.9594	0.0058	0.1349	21

Figure 15 – The HT-6 to HT-3 MOG at 236.5 m msl (776.81 ft msl).

A well-pair test is complete after the source has traversed the entire length of its respective well screen (Fig. 13). Generally, 28 MOGs were collected from each source well, although only 27 MOG data sets were collected in HT-1 to HT-3 and HT-GP to HT-2 because the well screen was shorter and thereby reduced the test interval. The source and receiver positions determine the ray path density of the tomographic data sets. The ray path density is greatest near the center of the aquifer test interval where most rays cross and least near the top and bottom where only a single horizontal ray crosses (Fig. 13). Heterogeneity resolution is, therefore, greatest towards the center of the aquifer test interval where most of the ray paths cross and least near the top and bottom. Earlier modeling studies by Wachter (2008) compared results from the spatially weighted ray tracing method to a numerical model and determined that an optimal model grid of the aquifer had finer zones in the center and coarser zones at the top and bottom of the test interval. Greater model accuracy occurs towards the center of the grid due to greater ray path density and less accuracy occurs at the edges where few rays cross the model grid. This modeling study indicated that the hydraulic tomography method can resolve K zones over lengths of about 1 m (3.28 ft) where adequate ray density occurs.

Additionally, the total number of rays in a MOG will vary. For instance, a well pair with 28 source locations has 6 receiver positions per source, each with 5 transducers per receiver position [minus the 240.5 to 240.8 m msl (789 and 790 ft msl) locations in the well casing] and results in a ray path density of 784 diagonal and horizontal rays. If only the ZOP data are considered, this results in a data set with 28 horizontal ray paths (i.e., 28 source and receiver locations at the same elevation). The collective analysis of the different ray paths is the basis of the tomographic study. Data processing, modeling, inversion and K solution from diffusivity is further discussed in the next sections.

Data Processing

In contrast to the localized area of a slug test or bulk average of a pumping test, it is expected that more specific K values can be determined from the aquifer response along a ray path. In general, greater hydraulic conductivity detail will be gathered by using a spatially weighted ray-path analytical model for the ZOP and MOG ray paths. With the spatially weighted approximation, data analysis does not require a nonlinear regression and iterative solution of a numerical model typical of other hydraulic tomography methods.

Other hydraulic tomography methods typically use nonlinear least squares fitting with iteration, a method which typically takes a great deal of time and computing power to complete. But because the spatially weighted ray path method is analytical (i.e., a numerical model solution of groundwater equations is not necessary), it is much quicker and does not require a great deal of computing power, making the method accessible to desktop computers and Visual Basic computer language programs.

Data processing steps include head data extraction, sine wave fitting, phase shift and amplitude decay evaluation, ZOP and MOG ray path estimation, modeling, and linear tomographic inversion to estimate K, which is derived from the diffusivity ratio and an estimate of Ss. Ss is difficult to measure and, typically, representative values are usually just assumed from literature references (Fetter, 2001). But because K in this research is derived from the diffusivity ratio, a corrected Ss estimated from baseline HRST K and the experimental phase data were used during the modeling and inversion process to best represent the aquifer storage characteristics at GEMS.

In general, data processing began with the relatively more accurate ZOP phase shift data, which was used to calculate a representative K and model domain for the full data set MOG analysis. Corrected Ss was either estimated at the beginning of the ZOP modeling process with the calculation of a HRST-based surrogate phase which was sometimes used to replace poor experimental data, or after ZOP-determined K was calculated (Fig. 16 and Fig. 17). In the well pairs that did not require data replacement, ZOP analysis simply used a representative Ss value until the ZOP-determined K and Ss were adjusted to site-specific HRST K and the experimental phase before beginning the MOG analysis. The adjusted ZOP-determined K data and Ss were used for the subsequent MOG model domains. The corrected Ss and/or K were calculated based on the linear relationship of $\sqrt{S_S/K}$ in the basic equation (2). In addition to the ZOP and MOG data analysis, various data processing techniques to improve the fit of phase data to the model layers, such as anisotropy ratios and linear constraint, were also used to evaluate heterogeneity.

Data processing steps for this research were performed with a series of Visual Basic computer programs written by Dr. Carl McElwee called, FitAmpPhase, HydraulicTomAnal, and LeastSquaresSVD. In general, analysis for this study used higher quality ZOP data to estimate K at relatively discrete locations and to develop a model grid to represent the aquifer between the well pairs. Then the full MOG data sets were used to evaluate aquifer heterogeneity within the representative model of the aquifer. The tomographic conceptual model was updated in conjunction with the data processing and modeling steps by these programs (Fig. 16 and Fig. 17). The data processing steps and programs are further discussed in detail in the subsequent sections.

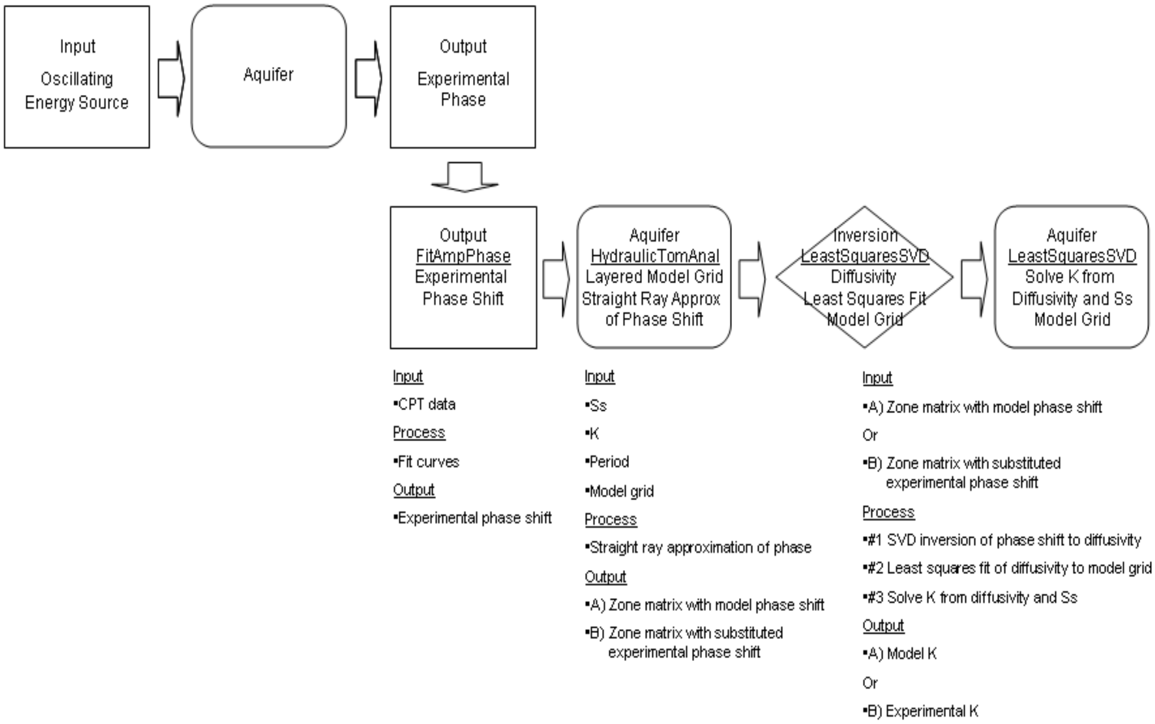

Figure 16 – Hydraulic tomography data processing steps.

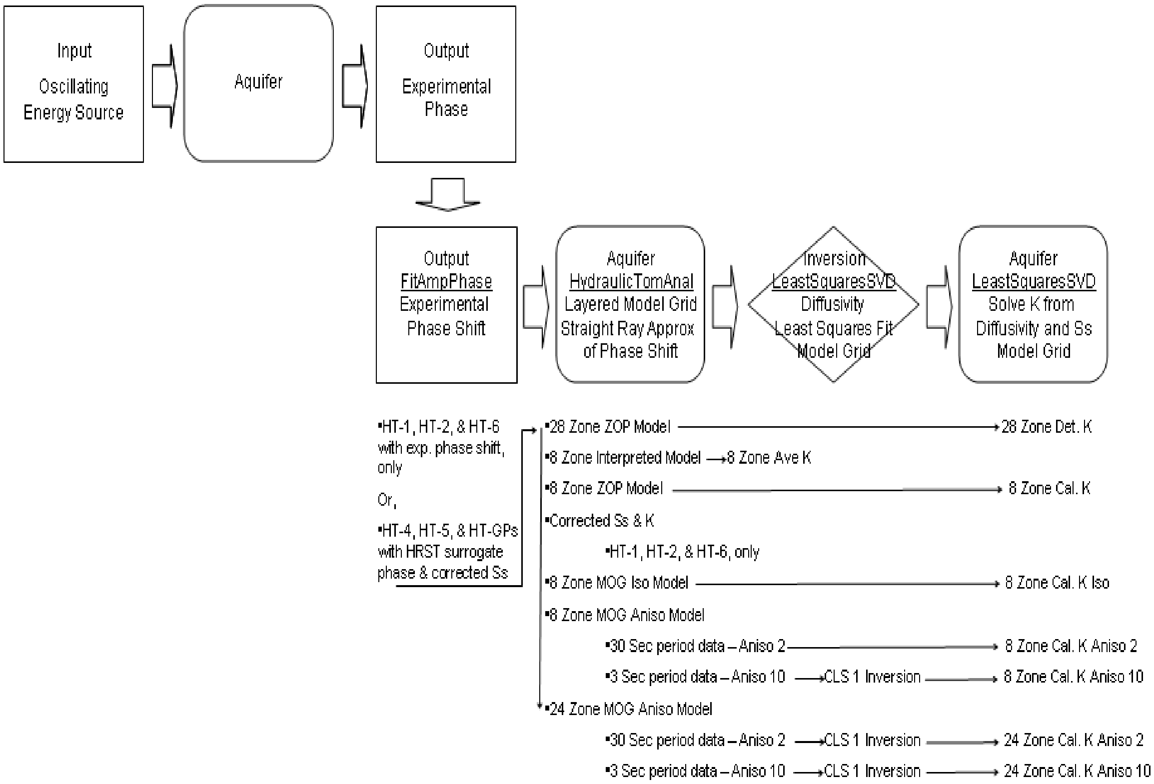

Figure 17 – Hydraulic tomography modeling steps.

FitAmpPhase

Head data were extracted from the data logger records and fitted to an idealized sine wave with a Visual Basic program, FitAmpPhase, written by Dr. Carl McElwee. Head data processing was repeated for each of the six data records associated with a source location. A 21-point filter was applied to all the recorded data. The filtering uses a moving average centered about 21 points to reduce spurious data noise. Both the amplitude and phase shift value can be related to the aquifer's physical property to facilitate flow as expressed by, *d*, in the basic theory equation (5). FitAmpPhase analyzes head data from the source and the five receiver transducers at once and, according to basic theory, estimates the amplitude (3), and phase shift (5). Engard (2006), determined that phase data should be the easiest to use to estimate diffusivity. Amplitude decays with distance and requires a correction based on the radial distance from the source, conversely, phase shift is equal to *d* without correction and is consequently used in this paper to estimate diffusivity and ultimately K. Phase shift calculations are further discussed below.

Experimental Phase Shift

FitAmpPhase generates a graph of the source and receiver amplitudes with their fitted sine curves (Fig. 18 and Fig. 19). These curves were visually inspected to evaluate the quality of the field data and to ensure that the program provided a representative approximation of the experimental sine waves collected in the field. The relative signal attenuation between the source and receiver can be judged from the amplitude difference between the sine curves. Figure 18 and Figure 19 depict the ZOP source and receiver signal, respectively, between HT-6 to HT-3 at the 236.8 m msl (776.8 ft msl) CPT location (Fig. 15). Head amplitude varies from approximately 0.91 m (3 ft) to 0.012 m (0.04 ft), between the two locations.

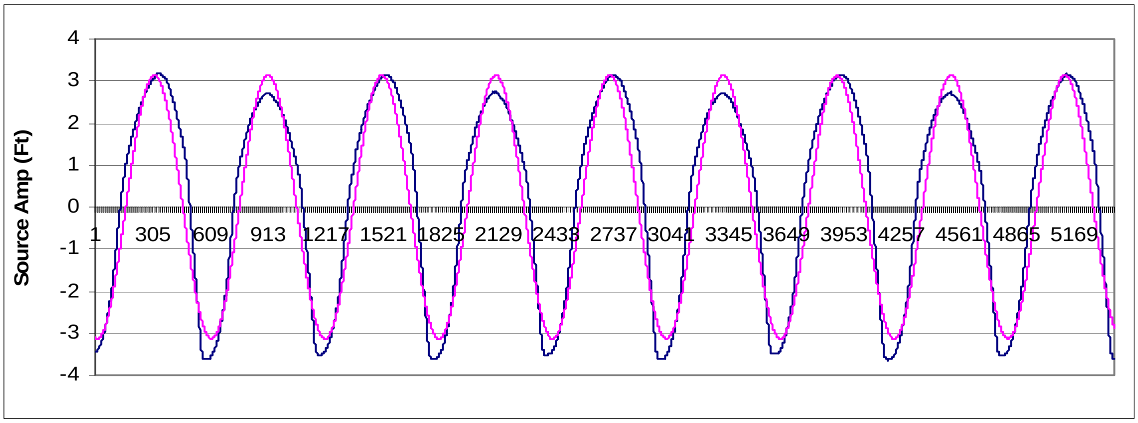

Figure 18 – HT-6 to HT-3 wave diagram of the CPT source at 235.8 m msl (776.8 ft msl) with experimental data (blue) and the FitAmpPhase-fitted curve (pink).

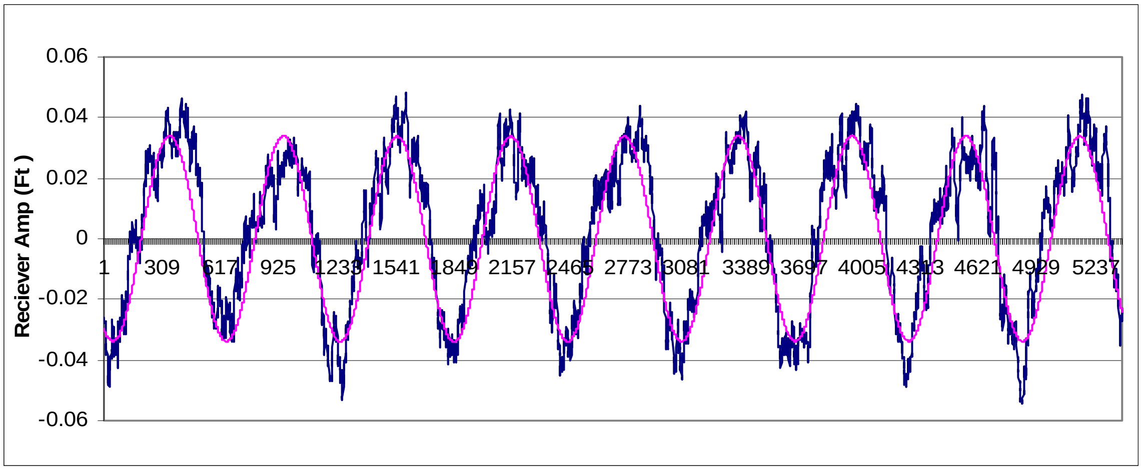

Figure 19 – HT-6 to HT-3 wave diagram of the attenuated receiver signal at 236.8 m msl (776.8 ft msl) with experimental data (blue) and the FitAmpPhase-fitted curve (pink).

The phase shift of a wave is the displacement of a specific point or benchmark in the cycle of the wave. The CPT produces a continuous sine waveform and the phase shift is an observable repositioning of this benchmark between successive locations. FitAmpPhase simply calculates the phase shift, Φ_r, by taking the difference between the fitted source and receiver phases (Fig 18 and 19). Experimental phase shift is measured in terms of 2π, so by programming convention the value will be between 0 and 1 (e.g., one cycle of a sine wave is 2π radians). Depending on the locations along the two sine curves which are used to calculate the phase shift, sometimes FitAmpPhase calculates a negative phase difference value (i.e., Delta Phase Source-Receiver, Fig. 15). The programming routine requires a positive phase value so this was manually corrected during data processing by adding a value of one, which is a unit cycle ($\Phi + 2\pi$), to the negative phase difference value. Adding an integral number of phase cycles does not change the sine wave.

After the experimental data were fit with a sine curve, FitAmpPhase plots amplitude ratio and phase shift of all receiver locations relative to ft msl based on the steel tape readings, correction factors, and well survey information. According to theory (5), the phase shift should plot nearly as a parabola or half parabola depending on the source location (Fig. 13). Any deviations from the parabolic shape are attributable to changes in K or, sometimes, poor data quality caused by a variety of conditions. Examples such as this can be seen on the phase shift graph between the source well, HT-6, and the receiver well, HT-3, at the 236.8 m msl (776.8 ft msl) MOG (Fig. 20). Deviations from the parabolic shape are attributable to changes in K between the two wells, except at the 240.5 and 240.8 m msl (788.8 and 789.8 ft msl) locations which are within the well casing and represent spurious data points that are removed from the MOG data set before further processing (Fig. 15).

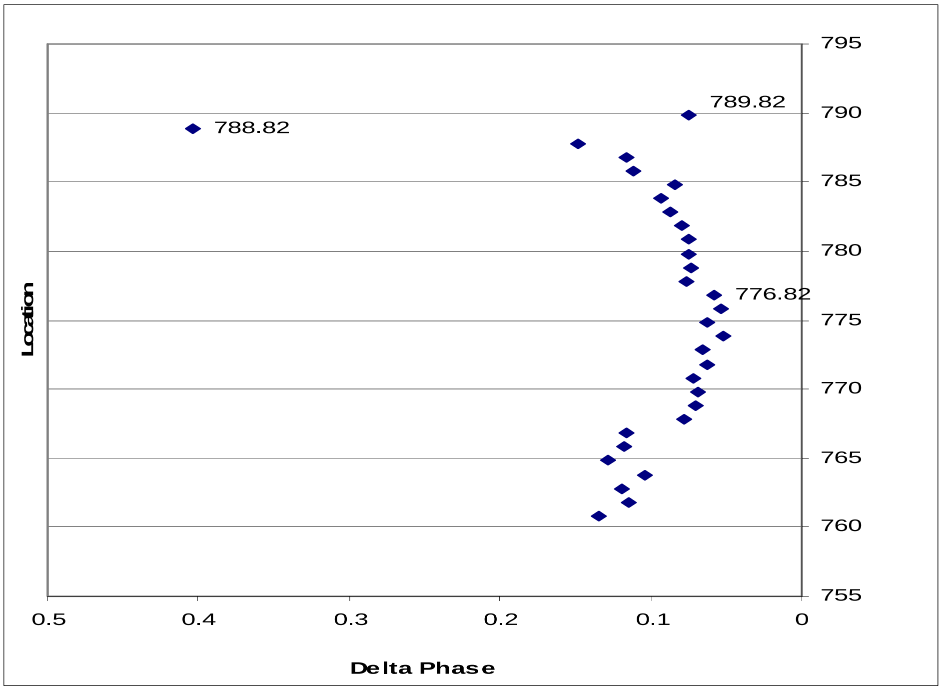

Figure 20 – HT-6 to HT-3 MOG phase shift at the 236.8 m msl (776.8 ft msl) source location. The 240.4 and 240.7 m msl (788.8 and 789.8 ft msl) locations are within the well casing. The 236.8 m msl (776.8 ft msl) location is the ZOP ray.

Sometimes the signal-to-noise ratio of the receiver amplitude data were poor and a discernable sine wave was not recovered for a particular ray path. Poor signal-to-noise data occurred in both the hydraulic and pneumatic data sets and resulted in head signals that could not be fitted by FitAmpPhase with a representative curve. Figure 21 depicts a typical source-receiver ray location with unusable head data at HT-5 to HT-3.

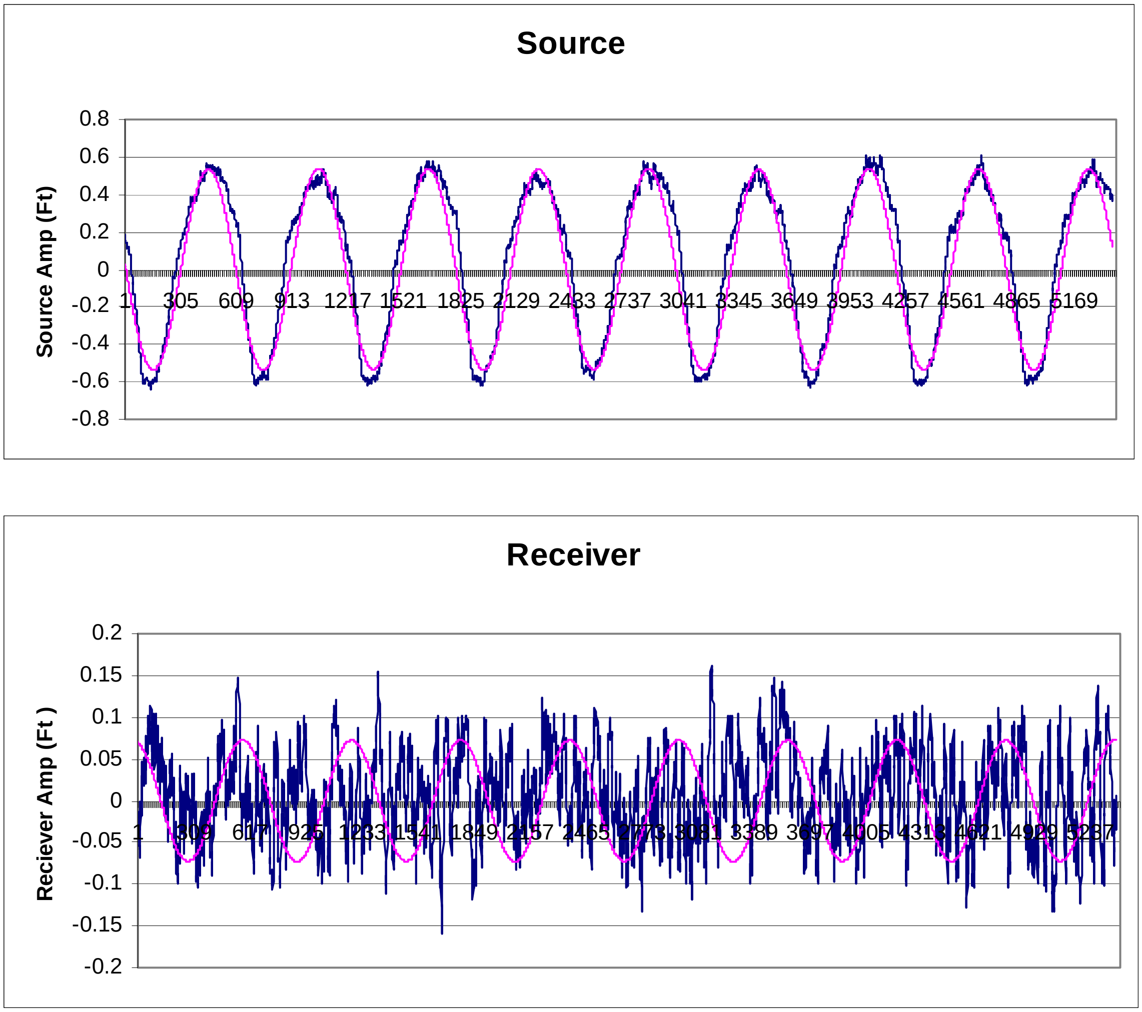

Figure 21 – HT-5 to HT-3 source receiver wave diagram from the 234.9 m msl (770.8 ft msl) source to the 233.1 m msl (764.8 ft msl) receiver.

Poor signal-to-noise data are attributable to several reasons. First, poor data possibly originate from a faulty source transducer which slowly failed during a portion of the hydraulic CPT, creating low signal-to-noise data in portions of the ZOP and MOG data sets. Also, low signal-to-noise data may have arisen from high frequency attenuation, low K materials and/or long offset distances. Additionally, stimulating energy from the pneumatic source to the formation could have been impeded due to energy loss up the casing past a ruptured packer and variable formation collapse around the well screen as the Geoprobe casing was retracted. A lower energy application would tend to exacerbate any signal attenuation associated with the high frequency signal of the pneumatic source.

MOG data sets with poor signal-to-noise data had a characteristic rough parabola shape with multiple outliers or sometimes a completely random pattern. Examples such as this can be seen on the 234.9 m msl (770.8 ft msl) MOG between HT-5 and HT-3 (Fig. 22). Spurious scatter pattern with deviations from the parabolic shape are attributable to poor signal-to-noise transducer data rather than heterogeneity. For example, the phase shift value generated from the source-receiver wave diagram presented in Figure 21 is visible at the 764.82 data point (Fig. 22).

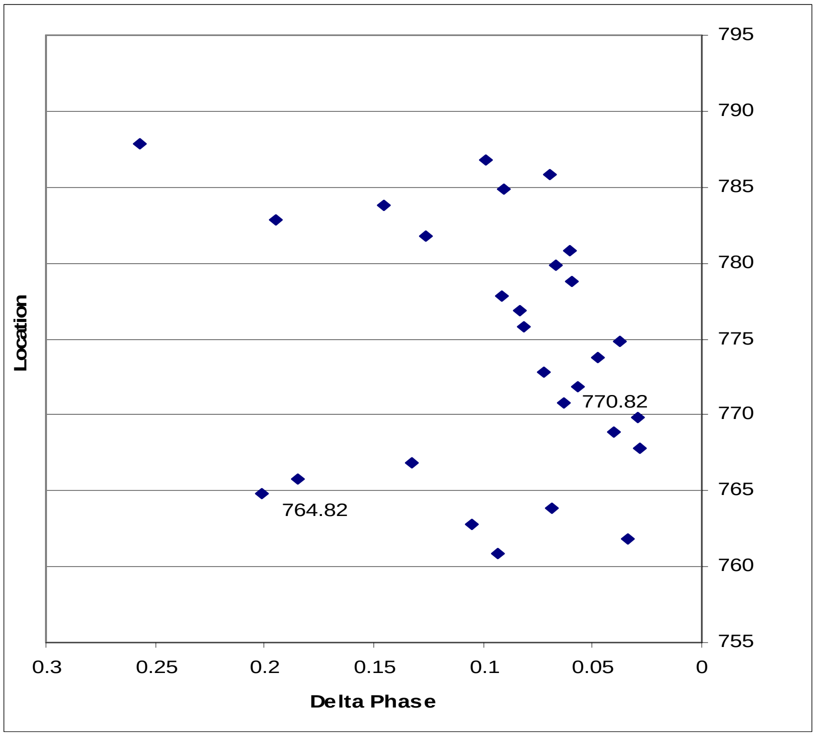

Figure 22 – Phase shift between the source well, HT-5, and the receiver well, HT-3, at the 234.9 m msl (770.8 ft msl) source location.

Well pairs HT-1 to HT-3, HT-2 to HT-3, and HT-6 to HT-3 had MOG data sets with relatively good phase shift data sets such as those in Figure 20. Well pairs HT-4 to HT-3, HT-5 to HT-3, HT-GP to HT-2, and HT-GP to HT-3 had some CPT locations with unusable phase shift data such as those depicted in Figure 22. At these locations, HRST K data were used to produce surrogate phase data for the questionable CPT locations.

Because phase shift should vary linearly with $\sqrt{S_S/K}$ it can be modeled to simulate the expected behavior of the phase data along a ray path according to baseline slug test data. Surrogate HRST phase and substitution is further discussed below.

HRST Surrogate Phase Shift and Corrected Ss

Well pairs from both the pumped hydraulic source (HT-4 to HT-3 and HT-5 to HT-3) and the pneumatic source (HT-GP to HT-2 and HT-GP to HT-3) had CPT locations with unusable ZOP or MOG experimental phase data (Fig. 17 and Tables 2 – 5).

To maximize the use of the variably impacted MOG data sets for tomographic analysis, the CPT source locations with spurious phase shift data were replaced with a surrogate values derived from HRST K data. All the hydraulic tomography wells were slug tested by Bret Engard, Brian Wachter and Pema Deki on 1-ft intervals that correspond to the CPT source and receiver locations (Deki, 2008; Wachter, 2008). The HRST methods provide a discrete interval, vertical profile of the aquifer K by well-known and scientifically accepted methods (Hvorslev, 1951; McElwee and Zenner, 1998; Zemansky and McElwee, 2005). The HRST K data provide a CPT benchmark and were used to linearly interpolate aquifer properties (i.e., phase) along a ray path in accordance with equation (5).

Surrogate phases for the different CPT locations with poor phase data (e.g., Fig. 22) were calculated through a multi-step process. Assuming Ss and a HRST K value, a theoretical phase was generated by manual calculation and with the ray path modeling program HydraulicTomAnal. As an example, the HT-4 to HT-3 ZOP calculation process is presented below (Fig. 23 and Table 2). First, HRST K data between the hydraulic source and receiver well (e.g., HT-4 to HT-3) was averaged to best incorporate the lateral heterogeneity between the two well locations. In the case of the pneumatic test data (HT-GP to HT-2 and HT-GP to HT-3), K data were only available in the receiver well(s);

therefore, only a single K value was used to represent the aquifer heterogeneity between the source and receiver for the pneumatic data sets.

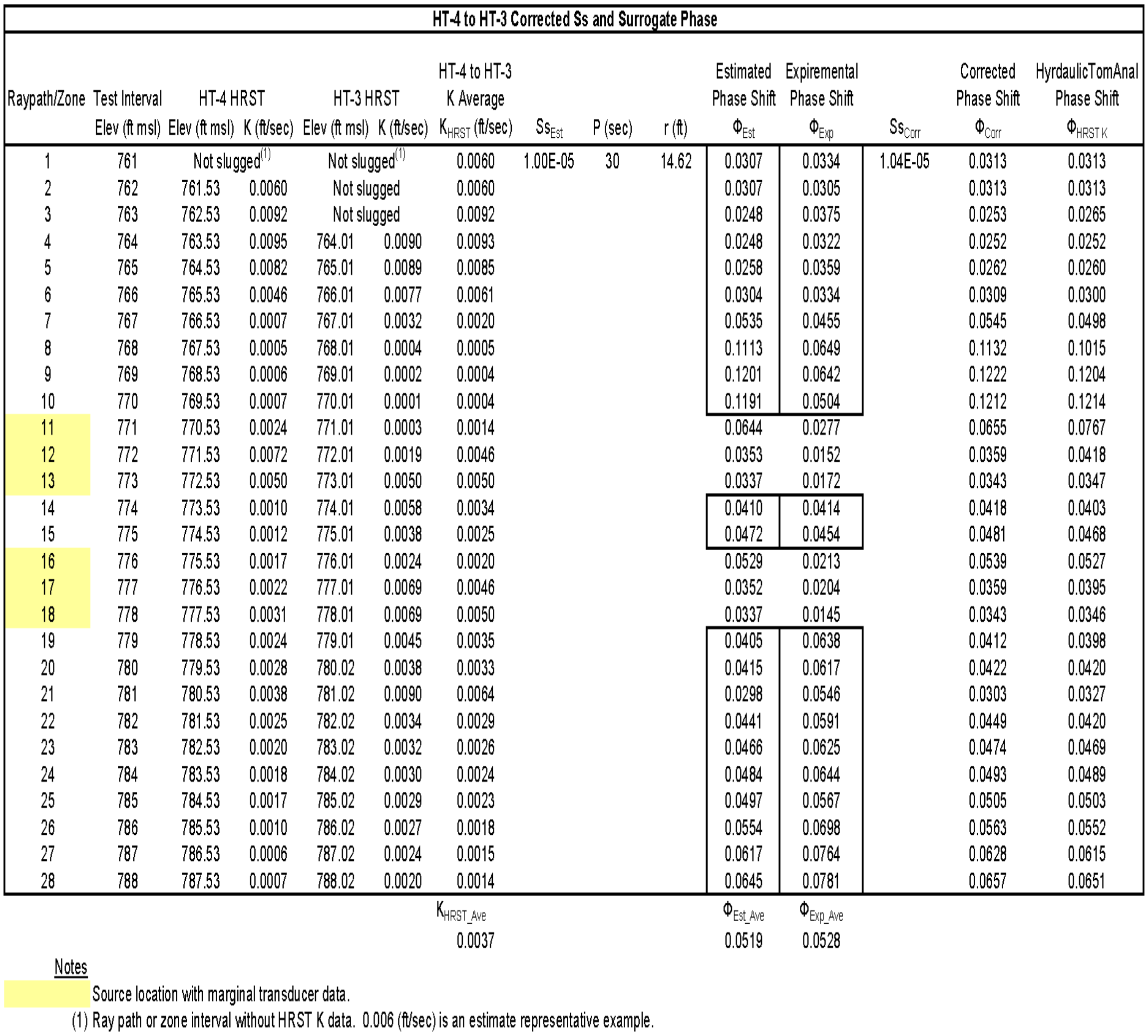

HT-4 to HT-3 Corrected Ss and Surrogate Phase

Raypath/Zone	Test Interval Elev (ft msl)	HT-4 HRST Elev (ft msl)	HT-4 HRST K (ft/sec)	HT-3 HRST Elev (ft msl)	HT-3 HRST K (ft/sec)	HT-4 to HT-3 K Average K_{HRST} (ft/sec)	Ss_{Est}	P (sec)	r (ft)	Estimated Phase Shift Φ_{Est}	Expiremental Phase Shift Φ_{Exp}	Ss_{Corr}	Corrected Phase Shift Φ_{Corr}	HyrdaulicTomAnal Phase Shift $\Phi_{HRST K}$
1	761	Not slugged(1)		Not slugged(1)		0.0060	1.00E-05	30	14.62	0.0307	0.0334	1.04E-05	0.0313	0.0313
2	762	761.53	0.0060	Not slugged		0.0060				0.0307	0.0305		0.0313	0.0313
3	763	762.53	0.0092	Not slugged		0.0092				0.0248	0.0375		0.0253	0.0265
4	764	763.53	0.0095	764.01	0.0090	0.0093				0.0248	0.0322		0.0252	0.0252
5	765	764.53	0.0082	765.01	0.0089	0.0085				0.0258	0.0359		0.0262	0.0260
6	766	765.53	0.0046	766.01	0.0077	0.0061				0.0304	0.0334		0.0309	0.0300
7	767	766.53	0.0007	767.01	0.0032	0.0020				0.0535	0.0455		0.0545	0.0498
8	768	767.53	0.0005	768.01	0.0004	0.0005				0.1113	0.0649		0.1132	0.1015
9	769	768.53	0.0006	769.01	0.0002	0.0004				0.1201	0.0642		0.1222	0.1204
10	770	769.53	0.0007	770.01	0.0001	0.0004				0.1191	0.0504		0.1212	0.1214
11	771	770.53	0.0024	771.01	0.0003	0.0014				0.0644	0.0277		0.0655	0.0767
12	772	771.53	0.0072	772.01	0.0019	0.0046				0.0353	0.0152		0.0359	0.0418
13	773	772.53	0.0050	773.01	0.0050	0.0050				0.0337	0.0172		0.0343	0.0347
14	774	773.53	0.0010	774.01	0.0058	0.0034				0.0410	0.0414		0.0418	0.0403
15	775	774.53	0.0012	775.01	0.0038	0.0025				0.0472	0.0454		0.0481	0.0468
16	776	775.53	0.0017	776.01	0.0024	0.0020				0.0529	0.0213		0.0539	0.0527
17	777	776.53	0.0022	777.01	0.0069	0.0046				0.0352	0.0204		0.0359	0.0395
18	778	777.53	0.0031	778.01	0.0069	0.0050				0.0337	0.0145		0.0343	0.0346
19	779	778.53	0.0024	779.01	0.0045	0.0035				0.0405	0.0638		0.0412	0.0398
20	780	779.53	0.0028	780.02	0.0038	0.0033				0.0415	0.0617		0.0422	0.0420
21	781	780.53	0.0038	781.02	0.0090	0.0064				0.0298	0.0546		0.0303	0.0327
22	782	781.53	0.0025	782.02	0.0034	0.0029				0.0441	0.0591		0.0449	0.0420
23	783	782.53	0.0020	783.02	0.0032	0.0026				0.0466	0.0625		0.0474	0.0469
24	784	783.53	0.0018	784.02	0.0030	0.0024				0.0484	0.0644		0.0493	0.0489
25	785	784.53	0.0017	785.02	0.0029	0.0023				0.0497	0.0567		0.0505	0.0503
26	786	785.53	0.0010	786.02	0.0027	0.0018				0.0554	0.0698		0.0563	0.0552
27	787	786.53	0.0006	787.02	0.0024	0.0015				0.0617	0.0764		0.0628	0.0615
28	788	787.53	0.0007	788.02	0.0020	0.0014				0.0645	0.0781		0.0657	0.0651
						K_{HRST_Ave}				Φ_{Est_Ave}	Φ_{Exp_Ave}			
						0.0037				0.0519	0.0528			

Notes

🟨 Source location with marginal transducer data.

(1) Ray path or zone interval without HRST K data. 0.006 (ft/sec) is an estimate representative example.

Figure 23 – HT-4 to HT-3 Corrected Ss and HRST K phase shift.

Next, an initial Ss value, Ss_{Est}, was chosen to calculate an estimated phase shift, Φ_{Est}, at each ZOP ray path or CPT location. Previous research at GEMS suggests that a Ss value of 0.00001 roughly represents the bulk compressive behavior and aquifer storage at GEMS. Along with the HRST K value, the estimated phase shift was calculated in Excel in accordance to equation (5), as presented below (8).

$$\Phi_{Est} = \sqrt{\frac{Ss_{Est}}{4\pi PK_{HRST}}}r \tag{8}$$

The estimated phase shift values were compared to the experimental phase shift data and a ratio of the two data sets were used to derive a corrected specific storage, Ss_{Corr}, based on the linear relationship between phase and the physical properties of the aquifer, $\sqrt{S_S/K}$. The phase shift ratio consisted of an average of the estimated phase, Φ_{Est_Ave}, and an average of the experimental phase, Φ_{Exp_Ave}. The ray path intervals with unusable phase data were excluded from both averages. If the HRST K and K in the experimental phase data are assumed to be equal at a given CPT or ray path, then the phase shift values should be equal. This allows a ratio of the average phase values to be solved for the different variables in the respective equations. With the HRST and experimental K held constant, K cancels out of the ratio along with the other non-variables, P, r, and 4π, leaving the corrected specific storage as the only unknown.

$$\Phi_{Exp\_Ave} = \sqrt{\frac{Ss_{Corr}}{4\pi PK_{Exp}}}r$$

$$\Phi_{Est\_Ave} = \sqrt{\frac{Ss_{Est}}{4\pi PK_{HRST}}}r$$

$$\frac{\Phi_{Exp\_Ave}}{\Phi_{Est\_Ave}} = \sqrt{\frac{\frac{Ss_{Corr}}{K_{Exp}}}{\frac{Ss_{Est}}{K_{HRST}}}} \qquad (9)$$

$$K_{Exp} = K_{HRST}$$

$$\frac{\Phi_{Exp\_Ave}}{\Phi_{Est\_Ave}} = \frac{\sqrt{Ss_{Corr}}}{\sqrt{Ss_{Est}}}$$

$$\left(\frac{\Phi_{Exp\_Ave}}{\Phi_{Est\_Ave}}\right)^2 Ss_{Est} = Ss_{Corr}$$

Using the corrected specific storage, Ss_{Corr}, along with the HRST K, Excel was used to calculate a corrected phase, Φ_{Corr}, to simulate the physical properties of the aquifer at a particular point.

$$\Phi_{Corr} = \sqrt{\frac{Ss_{Corr}}{4\pi PK_{HRST}}}r \qquad (10)$$

These corrected phase shift values were used as a check and compared to the estimated and experimental data to ensure that the ratio calculation method was plausible. The HydraulicTomAnal program was then used to model a straight ray approximation and phase shift from the HRST K, as described above, and the Ss_{Corr} value as inputs. The phase shift values derived by the HyraulicTomAnal program, $\Phi_{HRST\ K}$, were substituted into the experimental data sets as surrogates to replace the source locations with unusable data. HydraulicTomAnal was used to generate surrogate phase for both ZOP and MOG models at source locations with questionable data. Modeled phase and the resultant inverted K values were carried forward through each successive model run. The Ss_{Corr} was used for all subsequent modeling and inversion to ensure that K values derived from the diffusivity used the specific storage that best represented the site-specific aquifer storage characteristics at GEMS. Corrected specific storage was also calculated by a similar method for the other well pairs, too (Tables 6 – 8), and is further discussed below within the Data Processing section of the report.

HydraulicTomAnal Modeling

A Visual Basic program, HydraulicTomAnal, developed by Dr. Carl McElwee was used to generate ZOP and MOG ray path and phase data using a spatially weighted average method. A straight ray approximation was used to model the ray path data and estimate the phase shift within the test interval. With the spatially weighted approximation, data fitting does not require a nonlinear regression and iterative solution of a numerical model. The method solves for the path length in each element within a model grid and assumes that distances within the elements are linear and result from the boundary locations specified by model inputs at the source and receiver locations (Wang and Anderson, 1995).

The test interval or domain of the model consists of the area between the well screens of the tomographic well pair. The ray path model consists of a system of nodal points superimposed on a grid covering the test interval. Grid lines connect the node points and form subareas which are approximately evenly spaced boxes called elements

(Wang and Anderson, 1995). Zones are formed by one or more nodes (Fig. 24). Zones are simply regions of constant K and can encompass multiple elements or nodes.

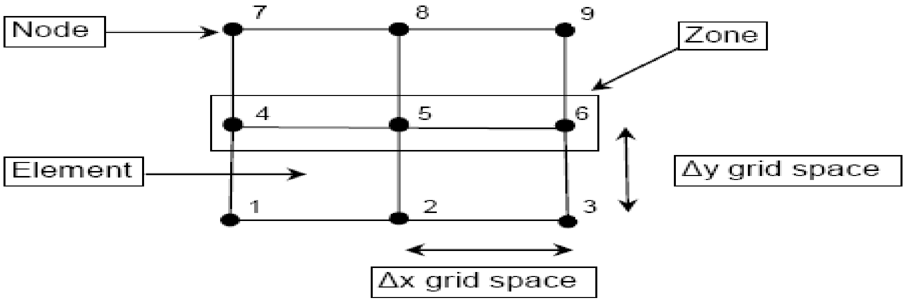

Figure 24 –Model grid with mesh-centered nodes. The zone is defined by Nodes 4, 5 and 6 and spans two elements.

While the HydraulicTomAnal program can specify zones by either elements or nodes, this research used the node option. The zones allow variable resolution across the model grid, both laterally and vertically to simulate heterogeneity.

Model inputs to HydraulicTomAnal are defined by the radial distance between wells, source and receiver elevation, Ss, as well as, the total number of nodes, elements, and K values. The HydraulicTomAnal program computes the distance of each ray path through every element based on the Pythagorean Theorem. The path length in each zone of differing K is multiplied by a coefficient involving K to get the phase. The path length is weighted by the K value at each node based on how close the node is to the ray path. Many nodes do not contribute because a ray is too far away. HydraulicTomAnal generates a matrix with ray path lengths and model phase output by nodes. The node matrix is reduced to a zone matrix by summing results for all nodes in a given zone.

Aquifer heterogeneity for this research was simulated with successive model runs using ZOP and MOG data sets (Fig. 16 and Fig. 17). In general, each of the well pairs had three modeling and corresponding inversion steps involving horizontal ZOP data to develop a reduced zone model to represent the aquifer, MOG data to evaluate aquifer anisotropy, and MOG data to evaluate aquifer lateral heterogeneity. First, ZOP data were modeled on a mesh grid spacing that corresponded to the 0.305 m (1 ft) spacing of the source-receiver, zero-offset profile locations within the well pair (Fig. 13). Depending on the number of source intervals in a well pair, either a 27 or 28 Zone model was used with the higher quality ZOP data to calculate an initial K for each source-receiver location. The vertical profile of this horizontal K data were used to develop a reduced 7 or 8 Zone model grid which better represents the expected resolution of the tomographic method. ZOP ray path estimation through the 7 or 8 Zone model and corresponding phase inversion determined another vertical distribution of K values which were subsequently used to define the MOG model runs. Second, the reduced 7 or 8 Zone model along with ZOP calculated K was used with the MOG data to simulate isotropic and varying anisotropic conditions. The anisotropic evaluation was completed for both the 3 and 30-sec period data sets. The shorter period (i.e., high frequency) data should have had greater resolution according to theory, so the tomography results might vary between the two CPT sources. For the 30-sec data, in addition to the isotropic model, three different anisotropic scenarios were evaluated at the HT-6 to HT-3 and HT-1 to HT-3 well pairs. The HT-GP to HT-2 well pair was used to evaluate 3-sec data set. These well pairs were used to determine the best anisotropy ratio to fit the experimental phase data to model phase generated by the straight ray approximation through the model grid. And finally, to evaluate lateral heterogeneity, the reduced zone model was modified to include three lateral zones within each horizontal zone, resulting in a 21 or 24 Zone model. The lateral model used MOG data along with the best fit anisotropy ratio for the 30 and 3-sec CPT data sets.

After ray path estimation, the zone matrix from each of the model runs were subsequently imported into LeastSquaresSVD for phase inversion and to solve for K from the diffusivity for the specified model zones. Model inversion and K results by LeastSquareSVD (Tables 9 – 15) are further discussed in the next section.

LeastSquareSVD

As discussed in the previous section, HydraulicTomAnal modeling first produces a node matrix and then a zone matrix with the theoretical geometry and computer generated phase for the model domain. The zone matrix is subsequently imported into LeastSquaresSVD, a Visual Basic program developed by Dr. Carl McElwee, for phase inversion to obtain diffusivity values and to solve K for the specified model zones. In general, Singular Value Decomposition (SVD) performs a least squares fitting inversion from phase to K using a set of linear equations (Aster et al., 2005). Because the equations are linear, iterations are not required. Deterministic calculation occurs when the number of rays is equal to the number of zones. Least squares fit calculation occurs when the number of rays exceeds the number of model zones.

The zone matrix, G, imported from HydraulicTomAnal, consists of an *m* by *n* matrix, where *m* is the number of ray paths and equations and *n* is the number of zones and unknowns. The SVD method divides G into the following equation:

$$G = UWV^T$$

Where U is a *m* by *m* orthogonal matrix, W is a *m* by *n* matrix with nonnegative diagonal elements known as singular values, V is an n by n orthogonal matrix, and the T indicates that V is a transpose matrix.

If the model phase and the zone matrix are inverted, it will give back the original input K used to define the model domain and verifies the model geometry. Conversely, substitution of experimental phase data and the zone matrix followed by inversion will result in the deterministic or least squares fit of K to the aquifer model grid. The chi squared value of the model inversion is so small that it is effectively zero, indicating the inversion reproduced the model nearly perfectly. In general, if the results were perfect, a chi squared value of 0 would be obtained.

The chi squared value and standard deviations will vary from the theoretical value and grow larger when information such as surrogate phase data, experimental data, ZOP-derived K values, model constraints and lateral anisotropy are introduced to simulate aquifer heterogeneity over the different, successive model runs. Evaluating whether the statistically calculated K values plausibly fit the model (e.g., “goodness of fit”) is indicated by the chi squared value. Also, a reasonable data fit to the model was indicated by standard deviation of the K value estimated from the fit. Generally, if the standard deviation value is about 10% of the fitted value or less it is usually considered a good fit. As the standard deviations become larger, the fit becomes poorer.

Earlier research by Wachter (2008) determined that data processing requires constraining to suppress anomalously large K values which are sometimes present as spurious artifacts due to instability in the inversion process. Some of the calculated singular values are so low that they are indistinguishable from zero within the diagonal matrix, effectively rendering them non-unique. SVD analysis was used to apply constraint to the linear analysis to reduce the effects of non-unique values that can arise as the model matrixes are generated. Constrained least squares factors of 1 and 10 were evaluated on the HT-6 to HT-3 and HT-1 to HT-3 well pair to determine the best data fit for the hydraulic CPT data. Constraint factors of 1, 10, and 100 were evaluated on the HT-GP to HT-3 well pair to determine the best data fit for the pneumatic CPT data. The constraint factor of 1 gives equal weight to both the initial input K values of the model domain as well as the calculated K values from the experimental data. The constraint factor of 10 strongly weights the initial guess and does not allow the data fit to stray far from the initial model domain. A 0 constraint factor has no weight and the data fit from the experimental phase to derived K can be vastly different from the initial guess. As indicated by chi squares and standard deviation values, an inversion constraint factor of 1 was selected as the most effective constraining factor. To suppress spurious data points in this research, some of the pneumatic CPT data (3-sec period) were constrained during the anisotropy evaluation and both the hydraulic CPT data (i.e., 30-sec period) and pneumatic CPT data (i.e., 3-sec period) were constrained for the final, lateral heterogeneity model inversion (Fig. 16 and Fig. 17).

At the completion of the successive model runs, the final, constrained, least squares fit K values were contoured against elevation and radial distance between source and receiver using a public domain program called QuickGrid. The program contours between points written in an x,y,z format, which corresponds to radius, elevation, and K values determined by the SVD analysis from this research. In all of the contour plots of K, the source well is on the left side and receiver well is on the right. Using the HT-6 to

HT-3 well pair as an example because it seemed to be the best initial data set, the modeling, inversion, statistical K determination, anisotropy evaluation and constraint factors are further discussed below.

ZOP Modeling And Inversion

Model – 27 or 28 Zone Zero-Offset Model

To obtain the expected, optimal 1 m (3.28 ft) grid resolution, ZOP data were initially modeled on a finer 0.3048 m (1 ft) vertical spacing in a 27 or 28 zone model (Fig. 25). This zone spacing corresponds to the experimental source and receiver locations in a well and the number of zones reflect the total number of source locations in CPT. ZOP data are expected to have the best quality within a MOG data set because they have the shortest ray path distance between the source and receiver (Fig. 13). As such, modeling with ZOP data should have somewhat greater quality than the offset diagonal rays. Consequently, ZOP data were used to develop a coarser model grid to represent the aquifer and better match the expected tomographic resolution so lateral heterogeneity could be evaluated. In the HT-6 to HT-3 ZOP model below (Fig. 25), source locations are on 0.3048 m (1ft) centers over the approximate well screen interval of 232.0 to 240.2 m msl (761 to 788 ft msl) and correspond to the odd numbered nodes, 3 – 57, within the model grid. Receiver locations are directly across from the source and correspond to the even number nodes, 4 – 58. Using K, Ss and ZOP data, HydraulicTomAnal modeled the 28 horizontal ray paths, each through their respective zone, to generate the model geometry and theoretical model phase for this grid. Either HRST K values or an average HRST K value (0.003 ft/sec) were input as reasonable initial constant K nodes to generate the model matrix and phase. The model grids used for this research are presented in Appendix A.

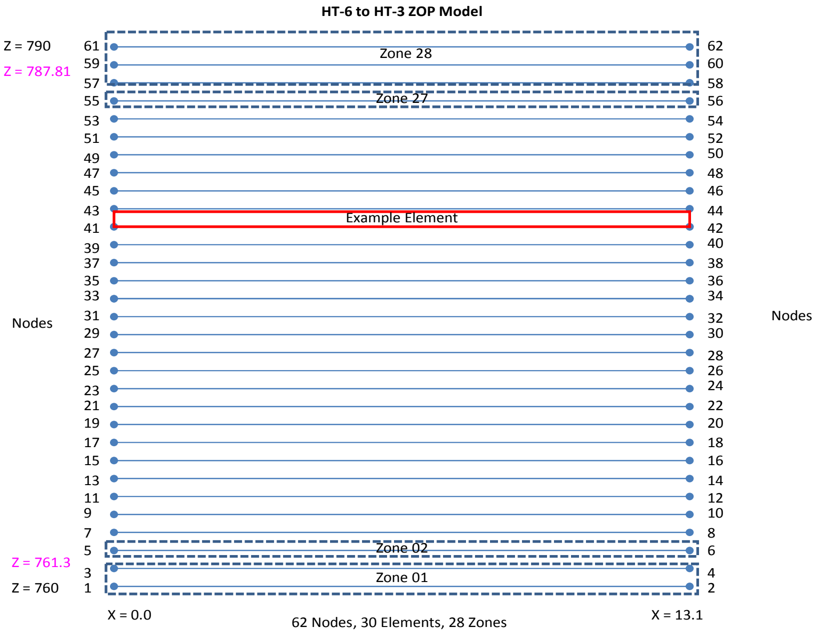

Figure 25 – Conceptual 28 zone finite difference model grid for HydraulicTomAnal.

SVD Inversion, Deterministic – 27 or 28 Zone Zero-Offset Phase Shift

As a representative data set, SVD analysis of the HT-6 to HT-3 was used to evaluate the deterministic K calculated from the ZOP data through the 28 zone model (Fig. 25). The K values correspond to the 28 zero-offset source and receiver locations in the ZOP data set (Fig. 26). This initial modeling and inversion with the high quality ZOP data (i.e., least amount of offset) has the same number of equations and unknowns and is a direct, deterministic 1:1 inversion. Inversion and data fit to the model resulting in a chi squared value so small (e.g., 3.45E-31) that it is effectively zero, indicating a close fit to the expected model. The vertical distribution of deterministic K plotted against the CPT location or ray path interval represent a profile of the aquifer between the well pair. The profile was interpreted into thicker hydrostratigraphic layers which better match the expected tomography resolution (Fig. 27). Inversion and modeling results are included in Tables 9 – 15. Deterministic K profiles are presented in Appendix B.

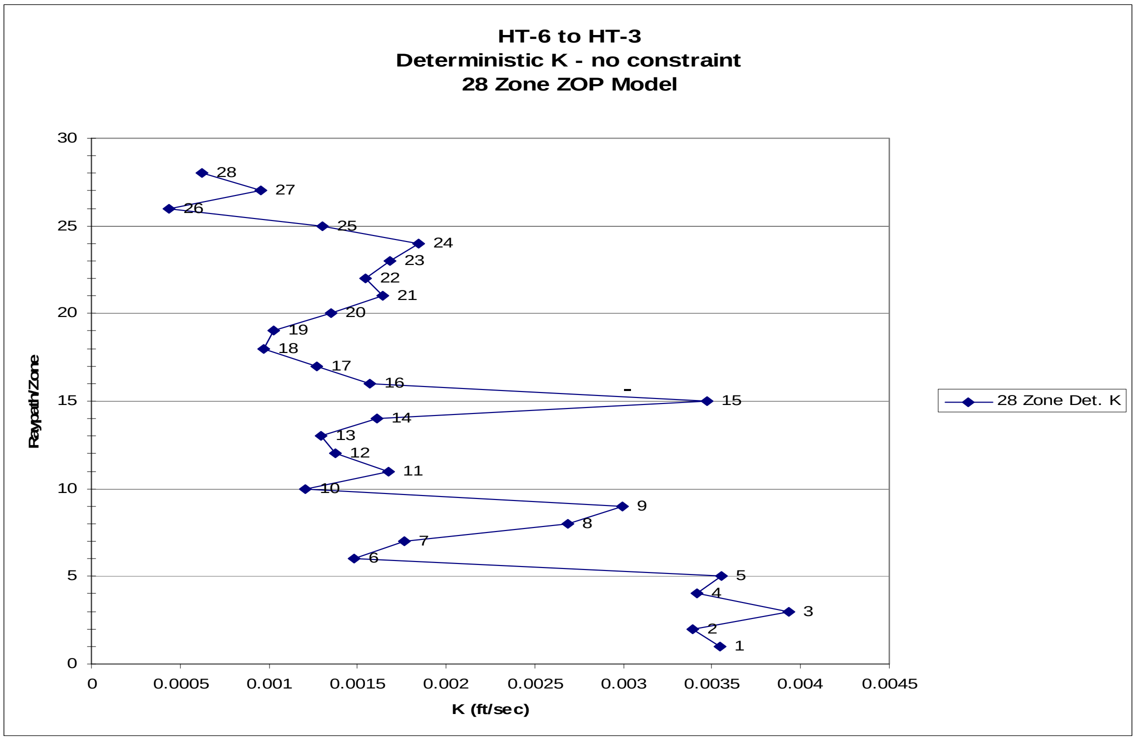

Figure 26 – HT-6 to HT-3 Deterministic calculated K from ZOP data set. K locations are on 0.305 m (1 ft) centers which correspond to the source and receiver locations.

Model – Interpreted Deterministic K

As discussed, the tomography source and receiver locations are on 0.305 m (1 ft) centers which result in deterministic K values on an interval that exceeds the expected resolution of the tomographic method (Fig. 26). Therefore, the profile of the experimental test interval was interpreted into a reduced zone model with thicker vertical zones that is more representative of the expected tomographic resolution. Typically, interpretation of the ZOP deterministic K between the different well pairs resulted in an either 7 or 8 reduced-zone model that represents larger hydrostratigraphic zones (Fig. 27).

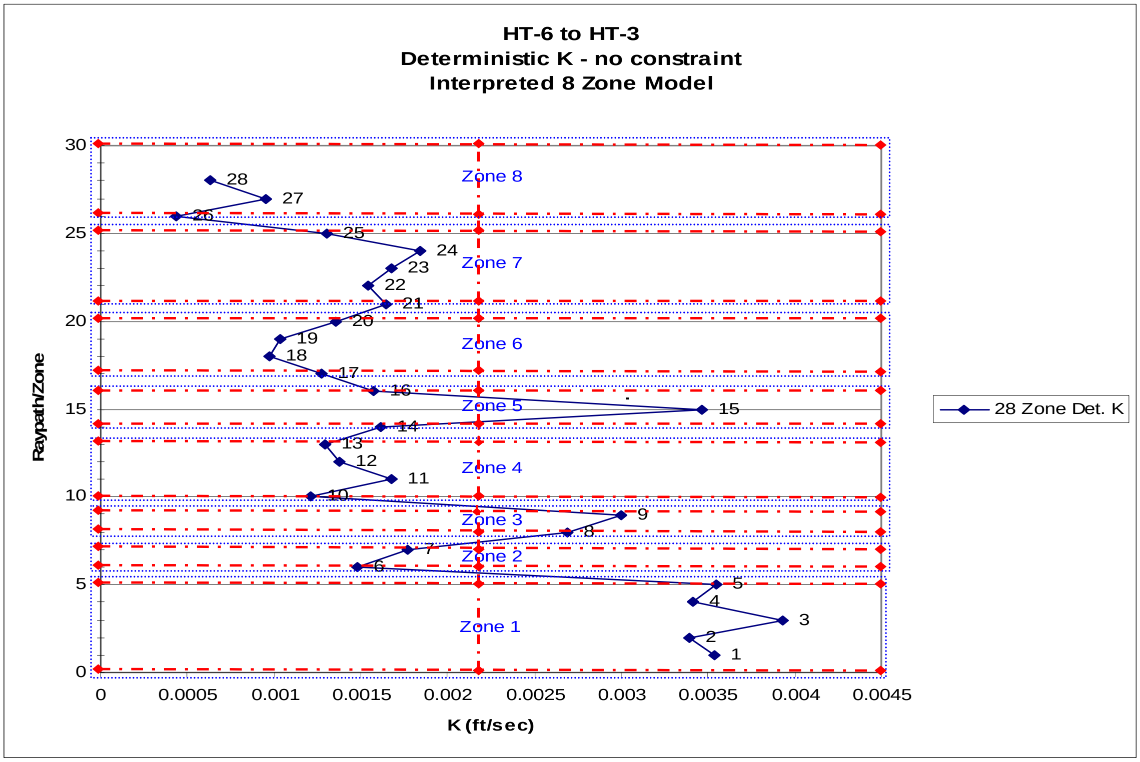

Figure 27 – HT-6 to HT-3 interpretation of ZOP deterministic K.

The K value for each zone is an average of the deterministic ZOP K values in the model zone. For example, zone 1 K is an arithmetic average of the deterministic K values derived from zones 1-5 in the initial ZOP model; zone 2 is an average of the deterministic K values from zone 6-7; and so forth. The average K values are used for the model domain parameter for the next ZOP model run, which simulates ZOP data through the reduced zone model to simulate the best possible representation of the aquifer for heterogeneity analysis with the MOG data sets. ZOP modeling through interpreted, reduced zone model is discussed in the next section.

Model – 7 or 8 Reduced Zone Model

The thicker vertical elements of the interpreted 7 or 8 Zone model (Fig. 27) more closely fall within the expected 1 m (3.28 ft) resolution of the tomographic method. The HT-6 to HT-3 example model has 8 zones, 30 elements, and 48 nodes over the approximate 232.0 to 240.2 m msl (761 to 788 ft msl) well screen interval (Fig. 28). Each zone is composed of either two elements or six nodes (Fig. 28). The center nodes in the model grid define two lateral elements; these extra nodes correspond to the midpoint between the source and receiver location. While the vertical space between the nodes typically increase, the source and receiver intervals for the ray paths are still on 0.3048 m (1ft) centers and, in many cases, more than one ZOP ray will travel through each zone.

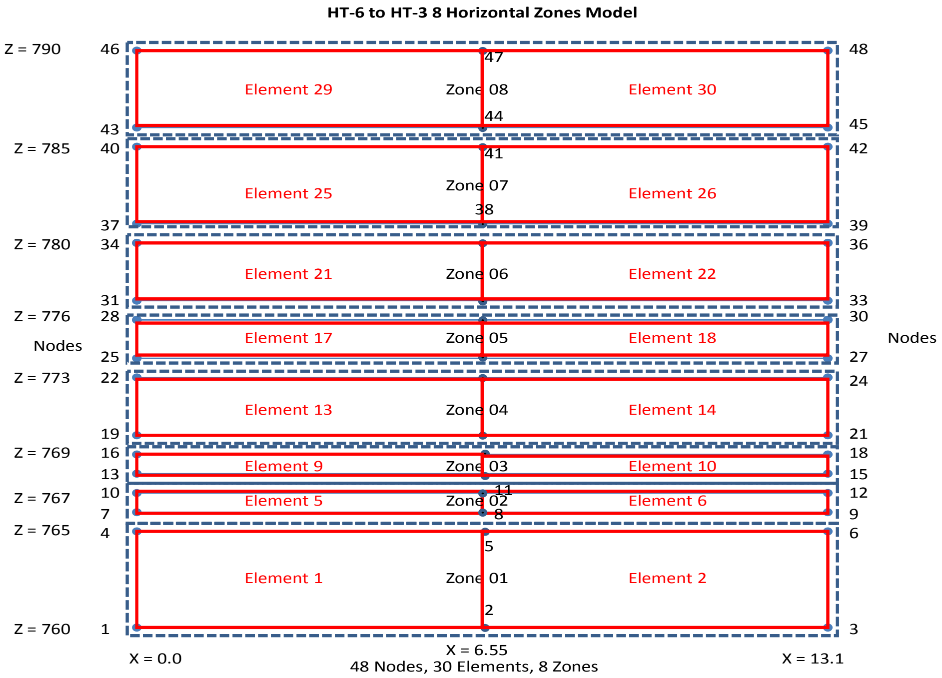

Figure 28 – Conceptual 8 zone model grid with 8 zones (blue) and 30 elements (red).

The Ss, average deterministic K of the different hydrostratigraphic layers, and source-receiver locations along with the model grid, were input into the

HydraulicTomAnal program to generate the model phase and geometry for the 8 zone model. The average deterministic K values are held constant across the respective zones (i.e., across two elements). This model should be a close approximation of the different hydrostratigraphic layers in the CPT test interval and was subsequently used to evaluate aquifer heterogeneity with the diagonal rays in the MOG data sets.

To check if the 7 or 8 zone model adequately represents the larger ZOP data set, the reduced zone model phase was plotted against the ZOP experimental phase (Fig. 29). 28 ZOP rays were used to generate the model matrix and phase by straight ray approximation for both the reduced zone ZOP model (e.g., 7 or 8 zones) and the initial ZOP model (e.g., 27 or 28 zones). The initial ZOP model used either HRST K or an average of the HRST K (0.003 ft/sec) inputs to represent the hydraulic conductivity at GEMS. However, this reduced zone model used K value inputs determined from the inversion of the initial ZOP model matrix and ZOP experimental phase shift. Consequently, the phase shift produced by the reduced zone model should be an average of the ZOP experimental phase shift because its input K values are an average of the deterministic K values. At HT-6 to HT-3, the smoother curve of the 8 zone model phase reflects the average value of the deterministic K assigned to the thicker layers of the model. The sharper curve of the experimental phase reflects the experimental phase at each of the initial 0.3048 m (1ft) layers used in the 28 zone model. When plotted together, the different phase results should have a similar curve shape and the smoother curve reflects the average K values applied to the thicker layers of the 7 or 8 zone model (Fig. 29). The node data summaries for all the well pairs are presented in Appendix C.

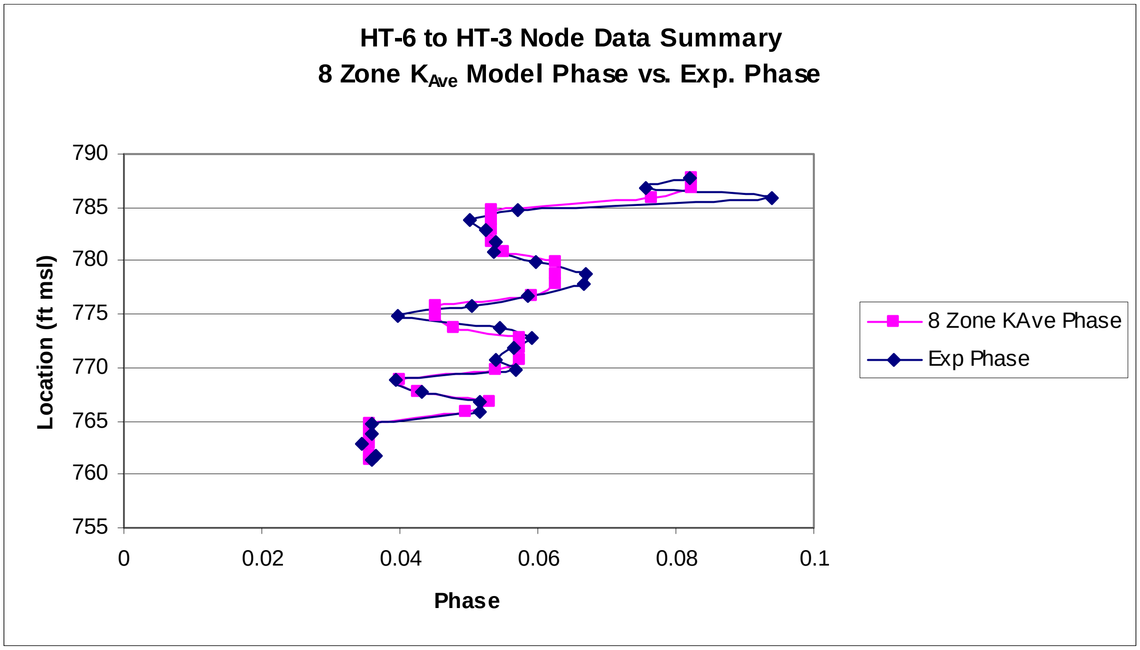

Figure 29 – Experimental ZOP phase shift plotted against ZOP 8 zone model phase shift.

SVD Inversion, Least Squares Fit – 7 or 8 Reduced Zone Phase Shift

SVD analysis of the reduced zone model with the ratio of zones to rays no longer 1:1, generates a least squares fit of K that corresponds to the six nodes in each zone (Fig. 28). Similar to the reduced zone phase plot against the experimental ZOP phase (Fig. 29), the reduced zone calculated K is an average value of the deterministic K in each zone (Fig. 30). Up to this point SVD analysis and modeling used a Ss estimate of 0.00001 to derive K from diffusivity. The initial 1E-05 value is considered to be representative of the aquifer storage characteristic at GEMS based on literature references and previous work by Wachter (2008) and others. In many research applications, Ss values are simply assumed from literature references because Ss values are quite small and difficult to measure in situ; but, since K is related to diffusivity in this method, the Ss value and K from this inversion was further corrected to more closely match the baseline

HRST K data and the phase shift data before further modeling with the MOG data sets. Ss and K correction are further discussed in the next section and the ZOP deterministic K verses least squares calculated K plots are presented in Appendix D.

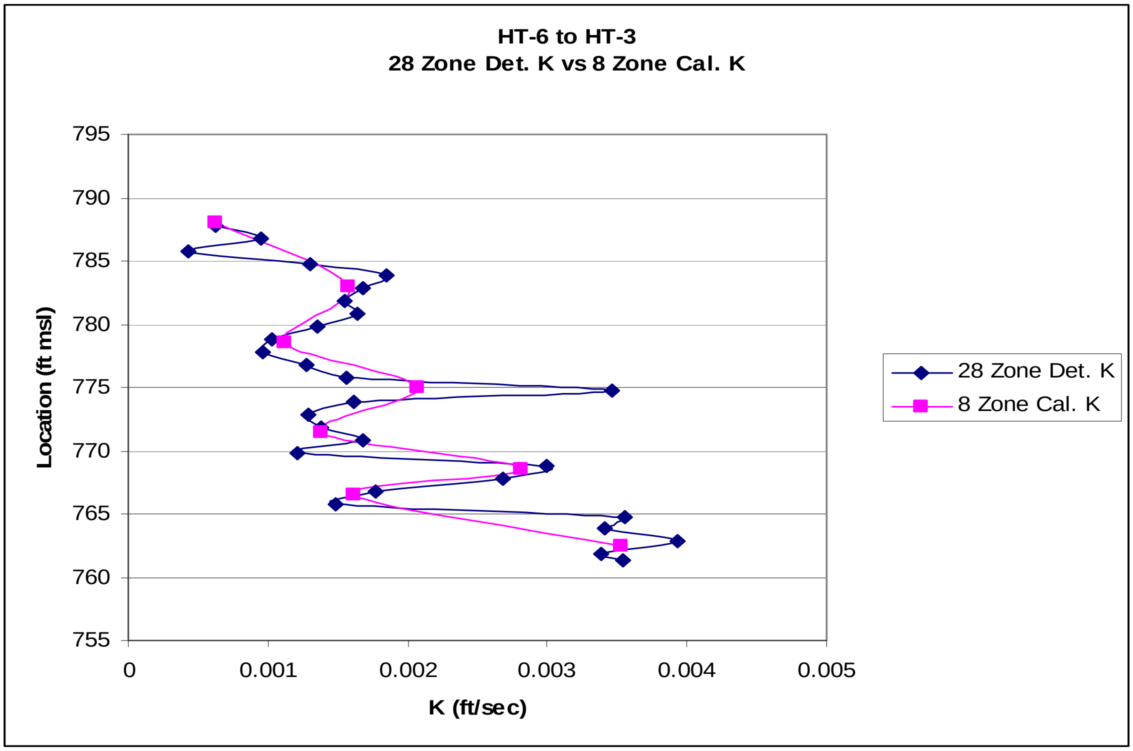

Figure 30 – 28 Zone deterministic K plotted against 8 Zone calculated K.

Corrected Ss and K

Much like the procedure used to calculate a surrogate phase from HRST Ks, Ss and K were corrected to match GEMS conditions before further modeling with the MOG data sets was completed. Because phase should vary linearly with $\sqrt{S_S/K}$, the corrected Ss value, Ss_{Corr}, was calculated from the average HSRT K values, $K_{\text{HRST\_Ave}}$, and the average deterministic K values from the 28 zone ZOP model, $K_{Det\_ZOP\_Ave}$. Assuming the phase shift at the HRST and CPT locations are equal, the corrected *Ss* is calculated from their ratio using Equation (5).

$$
\begin{aligned}
&\Phi_{HRST} = \sqrt{\frac{Ss_{Corr}}{4\pi PK_{HRST\_Ave}}r} \\
&\Phi_{Det\_ZOP} = \sqrt{\frac{Ss_{Est}}{4\pi PK_{Det\_ZOP\_Ave}}r} \\
&\frac{\Phi_{HRST}}{\Phi_{Det\_ZOP}} = \frac{\sqrt{\frac{Ss_{Corr}}{4\pi PK_{HRST\_Ave}}r}}{\sqrt{\frac{Ss_{Est}}{4\pi PK_{Det\_ZOP\_Ave}}r}} \\
&\Phi_{HRST} = \Phi_{Det\_ZOP} \\
&\frac{\Phi_{HRST}}{\Phi_{Det\_ZOP}} = 1 = \frac{\sqrt{\frac{Ss_{Corr}}{4\pi PK_{HRST\_Ave}}r}}{\sqrt{\frac{Ss_{Est}}{4\pi PK_{Det\_ZOP\_Ave}}r}} \\
&\frac{Ss_{Est}}{K_{Det\_ZOP\_Ave}} = \frac{Ss_{Corr}}{K_{HRST\_Ave}} \\
&\frac{Ss_{Est}}{K_{Det\_ZOP\_Ave}} K_{HRST\_Ave} = Ss_{Corr}
\end{aligned}
\tag{11}
$$

where Ss_{Est} is the initial value of 0.00001; $K_{Det\_ZOP\_Ave}$ is the average of the deterministic K values; and K_{HRST_Ave} is the average HRST K between the source and receiver wells.

Based on this assumption, all analyses were simply adjusted to the new Ss_{Corr} value with a correction factor derived from a ratio of the average slug test and model deterministic K values:

$$\frac{K_{HRST\_Ave}}{K_{Det\_ZOP\_Ave}} = \text{Correction Factor} \tag{12}$$

When phase shift is constant, the relationship between Ss and K in the basic phase shift Equation (5) is linear so changes to K or Ss will vary in proportion to each other (e.g., reduction of Ss by a factor 0.5 will reduce K by a factor of 0.5). Accordingly, the deterministic and least squares calculated K values were multiplied by the correction factor to reflect the corrected Ss for HT-1 to HT-3, HT-2 to HT-3, and HT-6 to HT-3 well pairs (Tables 6 – 7). As previously discussed, corrected Ss in well pairs with poor phase data (i.e., HT-4, HT-5 and both HT-GP locations) was calculated by a similar method during generation of HRST surrogate phase (Table 2 – 5). As an example, the corrected HT-6 to

HT-3 deterministic K values and those from the reduced zone model are presented below (Fig. 31) and as Table 8.

HT-6 to HT-3 Corrected Ss and K

HRST Well	HRST K_{Ave}	28 Zone ZOP Model	28 Zone Det. K (ft/sec)	Corr. Factor	28 Zone Det. K (ft/sec)	8 Zone ZOP Model	8 Zone Cal. K (ft/sec)	Corr. Factor	8 Zone Cal. K (ft/sec)
		Ss_{Est} 1.00E-05		1.6265	Ss_{Corr} 1.63E-05	Ss_{Est} 1.00E-05		1.6924	Ss_{Corr} 1.69E-05
HT-6	0.0025	1	0.0035		0.0058	1	0.0035		0.0060
HT-3	0.0038	2	0.0034		0.0055	2	0.0016		0.0027
		3	0.0039		0.0064	3	0.0028		0.0048
		4	0.0034		0.0056	4	0.0014		0.0023
		5	0.0036		0.0058	5	0.0021	x 1.6924 =	0.0035
		6	0.0015		0.0024	6	0.0011		0.0019
		7	0.0018		0.0029	7	0.0016		0.0027
		8	0.0027		0.0044	8	0.0006		0.0011
		9	0.0030		0.0049				
		10	0.0012		0.0020				
		11	0.0017		0.0027				
		12	0.0014		0.0022				
		13	0.0013		0.0021				
		14	0.0016	x 1.6265 =	0.0026				
		15	0.0035		0.0056				
		16	0.0016		0.0026				
		17	0.0013		0.0021				
		18	0.0010		0.0016				
		19	0.0010		0.0017				
		20	0.0014		0.0022				
		21	0.0016		0.0027				
		22	0.0015		0.0025				
		23	0.0017		0.0027				
		24	0.0018		0.0030				
		25	0.0013		0.0021				
		26	0.0004		0.0007				
		27	0.0010		0.0016				
		28	0.0006		0.0010				
	Ave K_{HRST_Ave}		Ave K_{Det_Est}		Ave K_{Det_Corr}		Ave 8 Zone K_{ZOP_Est}		Ave 8 Zone K_{ZOP_Corr}
	0.0031		0.0019		0.0031		0.0018		0.0031

Figure 31 – HT-6 to HT-3 correction for Ss and 8 zone ZOP K.

The correction factor was calculated using both the 28 zone deterministic K and the 8 zone calculated K to evaluate if there was any significant difference between the two data sets. After correction, the average K value between the 28 and 8 zone K values were the same as the average HRST K, so the correction factor was valid for either data set. A comparison of the corrected K vertical profile, which best represents the storage characteristic of the aquifer, to the uncorrected values is presented in Figure 32. The corrected K and Ss values were used for the initial values of the MOG model to evaluate anisotropy and lateral heterogeneity.

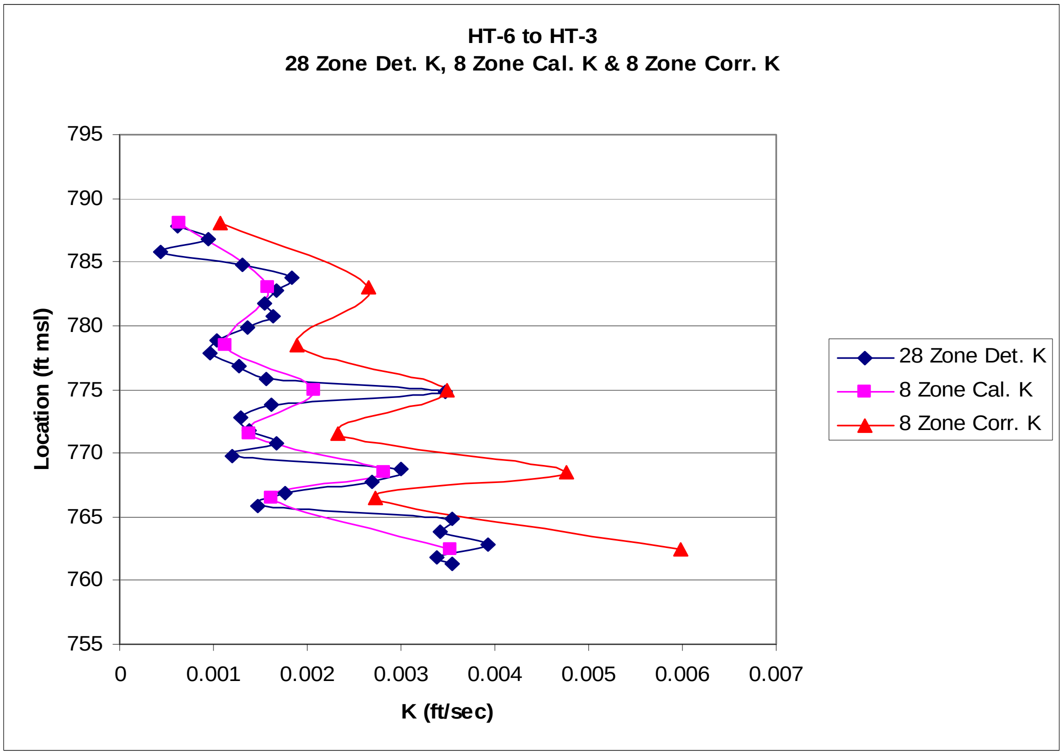

Figure 32 – HT-6 to HT-3 K vertical profile adjusted for the calculated Ss that represents site-specific aquifer storage characteristics.

In the case of well pairs using HRST K as surrogate data, as discussed earlier, the corrected Ss was calculated from the outset so there was no need to correct the K values before MOG data analysis. In these instances, deterministic and calculated K was carried forward through each successive model run and inversion (Tables 2-5). The corrected ZOP K plots for HT-1 to HT-3, HT-2 to HT-3, and HT-6 to HT-3 are presented in Appendix E.

MOG Modeling And Inversion

Model – 7 or 8 Zone Isotropic and Anisotropic Models

After the 7 or 8 reduced-zone model geometry was developed and verified, and the Ss and calculated K were corrected to site-specific conditions (through either surrogate phase calculation or normalization to HRST K), modeling with MOG data sets was initiated with the reduced-zone model to determine a representative anisotropy ratio for data processing. The appropriate anisotropy ratio will be applied to the final MOG model used to evaluate the lateral heterogeneity in the aquifer. Anisotropic evaluation was completed for both the pumped hydraulic CPT data (30-sec period) and the pneumatic CPT data (3-sec period). Different anisotropy ratios were evaluated with HydraulicTomAnalV21Aniso, a new Visual Basic program developed by Dr. Carl McElwee, which generates MOG ray path data that simulates aquifer anisotropy across the model grid. HydraulicTomAnalV21Aniso functions the same as HydraulicTomAnalV21, but, instead of isotropic modeling, the computer code was modified to generate anisotropic effects across an element or zone. Anisotropy ratios can be applied in multiple combinations over different layers to simulate greater or lesser anisotropy.

Both HydraulicTomAnalV21Aniso and HydraulicTomAnalV21 used the same 7 or 8 zone model (Fig. 25) to generate MOG ray path data under anisotropic and isotropic conditions, respectively. Isotropic and anisotropic model runs with the MOG data sets were completed in a similar fashion to the ZOP data sets; however, the ray path density through the model is much greater (Fig. 13). A typical, complete CPT well pair may have 28 MOG data sets with 784 rays instead of just the 28 ZOP rays initially used to develop the reduced-zone model of the aquifer for heterogeneity evaluation. With the same K inputs between the anisotropic and isotropic models, varying anisotropy can be statistically evaluated after model inversion.

The 30-sec period (i.e., low frequency) phase data at HT-1 to HT-3 and HT-6 to HT-3 were initially modeled to evaluate anisotropy ratios of 10 and 2 because these data sets were judged the best overall quality. These anisotropy ratios simulate the dependency of K on direction within a geologic formation. In an idealized system, isotropic conditions are often assumed where $K_{Horizontal} = K_{Vertical}$ ($K_H = K_V$). In a natural system anisotropy usually prevails and $K_H >>> K_V$ (Domenico and Schwartz, 1998). The anisotropy ratios applied to the model simulate a more realistic flow regime to better imitate the directional dependency exhibited by alluvial sediments oriented by grain size and direction. In this case, an anisotropy ratio of 10 is $K_H = 10K_V$ and an anisotropy ratio of 2 is $K_H = 2K_V$, which is a less severe degree and closer to the isotropic condition. The offset MOG rays should measure the anisotropic variation in the aquifer, so an anisotropic correction should theoretically improve the data fit to the model.

The HT-1 to HT-3 evaluation included isotropic, anisotropic 2 and anisotropic 10 models. The HT-6 to HT-3 anisotropy evaluation included a layered model with anisotropy ratios of 2 and 10 applied to different layers in the model. It was anticipated that the best anisotropy ratio from HT-1 to HT-3 or HT-6 to HT-3 would be applied to the remaining well pairs and used for the final, lateral heterogeneity model. However, a significant statistical deviation occurred when processing the 3-sec data sets, so additional anisotropic evaluation was completed for the pneumatic data at HT-GP to HT-2 with isotropic, anisotropic 2 and anisotropic 10 models. Evaluation results suggested that different anisotropy ratios and data constraint are needed to adequately model CPT data with different oscillating periods. So, for the purposes of this research, after the initial assessment, different anisotropy ratios were applied to the 30 and 3-sec data sets, but all the model layers used a single, best case anisotropy ratio (e.g., 2 or 10). MOG inversion and discussion of the different anisotropic and isotropic ratios are presented below.

SVD Inversion, Least Squares Fit – 7 or 8 Zone Anisotropic and Isotropic Phase Shift

The inversion and least squares fit to the reduced zone model was evaluated under different constraints, as well as isotropic and anisotropy ratios of 2 and 10 for the two CPT sources. The best case data fit or anisotropy scenario was assumed for the subsequent 21 or 24 zone model to evaluate lateral heterogeneity.

Chi squared and standard deviation values from the hydraulic 30-sec data at HT-1 to HT-3 indicate that an anisotropy ratio of 10 produced a poorer data fit (Fig. 33). Both the isotropic and the anisotropic 2 models were relatively good, although the anisotropic model provided a slightly better data fit. Most of the K values solved from the anisotropic 2 model were near or less than 10% standard deviation.

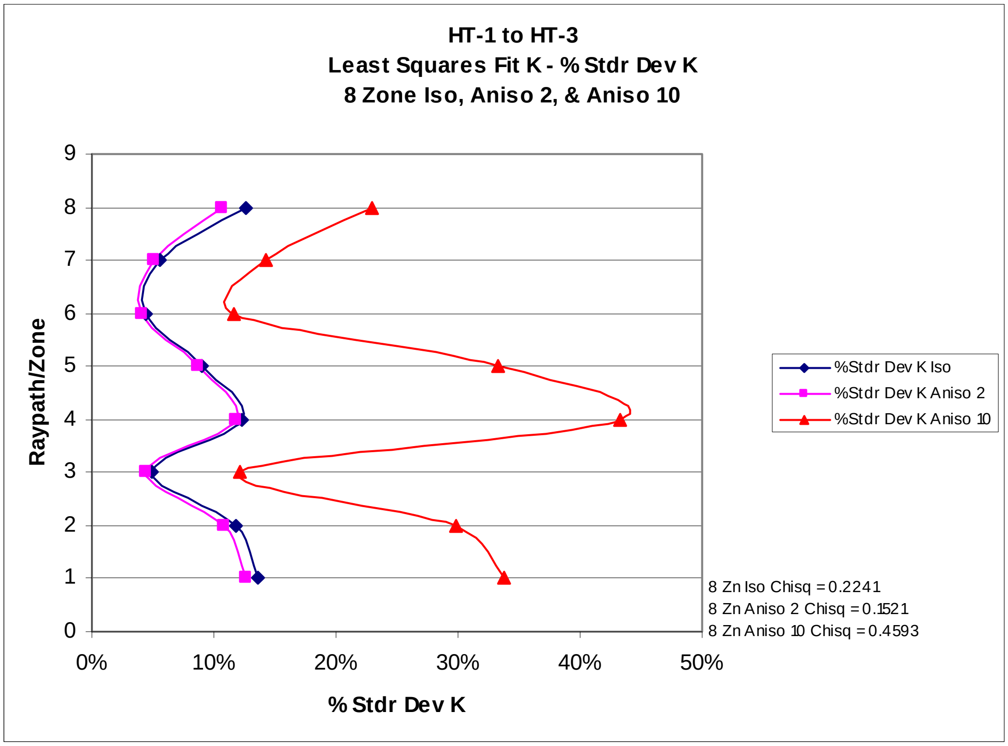

Figure 33 – HT-1 to HT-3 least squares fit K under isotropic, anisotropic-2, and anisotropic-10 conditions.

The overlap of field data and the calculated phase values (e.g., isotropic, anisotropic 2, anisotropic 10, etc.) indicate the relative goodness of fit between the experimental data to the straight ray approximation of the phase shift. According to theory, the phase shift should increase with distance and will plot nearly as a parabola or half parabola depending on the source location; any deviations from the basic shape are attributable to changes in K (Fig. 13). As an example, MOG data from the first CPT source location at HT-1 to HT-3 for the isotropic, anisotropic 2, and anisotropic 10 scenarios are presented below (Fig. 34 to 36). In this example, the CPT source location is near the bottom of HT-3 on the left and the 28 receiver locations in HT-1 are on the right. The ray path of the CPT must travel farther to reach the receivers located in the higher parts of the well screen, so the phase shift will increase with distance and form a half parabola at this location. The curves most closely match with an anisotropy ratio of 2 (Fig. 35), which correlates with the data fit indicated by the percent standard deviation results displayed in Figure 33.

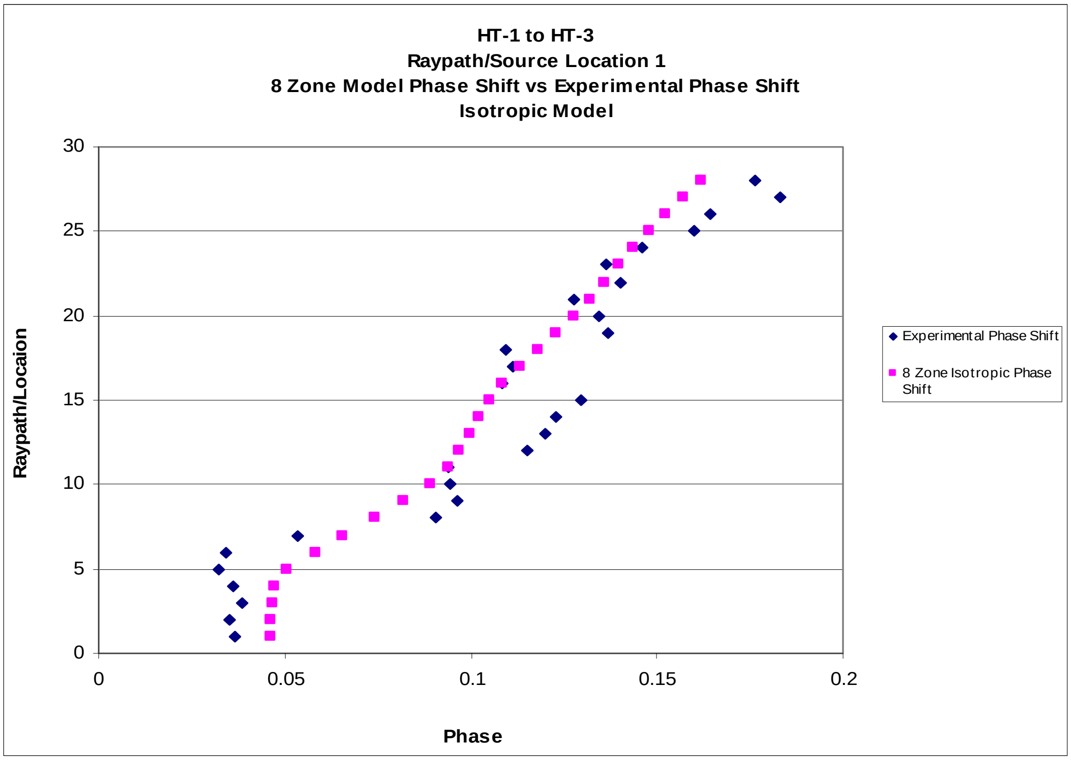

Figure 34 – HT-1 to HT-3 experimental phase shift and SVD calculated phase shift under isotropic conditions. The MOG data set is from CPT source location 1 (232.0 m/msl [761.3 ft/msl]).

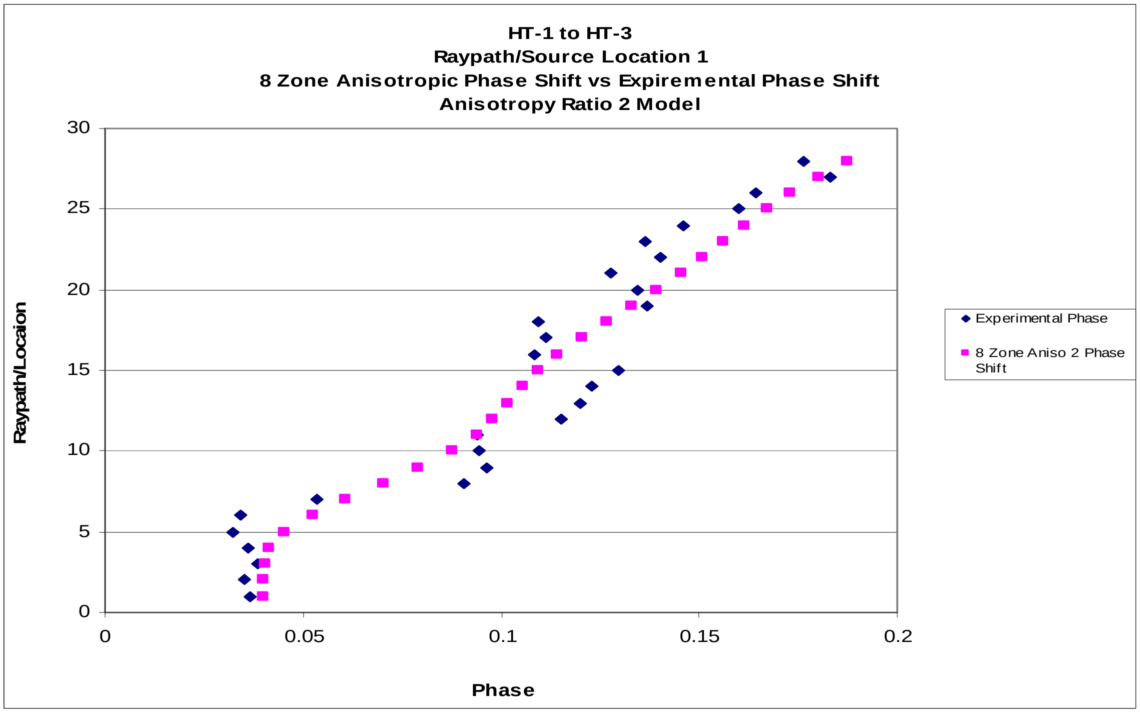

Figure 35 – HT-1 to HT-3 experimental phase shift and SVD calculated phase shift with an anisotropy ratio 2. The MOG data set is from CPT source location 1 (232.0 m/msl [761.3 ft/msl]).

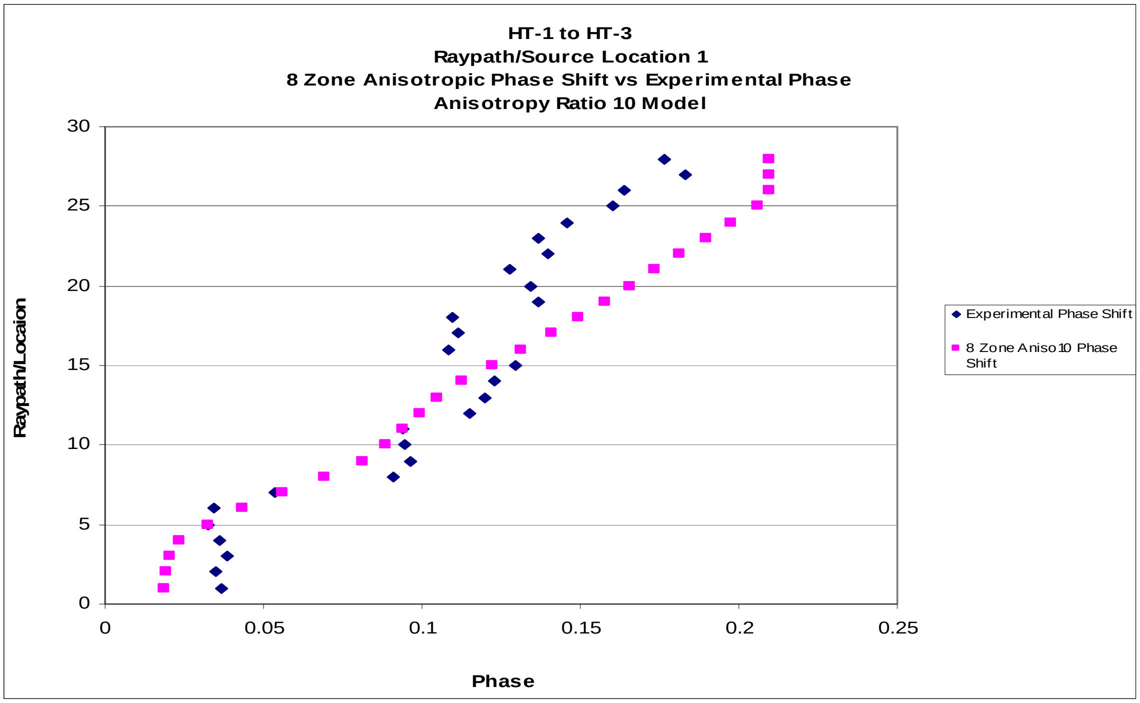

Figure 36 – HT-1 to HT-3 experimental phase shift and SVD calculated phase shift with an anisotropy ratio 10. The MOG data set is from CPT source location 1 (232.0 m/msl [761.3 ft/msl]).

Additional heterogeneity modeling was completed on HT-6 to HT-3 data to evaluate variable application of anisotropy ratios to different model layers in an attempt to improve the data fit by accounting for the interpreted hydrostratigraphic zones in the aquifer. Based on the interpretation of the deterministic K vertical profile, higher K hydrostratigraphic layers were given an anisotropy ratio of 2 and lower K hydrostratigraphic layers were given an anisotropy ratio of 10 to simulate varying degrees of anisotropic flow dependence through the aquifer. Although the standard deviation of the data fit improved, anisotropic application by layers still resulted in a relatively poorer fit (Fig. 37). So, based on the multi-layer statistical evaluation, an anisotropy ratio of 2 was chosen to evaluate all the MOG data sets for the 30-sec CPT data (i.e., the pumped hydraulic source).

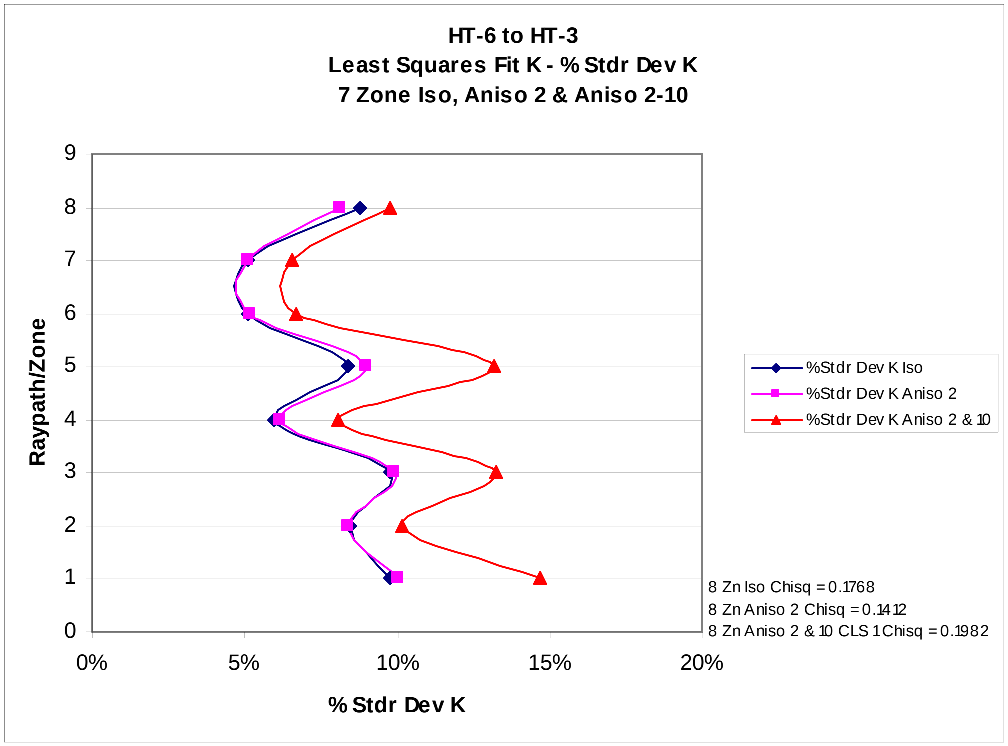

Figure 37 – HT-6 to HT-3 least squares fit K under isotropic, anisotropic-2, and anisotropic-2 & 10 conditions.

Conversely, pneumatic data modeling at HT-GP to HT-2 using an anisotropy ratio of 2 did not result in the best data fit. Large chi squared and standard deviation values resulted from the inversion of this anisotropic scenario (Fig. 38).

HT-GP to HT-2 contains surrogate HRST phase for some of the CPT locations (Table 4) and it was expected that the inversion of the synthetic data, such as that using the HRST phase, should almost perfectly match the model generated phase. When it did not, it suggested that the inverse required some constraint (Fig. 39).

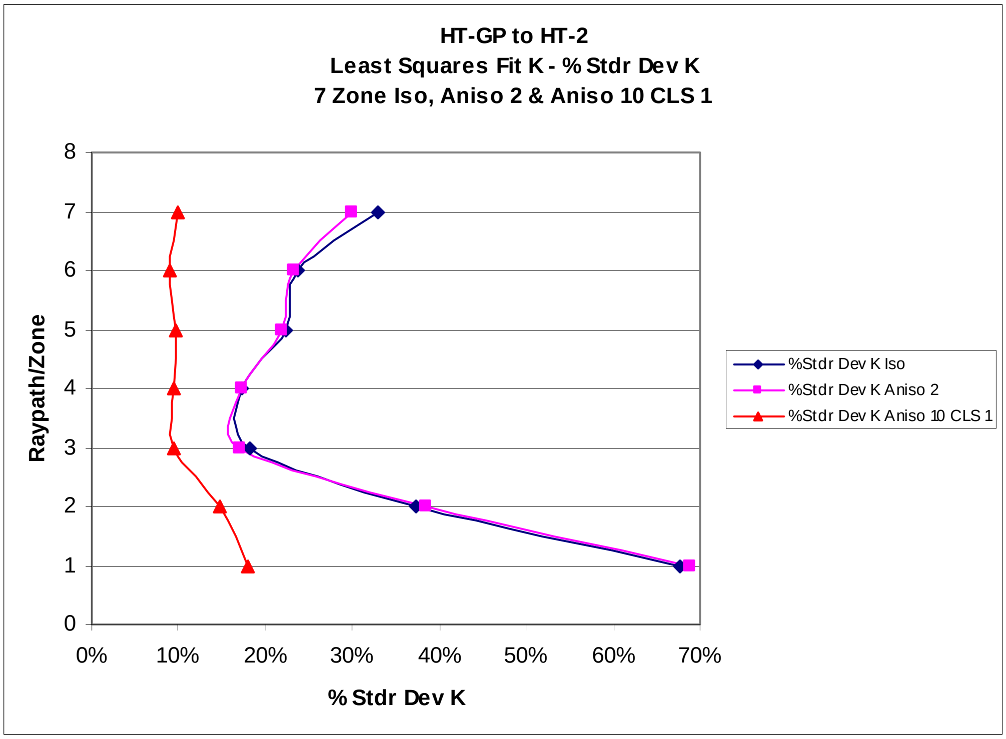

Figure 38 – HT-GP to HT-2 least squares fit K under isotropic, anisotropic-2, and anisotropic-10 CLS 1 conditions.

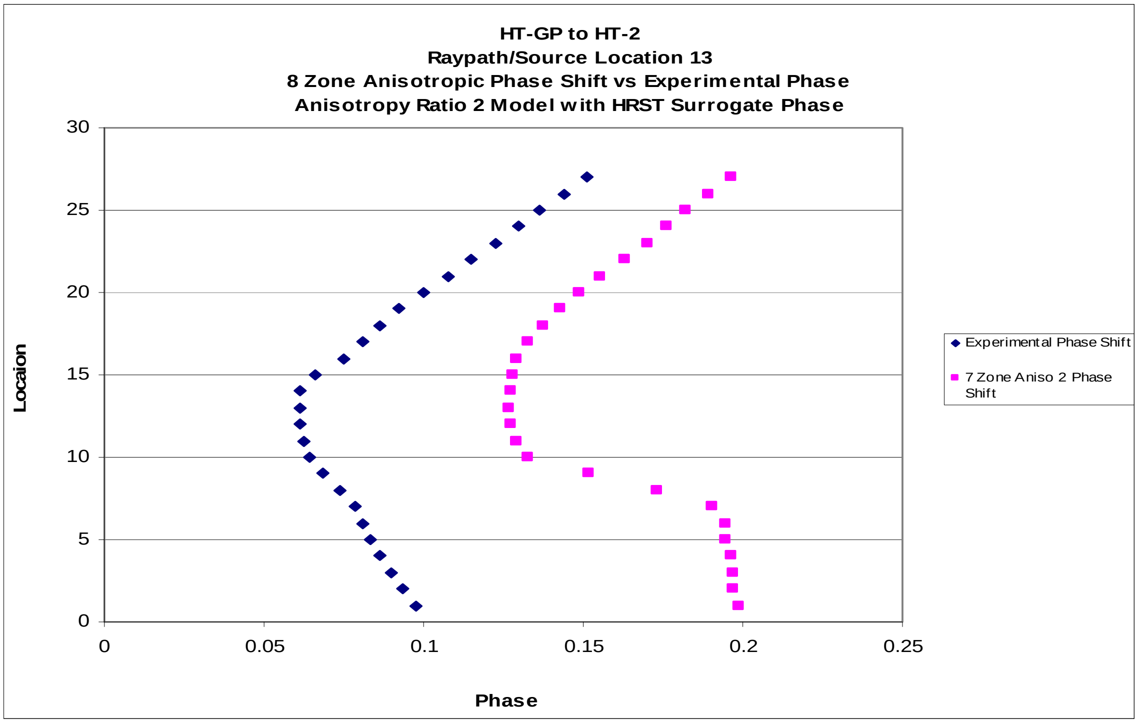

Figure 39 – Poor fit between experimental phase shift and SVD calculated phase shift with an anisotropy ratio 2 at HT-GP to HT-2. The MOG data set is derived from HRST K.

Inverse problems are sometimes constrained by other sources of data or by mathematical methods if the results prove to be unrealistic. In some of the earlier tomographic research on this project, Wachter (2008) found that some of the calculated K values were an order of magnitude higher than the rest of the data set and a weighting factor within the LeastSquaresSVD program was used to constrain the inversion closer to site-specific HRST K values. Some of the K zone sensitivities within the model matrix during the transformation process are small enough that the SVD analysis does not recognize some of the zones as unique values and sometimes results in anomalously high K values. A weighting factor can be employed as a means to address non-unique data during the inversion process. As discussed, the weighting factor determines to what extent the inversion results are constrained to remain close to the input K of the zone. Up to this point in the data processing, all the ZOP and anisotropy model inversions were completed with a constraint factor of 0, which is unconstrained. Increasing constraint values gives more weight to input K values and therefore restrict deviations of the inversion results from the model domain K. Accordingly, SVD constraint should prevent the deviation of the inverse calculated phase away from the known value of the HRST-derived experimental phase shift (Fig. 39).

The 3-sec data from the pneumatic HT-GP to HT-2 well pair were remodeled with isotropic, anisotropic 2, and anisotropic 10 models to determine a better aquifer model and inversion for the pneumatic data. A constraint factor of 1 on the anisotropic 10 model was chosen for SVD analysis, which still lends equal weight to both the input K of the model and the inverted results to help avoid an artificial data fit to the model. The data fit was much improved; the constraint factor of 1 fit the surrogate phase data to the model relatively well (Fig. 40).

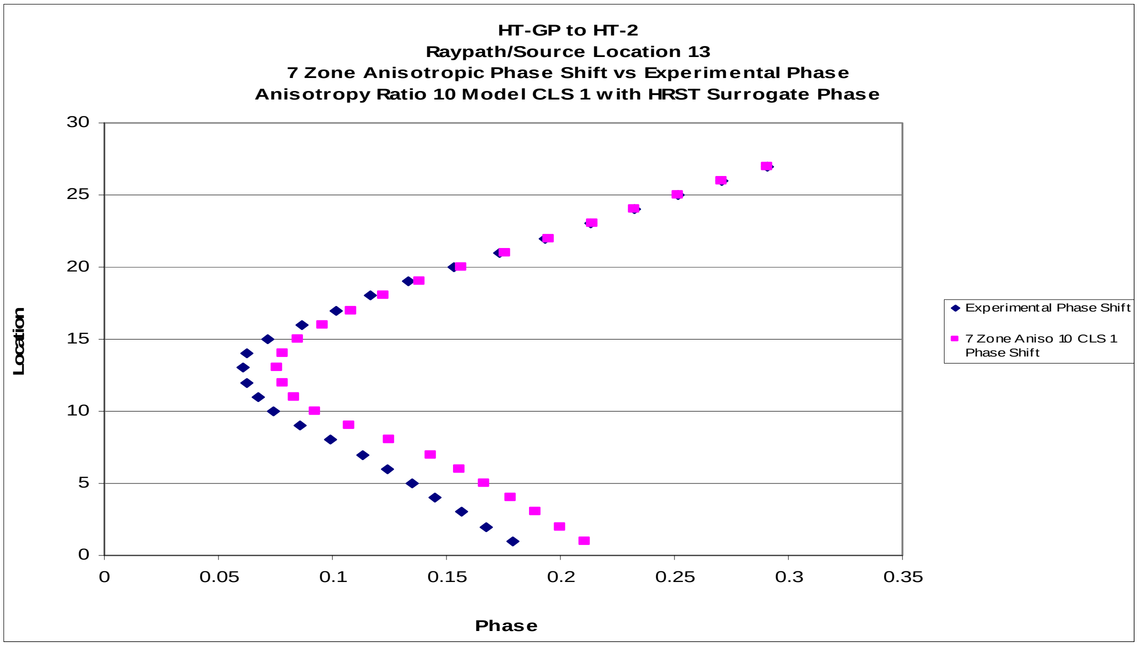

Figure 40 – Good fit between experimental phase shift and SVD calculated phase shift with an anisotropy ratio 2 at HT-GP to HT-2. The MOG data set is derived from HRST K.

Interestingly, the larger anisotropy ratio improved the overall data fit of the offset diagonal rays in the MOG pneumatic data. Initial inversion of the anisotropic 2 model resulted in a relatively good fit between the experimental phase shift data and the model generated phase shift for many of the MOGs at HT-GP to HT-2, although the fit of the offset rays increasingly deteriorated with distance (Fig. 41). This was somewhat expected for the short period data sets since higher frequencies are more strongly attenuated. The phase shift is inversely proportional to the period and the resolution increases with decreasing period, attenuation works against the resolution not only with increasing radial distance, but with decreasing K and period. Attenuation of the signal is inversely proportional to K of the medium and the period, so the factor of 10 difference between the two CPT the periods and low K alluvium in the upper portion of the test interval will exacerbate the attenuation (2). It was unknown if the attenuation with distance through low K material would negate the greater resolution gained by the short period CPT source, but data analysis of MOG phase data at HT-GP to HT-2 suggests that a greater anisotropy ratio seems to help fit the low K data points (i.e., high phase) of the long offset rays. The calculated anisotropic 10 phase from the longest rays or uppermost receivers more closely fits the experimental data set than the calculated anisotropic 2 phase (Fig. 42 vs. Fig. 41). The 30-sec period data sets were relatively insensitive to different anisotropy ratios greater than 2, so this suggests that the 3-sec CPT period data are more sensitive to aquifer anisotropy than the 30-sec CPT period data in spite of signal attenuation associated with increasing radial distance, decreasing K, and decreasing period.

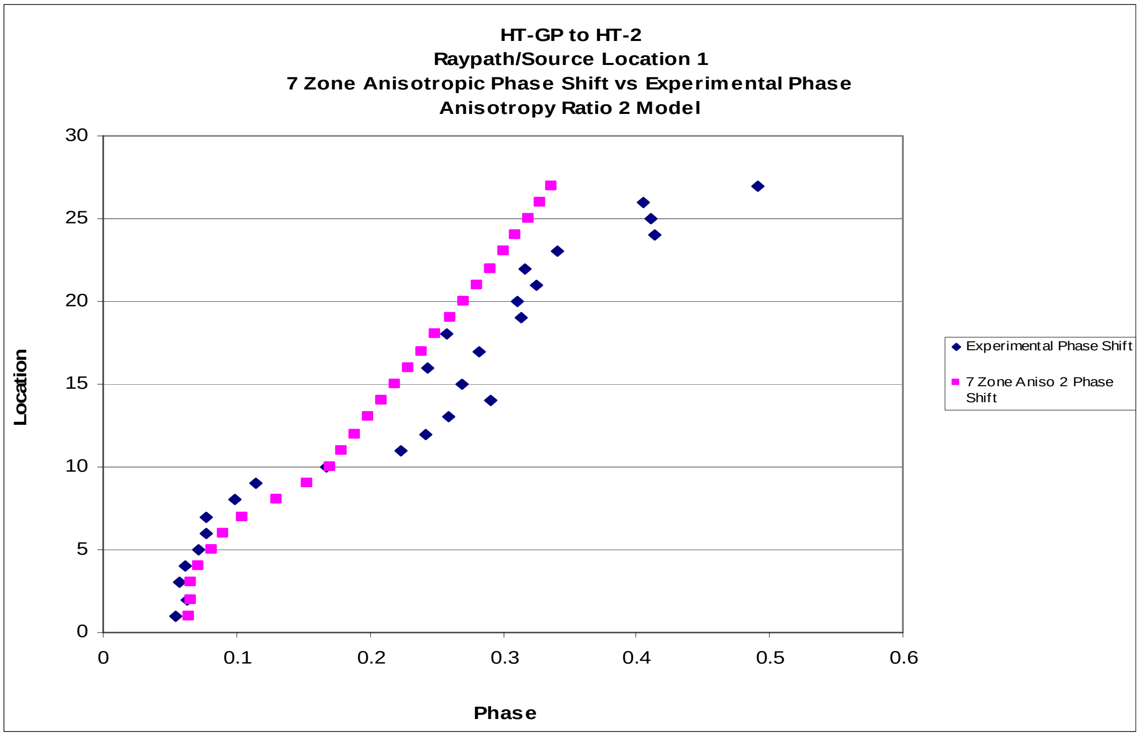

Figure 41 – Experimental field phase shift and phase shift calculated using unconstrained SVD for the first MOG from HT-GP to HT-2.

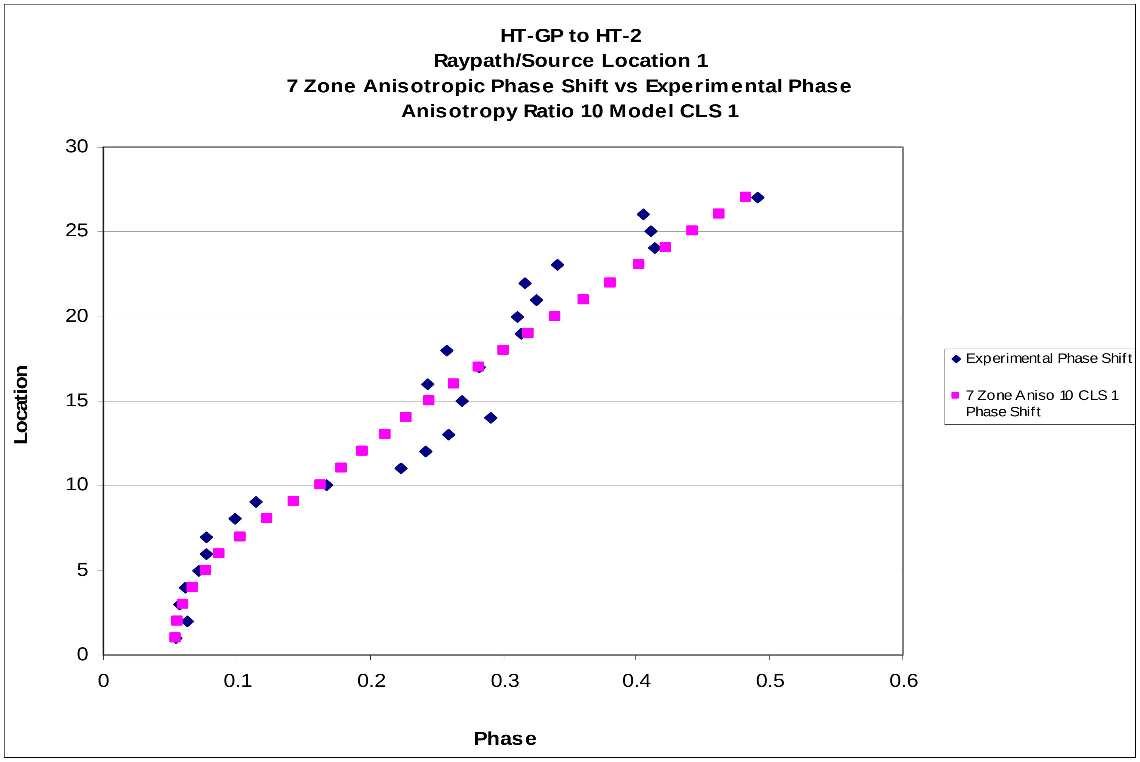

Figure 42 – Experimental field phase shift and phase shift calculated using constrained SVD for the first MOG from HT-GP to HT-2.

Most of the zones from the constrained SVD analysis of the anisotropic 10 model at HT-GP to HT-2 had an approximately 10% standard deviation value, although two zones in the basal, higher K portion of the aquifer were somewhat higher, but still remained less than 20% (Fig. 38). Based on the statistical evaluation of the SVD inversion, an anisotropy ratio of 10 and constrained least squares factor of 1 was chosen to evaluate all the MOG data sets with a 3-sec oscillation period (i.e., pneumatic source) for lateral heterogeneity. Lateral heterogeneity modeling and inversion constraint are further discussed in the subsequent section.

Model – 21 or 24 Zone Lateral Heterogeneity Model

Finally, the effect of lateral heterogeneity was evaluated with a 21 or 24 zone model (Fig. 43). Each of the horizontal zones that correspond to the interpreted hydrostratigraphic layers of the GEMS aquifer (Fig. 27) was subdivided to include three lateral zones. The HT-6 to HT-3 example model has 24 zones, 30 elements, and 48 nodes over the approximate 232.0 to 240.2 m msl (761 to 788 ft msl) well screen interval. The nodes at the source well (e.g., node 1 and 4) and the midpoint between the well pair (e.g., node 2 and 5) and receiver well (node 3 and 6) define the lateral zones. Instead of holding K constant across a single horizontal zone, the K value for each layer was allowed to vary laterally at these nodal points. HydraulicTomAnalV21Aniso linearly interpolates between the nodes to simulate the effects of lateral heterogeneity across the model (Fig. 43). As determined by the MOG anisotropy evaluation, phase data were simulated through the aquifer with an anisotropy ratio of 2 for the 30-sec data and an anisotropy ratio of 10 for the 3-sec data. SVD inversion and least squares fit of the MOG data to recover diffusivity and K is further discussed in the next section.

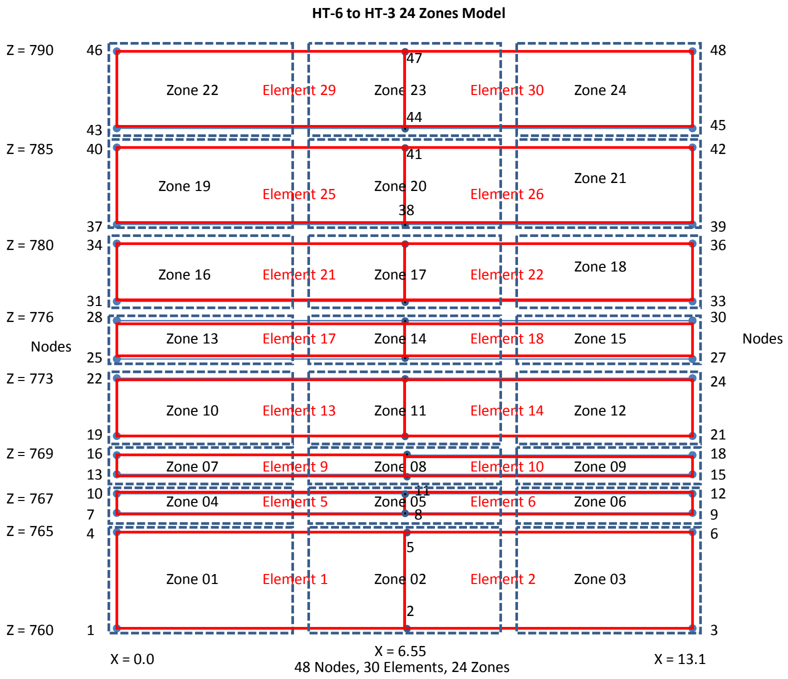

Figure 43 – Conceptual 24 zone model grid for HydraulicTomAnalAniso.

SVD Inversion, Least Squares Fit – 21 or 24 Zone Lateral Heterogeneity Phase Shift

The inversion and least squares fit to the lateral heterogeneity model for the 30-sec and 3-sec period CPT data were evaluated under different constraints. As discussed in the previous section, MOG ray path estimation was generated through the lateral heterogeneity model for the 30 and 3-sec data sets with anisotropy ratios of 2 and 10, respectively. The lateral subdivision of the reduced zone model adds more variables to the SVD inversion, possibly increasing the generation of non-unique results or uncertainty within the data fit. This uncertainty was evaluated with different constraint factors at HT-6 to HT-3 and HT-1 to HT-3 to determine if the inversion required additional data constraint to obtain plausible K data from the lateral heterogeneity model. Initially, a constraint factor of 1 was assumed for both CPT periods, but some of the pneumatic data sets had somewhat poorer than expected data fit, so different constraint scenarios were evaluated for the pneumatic data, too. Constraint factors of 1 and 10 were applied to the inversion at HT-1 to HT-3 and HT-6 to HT-3 to evaluate the 30-sec MOG data and also for the inversion at HT-GP to HT-2 and HT-GP to HT-3 to evaluate the 3-sec MOG data. SVD constraint factor analysis for the 30 and 3-sec CPT data sets are further discussed below.

Chi squared and standard deviation values for the calculated K from the 30-sec data at HT-1 to HT-3 and HT-6 to HT-3 indicate that a constraint factor of 1 is generally acceptable for the inversion of the pumped hydraulic CPT data (Fig. 44 and Fig. 45). Most of the standard deviation values are approximately 10%. However, the fit is less good in the basal, high K portions of the aquifer although the percent standard deviation does remain below 20%. The calculated K values from the 30-sec MOGs are still within the range typically encountered at GEMS, so a constraint factor of 1 was chosen to evaluate lateral heterogeneity for the 30-sec CPT data. The percent standard deviations on K for the lateral heterogeneity models for the 30-sec CPT data are presented in Appendix F.

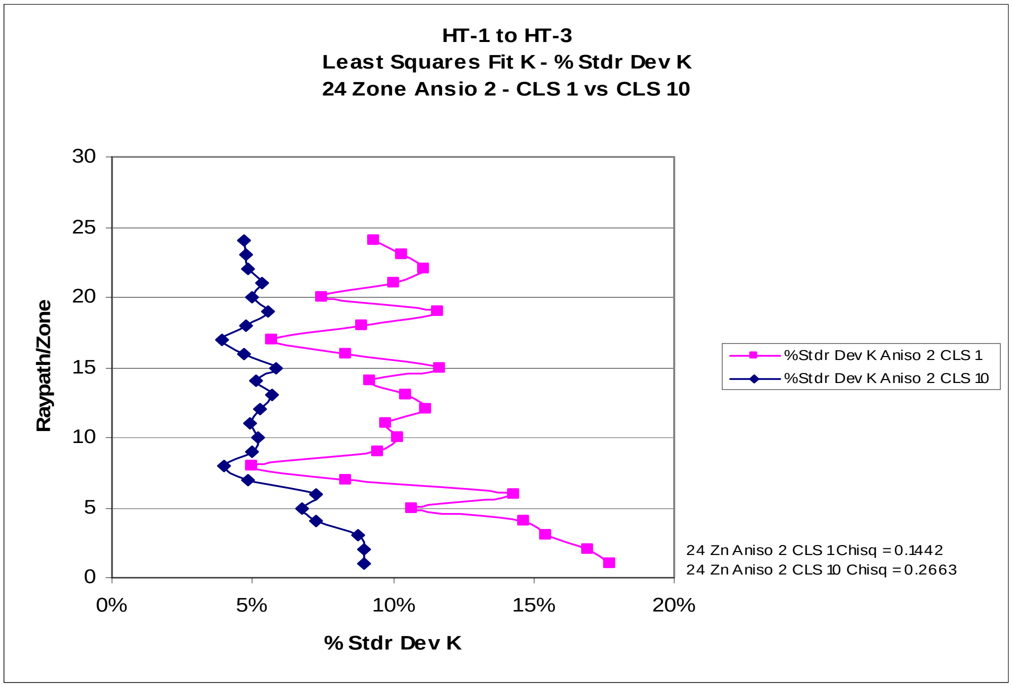

Figure 44 – HT-1 to HT-3 least squares fit K under anisotropy-2 CLS 1 (Ave 10.73 %) and anisotropy-2 CLS 10 (Ave 5.72%) conditions.

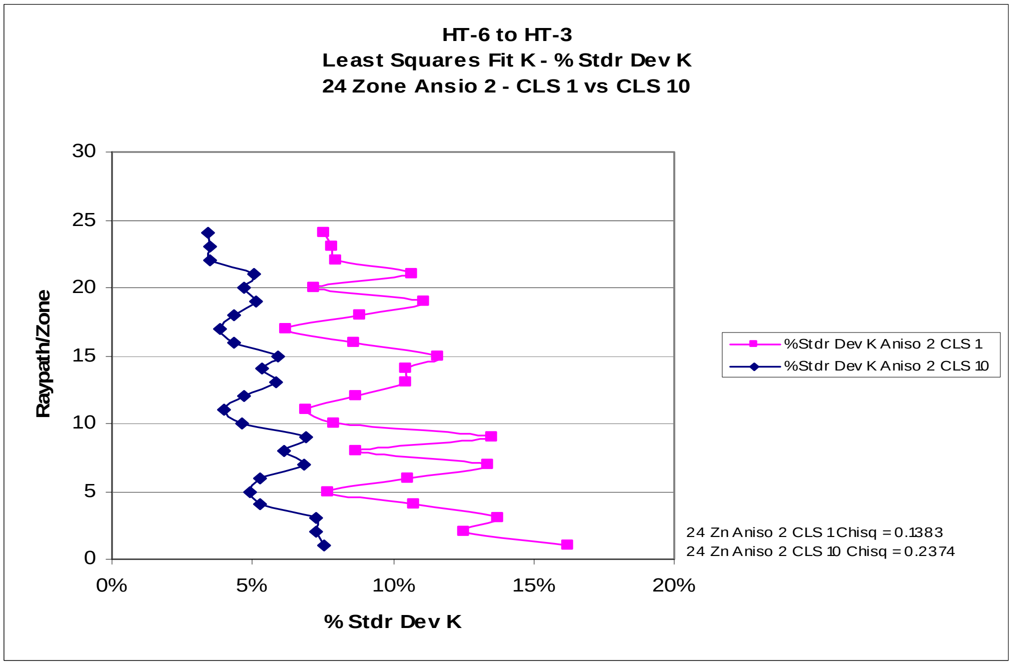

Figure 45 – HT-6 to HT-3 least squares fit K under anisotropy-2 CLS 1 (Ave 9.95%) and anisotropy-2 CLS 10 (Ave 5.23%) conditions.

Initially, a constraint factor of 1 was used for the 3-sec CPT data inversion. However, once the HT-GP to HT-2 data were processed, the chi squared and percent standard deviation values of the calculated K from the SVD analysis increased markedly (33.6 % vs. the approximate 10% average of the hydraulic data), and indicated that the pneumatic data were responding differently to the inversion and fit to the lateral heterogeneity model (Fig. 46 and Appendix G). An additional SVD inversion with a constraint factor of 10 was completed to evaluate the pneumatic data at HT-GP to HT-2. Some error was removed with the additional constraint and the average percent standard deviation was reduced to about 12%, although a plot of the percent standard deviation has little variability so the data fit appears somewhat artificially constrained. The calculated K values with a least squares constraint of 1 are still within the expected range of reported K values at GEMS so this constraint factor was still assumed for this CPT well pair. Again, generally, the fit is less good in the basal portion of the aquifer.

In contrast to the other hydraulic and pneumatic CPT well pairs, the remaining pneumatic location, HT-GP to HT-3, required a constraint factor of 10 to generate K values within the expected range at GEMS (Fig. 47 and Appendix G). Although a constraint factor of 1 still resulted in a slightly better data fit than the other pneumatic well pair, (29.2% vs. 33.6% average standard deviation) the K values deviated from the expected range and, in particular, one K value from Zone 19 (0.0624 ft/sec) was an order of magnitude greater than the rest of the data set with a percent standard deviation error of 243% (Fig. 47). A constraint factor of 10 resulted in reasonable K values and percent standard deviation (16.9%); therefore, it was used for lateral heterogeneity evaluation at HT-GP to HT-3.

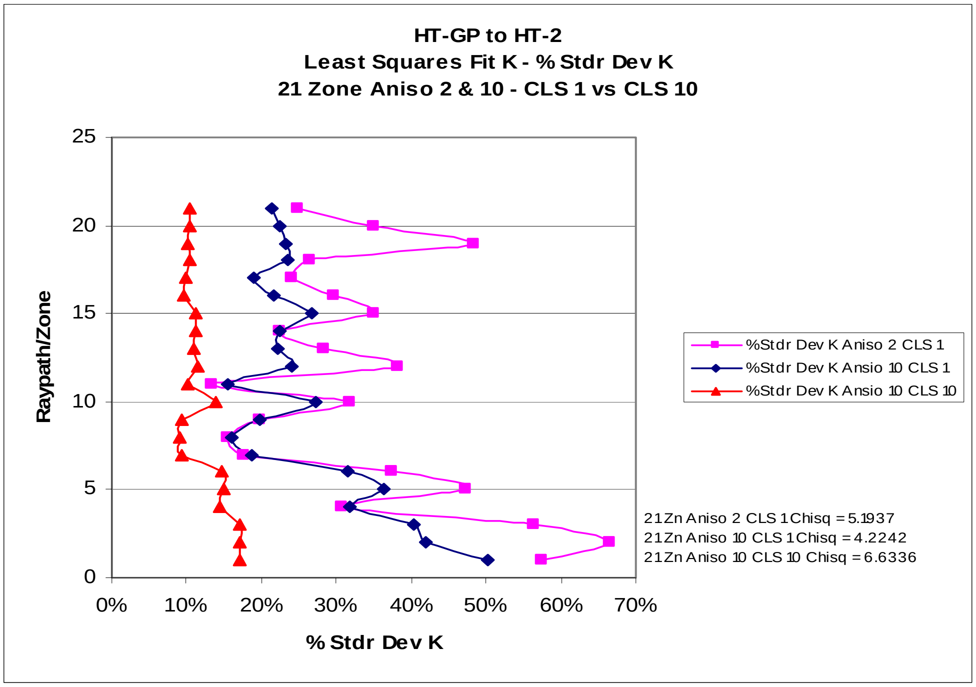

Figure 46 – HT-GP to HT-2 least squares fit K under anisotropic-2 CLS 1 (Ave 33.6%), anisotropic-10 CLS 1 (Ave 26.5%), anisotropic-10 CLS 10 (Ave 12.1%) conditions.

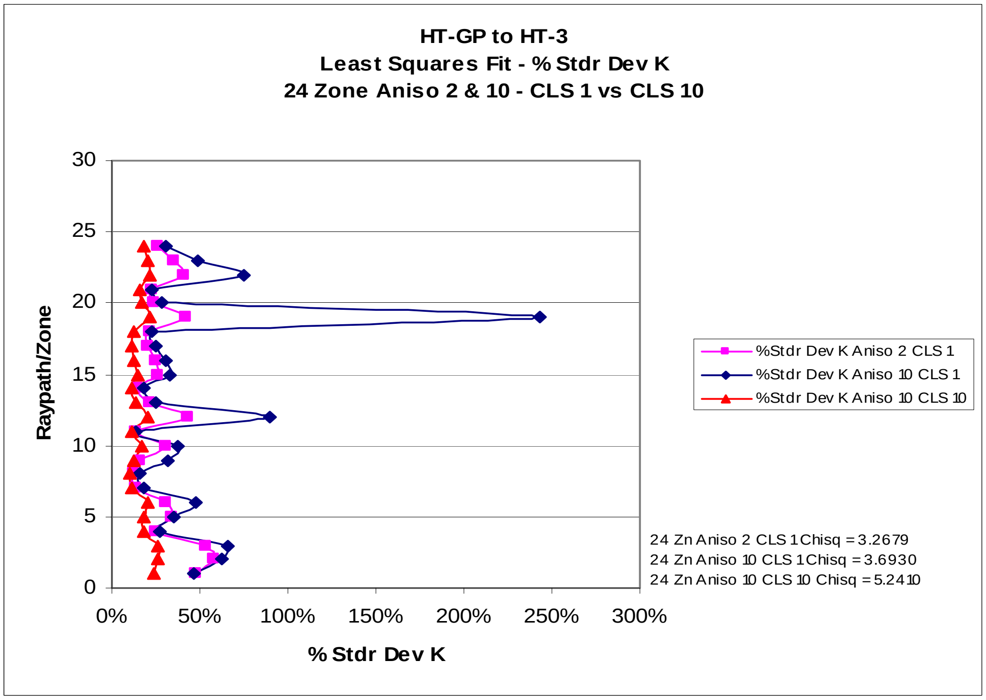

Figure 47 – HT-GP to HT-3 least squares fit K under anisotropic-2 CLS 1 (Ave 45.5%), anisotropic-10 CLS 1 (Ave 29.2%), anisotropic-10 CLS 10 (Ave 16.9%) conditions.

Numerical Modeling of the Heterogeneous Extension

As discussed previously in the Theory section, basic tidal equations can be generalized for a CPT point source that spreads out in all directions in a homogenous, spherical, radial system (2). This equation can be adapted for the heterogeneous case with an approximate extension that uses a distance weighted average for the K along the ray path (6). Since the heterogeneous case does not have an analytical solution, a numerical method must be used to verify the heterogeneous extension. Modeling studies were performed to compare results from the spatially weighted ray tracing method with those from a numerical model. The numerical model and straight ray method were both used to simulate the phase shift of 108 rays between a theoretical well pair with three CPT source locations, each with 36 corresponding receiver locations. Modeling was completed for both the 3-sec and 30-sec CPTs to compare the difference between the two source methods. The aquifer between the well pair was simulated by a 3-element, 8-node, model which corresponds to the screen interval [10.68 m (35 ft)] and radial distance [5.85 m (19.20 ft)] between the theoretical well pair. The upper, middle and lower elements are, respectively, 4.88 m (16 ft), 0.92 m (3 ft), and 4.88 m (16 ft) thick. The upper, middle and lower elements have K values of 0.0009 m/sec (0.003 ft/sec), 0.0018 m/sec (0.006 ft/sec), and 0.0009 m/sec (0.003 ft/sec), respectively (Fig. 48). A representative Ss value of 0.00018 was also assumed for the verification modeling. Although these values were arbitrarily chosen, they fall within the range of values observed at GEMS and are consistent with Wachter's (2008) earlier verification of the heterogeneity extension using a 4-sec pneumatic CPT. The numerical phase data from this model comprise a theoretically perfect CPT data set and phase data from the straight ray model should closely approximate it. However, the numerical model does use a barrier boundary on the top and bottom rather than an infinite domain, so some boundary effects are expected. In any case, good agreement between the two methods is a line of evidence supporting the heterogeneous extension (6) adapted for this research.

Wachter's (2008) 4-sec CPT numerical validation of the heterogeneity extension was reproduced with the latest version(s) of the Visual Basic data processing programs so his verification could be compared to the numerical verification of the 30-sec CPT work completed for this research. Numerical modeling simulated three MOG data sets from source locations at 0.305-0.610 m (1-2 ft), 5.486-5.791 m (18-19 ft), and 10.668-10.973 m (35-36 ft), which correspond to the lower, middle, and upper intervals of the aquifer model (Fig. 48 – 50). The numerical model had 36 rows to simulate each of the 36 theoretical receiver locations in a MOG. To simulate a file of head data from the CPT source and receiver transducers, numerical phase data were parsed from the numerical model rows at radial distances which correspond to the center of the source and receiver well locations (e.g., 0.25 m [0.833 ft]) and 5.85 m [19.20 ft]) and were saved to a text file. FitAmpPhase used the text files to calculate the numerical phase shift for each of the MOGs. HydraulicTomAnal was used to create an element matrix of the aquifer and apply the straight ray approximation method through the matrix to generate the straight-ray phase shift data for all three MOGs. The element matrix was imported into LeastSquaresSVD and both numerical and straight-ray phase shift data for the three MOGs were inverted through the element matrix to calculate diffusivity and solve for K. The degree to which the inverted straight ray and numerical phase shift data can reproduce the model K values indicates the resolution of the CPT tomography method used for this research, and produces a comparison between 4 and 30-sec period CPT sources. The current version of the SVD inversion program also has the ability to perform Monte Carlo simulations using random error, rather than running individual simulations. Monte Carlo simulations were run with both 5% and 10% random noise for 1000 simulations. The 5% random noise approximates the expected variation in the field due to instrument imprecision and ambient noise and the 10% random noise simulates the expected worse-case scenario of signal inference. Verification of the heterogeneity extension and comparison of the 4 and 30-sec CPT sources are further discussed below.

The numerical phase shift from the 4-sec CPT sources were compiled and compared to their corresponding straight-ray approximation to evaluate the relative goodness of fit between the simulated field data and its model approximation (Fig. 48 – 53). Because the phase originates from synthetic data, the two curves should fit relatively close. The 4-sec CPT phase shift values from the spatially weighted ray method and the numerical model for the upper, middle, and lower source locations were in good agreement with each other except for some slight boundary effects (Fig. 48 – 50). There was some deviation of the straight ray phase shift at the middle source location through the thinner, middle layer (Fig. 49). Straight rays projected through this element more directly measure the K without the averaging across the middle layer from the numerical model due to wavelength considerations and result in the higher K values (i.e., low phase) seen in this layer of the graph. Overall, the data fit is good indicating resolution of about 1 m (3 ft) layers with a 4-sec period, reconfirming Wachter’s (2008) assessment of the resolution.

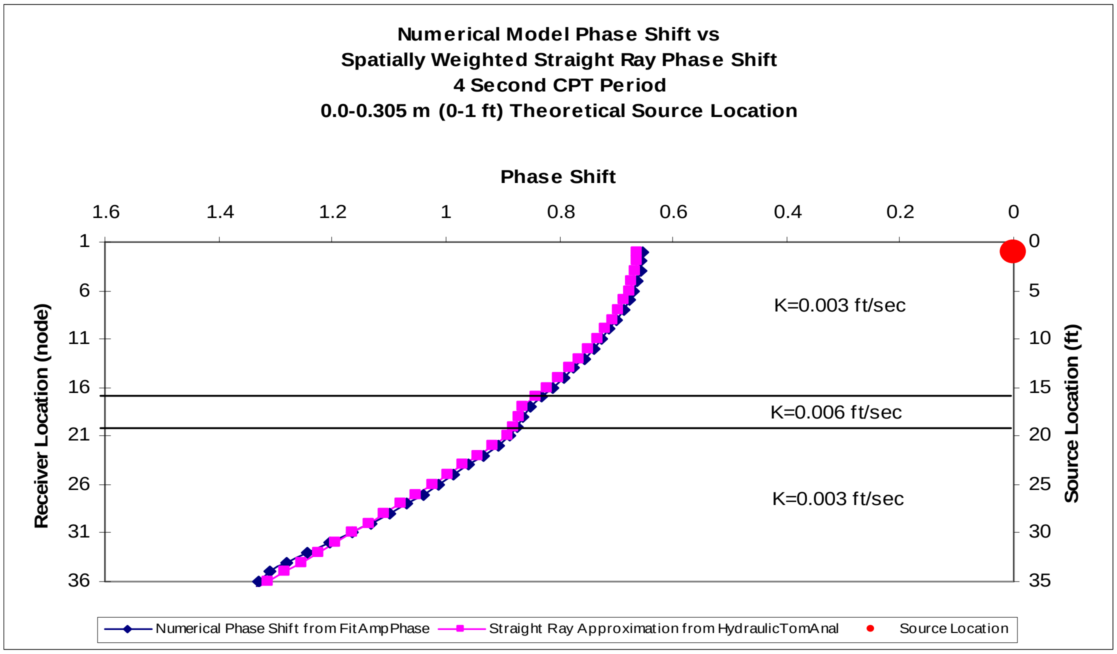

Figure 48 – A comparison of 4 second CPT period phase shift values from a numerical model and the spatially weighted ray path method at the 0.0-0.305 m (0-1 ft) source location.

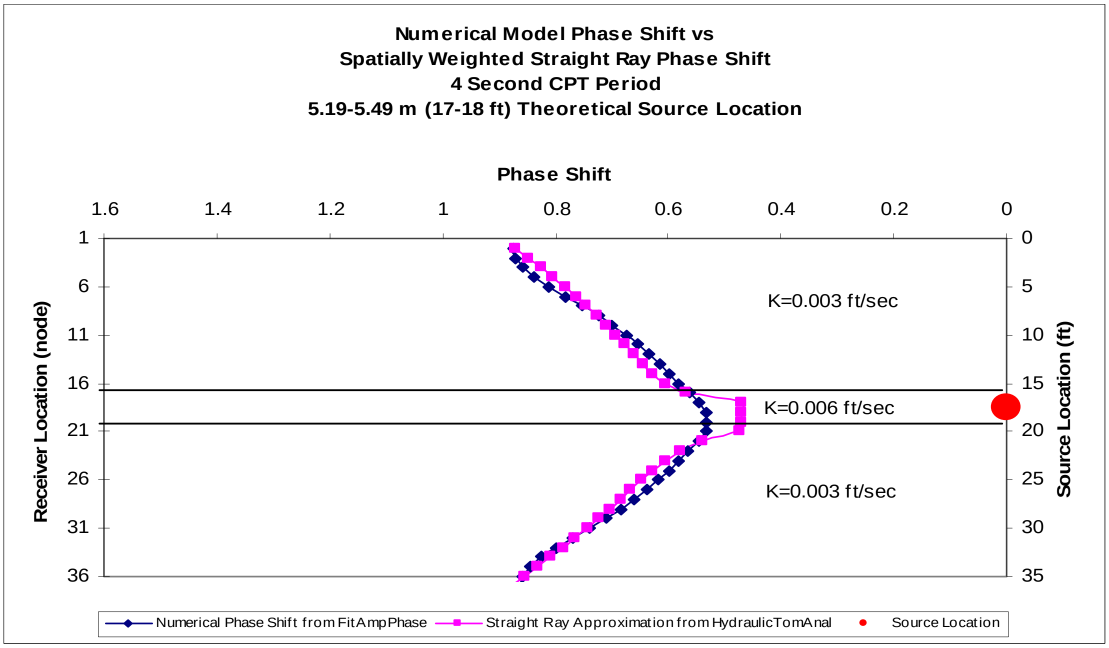

Figure 49 – A comparison of 4 second CPT period phase shift values from a numerical model and the spatially weighted ray path method at the 5.19-5.49 m (17-18 ft) source location.

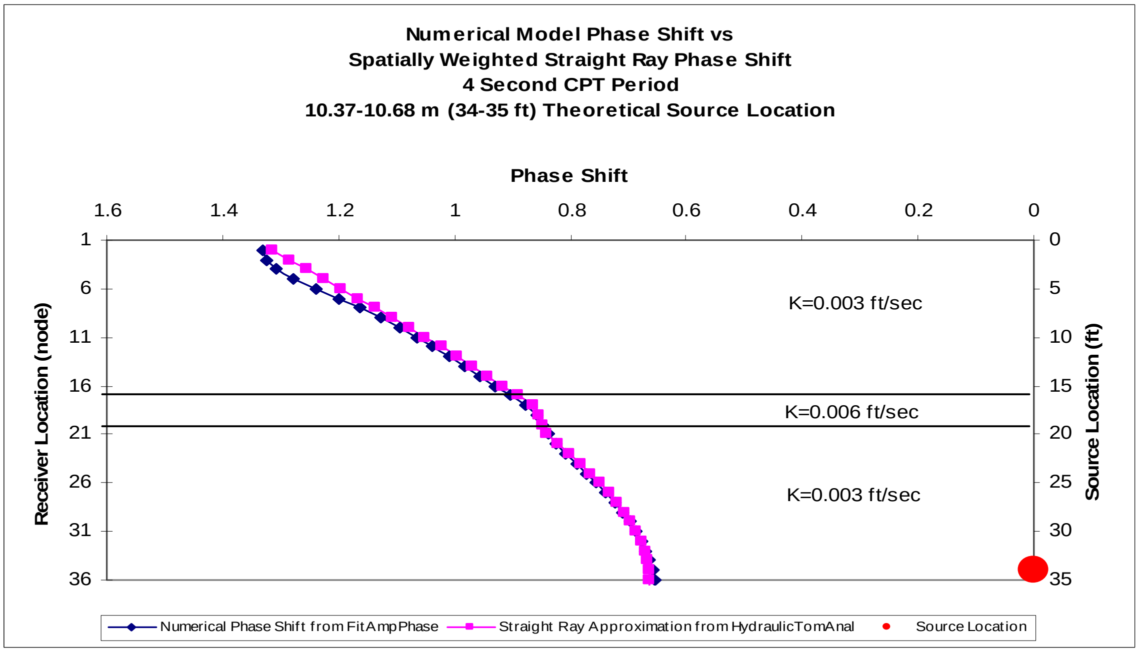

Figure 50 – A comparison of 4 second CPT period phase shift values from a numerical model and the spatially weighted ray path method at the 10.37-10.68 m (34-35 ft) source location.

The 30-second CPT phase shift values from the spatially weighted ray method and the numerical model at the upper, middle, and lower source locations were in reasonable agreement although the data resolution or overlap of the two curves was not as precise as the 4-second MOG data sets. As discussed in the theory section, the resolution of a longer period is expected to be less and results such as this are a piece of evidence to support this theory. In general, the data curves are similar and the slight boundary effects are still present (Fig. 51 - 53). Again, there was some deviation of the straight ray phase shift through the thinner, middle layer (Fig. 52). Also, the two phase shift curves were offset slightly at this CPT location. The offset behavior is similar to the lack of fit seen between HRST-derived phase and its corresponding straight ray approximation. Figures 51 and 53 show nearly mirror symmetrical plots which can lead to non-unique data and inversion problems. Non-unique data were encountered in some of the simple, early developmental models which used only a few symmetrical rays for each source and suggest that non-unique data can arise from ray path simulation through theoretical models. These plots suggest that some constraint may be required during inversion and is further discussed below.

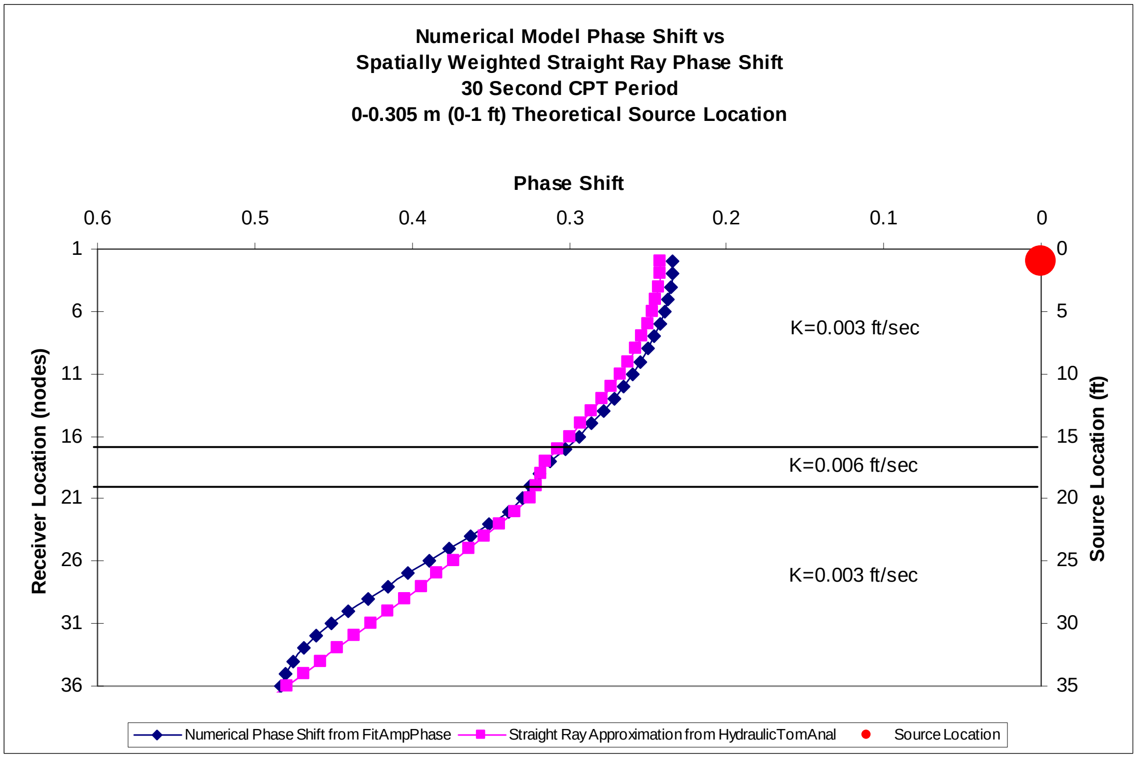

Figure 51 – A comparison of 30-sec CPT period phase shift values from a numerical model and the spatially weighted ray path method at the 0-0.305 m (0-1 ft) source location.

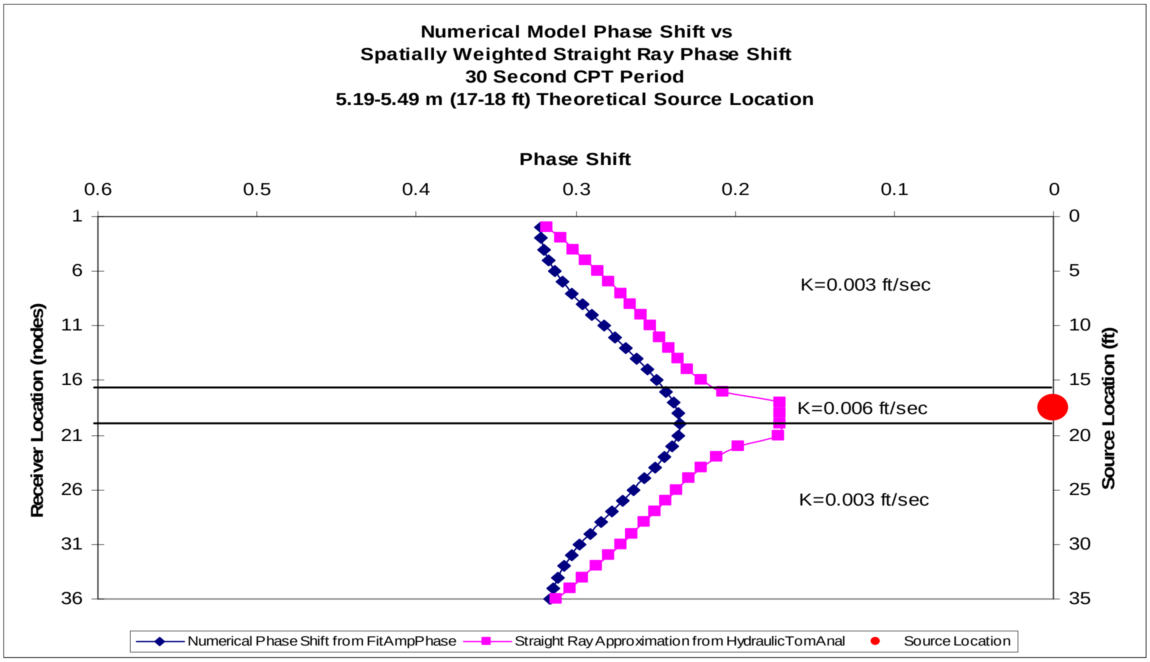

Figure 52 – A comparison of 30-sec CPT period phase shift values from a numerical model and the spatially weighted ray path method at the 5.19-5.49 m (17-18 ft) source location.

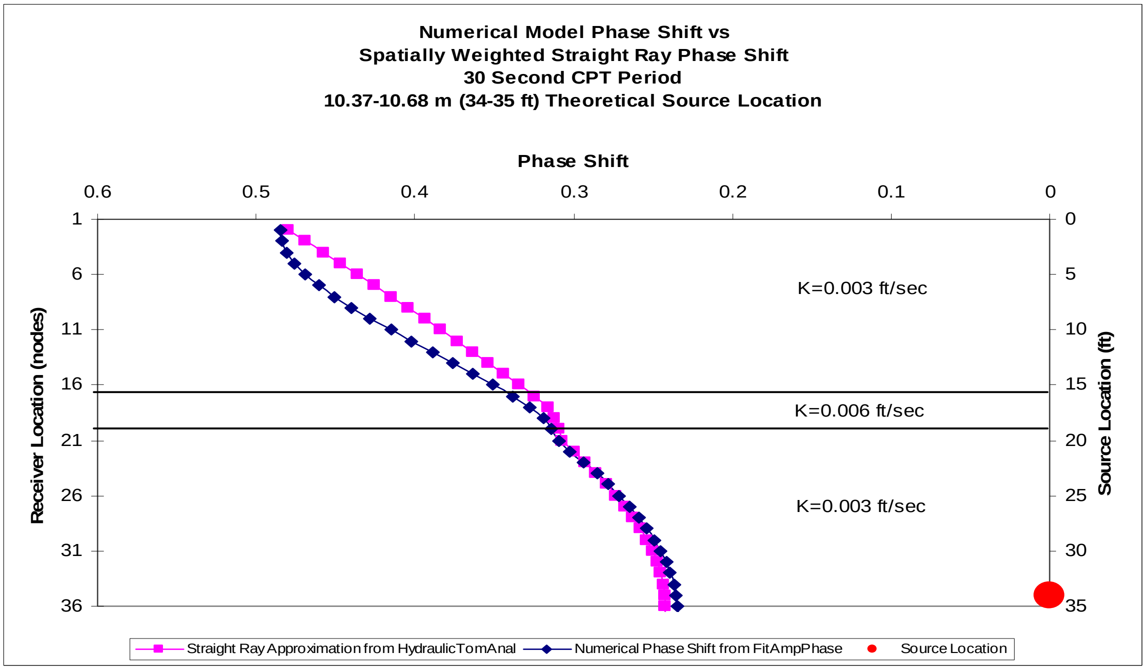

Figure 53 – A comparison of 30-sec CPT period phase shift values from a numerical model and the spatially weighted ray path method at the 10.37-10.68 m (34-35 ft) source location.

After the goodness of fit between the straight ray and numerical phase shift data were evaluated, the straight ray phase shift data (Table 16), along with the numerical phase shift data (Table 17) were inverted through the element matrix by SVD analysis, a method of least squares fitting and inversion. As expected, direct inversion of the straight ray model data reproduced the input model K values for each of the layers with practically no error (Table 16). The percent standard deviation on the K values for each of the elements were essentially zero, implying the inversion was almost perfect for a data set with no noise. Random error of 5% and 10% was applied by Monte Carlo simulation to replicate a normal and worst-case scenario of ambient noise. The 2.5% - 5.2% range indicates the inherent error associated with levels of random noise in the middle layer and a 4-sec CPT period (Table 16). In contrast, the 6.9% - 14.5% range is the inherent error associated with the levels of random noise in the middle layer and a 30-sec period and indicates that the period difference tends to amplify the effect of random error.

Inversion of the 4-sec period numerical phase shift data through the element matrix was also reasonable and the percent standard deviation on the K values for the middle elements was 3.1% (Table 17), in the absence of random noise. The error associated with the straight ray method is about 14.1 % error in the recovery of the 0.006 ft/sec K by the straight ray method (i.e., 0.006 vs. 0.005s ft/sec). These error percents indicates that the spatially weighted straight ray model and 4-sec CPT period can resolve layers of about 1 m (3 ft) in thickness with about 16 – 19 % total error.

Spatially Weighted Straight Ray SVD Analysis			
4-Sec CPT Period			
Monte Carlo – No Error			
Element	K (ft/sec)	Stdr Dev K	% Stdr Dev K
1	0.003	3.616E-19	0.00
2	0.006	3.137E-18	0.00
3	0.003	3.870E-19	0.00
Monte Carlo - 5% Error			
Element	K (ft/sec)	Stdr Dev K	% Stdr Dev K
1	0.003	1.849E-05	0.62
2	0.005999	1.515E-04	2.52
3	0.003	1.899E-05	0.63
Monte Carlo – 10% Error			
Element	K (ft/sec)	Stdr Dev K	% Stdr Dev K
1	0.002999	3.482E-05	1.16
2	0.006018	3.098E-04	5.15
3	0.003001	3.702E-05	1.23

Spatially Weighted Straight Ray SVD Analysis			
30-Sec CPT Period			
Monte Carlo - No Error			
Element	K (ft/sec)	Stdr Dev K	% Stdr Dev K
1	0.003	8.636E-19	0.00
2	0.006	7.492E-18	0.00
3	0.003	9.242E-19	0.00
Monte Carlo - 5% Error			
Element	K (ft/sec)	Stdr Dev K	% Stdr Dev K
1	0.003	5.063E-05	1.69
2	0.006012	4.159E-04	6.92
3	0.003001	5.205E-05	1.73
Monte Carlo - 10% Error			
Element	K (ft/sec)	Stdr Dev K	% Stdr Dev K
1	0.003	9.542E-05	3.18
2	0.006109	8.869E-04	14.52
3	0.003005	1.017E-04	3.38

Table 16 – SVD analysis of spatially weighted straight ray approximation phase shift through a 3-element, 8-node, 10.68 m (35 ft) thick model used to verify the heterogeneous extension.

Inversion of the 30-sec period numerical phase shift data through the element matrix had 3.6% percent standard deviation on the K values for the middle element (Table 17), in the absence of random noise. This inversion was constrained slightly; the offset curves (Fig. 52) and nearly mirror symmetric plots in the upper and lower elements (Fig. 51 and Fig. 53) tend to suggest non-uniqueness data issues were arising during inversion. The SVD analysis was slightly weighted with a constrained least squares factor of 0.25, which gives a small weight to the initial estimates of K to overcome non-unique data and shouldn’t unnecessarily restrain the analysis. The error associated with the straight ray method is about 25% error in the recovery of the 0.006 ft/sec K by the straight ray method (i.e., 0.006 vs. 0.0045 ft/sec). These error percents indicate that the spatially weighted straight ray model and 30-sec CPT period can resolve layers of about 1 m (3 ft) in thickness with about 27 - 29% total error.

Numerical/Straight Ray Model SVD Analysis			
4 Sec CPT Period			
Monte Carlo No Error			
Element	K (ft/sec)	Stdr Dev K	% Stdr Dev K
1	0.003032	2.365E-05	0.78
2	0.005155	1.608E-04	3.12
3	0.002986	2.474E-05	0.83
Monte Carlo 5% Error			
Element	K (ft/sec)	Stdr Dev K	% Stdr Dev K
1	0.003032	1.875E-05	0.62
2	0.005154	1.206E-04	2.34
3	0.002986	1.885E-05	0.63
Monte Carlo 10% Error			
Element	K (ft/sec)	Stdr Dev K	% Stdr Dev K
1	0.003031	3.545E-05	1.17
2	0.005169	2.464E-04	4.77
3	0.002987	3.675E-05	1.23

Numerical/Straight Ray Model SVD Analysis			
30 Sec CPT Period			
Monte Carlo No Error - CLS 0.25			
Element	K (ft/sec)	Stdr Dev K	% Stdr Dev K
1	0.002869	4.125E-05	1.44
2	0.004514	1.644E-04	3.64
3	0.002847	4.256E-05	1.49
Monte Carlo 5% Error - CLS 0.25			
Element	K (ft/sec)	Stdr Dev K	% Stdr Dev K
1	0.002869	3.830E-05	1.33
2	0.004513	9.347E-05	2.07
3	0.002848	3.703E-05	1.30
Monte Carlo 10% Error - CLS 0.25			
Element	K (ft/sec)	Stdr Dev K	% Stdr Dev K
1	0.00287	7.678E-05	2.67
2	0.004515	1.869E-04	4.14
3	0.002849	7.419E-05	2.60

Table 17 – SVD analysis of spatially numerical phase shift through a 3-element, 8-node, 10.68 m (35 ft) thick model used to verify the heterogeneous extension.

Results

Pumped hydraulic CPT data with a 30-sec period was collected from a radial well array with a central receiver well (HT-3) and five source wells (HT-1, HT-2, HT-4, HT-5 and HT-6). Additionally a new, in-situ pneumatic source with a 3-sec period was developed and deployed by a Geoprobe rig (HT-GP) to evaluate the feasibility of tomographic application by direct-push technology. A new, multilevel receiver was constructed and pneumatic MOG data were recorded simultaneously in two receiver wells (i.e., HT-2 and HT-3). The five hydraulic CPT well pairs and two pneumatic CPT well pairs provide hydraulic conductivity estimation in a 360-degree radial array over an extended area at GEMS.

Lateral Heterogeneity – Pumped Hydraulic CPT Source

Contour plots were made of K values plotted against elevation and the radial distance between a well pair using the graphing program, QuickGrid. The program contours between points written in an x,y,z format, which corresponds to the radius, elevation, and constrained K value determined from SVD analysis. Five pumped hydraulic CPT well pairs were plotted with the receiver well on the left (HT-3) and the source wells on the right (HT-1, HT-2, HT-4, HT-5 and HT-6). The K values from this radial array were obtained with the pumped hydraulic CPT source which had a 30-sec oscillating period. A best case anisotropy ratio and inversion constraint factor for the lateral model grid and SVD inversion, respectively, were chosen based on the evaluation of different anisotropic scenarios of the reduced zone MOG model at HT-3 to HT-6 and HT-3 to HT-1, as well as, the expected range of K values at GEMS (0.0003 to 0.003 m/sec [0.001 to 0.0098 ft/sec]). In particular, the well pair at HT-3 to HT-6 was thought to have the best overall data and was used as a benchmark reference for the other data sets. K evaluation by individual well pair is further discussed below.

The K values in Figure 54 for the CPT well pair HT-3 to HT-6 are presented in Table 13. The K values (0.0003 to 0.0018 m/sec [0.0010 to 0.0058 ft/sec]) are within the range expected at GEMS. The contour trend follows the expected results for the GEMS lithology (Fig. 2) and HRST results, with high K values in the coarser, basal portion of the aquifer and low K values in the finer, upper portion of the aquifer. The HT-3 to HT-6 data set did not have any surrogate phase data and the data fit (9.95% average standard deviation K) was relatively good. Some of the larger percent standard deviation occurred in the high K portions of the test interval (Fig. 45 and Appendix F).

The K values in Figure 55 for the well pair HT-3 to HT-1 are presented in Table 9. The K values (0.0002 to 0.0017 m/sec [0.0008 to 0.0056 ft/sec]) are generally within the range expected at GEMS, although the low range K value is slightly lower than what has been reported in the past for the fine grained portion of the GEMS aquifer (0.0002 vs. 0.0003). However, the slight deviation is not considered significant and the overall contour trend of the plot still follows the expected GEMS lithology (Fig. 2) and HRST results. The HT-3 to HT-1 data set did not have any surrogate phase data and the data fit (10.7% average standard deviation K) was relatively good. Some of the larger percent standard deviation occurred in the high K portions of the test interval (Fig. 44 and Appendix F).

The data set presented in Figure 56 from HT-3 to HT-2 is summarized in Table 10. The ranges of K values (0.0002 to 0.0016 m/sec [0.0005 to 0.0051 ft/sec]) are within the expected range at GEMS and the contour plot depicts the expected K distribution. The well pair did not have any surrogate phase data but the data set was not quite as good as the benchmark well pairs. The amount of error between calculated and observed phases (14.6% average standard deviation K) was greater than the benchmark well pairs at HT-6 to HT-3 and HT-1 to HT-3 (Appendix F). Some of the error could likely be removed from the data set with greater constraint during SVD analysis, but because the K trends remain reasonable, additional constraint was deemed unnecessary.

The CPT data presented in Figure 57 from HT-3 to HT-4 is summarized in Table 11 and include surrogate phase data which replaced some unusable field data in the middle of the test section (Table 2). The ranges of K values (0.0002 to 0.0019 m/sec [0.0006 to 0.0061 ft/sec]) are within the expected range and the contour plot depicts a reasonable K distribution, although some of the heterogeneity graduation seen between the lower and upper zones in the benchmark well pairs seems to be suppressed or absent in the zones with surrogate phase. The K values are still within the order of other K data and the amount of error between calculated and observed phases is relatively good (9.43% average standard deviation), so the plot appears to be a representative depiction of the aquifer heterogeneity expected at GEMS. Comparison of this plot to Wachter's (2008) interpretation of the well pair would tend to confirm this lack of heterogeneity in this portion of the aquifer. The upper and middle zones are largely low K alluvium with the high K alluvium limited to just the basal portion of the aquifer, although the K values in the basal portion from this research are somewhat lower in magnitude and not as consistently extensive across the section (0.006 vs. 0.002 to 0.006 m/sec [0.0197 vs. 0.0066 to 0.0197 ft/sec]).

The CPT data shown in Figure 58 from HT-3 to HT-5 is summarized in Table 12 and include surrogate phase data for over half of the upper test interval (Table 3). The ranges of K values (0.0002 to 0.0024 m/sec [0.0005 to 0.0079 ft/sec]) are within the expected range at GEMS. Compared to the other hydraulic CPT well pair with surrogate phase (HT-4 to HT-3), the data fit is not as good (11.6% vs. 9.43% average standard deviation). However, the amount of error between calculated and observed phases at this well pair (11.6% average standard deviation K) is still consistent with HT-1 to HT-3 (10.7% average standard deviation K), which is one of the benchmark well pairs. The greatest error again appears in the lower high K zone (Appendix F). The heterogeneity trends are consistent with the other well pairs, but a higher K zone in the upper portion of the aquifer near the source well (HT-3) seems somewhat more pronounced and probably reflects the direct measurement of the HRST K point source data used to estimate the surrogate phase data for the CPT well pair.

The pumped hydraulic CPT data (30-sec period) collected from the radial well area replicate the aquifer interval that Wachter (2008) tested with a pneumatic CPT source (3 to 4-second period). The summary results of that earlier research were evaluated and compared to this research to evaluate the difference between the two different CPT source methods. Wachter, to identify the best model to evaluate heterogeneity as well as inversion constraint, used a number of different model configurations, ray paths and different Ss values (1E-05 and 1.5E-05). The phase depends on a ratio between Ss and K, so changes in Ss will also result in changes in K. This introduces a potential source of error, due to the difficulty of measuring Ss in situ. In this research, an attempt to limit this error was implemented by correlating Ss using the measured phase and HRST or ZOP K. The corrected Ss was used for modeling and inversion. Wachter determined that a Ss value of 1.5E-05 and about 750 rays produced the best results. The corrected Ss values (about 1.1E-05 to 1.69E-05) and MOG rays (756 to 784) used for this research were comparable to Watcher's earlier tomographic work. Wachter's model configurations were slightly different, which used elements instead of nodes for straight ray approximation through the model grids and his model generally had fewer total zones (e.g., 16 vs. 21 or 24). The different model configuration for this research was developed from the use of the relatively unattenuated ZOP data to create a representative aquifer model. It was expected that utilizing a node model grid along with more vertical and lateral zones and initial use of ZOP phase data could improve the resolution of the method.

The range of K values derived by Wachter (2008) with the 3 to 4-second CPT period are relatively consistent with the ones in this research and follow the expected trends based on the aquifer lithology and range of reported K values at GEMS. However, in general, there was some difference in heterogeneity resolution between the two CPT sources. Wachter, with the exception of the HT-4 to HT-3 well pair, was able to resolve a somewhat higher K zone (e.g., 0.0015 – 0.0045 m/sec [0.0049 – 0.0148 ft/sec]) in the middle of the aquifer. In contrast, the K values derived with the pumped hydraulic CPT were mostly lower in the intermediate zone (e.g., 0.0006 to 0.001 m/sec [0.0020 to 0.0033 ft/sec]). Although, as an exception, the HT-5 to HT-3 well pair did have somewhat higher K values (e.g., 0.0015 m/sec [0.0049 ft/sec]) through this zone.

This heterogeneity difference through the middle zone could reflect the way the data plots were constrained during contouring or a difference between the periods of the two CPT sources. Wachter's contour plots used SVD-determined K values which were constrained by HRST K data along the source and receiver well locations. The contour plots for this research were not constrained by HRST K because phase data inversion and SVD analysis node points define the model boundary at the source and receiver wells. The HT-5 to HT-3 contour (Fig. 58) may reflect this constraint difference. This well pair had a significant portion of the field data replaced with surrogate phase data which are estimated from HRST K, so the SVD analysis there may be replicating some of the HRST K constraint within the 3 to 4-second CPT period data sets. Also, in consideration of the period differences, results from the numerical modeling of the heterogeneity extension indicate that the 30-second CPT period does not have as much resolution as the

3 to 4-second CPT period, so some of this heterogeneity loss is possibly due to the different CPT source periods.

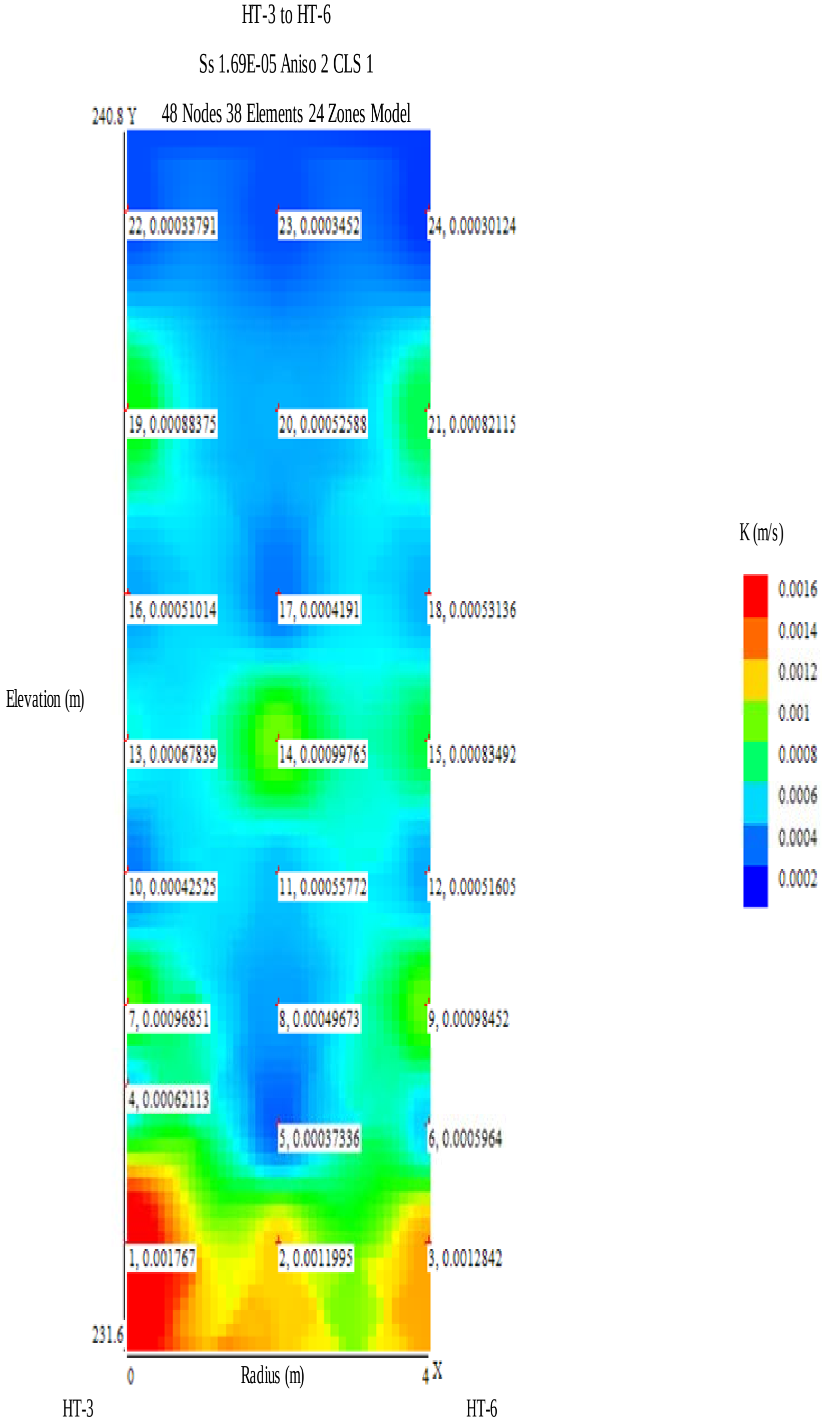

Figure 54 – K values from constrained SVD analysis of 784 rays at HT-3 (receiver) to HT-6 (source). K values range from 0.0003 to 0.0018 m/sec (0.0010 to 0.0058 ft/sec).

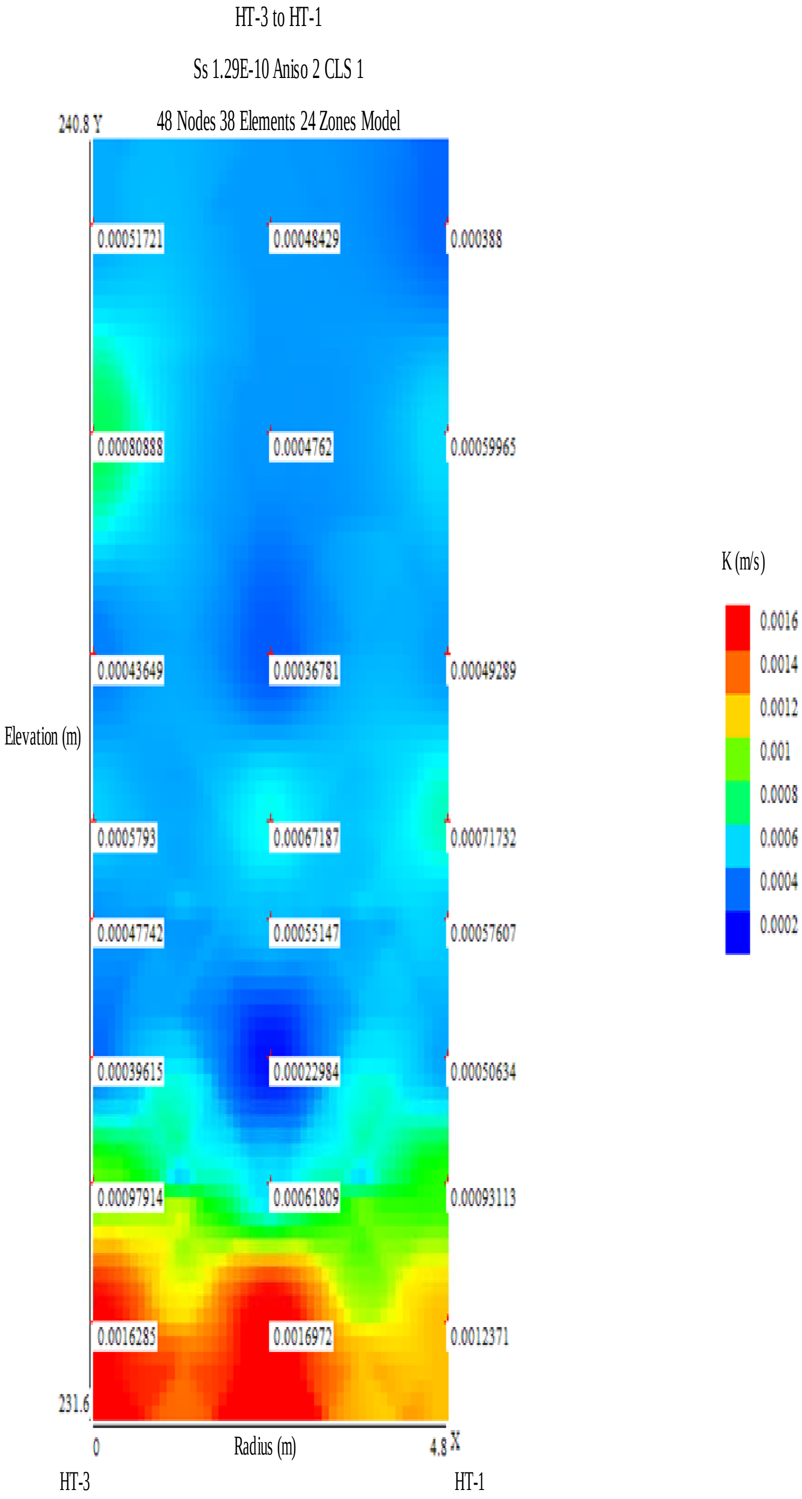

Figure 55 – K values from constrained SVD analysis of 756 rays at HT-3 (receiver) to HT-1 (source). K values range from 0.0002 to 0.0016 m/sec (0.0005 to 0.0051 ft/sec).

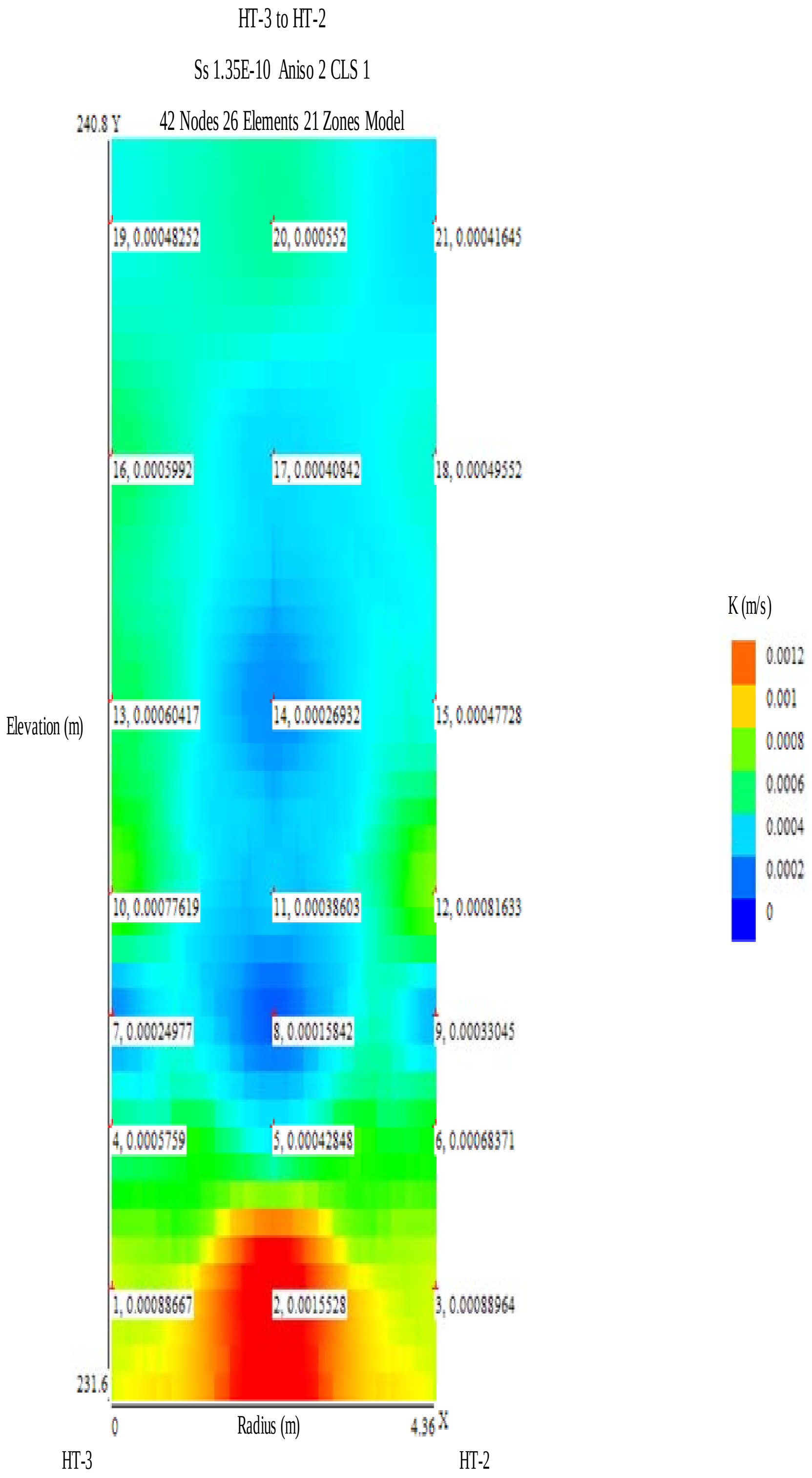

Figure 56 – K values from constrained SVD analysis of 756 rays at HT-3 (receiver) to HT-2 (source). K values range from 0.0002 to 0.0016 m/sec (0.0005 to 0.0051 ft/sec).

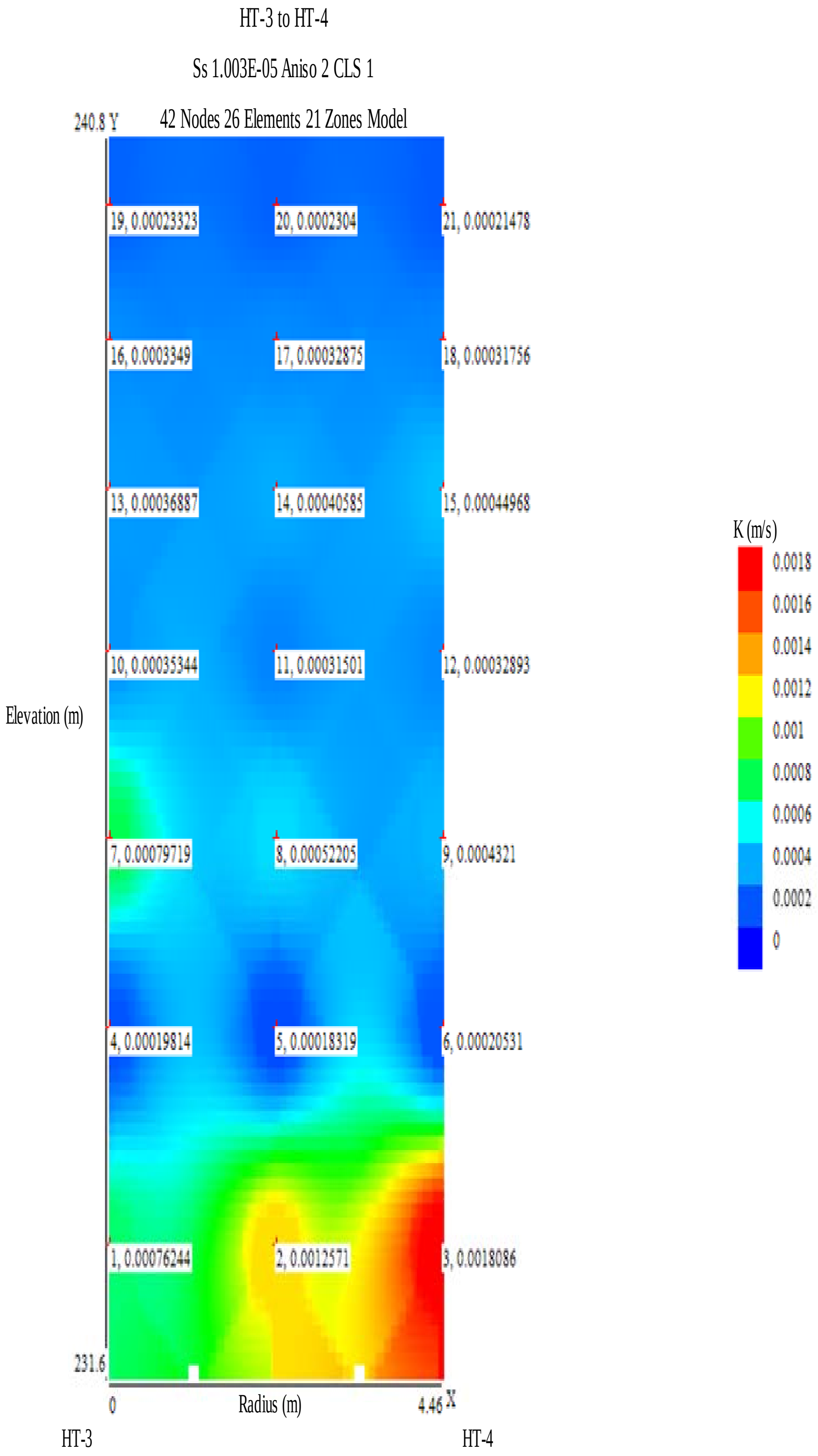

Figure 57 – K values from constrained SVD analysis of 784 rays at HT-3 (receiver) to HT-4 (source). K values range from 0.0002 to 0.0019 m/sec (0.0006 to 0.0061 ft/sec).

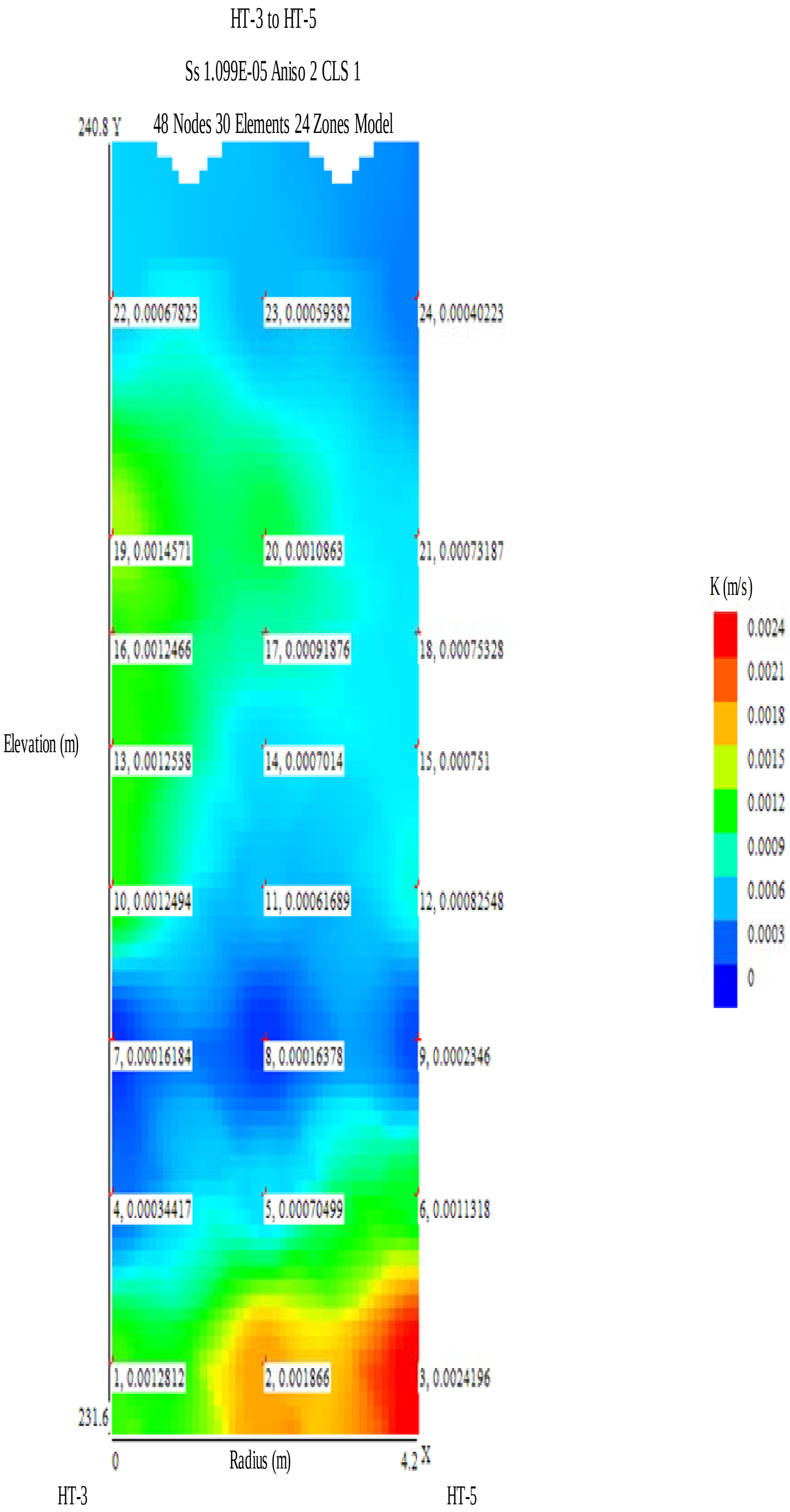

Figure 58 – K values from constrained SVD analysis of 784 rays at HT-3 (receiver) to HT-5 (source). K values range from 0.000 to 0.00 m/sec (0.000 to 0.00 ft/sec).

Lateral Heterogeneity – Pneumatic CPT Source

Contour plots were made of K values plotted against elevation and the radial distance between the Geoprobe source location and two receiver wells using the graphing program, QuickGrid. Results for K were plotted with the source location (HT-GP) on the left and receiver wells on the right (i.e., HT-2 or HT-3). The K values from this triangular array (Fig. 1) were obtained with the pneumatic CPT source and a 3-sec oscillating period. A best case anisotropy ratio and inversion constraint factor for the lateral model grid and SVD inversion, respectively, were chosen based on the anisotropic evaluation of the reduced-zone MOG model and the lateral heterogeneity model at HT-GP to HT-2. The data fit to these models was significantly improved with a constraint factor of 1 (which fit the surrogate phase to the model phase) and, by increasing the anisotropy ratio from 2 to 10 (which better fit the farthest offset rays of the MOG). This improved fit due to the application of a larger anisotropy ratio was not apparent in the 30-sec CPT data sets and suggests that the 3-sec data sets were more sensitive to anisotropy. However, as discussed previously, additional inversion constraint was needed for the HT-GP to HT-3 well pair to suppress a K data point that was an order of magnitude greater than the rest of the K values in the lateral model. These constraints, anisotropy, and the expected range of K values at GEMS (0.0003 to 0.003 m/sec [0.001 to 0.0098 ft/sec]) were used to evaluate the lateral heterogeneity. K evaluation by individual well pair is further discussed and presented below.

The K values presented in Figure 59 from HT-GP to HT-2 are summarized in Table 14 and include surrogate phase data which replaced some unusable field data in the middle and upper portion of the test section (Table 4). The ranges of K values (0.0003 to

0.002 m/sec [0.0009 to 0.0067ft/sec]) are within the expected range at GEMS. Different anisotropy ratios and constraint factors were considered for this data set, and larger anisotropy ratios showed some good improvement of the data fit to the reduced zone model, indicating that the low period data are more sensitive to the anisotropy of the aquifer. But when considering the lateral heterogeneity, compared to the pumped hydraulic CPT locations with surrogate data (26.47% vs. 11.6% average standard deviation), the fit between the model and measured data are not as good (Fig. 46 and Appendix G). However, most of the error in the lateral heterogeneity model occurs around the six nodes in the basal high K portion of the aquifer (Fig. 59). Fewer multiple intersecting rays through the zones may exacerbate this; diagonal rays are needed for good lateral resolution. If these zones are not considered, the average percent standard deviation is lowered to about 22%, which is improved and more comparable to the error in the other pneumatic data set.

The K values presented in Figure 60 from HT-GP to HT-3 are summarized in Table 15 and include surrogate phase data which replaced some unusable field data in the middle and upper portion of the test section (Table 5). The ranges of K values (0.0002 to 0.001 m/sec [0.0006 to 0.0037ft/sec]) are within the expected range at GEMS. Inversion of the experimental phase shift with an anisotropy ratio of 10 produced K values that exceeded the expected range and several orders of magnitude greater than the data set. A larger constraint factor of 10 produced reasonable K values with an average percent standard deviation of about 17%; but the data fit tends to be more biased towards the initial K estimates than the full experimental data set would suggest (Fig. 47 and

Appendix G). In contrast to the other CPT data sets, the data fit in the high K portion of the aquifer is comparable to the fit in the rest of the aquifer.

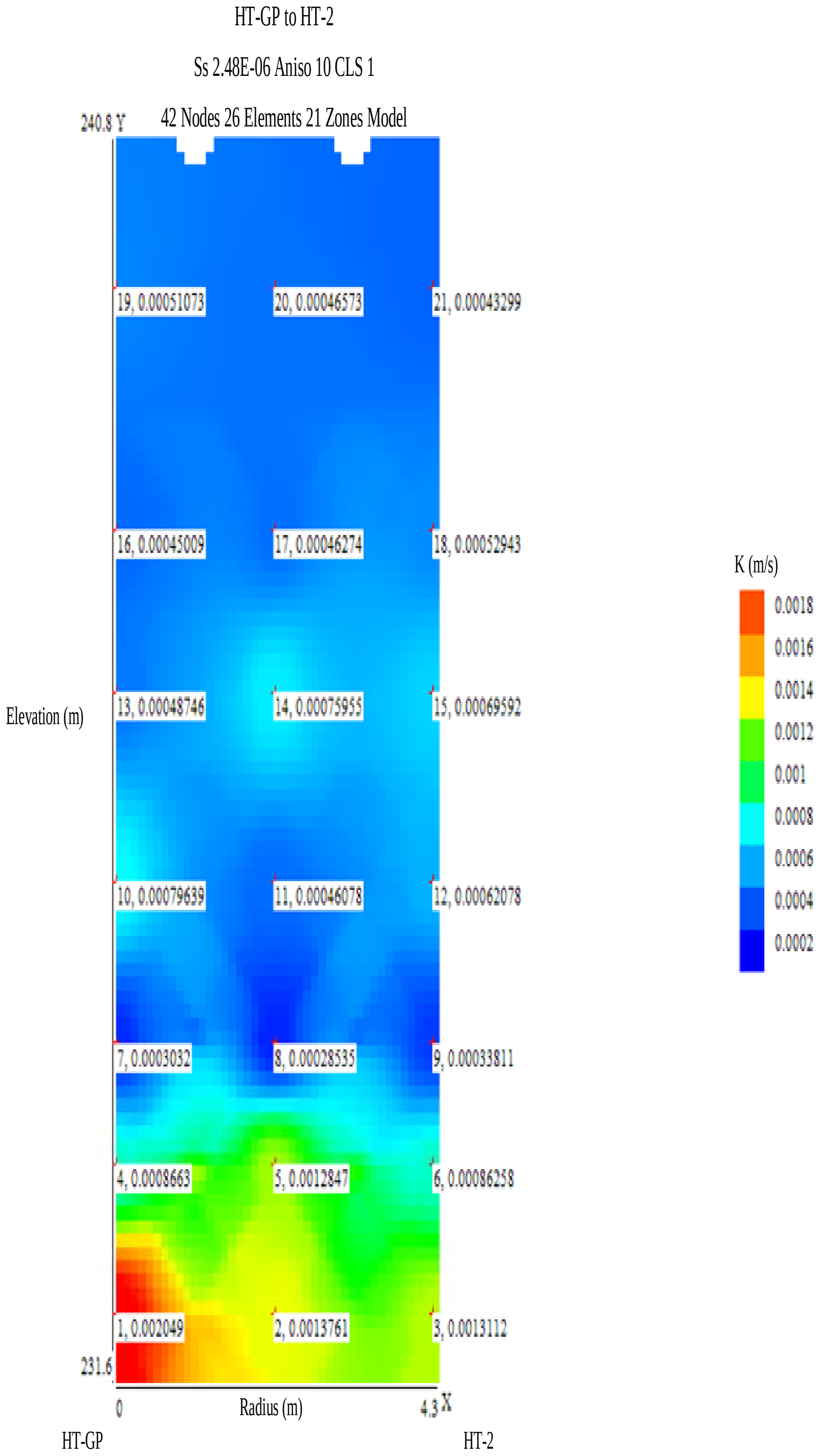

Figure 59 – K values from constrained SVD analysis of 729 rays at HT-GP (source) to HT-2 (receiver). K values range from 0.0003 to 0.002 m/sec (0.0009 to 0.0067 ft/sec).

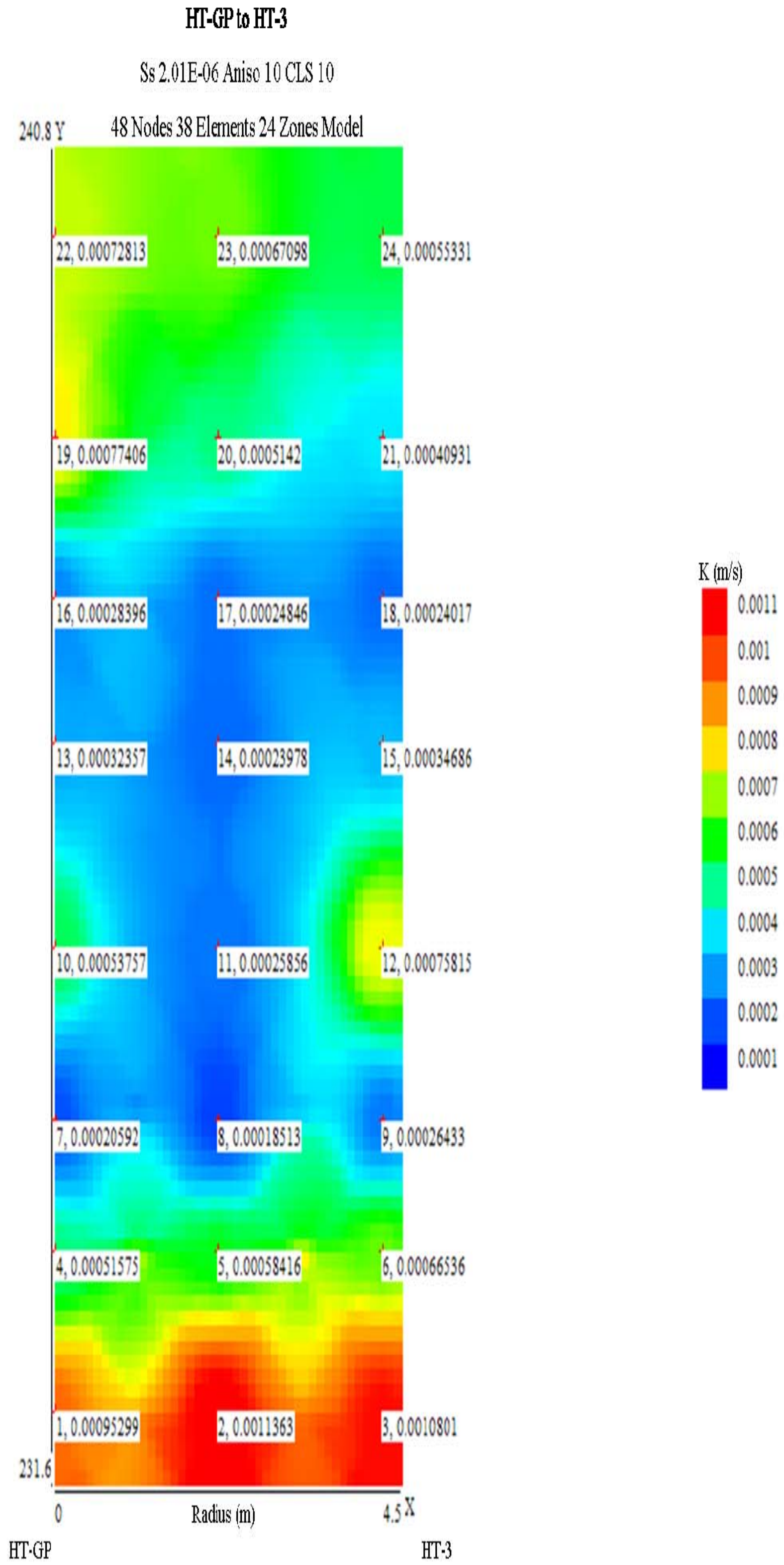

Figure 60 – K values from constrained SVD analysis of 784 rays at HT-GP (source) to HT-3 (receiver). K values range from 0.0002 to 0.0011 m/sec (0.0006 to 0.0037 ft/sec).

Summary And Conclusions

As stated in the objectives section of this report, the goal of this research was to develop and evaluate equipment and to collect field data which can efficiently measure high-resolution hydraulic conductivity by tomography with a sinusoidal pressure source (i.e., CPT). Different data processing procedures were evaluated to develop representative models to evaluate the lateral heterogeneity and anisotropy of an extended area of the aquifer at the University of Kansas GEMS site. New equipment adaptations included evaluating a pumped hydraulic oscillatory source with a computer controlled 30-sec period in lieu of a pneumatic CPT source with a 3-4 sec period (manually set by frequency generator) that was used during previous research. Pumped hydraulic CPT data were collected from a radial well array with a central source well (HT-3) and five receiver wells (HT-1, HT-2, HT-4, HT-5 and HT-6). A complete tomography survey using a 30-sec CPT source had not been completed at GEMS location. It generated a large tomography data set which was used to evaluate the variation of K across the area. The resolution of the 30-sec period method relative to the earlier 4-sec CPT tomographic survey was evaluated numerically. Additionally an, in-situ pneumatic source with a computer controlled 3-sec period was developed and deployed by a Geoprobe rig (HT-GP) to evaluate the feasibility of tomographic application by direct-push technology. CPT has not been deployed by Geoprobe in the past, so this new adaptation allowed evaluation of the method relative to a conventional CPT test. A new, multilevel receiver was constructed and Geoprobe pneumatic MOG data were recorded simultaneously in two receiver wells (i.e., HT-2 and HT-3). The simultaneous collection of data in two receiver wells had not been attempted in the past and the second receiver allowed data collection at a much greater rate. The five hydraulic CPT well pairs and two pneumatic CPT well pairs provide hydraulic conductivity estimation in a 360-degree radial array over an extended area at GEMS.

CPT data analysis is similar to that used to understand to the effect of tides on groundwater levels. It is known that tidal signals decay exponentially and phase shift occurs in proportion to the distance from shore. These equations can be generalized to a point source that spreads out in all directions in a homogenous aquifer. Basic theory states that the phase shift of an oscillating signal incorporates the hydraulic conductivity term and is related to the aquifer's physical property called diffusivity (ratio of K to Ss). The homogenous case is transformed to the heterogeneous case with a simple approximation of the phase by using a distance weighted average for the hydraulic conductivity. Phase shift data for this research were collected in MOG data sets between an oscillating CPT source and multiple receivers. The analysis of many MOGs and their intersecting, offset rays is the basis of the tomographic method. The use of a CPT coupled with tomographic imaging techniques for this research is unique from other hydraulic tomographic methods which typically measure the aquifer response as pumping-induced drawdown at steady state. Researches have found that the inversion for the K distribution is sensitive to a correct description of the boundary conditions and may require excessively long periods of pumping. In contrast, the CPT signal can be measured quickly and it carries information about the physical properties of the aquifer it traveled through.

Data for this research were analyzed using Visual Basic computer programs to process, model, and invert the phase shift to evaluate the hydraulic conductivity distribution at GEMS. Data processing was completed during 2010. Typically, the hydraulic tomography inversion process requires a nonlinear fitting process requiring a numerical aquifer model to be solved iteratively, which is time and computer intensive. Adoption of the straight ray approximation method (with spatial K weighting) to model the ray paths though a model grid designed to represent the aquifer between the different well pairs allows a quick and efficient inversion without iterations. K values were determined by SVD analysis, a method of least squares statistical analysis that allows solution for diffusivity, which allows K determination if Ss is assumed.

The large tomography data sets were used to evaluate the GEMS aquifer in a new level of detail. High resolution zero offset profile data were used to construct representative models of the aquifer between the different well pairs. The multiple intersecting rays of the MOG data sets allowed the evaluation of anisotropy and lateral heterogeneity to a greater degree than what has been attempted before in this research project. In some instances, in the case of the pumped hydraulic CPT testing, poor data were collected due to transducer failure or, in the case of pneumatic CPT, due to energy loss from a packer failure, variable formation collapse around the tool, and high frequency attenuation. To address that data loss, a method was devised based on the relationship between the phase and hydraulic conductivity and Ss to calculate and substitute surrogate phase derived from constraining HRST K point source data. Surrogate phase replaced questionable CPT locations so the larger data sets of multiple MOGs in a well pair could be preserved and tomographically analyzed as a whole. Various anisotropic and isotropic models were used to evaluate anisotropy and lateral heterogeneity cases. Different degrees of constraint were evaluated to determine the best data fit by SVD analysis. Contour plots of the calculated K values were graphed with the public domain software program, QuickGrid, to represent the aquifer between the different well pairs. The ranges of calculated K values were compared to the lithology of the aquifer and HRST K values from the well array to evaluate the success of the inversion. Tomographic analysis from this research generated K values that fell within these guidelines, indicating good performance of the CPT equipment and data processing techniques.

The 3 and 30-sec CPT period data sets were used to evaluate the resolution and differences between the two sources. Theory indicates that a 30-sec CPT source will propagate further but have less resolution; it was unknown if the greater resolution 3-sec CPT data would be effective at the long-offset ray path locations. Data analysis indicated that the 3-sec period, in some cases, was more sensitive to vertical anisotropy than had been expected. Modeling with a greater degree of anisotropy allowed a better fit for K values in fine-grained material and long-offset rays, while the 30-sec CPT period data seemed somewhat insensitive to degrees of anisotropy ratio greater than 2. In contrast to the anisotropy results, statistical analysis indicates that lateral heterogeneity resolution is somewhat better with 30-sec data than 4-sec data. However, data fit to models, according to the percent standard deviation, from both of the CPT sources decline as more lateral model zones are added, indicating the performance of the inversion is sensitive to addition of model variables used to define the aquifer in greater detail.

Since analytical solutions do not exist for the heterogeneous case, numerical modeling was performed to check the spatially weighted straight ray approximation. Synthetic data were generated with a numerical finite difference model and modeling studies were preformed to demonstrate that data could be inverted with reasonable amounts of error. Zones could be resolved using the SVD program to dimensions of about 1 m (3 ft). Comparison of the 4 and 30-sec CPT modeling studies indicate that the 30-sec period CPT does have more inherent error than the 4-sec CPT, but error associated with the inversion of field data are comparable between the two sources. The 30-sec CPT has about 27 - 29% total error and the 4-sec CPT has about 16 - 19% total error associated with the straight ray method, ambient noise, and the inversion of field data.

The goals of this research were successfully achieved. New equipment was developed to test a previously unevaluated 30-sec period, pumped source CPT; in addition, a new direct push deployment platform with multiple receiver arrays was used to collect data. Five pumped hydraulic well pairs and two direct push well pairs were analyzed and had reasonable inter-well K distributions. The 30-sec CPT data were compared to previous research completed with a pneumatic 3-4 sec CPT period. Data trends and K values were similar and within the general range seen with HRST, although the 30-sec data did not have some of the resolution obtained with the short period CPT source used for earlier research and the direct push CPT used in this research. Problems can be explained by equipment difficulties which sometimes generated variable data quality before it was noticed and corrected in the field. Surrogate phase data were developed and used to replace questionable data where possible so the entire data set could be analyzed by the tomographic techniques described in this research. Resolution is dependent upon period, so additional research with periods between 3 and 30-sec can determine the optimal frequency to achieve the best signal to evaluate heterogeneity.

This research was supported in part by the U.S. Department of Defense, through the Strategic Environmental Research and Development Program (SERDP).

References

Aster, R.C., Borchers, B., and Thurber, C.H., 2005, Parameter estimation and inverse problems: Amsterdam, Elsevier Academic Press, 301 p.

Black, J.H., and Kipp Jr, K.L., 1981, Determination of hydrogeological parameters using sinusoidal pressure tests: a theoretical appraisal: Water Resources Research, v. 17, p. 686-692.

Bohling, G.C., 1999, Evaluation of an induced gradient tracer test in an alluvial aquifer: Kansas Geological Survey Open-file Report no. 99-6, p. 224.

Bohling, G.C., Zhan, X., Butler Jr, J.J., and Zheng, L., 2002, Steady shape analysis of tomographic pumping tests for characterization of aquifer heterogeneities: Water Resources Research, v. 38, p. 601-6015.

Brauchler, R., Liedl, R., and Dietrich, P., 2003, A travel time based hydraulic tomographic approach: Water Resources Research, v. 39, p. SBH201-SBH2012.

Butler, J.J., Jr., Lanier, A., A., Healy, J., Sellwood, S., M., McCall, W., and Garnett, E., 2000, Direct-push hydraulic profiling in an unconsolidated alluvial aquifer: Kansas Geological Survey Open-file Report no. 2000-62.

Butler Jr, J.J., Healy, J., Zheng, L., McCall, W., and Schulmeister, M.K., 1999, Hydrostratigraphic characterization of unconsolidated alluvial deposits with direct-push sensor technology: Kansas Geological Survey Open-file Report no. 99-40.

Butler Jr., J.J., 2007, The design, performance, and analysis of slug tests, Lewis Publishers, 252 p.

—, 2008, Pumping tests for aquifer evaluation;time for a change?, Ground Water, p. 615-617.

Cooper, H.H., Jr., Bredehoeft, J.D., and Papadopulos, I.S., 1967, Response of a finite-diameter well to an instantaneous charge of water: Water Resources Research, v. 3, p. 241-244.

Deki, P., 2008, Comparing Slug Tests to Oscillatory Stress Tests: Lawrence, University of Kansas, p. 18.

Domenico, P., A., and Schwartz, F., W., 1998, Physical and Chemical Hydrogeology: New York, John Wiley & Sons, 506 p.

Engard, B.R., 2006, Estimating Aquifer Parameters From Horizontal Pulse Tests [Master of Science thesis]: M.S. Dissertation, The University of Kansas.

Ferris, J.G., 1952, Cyclic fluctuations of water level as a basis for determining aquifer transmissibility: IAHS Publication, v. 33, p. 148-155.

Fetter, C.W., 2001, Applied hydrogeology, Prentice-Hall. Upper Saddle River, NJ, United States. Pages: 598. 2001.

Hantush, M.S., 1960, Lectures at New Mexico Institute of Mining and Technology, compiled by Steve Papadopulos, p. 119.

Healy, J., McElwee, C.D., and Engard, B.R., 2004, Delineating hydraulic conductivity with direct-push electrical conductivity and high resolution slug testing, American GeophysicalUnion Poster H23A-1118.

Huettl, T.J., 1992, An evaluation of a borehole induction single-well tracer test to characterize the distribution of hydraulic properties in an alluvial aquifer [Master of Science thesis]: M.S. Dissertation

The University of Kansas.

Hvorslev, M.J., 1951, Time lag and soil permeability in ground-water observations, waterway experimental station, Corps of Engineers, US Army: Bulletin no. 36, p. 50.

Johnson, C.R., 1968, Pulse-testing; a new method for measuring reservoir continuity between wells, *in* Greenkorn, R.A., and Woods, E.G., eds., Special Paper - Geological Society of America: United States, Geological Society of America (GSA) : Boulder, CO, United States, p. 109-109.

Kruseman, G.P., and de Ridder, N.A., 1991, Analysis and evaluation of pumping test data: Netherlands, Int. Inst. Land Reclamation Improvement : Wageningen, Netherlands.

Lane, J.W., Day-Lewis, F.D., and Casey, C.C., 2006, Geophysical monitoring of a field-scale biostimulation pilot project: Ground Water, v. 44, p. 430-443.

Lane, J.W., Jr., Day-Lewis, F.D., Joesten, P.K., Miller, R.D., and Liner, C., 2007, Monitoring engineered remediation with borehole radar.; Near surface/ seismic to radar: The Leading Edge (Tulsa, OK), v. 26, p. 1032-1035.

Lee, J., 1982, Well testing:, Soc. Pet. Eng. AIME : New York, NY, United States.

McElwee, C.D., Butler Jr, J.J., Macpherson, G.L., Bohling, G.C., Miller, R.D., Mennicke, C.M., Huettl, T.J., Zenner, M., Hyder, Z., Liu, W., Orcutt, M., Beilfuss, M.L., and Gonuguntla, S., 1995, Characterization of heterogeneities controlling transport and fate of pollutants in unconsolidated sand and gravel aquifers, final report: Kansas Geological Survey Open-file Report no. 95-16, p. 559.

McElwee, C.D., and Zenner, M.A., 1998, A nonlinear model for analysis of slug-test data: Water Resour. Res., v. 34, p. 55-66.

O'Conner, H.G., 1960, Geology and ground-water resources of Douglas County, Kansas: Kansas Geological Survey Bulletin 148, p. 200.

Oldenburg, D.W., and Li, Y., 2005, Inversion for applied geophysics: A tutorial; *in,* Butler, D.K. (ed.), Near surface geophysics: Tulsa, Society of Exploration Geophysicists, 89-150 p.

Prosser, D.W., 1981, A method of performing response tests on highly permeable aquifers: Ground Water, v. 19, p. 588-592.

Ricciardi, K.L., 2009, Remediation of Heterogeneous Aquifers Subject to Uncertainty, Ground Water, p. 675-685.

Ross, H.C., 1997, Utility of multi-level slug tests to define spatial variation of hydraulic conductivity in an alluvial aquifer, Northeastern Kansas [Master of Science thesis]: M.S. dissertation, The University of Kansas.

Ross, H.C., and McElwee, C.D., 2007, Multi-level slug tests to measure 3-D hydraulic conductivity distributions: Natural Resources Research.

Schad, H., and Teutsch, G., 1994, Effects of the investigation scale on pumping test results in heterogeneous porous aquifers: Journal of Hydrology, v. 159, p. 61-77.

Sudicky, E.A., 1986, A natural gradient experiment on solute transport in a sand aquifer; spatial variability of hydraulic conductivity and its role in the dispersion process: Water Resources Research, v. 22, p. 2069-2082.

Theis, C.V., 1989, The relation between the lowering of the piezometric surface and the rate and duration of discharge of a well using ground-water storage: United States, Am. Inst. Hydrol. : Minneapolis, MN, United States, xiii-xvii p.

Wachter, B.J., 2008, Characterizing Aquifer Heterogeneity Using Hydraulic Tomography [Master of Science thesis]: M.S. Dissertation, The University of Kansas.

Wang, H., and Anderson, M., 1995, Introduction to groundwater modeling: finite difference and finite element methods, Academic Press.

Yeh, T.-C.J., and Lee, C.-H., 2007, Time to Change the Way We Collect and Analyze Data for Aquifer Characterization: Ground Water, v. 45, p. 116-118.

Yeh, T.C.J., and Liu, S., 2000, Hydraulic tomography: Development of a new aquifer test method: Water Resources Research, v. 36, p. 2095-2105.

Zemansky, G.M., and McElwee, C.D., 2005, High-resolution slug testing: Ground Water, v. 43, p. 222-230.

Tables

Tomography Survey Data		
Location	Elevation (ft msl)	Elevation (m msl)
Corps BM	827.56	252.24
HT-1	830.01	252.99
HT-2	829.66	252.88
HT-3	829.71	252.89
HT-4	830.13	253.02
HT-5	829.65	252.88
HT-6	830.27	253.07
7-1	828.34	252.48
11-1	828.36	252.48
Inj Well	829.79	252.92
Geoprobe BM	828.82	252.62

Well	Radius (m)	Radius (ft)
HT-3 to HT-1	4.77	15.65
HT-3 to HT-2	4.36	14.31
HT-3 to HT-4	4.46	14.62
HT-3 to HT-5	4.21	13.81
HT-3 to HT-6	3.99	13.10
HT-GP to HT-2	4.23	13.88
HT-GP to HT-3	4.25	13.94

Table 1 – Survey elevation and radial distances between wells.

HT-4 to HT-3 Corrected Ss and Surrogate Phase

Raypath/Zone	Test Interval Elev (ft msl)	HT-4 HRST Elev (ft msl)	HT-4 HRST K (ft/sec)	HT-3 HRST Elev (ft msl)	HT-3 HRST K (ft/sec)	HT-4 to HT-3 K Average K_{HRST} (ft/sec)	Ss_{Est}	P (sec)	r (ft)	Estimated Phase Shift Φ_{Est}	Expiremental Phase Shift Φ_{Exp}	Ss_{Corr}	Corrected Phase Shift Φ_{Corr}	HyrdaulicTomAnal Phase Shift $\Phi_{HRST K}$
1	761	Not sluged(1)		Not slugged(1)		0.0060	1.00E-05	30	14.62	0.0307	0.0334	1.04E-05	0.0313	0.0313
2	762	761.53	0.0060	Not slugged		0.0060				0.0307	0.0305		0.0313	0.0313
3	763	762.53	0.0092	Not slugged		0.0092				0.0248	0.0375		0.0253	0.0265
4	764	763.53	0.0095	764.01	0.0090	0.0093				0.0248	0.0322		0.0252	0.0252
5	765	764.53	0.0082	765.01	0.0089	0.0085				0.0258	0.0359		0.0262	0.0260
6	766	765.53	0.0046	766.01	0.0077	0.0061				0.0304	0.0334		0.0309	0.0300
7	767	766.53	0.0007	767.01	0.0032	0.0020				0.0535	0.0455		0.0545	0.0498
8	768	767.53	0.0005	768.01	0.0004	0.0005				0.1113	0.0649		0.1132	0.1015
9	769	768.53	0.0006	769.01	0.0002	0.0004				0.1201	0.0642		0.1222	0.1204
10	770	769.53	0.0007	770.01	0.0001	0.0004				0.1191	0.0504		0.1212	0.1214
11	771	770.53	0.0024	771.01	0.0003	0.0014				0.0644	0.0277		0.0655	0.0767
12	772	771.53	0.0072	772.01	0.0019	0.0046				0.0353	0.0152		0.0359	0.0418
13	773	772.53	0.0050	773.01	0.0050	0.0050				0.0337	0.0172		0.0343	0.0347
14	774	773.53	0.0010	774.01	0.0058	0.0034				0.0410	0.0414		0.0418	0.0403
15	775	774.53	0.0012	775.01	0.0038	0.0025				0.0472	0.0454		0.0481	0.0468
16	776	775.53	0.0017	776.01	0.0024	0.0020				0.0529	0.0213		0.0539	0.0527
17	777	776.53	0.0022	777.01	0.0069	0.0046				0.0352	0.0204		0.0359	0.0395
18	778	777.53	0.0031	778.01	0.0069	0.0050				0.0337	0.0145		0.0343	0.0346
19	779	778.53	0.0024	779.01	0.0045	0.0035				0.0405	0.0638		0.0412	0.0398
20	780	779.53	0.0028	780.02	0.0038	0.0033				0.0415	0.0617		0.0422	0.0420
21	781	780.53	0.0038	781.02	0.0090	0.0064				0.0298	0.0546		0.0303	0.0327
22	782	781.53	0.0025	782.02	0.0034	0.0029				0.0441	0.0591		0.0449	0.0420
23	783	782.53	0.0020	783.02	0.0032	0.0026				0.0466	0.0625		0.0474	0.0469
24	784	783.53	0.0018	784.02	0.0030	0.0024				0.0484	0.0644		0.0493	0.0489
25	785	784.53	0.0017	785.02	0.0029	0.0023				0.0497	0.0567		0.0505	0.0503
26	786	785.53	0.0010	786.02	0.0027	0.0018				0.0554	0.0698		0.0563	0.0552
27	787	786.53	0.0006	787.02	0.0024	0.0015				0.0617	0.0764		0.0628	0.0615
28	788	787.53	0.0007	788.02	0.0020	0.0014				0.0645	0.0781		0.0657	0.0651
						K_{HRST_Ave}				Φ_{Est_Ave}	Φ_{Exp_Ave}			
						0.0037				0.0519	0.0528			

Notes

Source location with marginal transducer data.

(1) Ray path or zone interval without HRST K data. 0.006 (ft/sec) is an estimate representative example.

Table 2 – HT-4 to HT-3 corrected Ss and surrogate phase.

Raypath/Zone	Test Interval	HT-5 HRST		HT-3 HRST		HT-5 to HT-3 K Average				Estimated Phase Shift	Expiremental Phase Shift		Corrected Phase Shift	HyrdaulicTomAnal Phase Shift
	Elev (ft msl)	Elev (ft msl)	K (ft/sec)	Elev (ft msl)	K (ft/sec)	K_{HRST} (ft/sec)	Ss_{Est}	P (sec)	r (ft)	Φ_{Est}	Φ_{Exp}	Ss_{Corr}	Φ_{Corr}	$\Phi_{HRST\,K}^{(1)}$
1	761	Not slugged		Not slugged		No data	1.00E-05	30	14.62	No data	0.0294	1.10E-05	No data	0.0431
2	762	762.05	0.0118	Not slugged		0.0118				0.0207	0.0220		0.0217	0.0260
3	763	763.05	0.0115	Not slugged		0.0115				0.0209	0.0343		0.0220	0.0219
4	764	764.05	0.0120	764.01	0.0090	0.0105				0.0220	0.0385		0.0230	0.0228
5	765	765.05	0.0098	765.01	0.0089	0.0093				0.0233	0.0400		0.0244	0.0241
6	766	766.05	0.0034	766.01	0.0077	0.0055				0.0302	0.0305		0.0317	0.0303
7	767	767.05	0.0012	767.01	0.0032	0.0022				0.0480	0.0440		0.0504	0.0466
8	768	768.05	0.0011	768.01	0.0004	0.0008				0.0814	0.0568		0.0854	0.0784
9	769	769.05	0.0014	769.01	0.0002	0.0008				0.0814	0.0317		0.0854	0.0854
10	770	770.05	0.0051	770.01	0.0001	0.0026				0.0440	0.0364		0.0461	0.0540
11	771	771.05	0.0082	771.01	0.0003	0.0043				0.0343	0.0759		0.0360	0.0380
12	772	772.05	0.0082	772.01	0.0019	0.0051				0.0316	0.0531		0.0332	0.0337
13	773	773.05	0.0043	773.01	0.0050	0.0046				0.0330	0.0062		0.0346	0.0343
14	774	774.05	0.0020	774.01	0.0058	0.0039				0.0360	0.0687		0.0378	0.0371
15	775	775.05	0.0022	775.01	0.0038	0.0030				0.0409	0.0481		0.0429	0.0419
16	776	776.05	0.0016	776.01	0.0024	0.0020				0.0504	0.0392		0.0529	0.0509
17	777	777.05	0.0014	777.01	0.0069	0.0041				0.0350	0.0593		0.0367	0.0399
18	778	778.05	0.0016	778.01	0.0069	0.0042				0.0346	0.0906		0.0363	0.0364
19	779	779.05	0.0024	779.01	0.0045	0.0035				0.0383	0.0487		0.0401	0.0394
20	780	780.05	0.0032	780.02	0.0038	0.0035				0.0381	0.9538		0.0399	0.0400
21	781	781.05	0.0022	781.02	0.0090	0.0056				0.0301	0.0545		0.0315	0.0332
22	782	782.05	0.0019	782.02	0.0034	0.0026				0.0438	0.0840		0.0459	0.0430
23	783	783.05	0.0019	783.02	0.0032	0.0026				0.0445	0.9538		0.0467	0.0465
24	784	784.05	0.0017	784.02	0.0030	0.0023				0.0466	0.0015		0.0488	0.0484
25	785	785.05	0.0015	785.02	0.0029	0.0022				0.0479	0.0179		0.0502	0.0499
26	786	786.05	0.0011	786.02	0.0027	0.0019				0.0516	0.0345		0.0541	0.0533
27	787	787.05	0.0007	787.02	0.0024	0.0015				0.0577	0.9538		0.0605	0.0592
28	788	788.05	0.0006	788.02	0.0020	0.0013				0.0619	0.9538		0.0649	0.0640
						K_{HRST_Ave}				Φ_{Est_Ave}	Φ_{Exp_Ave}			
						0.0042				0.0352	0.0369			

Notes

🟨 Source location replaced with HRST data.

(1) $\Phi_{HRST\,K}$ for Raypath/Zone 1 was calculated using a K value of 0.003 ft/sec which is an average representaive K value of the aquifer.

Table 3 – HT-5 to HT-3 corrected Ss and surrogate phase.

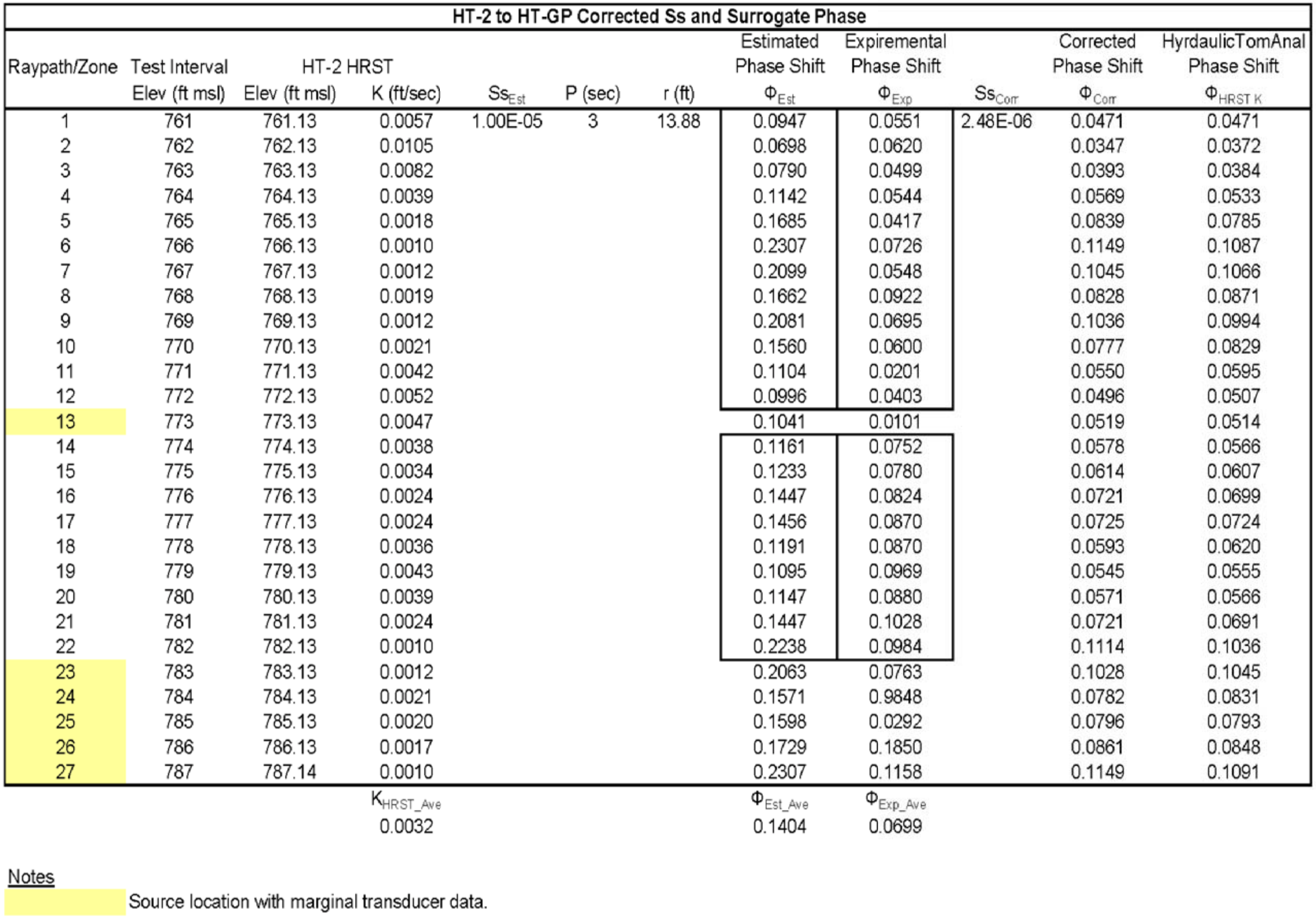

HT-2 to HT-GP Corrected Ss and Surrogate Phase

Raypath/Zone	Test Interval Elev (ft msl)	HT-2 HRST Elev (ft msl)	K (ft/sec)	Ss_{Est}	P (sec)	r (ft)	Estimated Phase Shift Φ_{Est}	Expiremental Phase Shift Φ_{Exp}	Ss_{Corr}	Corrected Phase Shift Φ_{Corr}	HyrdaulicTomAnal Phase Shift $\Phi_{HRST\ K}$
1	761	761.13	0.0057	1.00E-05	3	13.88	0.0947	0.0551	2.48E-06	0.0471	0.0471
2	762	762.13	0.0105				0.0698	0.0620		0.0347	0.0372
3	763	763.13	0.0082				0.0790	0.0499		0.0393	0.0384
4	764	764.13	0.0039				0.1142	0.0544		0.0569	0.0533
5	765	765.13	0.0018				0.1685	0.0417		0.0839	0.0785
6	766	766.13	0.0010				0.2307	0.0726		0.1149	0.1087
7	767	767.13	0.0012				0.2099	0.0548		0.1045	0.1066
8	768	768.13	0.0019				0.1662	0.0922		0.0828	0.0871
9	769	769.13	0.0012				0.2081	0.0695		0.1036	0.0994
10	770	770.13	0.0021				0.1560	0.0600		0.0777	0.0829
11	771	771.13	0.0042				0.1104	0.0201		0.0550	0.0595
12	772	772.13	0.0052				0.0996	0.0403		0.0496	0.0507
13	773	773.13	0.0047				0.1041	0.0101		0.0519	0.0514
14	774	774.13	0.0038				0.1161	0.0752		0.0578	0.0566
15	775	775.13	0.0034				0.1233	0.0780		0.0614	0.0607
16	776	776.13	0.0024				0.1447	0.0824		0.0721	0.0699
17	777	777.13	0.0024				0.1456	0.0870		0.0725	0.0724
18	778	778.13	0.0036				0.1191	0.0870		0.0593	0.0620
19	779	779.13	0.0043				0.1095	0.0969		0.0545	0.0555
20	780	780.13	0.0039				0.1147	0.0880		0.0571	0.0566
21	781	781.13	0.0024				0.1447	0.1028		0.0721	0.0691
22	782	782.13	0.0010				0.2238	0.0984		0.1114	0.1036
23	783	783.13	0.0012				0.2063	0.0763		0.1028	0.1045
24	784	784.13	0.0021				0.1571	0.9848		0.0782	0.0831
25	785	785.13	0.0020				0.1598	0.0292		0.0796	0.0793
26	786	786.13	0.0017				0.1729	0.1850		0.0861	0.0848
27	787	787.14	0.0010				0.2307	0.1158		0.1149	0.1091
			K_{HRST_Ave}				Φ_{Est_Ave}	Φ_{Exp_Ave}			
			0.0032				0.1404	0.0699			

Notes

🟨	Source location with marginal transducer data.

Table 4 – HT-GP to HT-2 corrected Ss and surrogate phase.

Table 5 – HT-GP to HT-3 corrected Ss and surrogate phase.

HT-GP to HT-3 Corrected Ss and Surrogate Phase											
Raypath/Zone	Test Interval Elev (ft msl)	HT-3 HRST Elev (ft msl)	HT-3 HRST K (ft/sec)	Ss_{Est}	P (sec)	r (ft)	Estimated Phase Shift Φ_{Est}	Expiremental Phase Shift Φ_{Exp}	Ss_{Corr}	Corrected Phase Shift Φ_{Corr}	HyrdaulicTomAnal Phase Shift $\Phi_{HRST K}$
1	761	Not slugged(1)	0.006	1.00E-05	3	13.94	0.0927	0.0543	2.01E-06	0.0415	0.0415
2	762	Not slugged(1)	0.006				0.0927	0.0582		0.0415	0.0415
3	763	Not slugged(1)	0.006				0.0927	0.0504		0.0415	0.0415
4	764	764.01	0.0090				0.0756	0.0587		0.0339	0.0354
5	765	765.01	0.0089				0.0763	0.0471		0.0342	0.0341
6	766	766.01	0.0077				0.0819	0.0748		0.0367	0.0362
7	767	767.01	0.0032				0.1264	0.0842		0.0567	0.0527
8	768	768.01	0.0004				0.3478	0.1127		0.1559	0.1360
9	769	769.01	0.0002				0.5573	0.0657		0.2498	0.2310
10	770	770.01	0.0001				0.6085	0.0777		0.2727	0.2682
11	771	771.01	0.0003				0.3923	0.0465		0.1758	0.1952
12	772	772.01	0.0019				0.1642	0.0462		0.0736	0.0940
13	773	773.01	0.0050				0.1020	0.0763		0.0457	0.0513
14	774	774.01	0.0058				0.0944	0.0769		0.0423	0.0430
15	775	775.01	0.0038				0.1157	0.0869		0.0519	0.0500
16	776	776.01	0.0024				0.1476	0.0885		0.0662	0.0633
17	777	777.01	0.0069				0.0864	0.0921		0.0387	0.0442
18	778	778.01	0.0069				0.0864	0.0980		0.0387	0.0387
19	779	779.01	0.0045				0.1071	0.1074		0.0480	0.0462
20	780	780.02	0.0038				0.1160	0.1002		0.0520	0.0512
21	781	781.02	0.0090				0.0758	0.1043		0.0340	0.0376
22	782	782.02	0.0034				0.1239	0.1106		0.0556	0.0512
23	783	783.02	0.0032				0.1264	0.0895		0.0567	0.0564
24	784	784.02	0.0030				0.1307	0.0495		0.0586	0.0582
25	785	785.02	0.0029				0.1322	0.1428		0.0593	0.0591
26	786	786.02	0.0027				0.1379	0.2282		0.0618	0.0613
27	787	787.02	0.0024				0.1480	0.2925		0.0663	0.0654
28	788	788.02	0.0020				0.1602	0.8153		0.0718	0.0707
			K_{HRST_Ave}				Φ_{Est_Ave}	Φ_{Exp_Ave}			
			0.0042				0.1744	0.0782			

Notes

🟨 Source location replaced with HRST data.

(1) Raypath/Zone interval 1, 2, and 3 not slug tested. 0.006 (ft/sec) K value is an estimated representative example.

HT-1 to HT-3 Corrected Ss and K									
HRST Well	HRST K_{Ave}	27 Zone ZOP Model	27 Zone Det. K (ft/sec)	Corr. Factor	27 Zone Det. K (ft/sec)	8 Zone ZOP Model	8 Zone Cal. K (ft/sec)	Corr. Factor	8 Zone Cal. K (ft/sec)
		Ss_{Est} 1.00E-05		1.2975	Ss_{Corr} 1.30E-05	Ss_{Est} 1.00E-05		1.2975	Ss_{Corr} 1.30E-05
HT-1	0.0025	1	0.0048		0.0063	1	0.0051		0.0066
HT-3	0.0038	2	0.0049		0.0063	2	0.0032		0.0042
		3	0.0059		0.0076	3	0.0016		0.0021
		4	0.0049		0.0064	4	0.0016		0.0021
		5	0.0034		0.0044	5	0.0021	x 1.2975 =	0.0027
		6	0.0033		0.0043	6	0.0015		0.0019
		7	0.0012		0.0016	7	0.0019		0.0025
		8	0.0022		0.0028	8	0.0012		0.0016
		9	0.0012		0.0015				
		10	0.0025		0.0032				
		11	0.0014		0.0018				
		12	0.0018		0.0024				
		13	0.0014		0.0018				
		14	0.0047	x 1.2975 =	0.0061				
		15	0.0014		0.0018				
		16	0.0020		0.0026				
		17	0.0015		0.0020				
		18	0.0012		0.0016				
		19	0.0018		0.0024				
		20	0.0012		0.0015				
		21	0.0022		0.0028				
		22	0.0018		0.0023				
		23	0.0020		0.0025				
		24	0.0018		0.0023				
		25	0.0020		0.0025				
		26	0.0015		0.0019				
		27	0.0011		0.0014				
	Ave K_{HRST_Ave}		Ave K_{Det_Est}		Ave K_{Det_Corr}		Ave 8 Zone K_{ZOP_Est}		Ave 8 Zone K_{ZOP_Corr}
	0.0031		0.0024		0.0031		0.0023		0.0030

Table 6 – HT-1 to HT-3 calculated K corrected for Ss.

HT-2 to HT-3 Corrected Ss and K									
HRST Well	HRST K_{Ave}	28 Zone ZOP Model	28 Zone Det. K (ft/sec)	Corr. Factor	28 Zone Det. K (ft/sec)	7 Zone ZOP Model	7 Zone Cal. K (ft/sec)	Corr. Factor	7 Zone Cal. K (ft/sec)
		Ss_{Est} 1.00E-05		1.3455	Ss_{Corr} 1.35E-05	Ss_{Est} 1.00E-05		1.3455	Ss_{Corr} 1.35E-05
HT-1	0.0034	1	0.0043		0.0058	1	0.0048		0.0065
HT-3	0.0038	2	0.0047		0.0063	2	0.0023		0.0031
		3	0.0046		0.0062	3	0.0010		0.0014
		4	0.0072		0.0097	4	0.0034		0.0045
		5	0.0040		0.0054	5	0.0016	x 1.3455 =	0.0022
		6	0.0024		0.0033	6	0.0020		0.0027
		7	0.0022		0.0029	7	0.0014		0.0019
		8	0.0012		0.0016				
		9	0.0008		0.0011				
		10	0.0012		0.0016				
		11	0.0023		0.0031				
		12	0.0106		0.0143				
		13	0.0018		0.0024				
		14	0.0025	x 1.3455 =	0.0033				
		15	0.0014		0.0019				
		16	0.0011		0.0015				
		17	0.0017		0.0023				
		18	0.0022		0.0030				
		19	0.0016		0.0022				
		20	0.0021		0.0029				
		21	0.0019		0.0026				
		22	0.0024		0.0033				
		23	0.0017		0.0022				
		24	0.0021		0.0028				
		25	0.0020		0.0027				
		26	0.0013		0.0017				
		27	0.0016		0.0021				
		28	0.0013		0.0018				
	Ave K_{HRST_Ave}		Ave K_{Det_Est}		Ave K_{Det_Corr}		Ave 8 Zone K_{ZOP_Est}		Ave 8 Zone K_{ZOP_Corr}
	0.0036		0.0027		0.0036		0.0024		0.0032

Table 7 – HT-2 to HT-3 calculated K corrected for Ss.

HT-6 to HT-3 Corrected Ss and K

HRST Well	HRST K_{Ave}	28 Zone ZOP Model	28 Zone Det. K (ft/sec)	Corr. Factor	28 Zone Det. K (ft/sec)	8 Zone ZOP Model	8 Zone Cal. K (ft/sec)	Corr. Factor	8 Zone Cal. K (ft/sec)
		Ss_{Est} 1.00E-05		1.6265	Ss_{Corr} 1.63E-05	Ss_{Est} 1.00E-05		1.6924	Ss_{Corr} 1.69E-05
HT-6	0.0025	1	0.0035		0.0058	1	0.0035		0.0060
HT-3	0.0038	2	0.0034		0.0055	2	0.0016		0.0027
		3	0.0039		0.0064	3	0.0028		0.0048
		4	0.0034		0.0056	4	0.0014		0.0023
		5	0.0036		0.0058	5	0.0021	x 1.6924 =	0.0035
		6	0.0015		0.0024	6	0.0011		0.0019
		7	0.0018		0.0029	7	0.0016		0.0027
		8	0.0027		0.0044	8	0.0006		0.0011
		9	0.0030		0.0049				
		10	0.0012		0.0020				
		11	0.0017		0.0027				
		12	0.0014		0.0022				
		13	0.0013		0.0021				
		14	0.0016	x 1.6265 =	0.0026				
		15	0.0035		0.0056				
		16	0.0016		0.0026				
		17	0.0013		0.0021				
		18	0.0010		0.0016				
		19	0.0010		0.0017				
		20	0.0014		0.0022				
		21	0.0016		0.0027				
		22	0.0015		0.0025				
		23	0.0017		0.0027				
		24	0.0018		0.0030				
		25	0.0013		0.0021				
		26	0.0004		0.0007				
		27	0.0010		0.0016				
		28	0.0006		0.0010				
	Ave K_{HRST_Ave}		Ave K_{Det_Est}		Ave K_{Det_Corr}		Ave 8 Zone K_{ZOP_Est}		Ave 8 Zone K_{ZOP_Corr}
	0.0031		0.0019		0.0031		0.0018		0.0031

Table 8 – HT-6 to HT-3 calculated K corrected for Ss.

HT-1 to HT-3 Model and Inversion Summary														
Source Elev. (ft msl)	27 Zone ZOP Model	27 Zone Det. K (ft/sec)	8 Zone ZOP Model	8 Zone Ave K (ft/sec)	8 Zone ZOP Model	8 Zone Cal. K (ft/sec)(3)	8 Zone MOG Iso Model(4)	8 Zone Cal. K Iso (ft/sec)	8 Zone MOG Aniso 2 Model(4)	8 Zone Cal. K Aniso 2 (ft/sec)	24 Zone MOG Aniso 2 Model(5)	24 Zone Cal. K Aniso 2 CLS1 (ft/sec)		
	Ss_{Est} 1.0E-05(1)		Interpreted		Ss_{Est} 1.0E-05(1)	Ss_{Corr} 1.30E-05(2)	Ss_{Corr} 1.30E-05(2)		Ss_{Corr} 1.30E-05(2)		Ss_{Corr} 1.30E-05(2)			
760.82	1	0.0048	1	0.0051	1	0.0066	1	0.0039	1	0.0053	1 2 3	0.0053	0.0056	0.0041
761.82	2	0.0049												
762.82	3	0.0059												
763.82	4	0.0049												
764.82	5	0.0034	2	0.0033	2	0.0042	2	0.0013	2	0.0017	4 5 6	0.0032	0.0020	0.0031
765.82	6	0.0033												
766.82	7	0.0012	3	0.0018	3	0.0021	3	0.0007	3	0.0009	7 8 9	0.0013	0.0008	0.0017
767.82	8	0.0022												
768.82	9	0.0012												
769.82	10	0.0025												
770.82	11	0.0014	4	0.0016	4	0.0021	4	0.0014	4	0.0020	10 11 12	0.0016	0.0018	0.0019
771.82	12	0.0018												
772.82	13	0.0014	5	0.0025	5	0.0027	5	0.0016	5	0.0023	13 14 15	0.0019	0.0022	0.0024
773.82	14	0.0047												
774.82	15	0.0014												
775.82	16	0.0020	6	0.0015	6	0.0019	6	0.0010	6	0.0013	16 17 18	0.0014	0.0012	0.0016
776.82	17	0.0015												
777.82	18	0.0012												
778.82	19	0.0018												
779.82	20	0.0012												
780.82	21	0.0022	7	0.0019	7	0.0025	7	0.0014	7	0.0019	19 20 21	0.0027	0.0016	0.0020
781.82	22	0.0018												
782.82	23	0.0020												
783.82	24	0.0018												
784.82	25	0.0020												
785.82	26	0.0015	8	0.0013	8	0.0016	8	0.0011	8	0.0012	22 23 24	0.0017	0.0016	0.0013
786.82	27	0.0011												
		Chi^2				Chi^2		Chi^2		Chi^2			Chi^2	
		2.67E-31				0.00063		0.22411		0.15205			0.14420	

Tomography Model	Interpreted Model	Tomography Model	Tomography Model Iso(4)	Tomography Model Aniso 2(4)	Tomography Model Aniso 2(5)
27 Zones 27 ZOP Rays K_{Est} Ss_{Est} 1.0E-05(1) radius 15.62 ft period 30 sec ⇩ K_{Est} Phase	Manual contour of 27 Zone Det. K 8 Zones Average K for each zone ⇩ 8 Zone ZOP Ave. K	8 Zones 27 ZOP Rays 8 Zone ZOP Ave. K Ss_{Est} 1.0E-05(1) radius 15.62 ft period 30 sec ⇩ 8 Zone ZOP Ave. K Phase	8 Zones 756 MOG Rays 8 Zone ZOP Cal. K Ss_{Corr} 1.30E-05(2) radius 15.62 ft period 30 sec ⇩ 8 Zone ZOP Cal. K Phase	8 Zones 756 MOG Rays 8 Zone ZOP Cal. K Ss_{Corr} 1.30E-05(2) radius 15.62 ft period 30 sec ⇩ 8 Zone ZOP Cal. K Phase	24 Zones 756 MOG Rays 8 Zone ZOP Cal. K Ss_{Corr} 1.30E-05(2) radius 15.62 ft period 30 sec ⇩ 24 Zone MOG Cal. K Phase
Phase Inversion		Phase Inversion	Phase Inversion	Phase Inversion	Phase Inversion CLS 1(6)
Exp. Phase Ss_{Est} 1.0E-05(1) ⇩ 27 Zone ZOP Det. K		Exp. Phase Ss_{Corr} 1.30E-05(2) ⇩ 8 Zone ZOP Cal. K(3)	Exp. Phase Ss_{Corr} 1.30E-05(2) ⇩ 8 Zone MOG Cal. K Iso	Exp. Phase Ss_{Corr} 1.30E-05(2) ⇩ 8 Zone MOG Cal. K Aniso 2	Exp. Phase Ss_{Corr} 1.30E-05(2) ⇩ 24 Zone MOG Cal. K Aniso 2 CLS 1

Notes

(1) - Ss_{Est} initial estimale of specific storage.

(2) - Ss_{Corr} value calculated from a correction factor derived from average HRST data, $K_{HRST\ Ave}$, and an average of the estimated ZOP deterministic data, $K_{Det\ Est}$.

(3) - 8 Zone ZOP caluated K derived from HydraulicTomAnal model and LeastSquaresSVD inversion with Ss_{Corr}. It defines the MOG model domains.

(4) - MOG model runs completed to compare isotropic and anisotropic conditions. The ZOP model runs are isotropic by default.

(5) - MOG model run for anisotropic condition with lateral variation.

(6) - Least squares inversion constraint factor of 1.

Table 9 – HT-1 to HT-3 model and inversion summary.

HT-1 to HT-3 Model and Inversion Summary														
Source Elev. (ft msl)	27 Zone ZOP Model	27 Zone Det. K (ft/sec)	8 Zone ZOP Model	8 Zone Ave K (ft/sec)	8 Zone ZOP Model	8 Zone Cal. K (ft/sec)$^{(3)}$	8 Zone MOG Iso Model$^{(4)}$	8 Zone Cal. K Iso (ft/sec)	8 Zone MOG Aniso 2 Model$^{(4)}$	8 Zone Cal. K Aniso 2 (ft/sec)	24 Zone MOG Aniso 2 Model$^{(5)}$	24 Zone Cal. K Aniso 2 CLS1 (ft/sec)		
	Ss_{Est} 1.0E-05$^{(1)}$		Interpreted		Ss_{Est} 1.0E-05$^{(1)}$	Ss_{Corr} 1.30E-05$^{(2)}$	Ss_{Corr} 1.30E-05$^{(2)}$		Ss_{Corr} 1.30E-05$^{(2)}$		Ss_{Corr} 1.30E-05$^{(2)}$			
760.82	1	0.0048	1	0.0051	1	0.0066	1	0.0039	1	0.0053	1 2 3	0.0053	0.0056	0.0041
761.82	2	0.0049												
762.82	3	0.0059												
763.82	4	0.0049												
764.82	5	0.0034	2	0.0033	2	0.0042	2	0.0013	2	0.0017	4 5 6	0.0032	0.0020	0.0031
765.82	6	0.0033												
766.82	7	0.0012	3	0.0018	3	0.0021	3	0.0007	3	0.0009	7 8 9	0.0013	0.0008	0.0017
767.82	8	0.0022												
768.82	9	0.0012												
769.82	10	0.0025												
770.82	11	0.0014	4	0.0016	4	0.0021	4	0.0014	4	0.0020	10 11 12	0.0016	0.0018	0.0019
771.82	12	0.0018												
772.82	13	0.0014	5	0.0025	5	0.0027	5	0.0016	5	0.0023	13 14 15	0.0019	0.0022	0.0024
773.82	14	0.0047												
774.82	15	0.0014												
775.82	16	0.0020	6	0.0015	6	0.0019	6	0.0010	6	0.0013	16 17 18	0.0014	0.0012	0.0016
776.82	17	0.0015												
777.82	18	0.0012												
778.82	19	0.0018												
779.82	20	0.0012												
780.82	21	0.0022	7	0.0019	7	0.0025	7	0.0014	7	0.0019	19 20 21	0.0027	0.0016	0.0020
781.82	22	0.0018												
782.82	23	0.0020												
783.82	24	0.0018												
784.82	25	0.0020												
785.82	26	0.0015	8	0.0013	8	0.0016	8	0.0011	8	0.0012	22 23 24	0.0017	0.0016	0.0013
786.82	27	0.0011												
		Chi^2 2.67E-31				Chi^2 0.00063		Chi^2 0.22411		Chi^2 0.15205			Chi^2 0.14420	

Tomography Model	Interpreted Model	Tomography Model	Tomography Model Iso$^{(4)}$	Tomography Model Aniso 2$^{(4)}$	Tomography Model Aniso 2$^{(5)}$
27 Zones 27 ZOP Rays K_{Est} Ss_{Est} 1.0E-05$^{(1)}$ radius 15.62 ft period 30 sec ⇩ K_{Est} Phase	Manual contour of 27 Zone Det. K 8 Zones Average K for each zone	8 Zones 27 ZOP Rays 8 Zone ZOP Ave. K Ss_{Est} 1.0E-05$^{(1)}$ radius 15.62 ft period 30 sec ⇩ 8 Zone ZOP Ave. K Phase	8 Zones 756 MOG Rays 8 Zone ZOP Cal. K Ss_{Corr} 1.30E-05$^{(2)}$ radius 15.62 ft period 30 sec ⇩ 8 Zone ZOP Cal. K Phase	8 Zones 756 MOG Rays 8 Zone ZOP Cal. K Ss_{Corr} 1.30E-05$^{(2)}$ radius 15.62 ft period 30 sec ⇩ 8 Zone ZOP Cal. K Phase	24 Zones 756 MOG Rays 8 Zone ZOP Cal. K Ss_{Corr} 1.30E-05$^{(2)}$ radius 15.62 ft period 30 sec ⇩ 24 Zone MOG Cal. K Phase
Phase Inversion	⇩	Phase Inversion	Phase Inversion	Phase Inversion	Phase Inversion CLS 1$^{(6)}$
Exp. Phase Ss_{Est} 1.0E-05$^{(1)}$ ⇩ 27 Zone ZOP Det. K	8 Zone ZOP Ave. K	Exp. Phase Ss_{Corr} 1.30E-05$^{(2)}$ ⇩ 8 Zone ZOP Cal. K$^{(3)}$	Exp. Phase Ss_{Corr} 1.30E-05$^{(2)}$ ⇩ 8 Zone MOG Cal. K Iso	Exp. Phase Ss_{Corr} 1.30E-05$^{(2)}$ ⇩ 8 Zone MOG Cal. K Aniso 2	Exp. Phase Ss_{Corr} 1.30E-05$^{(2)}$ ⇩ 24 Zone MOG Cal. K Aniso 2 CLS 1

Notes

(1) - Ss_{Est} initial estimate of specific storage.

(2) - Ss_{Corr} value calculated from a correction factor derived from average HRST data, $K_{HRST\ Ave}$, and an average of the estimated ZOP deterministic data, $K_{Det\ Est}$.

(3) - 8 Zone ZOP caluated K derived from HydraulicTomAnal model and LeastSquaresSVD inversion with Ss_{Corr}. It defines the MOG model domains.

(4) - MOG model runs completed to compare isotropic and anisotropic conditions. The ZOP model runs are isotropic by default.

(5) - MOG model run for anisotropic condition with lateral variation.

(6) - Least squares inversion constraint factor of 1.

Table 10 – HT-2 to HT-3 model and inversion summary.

HT-4 to HT-3 Model and Inversion Summary

Source Elev. (ft msl)	28 Zone ZOP Model	28 Zone Det. K (ft/sec)	7 Zone ZOP Model	7 Zone Ave K (ft/sec)	7 Zone ZOP Model	7 Zone Cal. K (ft/sec)	7 Zone MOG Iso Model(3)	7 Zone Cal. K Iso (ft/sec)	7 Zone MOG Aniso 2 Model(3)	7 Zone Cal. K Aniso 2 (ft/sec)	21 Zone MOG Aniso 2 Model(4)	21 Zone Cal. K Aniso 2 CLS 1 (ft/sec)		
	Ss_{Corr} 1.04E-05(1)		Interpreted		Ss_{Corr} 1.04E-05(1)		Ss_{Corr} 1.04E-05(1)		Ss_{Corr} 1.04E-05(1)		Ss_{Corr} 1.04E-05(1)			
761.11	1	0.0053	1	0.0053	1	0.0052	1	0.0029	1	0.0040	1 2 3	0.0026	0.0043	0.0061
761.82	2	0.0066												
762.82	3	0.0038												
763.82	4	0.0063												
764.82	5	0.0042												
765.82	6	0.0056												
766.82	7	0.0025	2	0.0020	2	0.0018	2	0.0006	2	0.0007	4 5 6	0.0007	0.0006	0.0007
767.82	8	0.0012												
768.82	9	0.0015												
769.82	10	0.0026												
770.82	11	0.0008	3	0.0035	3	0.0034	3	0.0015	3	0.0021	7 8 9	0.0027	0.0018	0.0015
771.82	12	0.0060												
772.82	13	0.0047												
773.82	14	0.0032												
774.82	15	0.0028												
775.82	16	0.0020	4	0.0032	4	0.0025	4	0.0009	4	0.0012	10 11 12	0.0012	0.0011	0.0011
776.82	17	0.0046												
777.82	18	0.0050												
778.82	19	0.0012												
779.82	20	0.0017	5	0.0017	5	0.0016	5	0.0010	5	0.0013	13 14 15	0.0013	0.0014	0.0015
780.82	21	0.0021												
781.82	22	0.0016												
782.82	23	0.0015												
783.82	24	0.0014	6	0.0015	6	0.0014	6	0.0009	6	0.0011	16 17 18	0.0011	0.0011	0.0011
784.82	25	0.0020												
785.82	26	0.0011												
786.82	27	0.0010	7	0.0010	7	0.0009	7	0.0007	7	0.0008	19 20 21	0.0008	0.0008	0.0007
787.82	28	0.0010												
		Chi^2 3.98E-31				Chi^2 0.00071		Chi^2 0.46213		Chi^2 0.27157			Chi^2 0.16932	

Tomography Model	Interpreted Model	Tomography Model	Tomography Model Iso(3)	Tomography Model Aniso 2(3)	Tomography Model Aniso 2(4)
28 Zones 28 ZOP Rays HRST K_{Ave} Ss_{Corr} 1.04E-05(1) radius 14.62 ft period 30 sec ⇩ HRST K_{Ave} Phase	Manual contour of 28 Zone Det. K 7 Zones Average K for each zone ⇩ 7 Zone ZOP Ave. K	7 Zones 28 ZOP Rays 7 Zone ZOP Ave. K Ss_{Corr} 1.04E-05(1) radius 14.62 ft period 30 sec ⇩ 7 Zone ZOP Ave. K Phase	7 Zones 784 MOG Rays 7 Zone ZOP Cal. K Ss_{Corr} 1.04E-05(1) radius 14.62 ft period 30 sec ⇩ 7 Zone ZOP Cal. K Phase	7 Zones 784 MOG Rays 7 Zone ZOP Cal. K Ss_{Corr} 1.04E-05(1) radius 14.62 ft period 30 sec ⇩ 7 Zone ZOP Cal. K Phase	21 Zones 784 MOG Rays 7 Zone MOG Cal. K Aniso 2 Ss_{Corr} 1.04E-05(1) radius 14.62 ft period 30 sec ⇩ 21 Zone MOG Cal. K Phase
Phase Inversion		Phase Inversion	Phase Inversion	Phase Inversion	Phase Inversion CLS 1(5)
Exp. & HRST Phase(2) Ss_{Corr} 1.04E-05(1) ⇩ 28 Zone ZOP Det. K		Exp. & 7 Zone ZOP Ave. K Phase(2) Ss_{Corr} 1.04E-05(1) ⇩ 7 Zone ZOP Cal. K	Exp. & 7 Zone ZOP Cal. K Phase(2) Ss_{Corr} 1.04E-05(1) ⇩ 7 Zone MOG Cal. K Iso	Exp. & 7 Zone ZOP Cal. K Phase(2) Ss_{Corr} 1.04E-05(1) ⇩ 7 Zone MOG Cal. K Aniso 2	Exp. & 21 Zone MOG Cal. K Phase Aniso 2(2) Ss_{Corr} 1.04E-05(1) ⇩ 21 Zone MOG Cal. K Aniso 2 CLS 1

Notes

(1) - Ss_{Corr} value calculated from average expiremental phase data, Φ_{Exp_Ave}, and the average estimated phase, Φ_{Est_Ave}, which was back calculated from HRST K data.

(2) - Experimental phase data set includes surrogate phase originally derived from HRST data. Surrogate phase replaces source locations with unusable transducer data. Calculated K and phase values are carried forward through each successive model run.

(3) - MOG model runs completed to compare isotropic and anisotropic conditions. The ZOP model runs are isotropic by default.

(4) - MOG model run for anisotropic condition with lateral variation.

(5) - Least squares inversion constraint factor of 1.

Table 11 – HT-4 to HT-3 model and inversion summary.

HT-5 to HT-3 Model and Inversion Summary

Source Elev. (ft msl)	28 Zone ZOP Model	28 Zone Det. K (ft/sec)	8 Zone ZOP Model	8 Zone Ave K (ft/sec)	8 Zone ZOP Model	8 Zone Cal. K (ft/sec)	8 Zone MOG Iso Model(3)	8 Zone Cal. K Iso (ft/sec)	8 Zone MOG Aniso 2 Model(3)	8 Zone Cal. K Aniso 2 (ft/sec)	24 Zone MOG Aniso 2 Model(4)	24 Zone Cal. K Aniso 2 CLS1 (ft/sec)		
	Ss_{Corr} 1.1E-05(1)		Interpreted		Ss_{Corr} 1.1E-05(1)		Ss_{Corr} 1.1E-05(1)		Ss_{Corr} 1.1E-05(1)		Ss_{Corr} 1.1E-05(1)			
761.11	1	0.0064	1	0.0080	1	0.0068	1	0.0048	1	0.0060	1 2 3	0.0042	0.0061	0.0079
761.82	2	0.0137												
762.82	3	0.0039												
763.82	4	0.0037	2	0.0042	2	0.0037	2	0.0017	2	0.0022	4 5 6	0.0011	0.0023	0.0037
764.82	5	0.0034												
765.82	6	0.0071												
766.82	7	0.0024												
767.82	8	0.0016	3	0.0017	3	0.0016	3	0.0006	3	0.0007	7 8 9	0.0005	0.0005	0.0008
768.82	9	0.0007												
769.82	10	0.0028												
770.82	11	0.0042	4	0.0045	4	0.0045	4	0.0027	4	0.0033	10 11 12	0.0041	0.0020	0.0027
771.82	12	0.0051												
772.82	13	0.0046												
773.82	14	0.0039												
774.82	15	0.0030	5	0.0030	5	0.0030	5	0.0025	5	0.0029	13 14 15	0.0041	0.0023	0.0025
775.82	16	0.0020												
776.82	17	0.0041												
777.82	18	0.0042	6	0.0038	6	0.0038	6	0.0029	6	0.0033	16 17 18	0.0041	0.0030	0.0025
778.82	19	0.0035												
779.82	20	0.0035	7	0.0039	7	0.0039	7	0.0032	7	0.0036	19 20 21	0.0048	0.0036	0.0024
780.82	21	0.0056												
781.82	22	0.0026												
782.82	23	0.0026	8	0.0020	8	0.0020	8	0.0018	8	0.0019	22 23 24	0.0022	0.0019	0.0013
783.82	24	0.0023												
784.82	25	0.0022												
785.82	26	0.0019												
786.82	27	0.0015												
787.82	28	0.0013												
		Chi^2 1.16E-31				Chi^2 0.0002		Chi^2 0.4574		Chi^2 0.2708			Chi^2 0.1014	

Tomography Model	Interpreted Model	Tomography Model	Tomography Model Iso(3)	Tomography Model Aniso 2(3)	Tomography Model Aniso 2(4)
28 Zones 28 ZOP Rays HRST K_{Ave} Ss_{Corr} 1.1E-05(1) radius 13.81 ft period 30 sec ⇩ HRST K_{Ave} Phase	Manual contour of 28 Zone Det. K 8 Zones Average K for each zone	8 Zones 28 ZOP Rays 8 Zone ZOP Ave. K Ss_{Corr} 1.1E-05(1) radius 13.81 ft period 30 sec ⇩ 8 Zone ZOP Ave. K Phase	8 Zones 784 MOG Rays 8 Zone ZOP Cal. K Ss_{Corr} 1.1E-05(1) radius 13.81 ft period 30 sec ⇩ 8 Zone ZOP Cal. K Phase	8 Zones 784 MOG Rays 8 Zone ZOP Cal. K Ss_{Corr} 1.1E-05(1) radius 13.81 ft period 30 sec ⇩ 8 Zone ZOP Cal. K Phase	24 Zones 784 MOG Rays 8 Zone MOG Cal. K Aniso 2 Ss_{Corr} 1.1E-05(1) radius 13.81 ft period 30 sec ⇩ 24 Zone MOG Cal. K Phase
Phase Inversion	⇩	Phase Inversion	Phase Inversion	Phase Inversion	Phase Inversion CLS 1(5)
Exp. & HRST Phase(2) Ss_{Corr} 1.1E-05(1) ⇩ 28 Zone ZOP Det. K	8 Zone ZOP Ave. K	Exp. & 8 Zone ZOP Ave. K Phase(2) Ss_{Corr} 1.1E-05(1) ⇩ 8 Zone ZOP Cal. K	Exp. & 8 Zone ZOP Cal. K Phase(2) Ss_{Corr} 1.1E-05(1) ⇩ 8 Zone MOG Cal. K Iso	Exp. & 8 Zone ZOP Cal. K Phase(2) Ss_{Corr} 1.1E-05(1) ⇩ 8 Zone MOG Cal. K Aniso 2	Exp. & 24 Zone MOG Cal. K Phase(2) Ss_{Corr} 1.1E-05(1) ⇩ 24 Zone MOG Cal. K Aniso 2 CLS 1

Notes

(1) - Ss_{Corr} value calculated from average expiremental phase data, Φ_{Exp_Ave}, and the average estimated phase, Φ_{Est_Ave}, which was back calculated from HRST K data.

(2) - Experimental phase data set includes surrogate phase originally derived from HRST data. Surrogate phase replaces source locations with unusable transducer data. Calculated K and phase values are carried forward through each successive model run.

(3) - MOG model runs completed to compare isotropic and anisotropic conditions. The ZOP model runs are isotropic by default.

(4) - MOG model run for anisotropic condition with lateral variation.

(5) - Least squares inversion constraint factor of 1.

Table 12 – HT-5 to HT-3 model and inversion summary.

HT-6 to HT-3 Model and Inversion Summary														
Source Elev. (ft msl)	28 Zone ZOP Model	27 Zone Det. K (ft/sec)	8 Zone ZOP Model	8 Zone Ave K (ft/sec)	8 Zone ZOP Model	8 Zone Cal. K (ft/sec)$^{(3)}$	8 Zone MOG Iso Model$^{(4)}$	8 Zone Cal. K Iso (ft/sec)	8 Zone MOG Aniso 2 Model$^{(4)}$	8 Zone Cal. K Aniso 2 (ft/sec)	24 Zone MOG Aniso 2 Model$^{(5)}$	24 Zone Cal. K Aniso 2 CLS1 (ft/sec)		
	Ss_{Est} 1.0E-05$^{(1)}$		Interpreted		Ss_{Est} 1.0E-05$^{(1)}$	Ss_{Corr} 1.69E-05$^{(2)}$	Ss_{Corr} 1.69E-05$^{(2)}$		Ss_{Corr} 1.69E-05$^{(2)}$		Ss_{Corr} 1.69E-05$^{(2)}$			
761.3	1	0.0035	1	0.0036	1	0.0060	1	0.0038	1	0.0056	1 2 3	0.0058	0.0039	0.0042
761.81	2	0.0034												
762.81	3	0.0039												
763.81	4	0.0034												
764.81	5	0.0036												
765.81	6	0.0015	2	0.0016	2	0.0027	2	0.0008	2	0.0010	4 5 6	0.0020	0.0012	0.0020
766.81	7	0.0018												
767.81	8	0.0027	3	0.0028	3	0.0048	3	0.0010	3	0.0014	7 8 9	0.0032	0.0016	0.0032
768.81	9	0.0030												
769.81	10	0.0012	4	0.0014	4	0.0023	4	0.0014	4	0.0020	10 11 12	0.0014	0.0018	0.0017
770.81	11	0.0017												
771.81	12	0.0014												
772.81	13	0.0013												
773.81	14	0.0016	5	0.0022	5	0.0035	5	0.0018	5	0.0028	13 14 15	0.0022	0.0033	0.0027
774.81	15	0.0035												
775.81	16	0.0016												
776.81	17	0.0013	6	0.0012	6	0.0019	6	0.0011	6	0.0016	16 17 18	0.0017	0.0014	0.0017
777.81	18	0.0010												
778.81	19	0.0010												
779.81	20	0.0014												
780.81	21	0.0016	7	0.0016	7	0.0027	7	0.0015	7	0.0021	19 20 21	0.0029	0.0017	0.0027
781.81	22	0.0015												
782.81	23	0.0017												
783.81	24	0.0018												
784.81	25	0.0013												
785.81	26	0.0004	8	0.0007	8	0.0011	8	0.0010	8	0.0011	22 23 24	0.0011	0.0011	0.0010
786.81	27	0.0010												
787.81	28	0.0006												
		Chi^2 3.45E-31				Chi^2 0.00052		Chi^2 0.17676		Chi^2 0.14116			Chi^2 0.13825	

Tomography Model	Interpreted Model	Tomography Model	Tomography Model Iso$^{(4)}$	Tomography Model Aniso 2$^{(4)}$	Tomography Model Aniso 2$^{(5)}$
28 Zones 28 ZOP Rays K_{Est} Ss_{Est} 1.0E-05$^{(1)}$ radius 13.1 ft period 30 sec ⇩ K_{Est} Phase	Manual contour of 28 Zone Det. K 8 Zones Average K for each zone ⇩	8 Zones 28 ZOP Rays 8 Zone ZOP Ave. K Ss_{Est} 1.0E-05$^{(1)}$ radius 13.1 ft period 30 sec ⇩ 8 Zone ZOP Ave. K Phase	8 Zones 784 MOG Rays 8 Zone ZOP Ave. K Ss_{Corr} 1.69E-05$^{(2)}$ radius 13.1 ft period 30 sec ⇩ 8 Zone ZOP Cal. K Phase	8 Zones 784 MOG Rays 8 Zone ZOP Ave. K Ss_{Corr} 1.69E-05$^{(2)}$ radius 13.1 ft period 30 sec ⇩ 8 Zone ZOP Cal. K Phase	24 Zones 784 MOG Rays 8 Zone ZOP Cal. K Ss_{Corr} 1.69E-05$^{(2)}$ radius 13.1 ft period 30 sec ⇩ 24 Zone MOG Cal. K Phase
Phase Inversion		Phase Inversion	Phase Inversion	Phase Inversion	Phase Inversion CLS 1$^{(6)}$
Exp. Phase Ss_{Est} 1.0E-05$^{(1)}$ ⇩ 28 Zone ZOP Det. K	8 Zone ZOP Ave. K	Exp. Phase Ss_{Corr} 1.69E-05$^{(2)}$ ⇩ 8 Zone ZOP Cal. K$^{(3)}$	Exp. Phase Ss_{Corr} 1.69E-05$^{(2)}$ ⇩ 8 Zone MOG Cal. K Iso	Exp. Phase Ss_{Corr} 1.69E-05$^{(2)}$ ⇩ 8 Zone MOG Cal. K Aniso 2	Exp. Phase Ss_{Corr} 1.69E-05$^{(2)}$ ⇩ 24 Zone MOG Cal. K Aniso 2 CLS 1

Notes

(1) - Ss_{Est} initial estimate of specific storage.

(2) - Ss_{Corr} value calculated from a correction factor derived from average HRST data, K_{HRST_Ave}, and an average of the estimated ZOP deterministic data, K_{Det_Est}.

(3) - 8 Zone ZOP caluated K derived from HydraulicTomAnal model and LeastSquaresSVD inversion with Ss_{Corr}. It defines the MOG model domains.

(4) - MOG model runs completed to compare isotropic and anisotropic conditions. The ZOP model runs are all isotropic by default.

(5) - MOG model run for anisotropic condition with lateral variation.

(6) - Least squares inversion constraint factor of 1.

Table 13 – HT-6 to HT-3 model and inversion summary.

HT-GP to HT-2 Model and Inversion Summary

Source Elev. (ft msl)	27 Zone ZOP Model	27 Zone Det. K (ft/sec)	7 Zone ZOP Model	7 Zone Ave K (ft/sec)	7 Zone ZOP Model	7 Zone Cal. K (ft/sec)	7 Zone MOG Iso Model(3)	7 Zone Cal. K Iso (ft/sec)	7 Zone MOG Aniso 10 Model(3)	7 Zone Cal. K Aniso 10 CLS 1 (ft/sec)	21 Zone MOG Aniso 10 Model(4)	21 Zone Cal. K Aniso 10 CLS1 (ft/sec)		
	Ss_{Corr} 2.48E-06(1)		Interpreted		Ss_{Corr} 2.48E-06(1)		Ss_{Corr} 2.48E-06(1)		Ss_{Corr} 2.48E-06(1)		Ss_{Corr} 2.48E-06(1)			
760.82	1	0.0042	1	0.0044	1	0.0041	1	0.0022	1	0.0042	1 2 3	0.0067	0.0045	0.0043
761.82	2	0.0031												
762.82	3	0.0059												
763.82	4	0.0040	2	0.0049	2	0.0042	2	0.0010	2	0.0033	4 5 6	0.0028	0.0042	0.0028
764.82	5	0.0088												
765.82	6	0.0019												
766.82	7	0.0055	3	0.0034	3	0.0023	3	0.0003	3	0.0014	7 8 9	0.0010	0.0009	0.0011
767.82	8	0.0012												
768.82	9	0.0034												
769.82	10	0.0036	4	0.0038	4	0.0034	4	0.0006	4	0.0022	10 11 12	0.0026	0.0015	0.0020
770.82	11	0.0036												
771.82	12	0.0054												
772.82	13	0.0047												
773.82	14	0.0019												
774.82	15	0.0021	5	0.0018	5	0.0018	5	0.0007	5	0.0018	13 14 15	0.0016	0.0025	0.0023
775.82	16	0.0018												
776.82	17	0.0016												
777.82	18	0.0017												
778.82	19	0.0013	6	0.0014	6	0.0013	6	0.0007	6	0.0015	16 17 18	0.0015	0.0015	0.0017
779.82	20	0.0017												
780.82	21	0.0011												
781.67	22	0.0014												
782.82	23	0.0011	7	0.0016	7	0.0016	7	0.0012	7	0.0016	19 20 21	0.0017	0.0015	0.0014
783.82	24	0.0021												
784.82	25	0.0020												
785.82	26	0.0017												
786.82	27	0.0010												
		Chi^2 6.92E-31				Chi^2 0.00154		Chi^2 8.55143		Chi^2 4.55003			Chi^2 4.22422	

Tomography Model	Interpreted Model	Tomography Model	Tomography Model Iso(3)	Tomography Model Aniso 10(3)	Tomography Model Aniso 10(4)
27 Zones 27 ZOP Rays HRST K_{Ave} Ss_{Corr} 2.48E-06(1) radius 13.88 ft period 3 sec ⇩ HRST K_{Ave} Phase	Manual contour of 27 Zone Det. K 7 Zones Average K for each zone ⇩ 7 Zone ZOP Ave. K	7 Zones 27 ZOP Rays 7 Zone ZOP Ave. K Ss_{Corr} 2.48E-06(1) radius 13.88 ft period 3 sec ⇩ 7 Zone ZOP Ave. K Phase	7 Zones 729 MOG Rays 7 Zone ZOP Cal. K Ss_{Corr} 2.48E-06(1) radius 13.88 ft period 3 sec ⇩ 7 Zone ZOP Cal. K Phase	7 Zones 729 MOG Rays 7 Zone ZOP Cal. K Ss_{Corr} 2.48E-06(1) radius 13.88 ft period 3 sec ⇩ 7 Zone ZOP Cal. K Phase	21 Zones 729 MOG Rays 7 Zone MOG Cal. K Aniso 10 Ss_{Corr} 2.48E-06(1) radius 13.88 ft period 3 sec ⇩ 21 Zone MOG Cal. K Phase
Phase Inversion		Phase Inversion	Phase Inversion	Phase Inversion CLS 1(5)	Phase Inversion CLS 1(5)
Exp. & HRST Phase(2) Ss_{Corr} 2.48E-06(1) ⇩ 27 Zone ZOP Det. K		Exp. & 7 Zone ZOP Ave. K Phase(2) Ss_{Corr} 2.48E-06(1) ⇩ 7 Zone ZOP Cal. K	Exp. & 7 Zone ZOP Cal. K Phase(2) Ss_{Corr} 2.48E-06(1) ⇩ 7 Zone MOG Cal. K Iso	Exp. & 7 Zone ZOP Cal. K Phase(2) Ss_{Corr} 2.48E-06(1) ⇩ 7 Zone MOG Cal. K Aniso 10	Exp. & 21 Zone MOG Cal. K Phase(2) Ss_{Corr} 2.48E-06(1) ⇩ 21 Zone MOG Cal. K Aniso 10 CLS 1

Notes

(1) - Ss_{Corr} value calculated from average expiremental phase data, Φ_{Exp_Ave}, and the average estimated phase, Φ_{Est_Ave}, which was back calculated from HRST K data.

(2) - Experimental phase data set includes surrogate phase originally derived from HRST data. Surrogate phase replaces source locations with unusable transducer data. Calculated K and phase values are carried forward through each successive model run.

(3) - MOG model runs completed to compare isotropic and anisotropic conditions. The ZOP model runs are isotropic by default.

(4) - MOG model run for anisotropic condition with lateral variation.

(5) - Least squares inversion constraint factor of 1.

Table 14 – HT-GP to HT-2 model and inversion summary.

HT-GP to HT-3 Model and Inversion Summary

Source Elev. (ft msl)	28 Zone ZOP Model	28 Zone Det. K (ft/sec)	8 Zone ZOP Model	8 Zone Ave K (ft/sec)	8 Zone ZOP Model	8 Zone Cal. K (ft/sec)	8 Zone MOG Iso Model(3)	8 Zone Cal. K Iso (ft/sec)	8 Zone MOG Aniso 10 Model(3)	8 Zone Cal. K Aniso 10 CLS 1 (ft/sec)	24 Zone MOG Aniso 10 Model(4)	24 Zone Cal. K Aniso 10 CLS1 (ft/sec)		
	Ss_{Corr} 2.01E-06(1)		Interpreted		Ss_{Corr} 2.01E-06(1)		Ss_{Corr} 2.01E-06(1)		Ss_{Corr} 2.01E-06(1)		Ss_{Corr} 2.01E-06(1)			
760.82	1	0.0035	1	0.0036	1	0.0035	1	0.0022	1	0.0040	1 2 3	0.0019	0.0038	0.0039
761.82	2	0.0030												
762.82	3	0.0045												
763.82	4	0.0028	2	0.0032	2	0.0028	2	0.0008	2	0.0027	4 5 6	0.0007	0.0015	0.0022
764.97	5	0.0054												
765.82	6	0.0015												
766.82	7	0.0014	3	0.0020	3	0.0013	3	0.0002	3	0.0010	7 8 9	0.0003	0.0003	0.0010
767.82	8	0.0007												
768.82	9	0.0038												
769.82	10	0.0015	4	0.0037	4	0.0031	4	0.0007	4	0.0030	10 11 12	0.0017	0.0004	0.0099
770.82	11	0.0075												
771.82	12	0.0044												
772.82	13	0.0038												
773.82	14	0.0015												
774.82	15	0.0013	5	0.0012	5	0.0012	5	0.0005	5	0.0014	13 14 15	0.0007	0.0006	0.0012
775.82	16	0.0013												
776.82	17	0.0012												
777.82	18	0.0010												
778.82	19	0.0009	6	0.0010	6	0.0009	6	0.0006	6	0.0010	16 17 18	0.0009	0.0008	0.0005
779.82	20	0.0011												
780.82	21	0.0009												
781.67	22	0.0008	7	0.0031	7	0.0023	7	0.0012	7	0.0022	19 20 21	0.0624	0.0011	0.0005
782.82	23	0.0057												
783.82	24	0.0027												
784.82	25	0.0030												
785.82	26	0.0027	8	0.0024	8	0.0024	8	0.0012	8	0.0023	22 23 24	0.0048	0.0022	0.0008
786.82	27	0.0024												
787.82	28	0.0020												
		Chi^2				Chi^2		Chi^2		Chi^2			Chi^2	
		3.22E-31				0.00397		5.70583		2.71014			3.69295	

Tomography Model	Interpreted Model	Tomography Model	Tomography Model Iso(3)	Tomography Model Aniso 10(3)	Tomography Model Aniso 10(4)
28 Zones 28 ZOP Rays HRST K_{Ave} Ss_{Corr} 2.01E-06(1) radius 13.94 ft period 3 sec ⇩ HRST K_{Ave} Phase	Manual contour of 28 Zone Det. K 8 Zones Average K for each zone ⇩ 8 Zone ZOP Ave. K	8 Zones 28 ZOP Rays 8 Zone ZOP Ave. K Ss_{Corr} 2.01E-06(1) radius 13.94 ft period 3 sec ⇩ 8 Zone ZOP Ave. K Phase	8 Zones 784 MOG Rays 8 Zone ZOP Cal. K Ss_{Corr} 2.01E-06(1) radius 13.94 ft period 3 sec ⇩ 8 Zone ZOP Cal. K Phase	8 Zones 784 MOG Rays 8 Zone ZOP Cal. K Ss_{Corr} 2.01E-06(1) radius 13.94 ft period 3 sec ⇩ 8 Zone ZOP Cal. K Phase	24 Zones 784 MOG Rays 8 Zone MOG Cal. K Aniso 10 Ss_{Corr} 2.01E-06(1) radius 13.94 ft period 3 sec ⇩ 24 Zone MOG Cal. K Phase
Phase Inversion		Phase Inversion	Phase Inversion	Phase Inversion CLS 1	Phase Inversion CLS 1(5)
Exp. & HRST Phase(2) Ss_{Corr} 2.01E-06(1) ⇩ 28 Zone ZOP Det. K		Exp. & 8 Zone ZOP Ave. K Phase(2) Ss_{Corr} 2.01E-06(1) ⇩ 8 Zone ZOP Cal. K	Exp. & 8 Zone ZOP Cal. K Phase(2) Ss_{Corr} 2.01E-06(1) ⇩ 8 Zone MOG Cal. K Iso	Exp. & 8 Zone ZOP Cal. K Phase(2) Ss_{Corr} 2.01E-06(1) ⇩ 8 Zone MOG Cal. K Aniso 10	Exp. & 24 Zone MOG Cal. K Phase(2) Ss_{Corr} 2.01E-06(1) ⇩ 24 Zone MOG Cal. K Aniso 10 CLS 1

Notes

(1) - Ss_{Corr} value calculated from average expiremental phase data, Φ_{Exp_Ave}, and the average estimated phase, Φ_{Est_Ave}, which was back calculated from HRST K data.

(2) - Experimental phase data set includes surrogate phase originally derived from HRST data. Surrogate phase replaces source locations with unusable transducer data. Calculated K and phase values are carried forward through each successive model run.

(3) - MOG model runs completed to compare isotropic and anisotropic conditions. The ZOP model runs are isotropic by default.

(4) - MOG model run for anisotropic condition with lateral variation.

(5) - Least squares inversion constraint factor of 1.

Table 15 – HT-GP to HT-3 model and inversion summary.

Spatially Weighted Straight Ray SVD Analysis			
4 Sec CPT Period			
Monte Carlo - No Error			
Element	K (ft/sec)	Stdr Dev K	% Stdr Dev K
1	0.003	3.616E-19	0.00
2	0.006	3.137E-18	0.00
3	0.003	3.870E-19	0.00
Monte Carlo - 5% Error			
Element	K (ft/sec)	Stdr Dev K	% Stdr Dev K
1	0.003	1.849E-05	0.62
2	0.005999	1.515E-04	2.52
3	0.003	1.899E-05	0.63
Monte Carlo - 10% Error			
Element	K (ft/sec)	Stdr Dev K	% Stdr Dev K
1	0.002999	3.482E-05	1.16
2	0.006018	3.098E-04	5.15
3	0.003001	3.702E-05	1.23

Spatially Weighted Straight Ray SVD Analysis			
30 Sec CPT Period			
Monte Carlo - No Error			
Element	K (ft/sec)	Stdr Dev K	% Stdr Dev K
1	0.003	8.636E-19	0.00
2	0.006	7.492E-18	0.00
3	0.003	9.242E-19	0.00
Monte Carlo - 5% Error			
Element	K (ft/sec)	Stdr Dev K	% Stdr Dev K
1	0.003	5.063E-05	1.69
2	0.006012	4.159E-04	6.92
3	0.003001	5.205E-05	1.73
Monte Carlo - 10% Error			
Element	K (ft/sec)	Stdr Dev K	% Stdr Dev K
1	0.003	9.542E-05	3.18
2	0.006109	8.869E-04	14.52
3	0.003005	1.017E-04	3.38

Table 16 – SVD analysis of spatially weighted straight ray approximation phase shift through a 3-element, 8-node, 10.68 m (35 ft) thick model used to verify the heterogeneous extension.

Numerical/Straight Ray Model SVD Analysis			
4 Sec CPT Period			
Monte Carlo No Error			
Element	K (ft/sec)	Stdr Dev K	% Stdr Dev K
1	0.003032	2.365E-05	0.78
2	0.005155	1.608E-04	3.12
3	0.002986	2.474E-05	0.83
Monte Carlo 5% Error			
Element	K (ft/sec)	Stdr Dev K	% Stdr Dev K
1	0.003032	1.875E-05	0.62
2	0.005154	1.206E-04	2.34
3	0.002986	1.885E-05	0.63
Monte Carlo 10% Error			
Element	K (ft/sec)	Stdr Dev K	% Stdr Dev K
1	0.003031	3.545E-05	1.17
2	0.005169	2.464E-04	4.77
3	0.002987	3.675E-05	1.23

Numerical/Straight Ray Model SVD Analysis			
30 Sec CPT Period			
Monte Carlo No Error - CLS 0.25			
Element	K (ft/sec)	Stdr Dev K	% Stdr Dev K
1	0.002869	4.125E-05	1.44
2	0.004514	1.644E-04	3.64
3	0.002847	4.256E-05	1.49
Monte Carlo 5% Error - CLS 0.25			
Element	K (ft/sec)	Stdr Dev K	% Stdr Dev K
1	0.002869	3.830E-05	1.33
2	0.004513	9.347E-05	2.07
3	0.002848	3.703E-05	1.30
Monte Carlo 10% Error - CLS 0.25			
Element	K (ft/sec)	Stdr Dev K	% Stdr Dev K
1	0.00287	7.678E-05	2.67
2	0.004515	1.869E-04	4.14
3	0.002849	7.419E-05	2.60

Table 17 – SVD analysis of numerical phase shift through a 3-element, 8-node, 10.68 m (35 ft) thick model used to verify the heterogeneous extension.

Appendix A – Model Grids

HT-1 to HT-3 ZOP Model

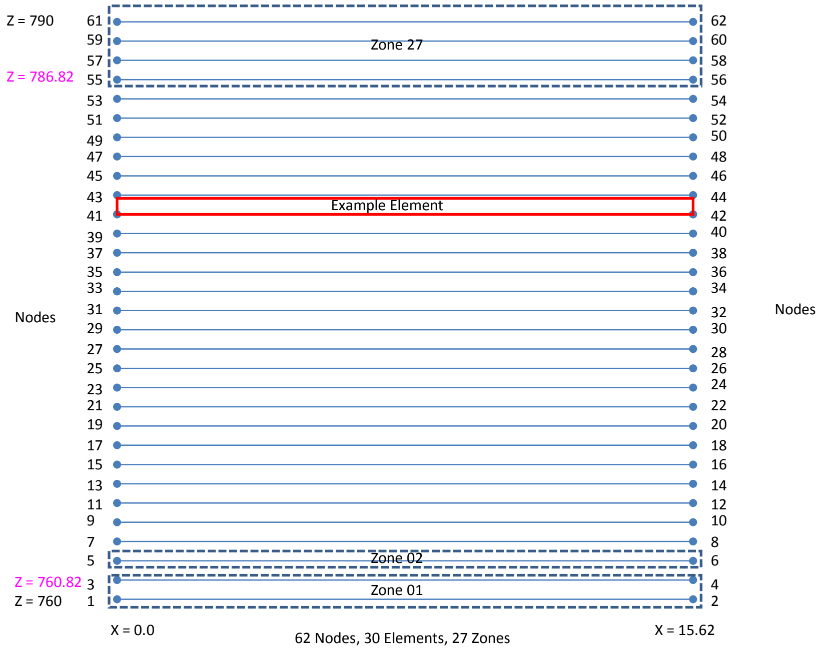

HT-1 to HT-3 8 Horizontal Zones Model

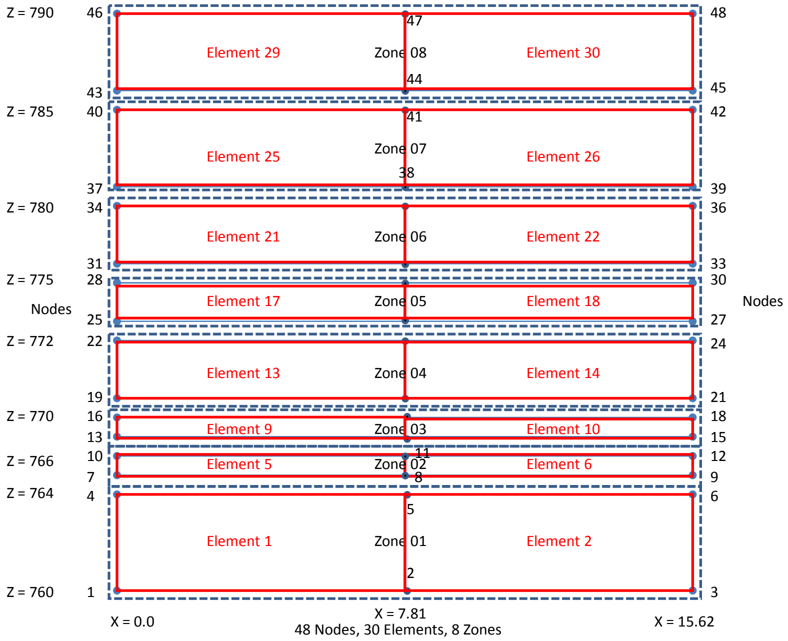

HT-1 to HT-3 24 Zones Model

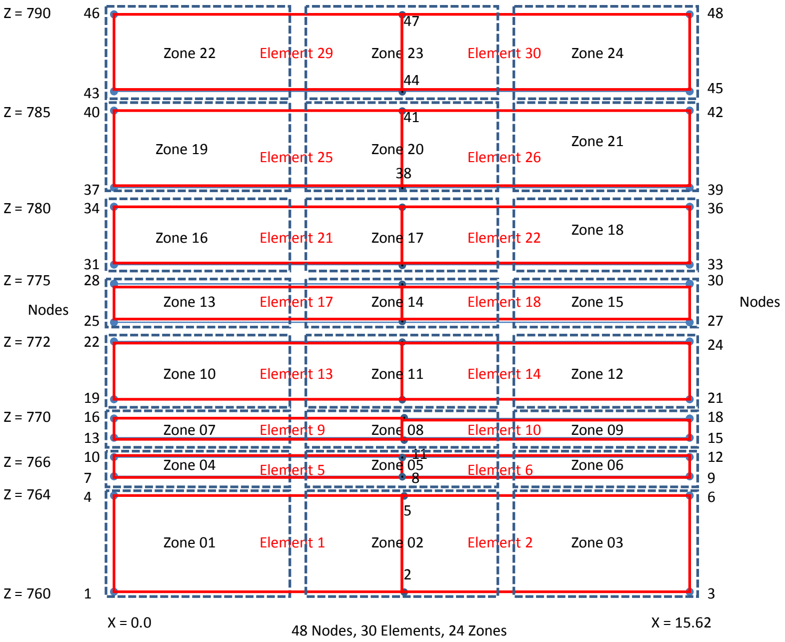

48 Nodes, 30 Elements, 24 Zones

HT-2 to HT-3 ZOP Model

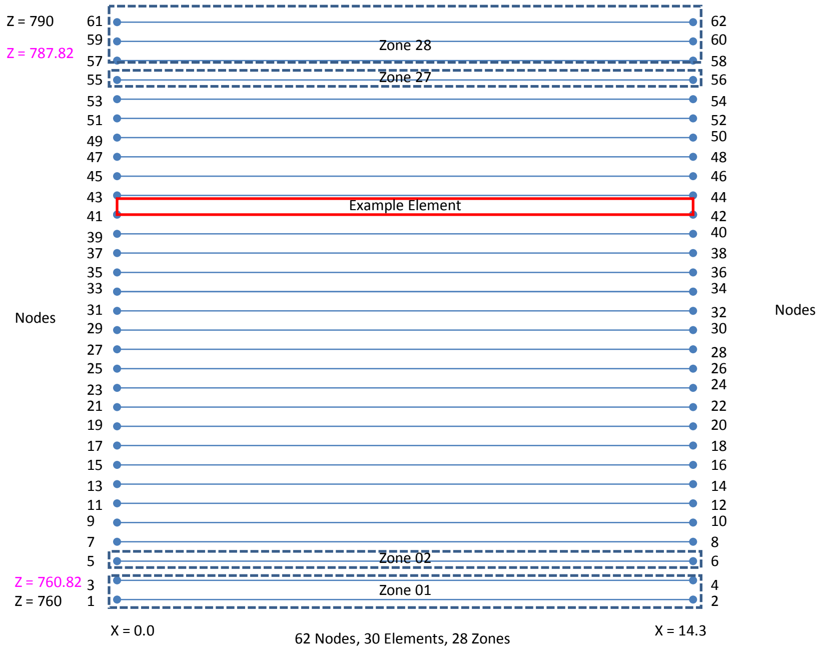

62 Nodes, 30 Elements, 28 Zones

HT-2 to HT-3 7 Horizontal Zones Model

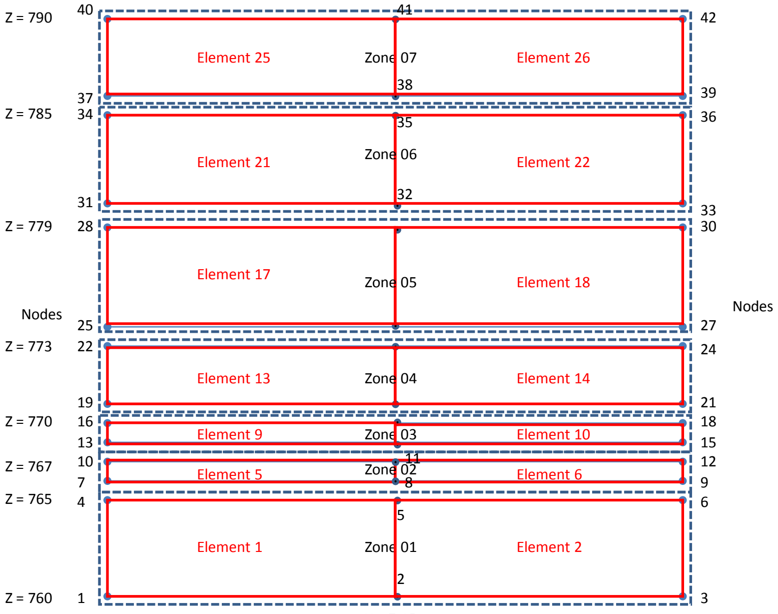

42 Nodes, 26 Elements, 7 Zones

HT-2 to HT-3 21 Horizontal Zones Model

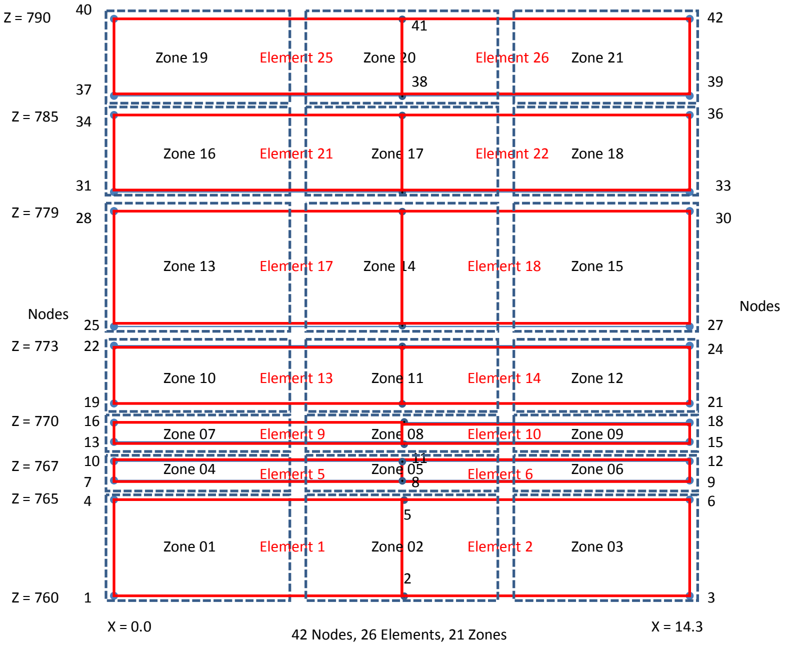

HT-4 to HT-3 ZOP Model

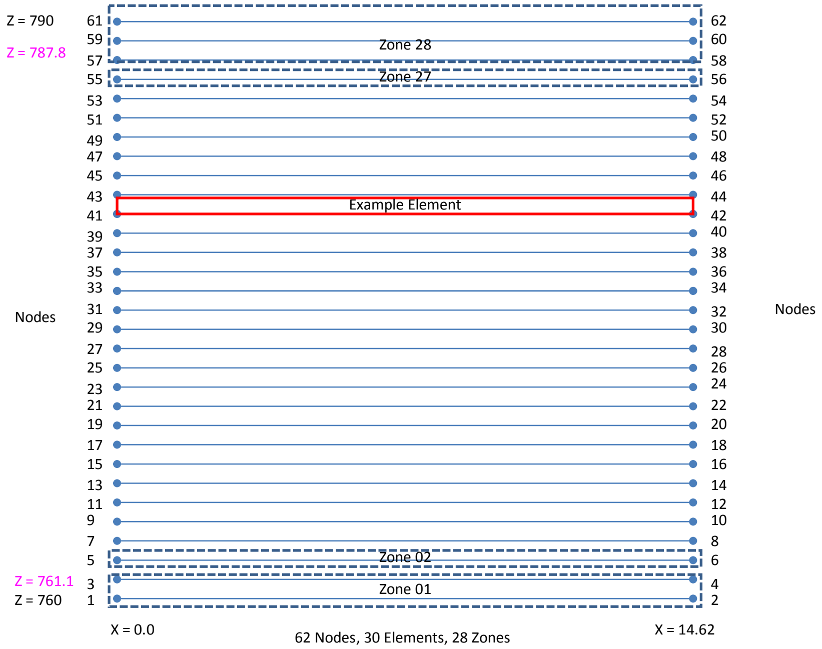

62 Nodes, 30 Elements, 28 Zones

HT-4 to HT-3 7 Horizontal Zones Model

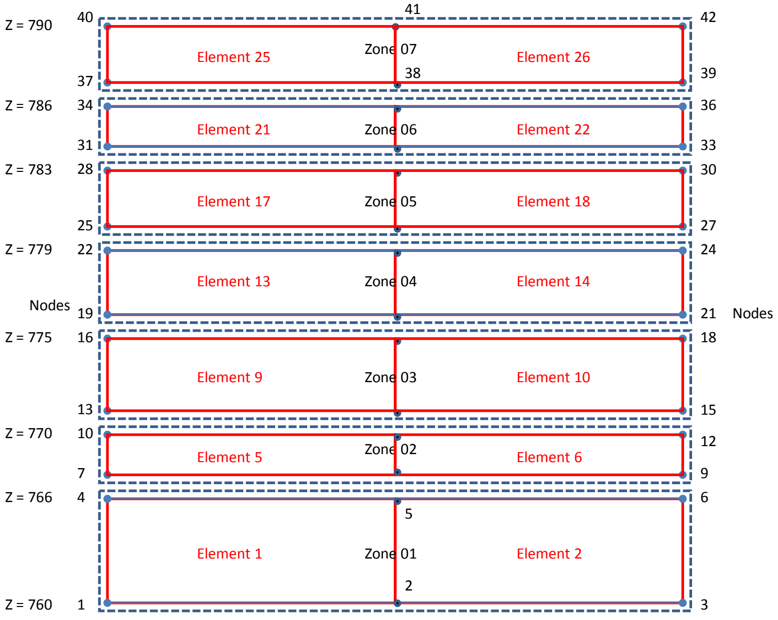

42 Nodes, 26 Elements, 7 Zones

HT-4 to HT-3 21 Horizontal Zones Model

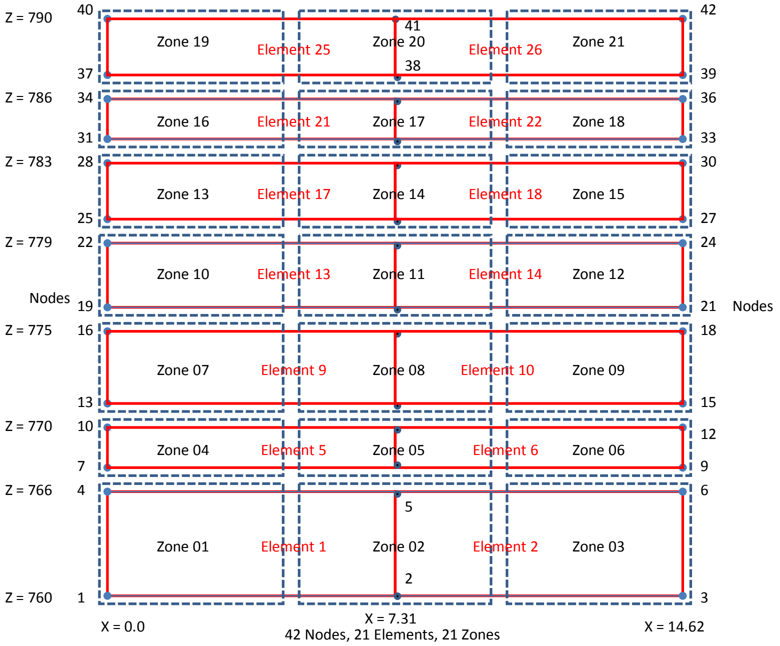

HT-5 to HT-3 ZOP Model

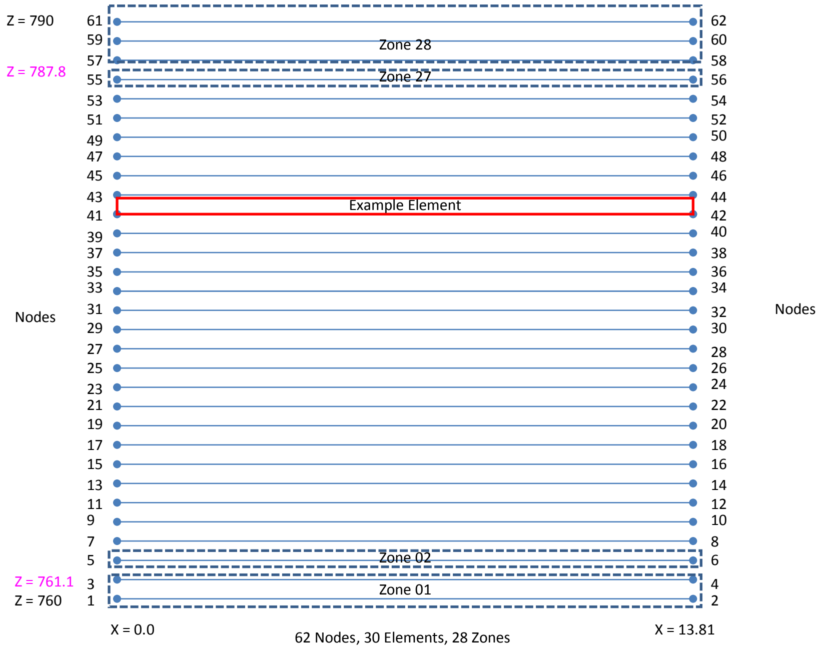

HT-5 to HT-3 8 Horizontal Zones Model

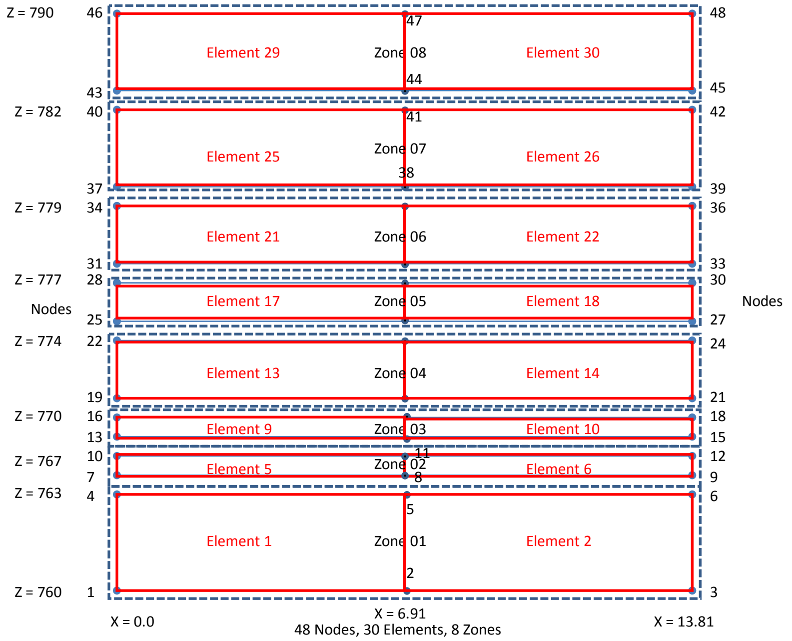

HT-5 to HT-3 24 Zones Model

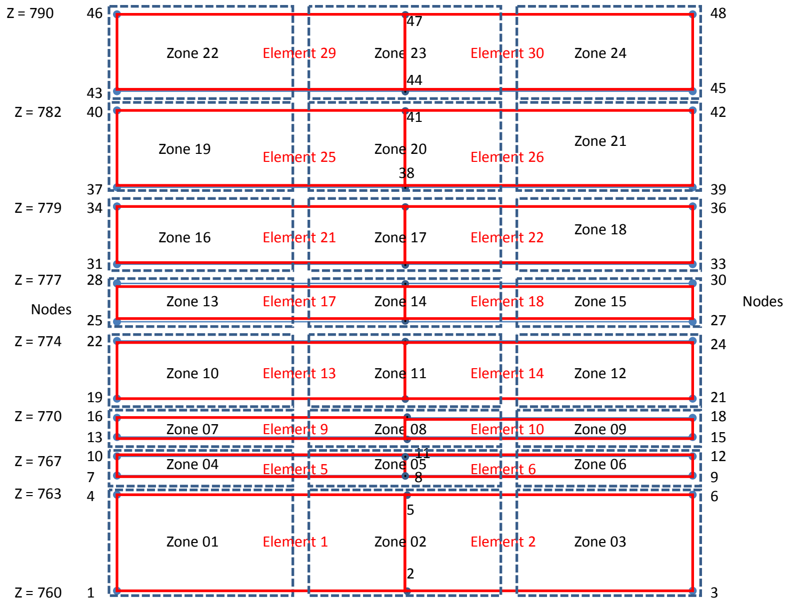

48 Nodes, 30 Elements, 24 Zones

HT-6 to HT-3 ZOP Model

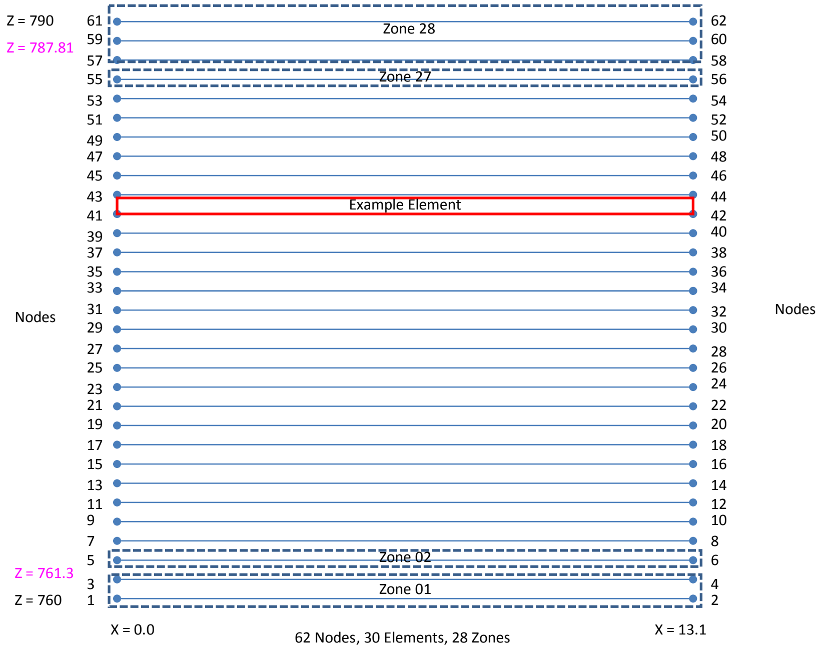

62 Nodes, 30 Elements, 28 Zones

HT-6 to HT-3 8 Horizontal Zones Model

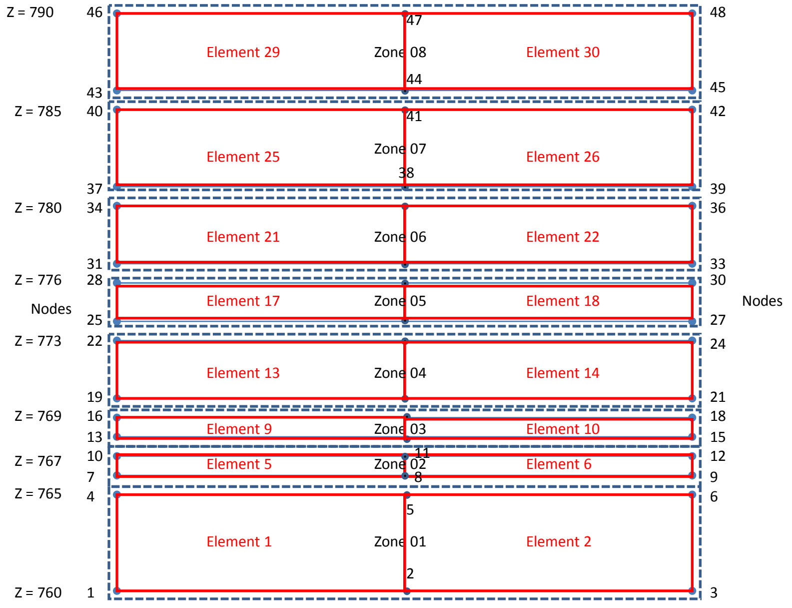

48 Nodes, 30 Elements, 8 Zones

HT-6 to HT-3 24 Zones Model

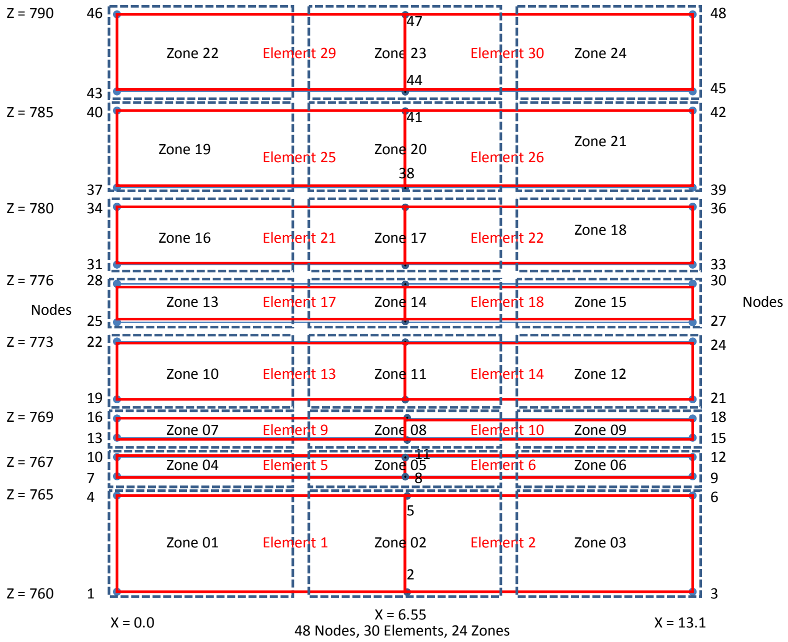

HT-GP to HT-2 ZOP Model

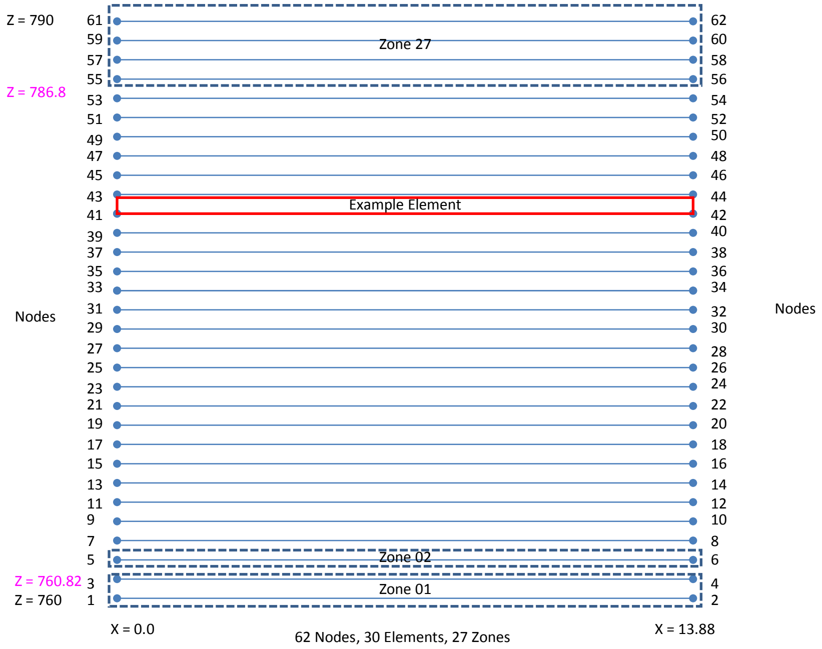

HT-GP to HT-2 7 Horizontal Zones Model

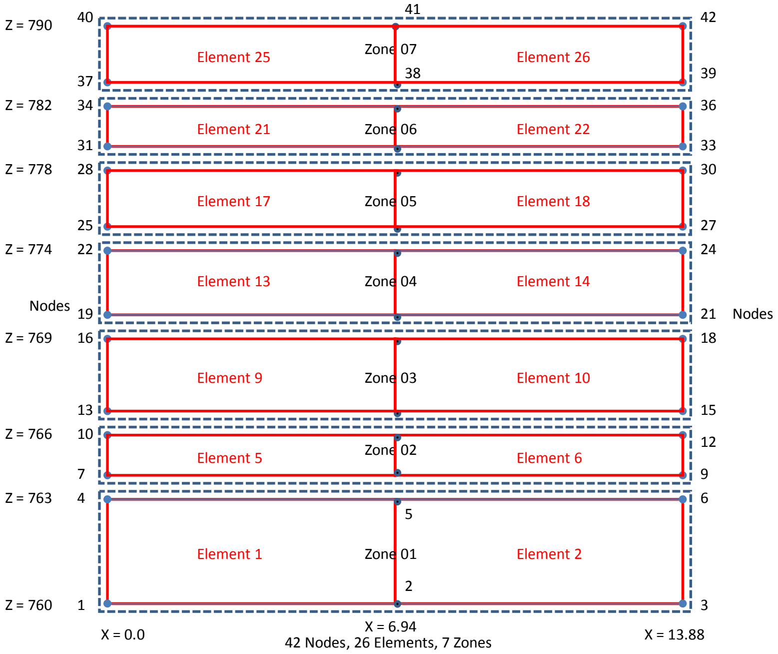

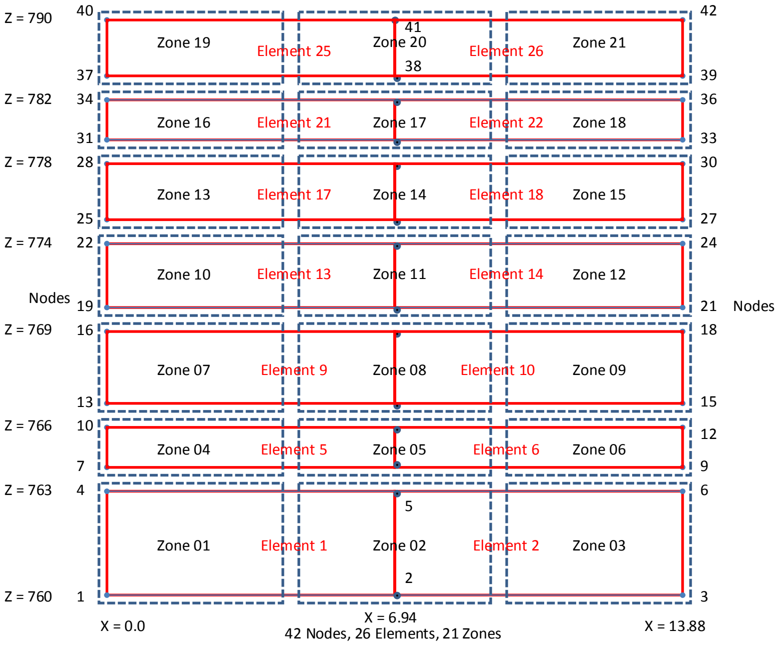

HT-GP to HT-2 21 Zones Model

42 Nodes, 26 Elements, 21 Zones

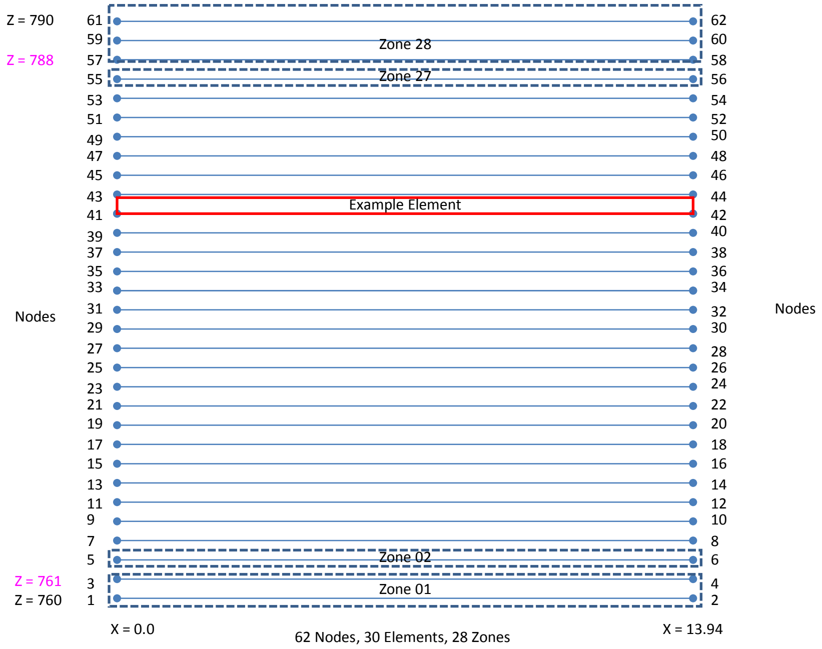

HT-GP to HT-3 ZOP Model

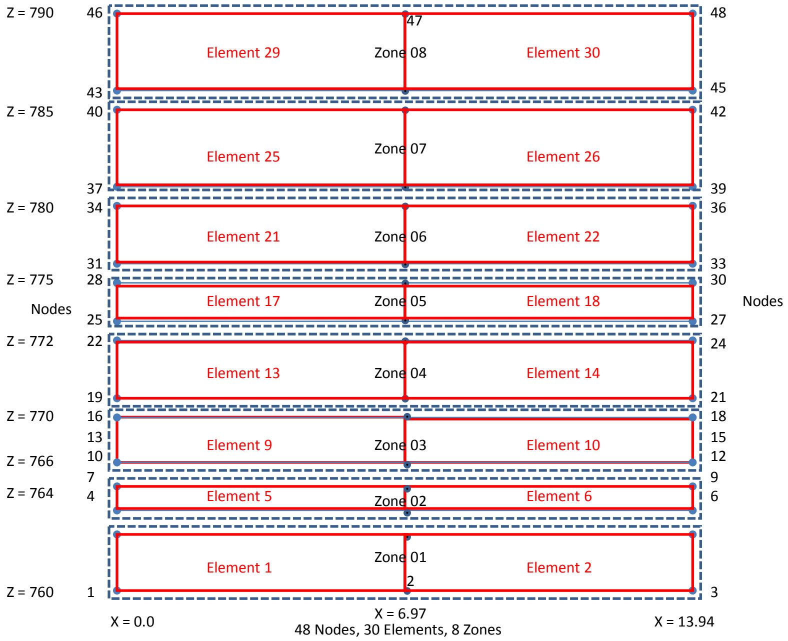

HT-GP to HT-3 8 Horizontal Zones Model

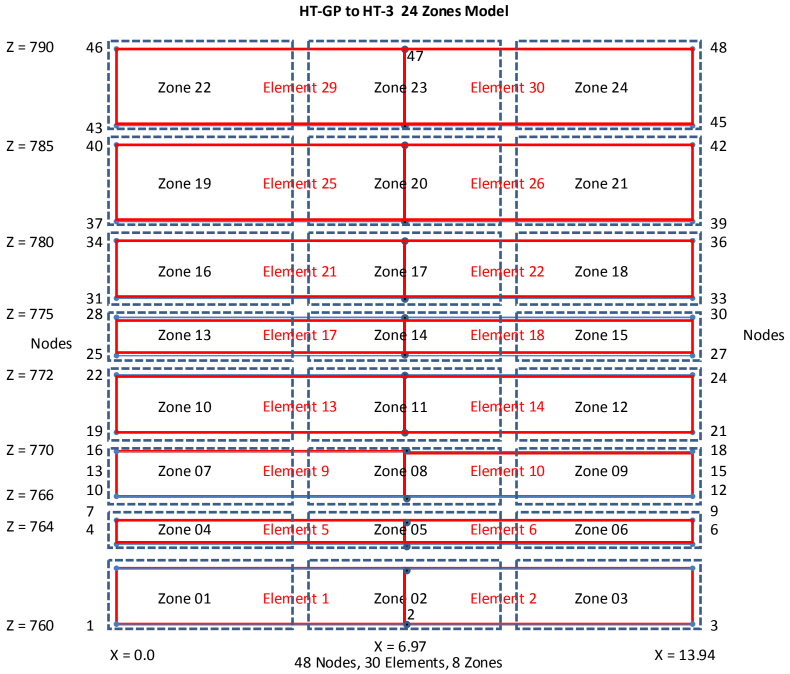
HT-GP to HT-3 24 Zones Model
Z = 790
Z = 785
Z = 780
Z = 775
Z = 772
Z = 770
Z = 766
Z = 764
Z = 760
Nodes
Nodes
46
47
48
43
45
40
42
37
39
34
36
31
33
28
30
25
27
22
24
19
21
16
18
13
15
10
12
7
9
4
6
1
2
3
Zone 22
Element 29
Zone 23
Element 30
Zone 24
Zone 19
Element 25
Zone 20
Element 26
Zone 21
Zone 16
Element 21
Zone 17
Element 22
Zone 18
Zone 13
Element 17
Zone 14
Element 18
Zone 15
Zone 10
Element 13
Zone 11
Element 14
Zone 12
Zone 07
Element 9
Zone 08
Element 10
Zone 09
Zone 04
Element 5
Zone 05
Element 6
Zone 06
Zone 01
Element 1
Zone 02
Element 2
Zone 03
X = 0.0
X = 6.97
X = 13.94
48 Nodes, 30 Elements, 8 Zones

Appendix B – Deterministic K Profiles

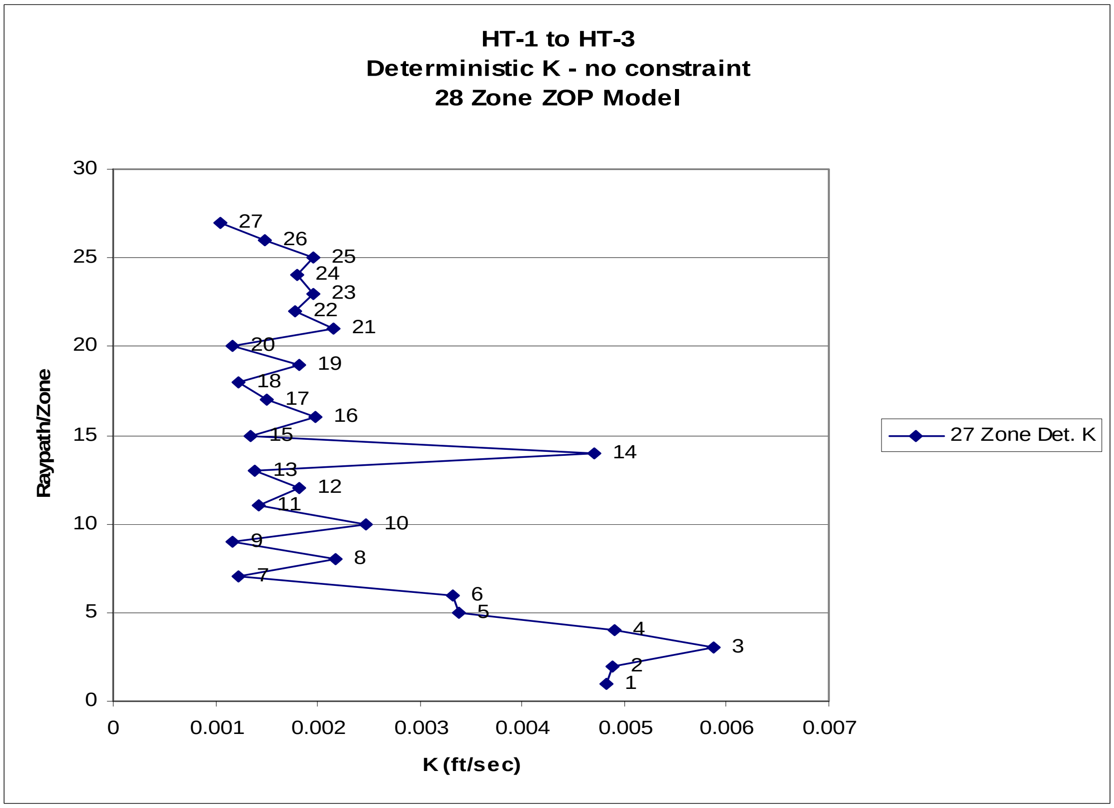
HT-1 to HT-3
Deterministic K - no constraint
28 Zone ZOP Model
Raypath/Zone
K (ft/sec)
0
5
10
15
20
25
30
0
0.001
0.002
0.003
0.004
0.005
0.006
0.007
27 Zone Det. K
1
2
3
4
5
6
7
8
9
10
11
12
13
14
15
16
17
18
19
20
21
22
23
24
25
26
27

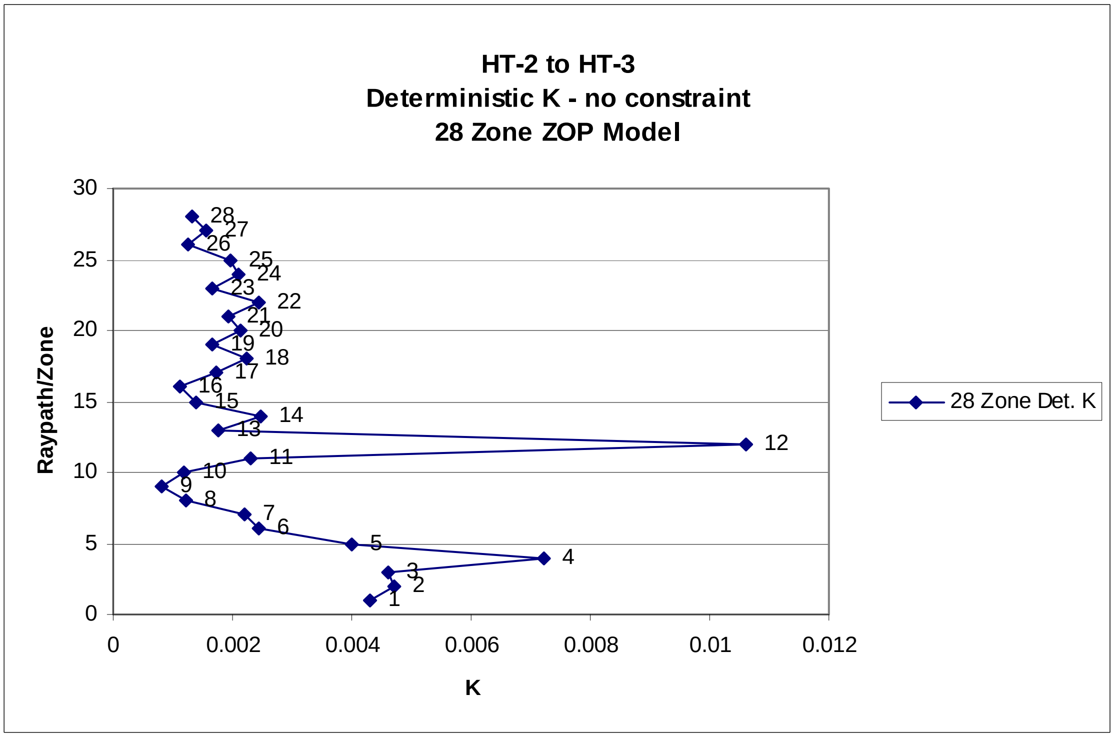
HT-2 to HT-3
Deterministic K - no constraint
28 Zone ZOP Model
Raypath/Zone
K
0
5
10
15
20
25
30
0
0.002
0.004
0.006
0.008
0.01
0.012
28 Zone Det. K
1
2
3
4
5
6
7
8
9
10
11
12
13
14
15
16
17
18
19
20
21
22
23
24
25
26
27
28

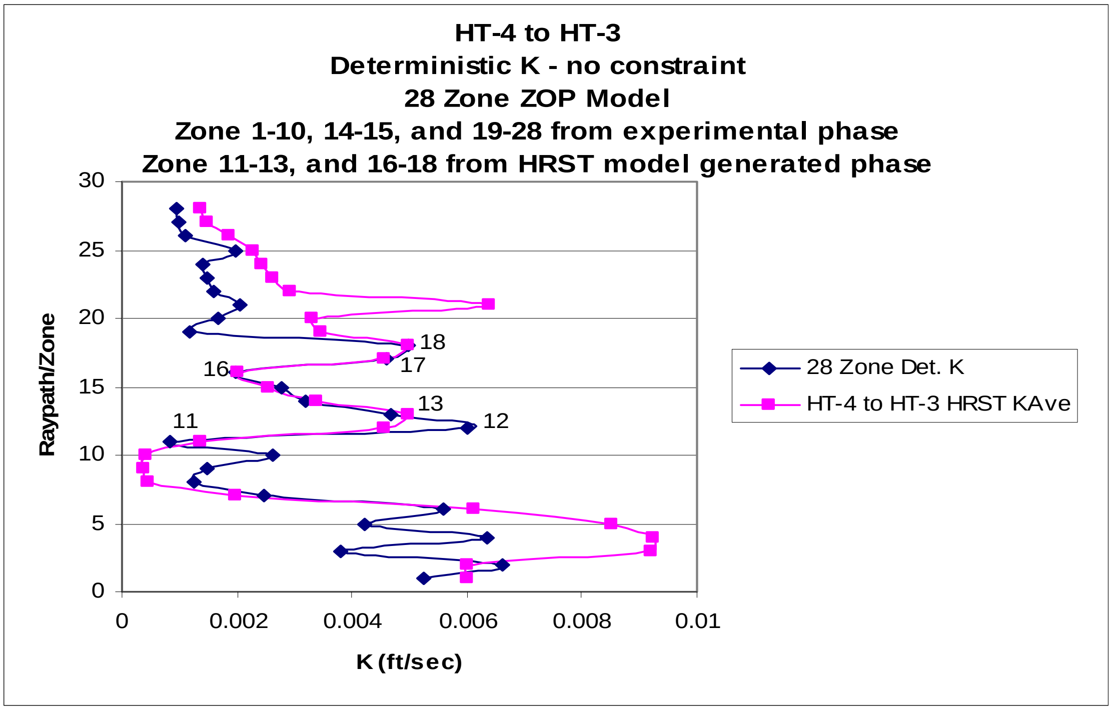
HT-4 to HT-3
Deterministic K - no constraint
28 Zone ZOP Model
Zone 1-10, 14-15, and 19-28 from experimental phase
Zone 11-13, and 16-18 from HRST model generated phase
Raypath/Zone
K (ft/sec)
0
5
10
15
20
25
30
0
0.002
0.004
0.006
0.008
0.01
18
17
16
13
12
11
28 Zone Det. K
HT-4 to HT-3 HRST KAve

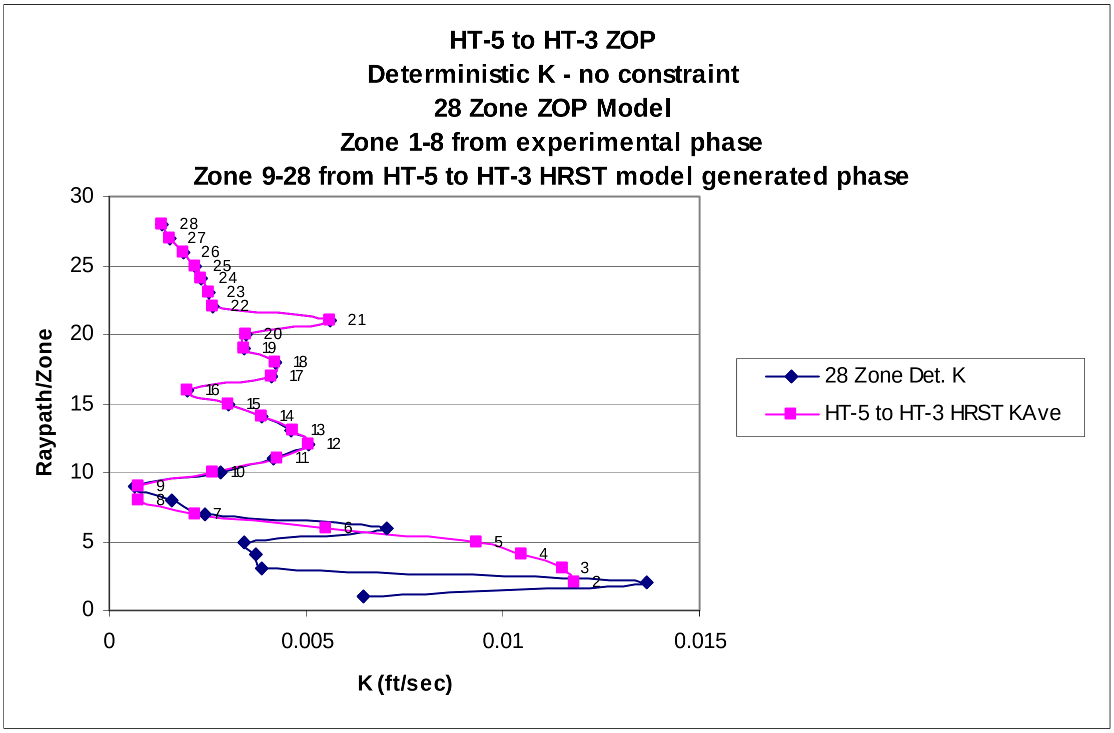
HT-5 to HT-3 ZOP
Deterministic K - no constraint
28 Zone ZOP Model
Zone 1-8 from experimental phase
Zone 9-28 from HT-5 to HT-3 HRST model generated phase
Raypath/Zone
K (ft/sec)
0
5
10
15
20
25
30
0
0.005
0.01
0.015
28
27
26
25
24
23
22
21
20
19
18
17
16
15
14
13
12
11
10
9
8
7
6
5
4
3
2
28 Zone Det. K
HT-5 to HT-3 HRST KAve

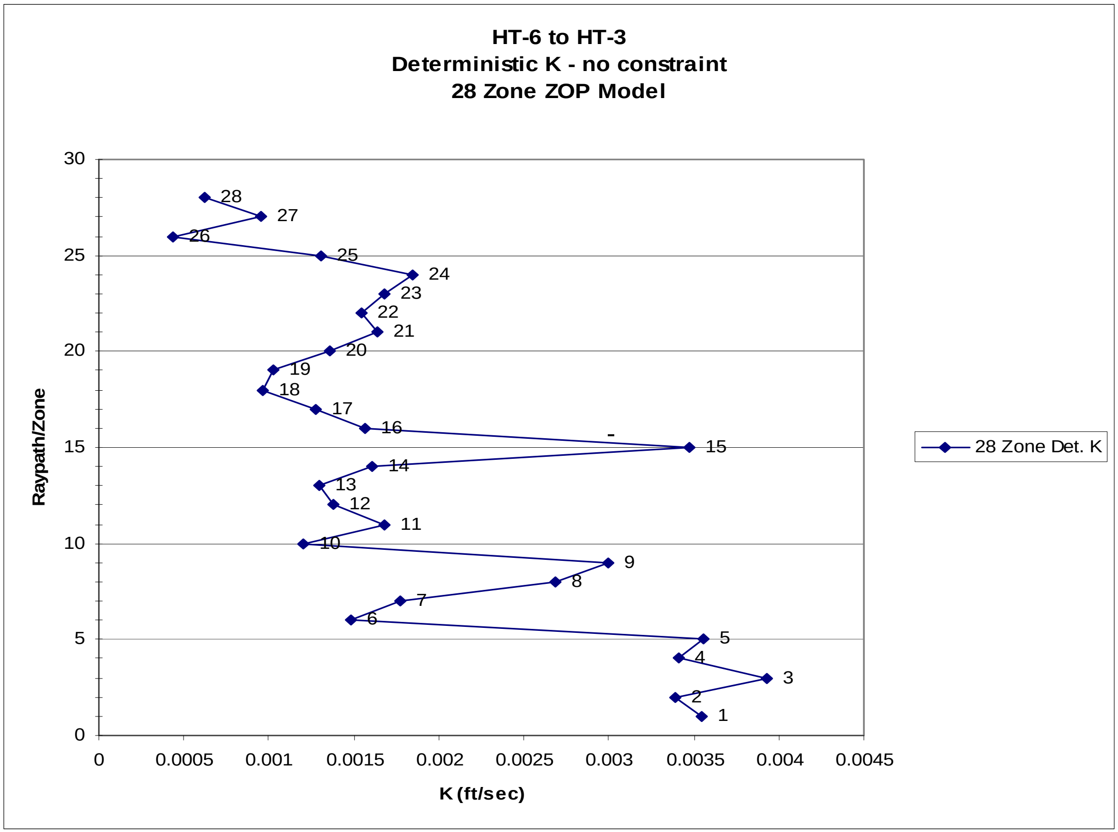
HT-6 to HT-3
Deterministic K - no constraint
28 Zone ZOP Model

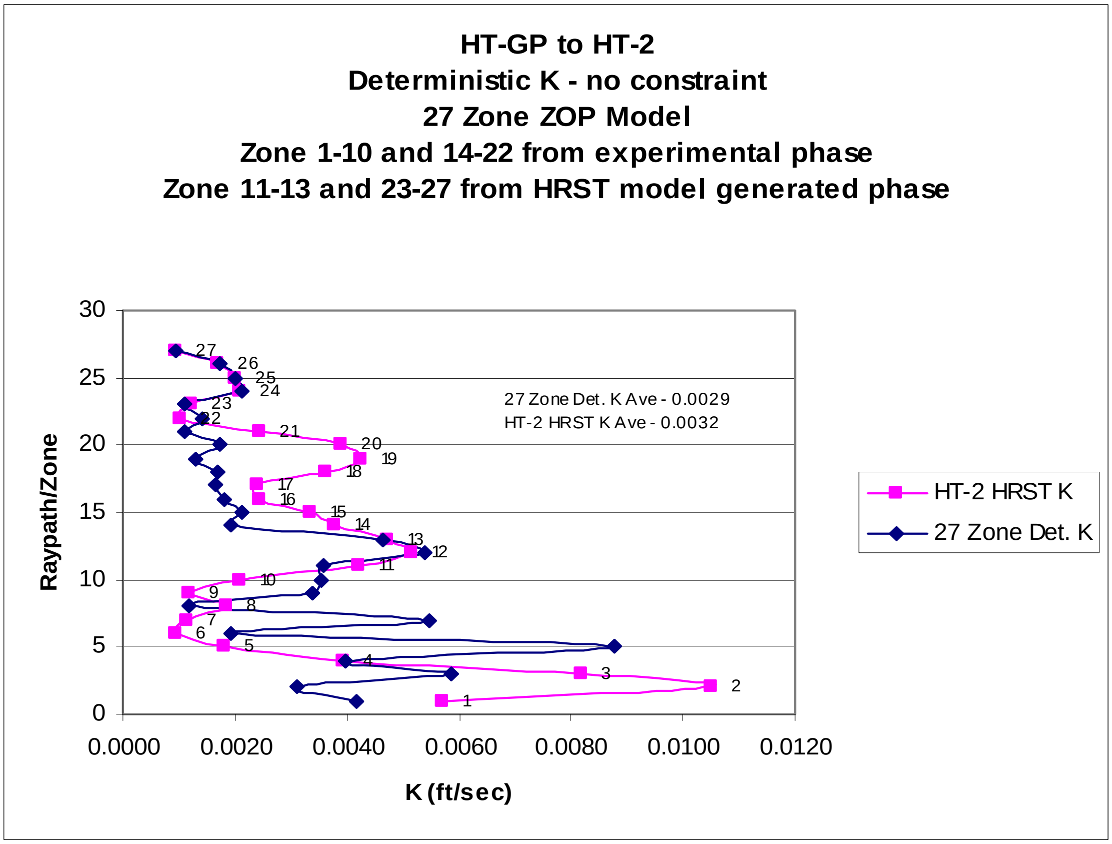
HT-GP to HT-2
Deterministic K - no constraint
27 Zone ZOP Model
Zone 1-10 and 14-22 from experimental phase
Zone 11-13 and 23-27 from HRST model generated phase

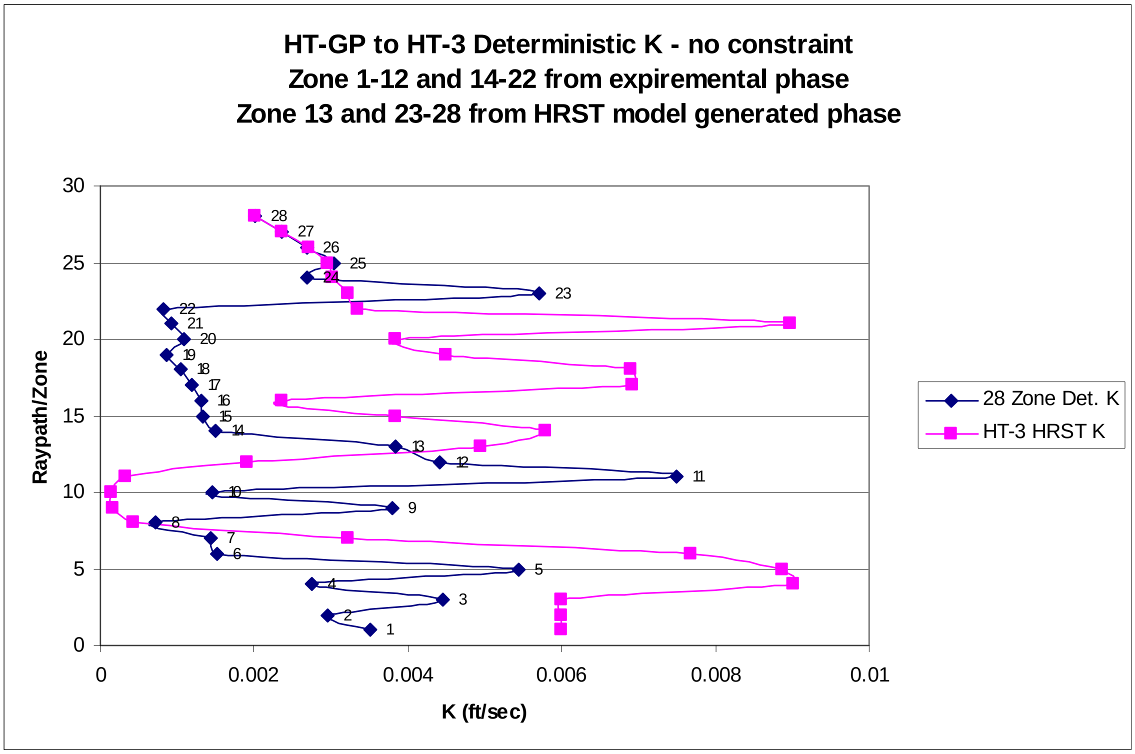
HT-GP to HT-3 Deterministic K - no constraint
Zone 1-12 and 14-22 from expiremental phase
Zone 13 and 23-28 from HRST model generated phase
Raypath/Zone
K (ft/sec)
0
5
10
15
20
25
30
0
0.002
0.004
0.006
0.008
0.01
28 Zone Det. K
HT-3 HRST K
1
2
3
4
5
6
7
8
9
10
11
12
13
14
15
16
17
18
19
20
21
22
23
24
25
26
27
28

Appendix C – Node Data Summary Charts

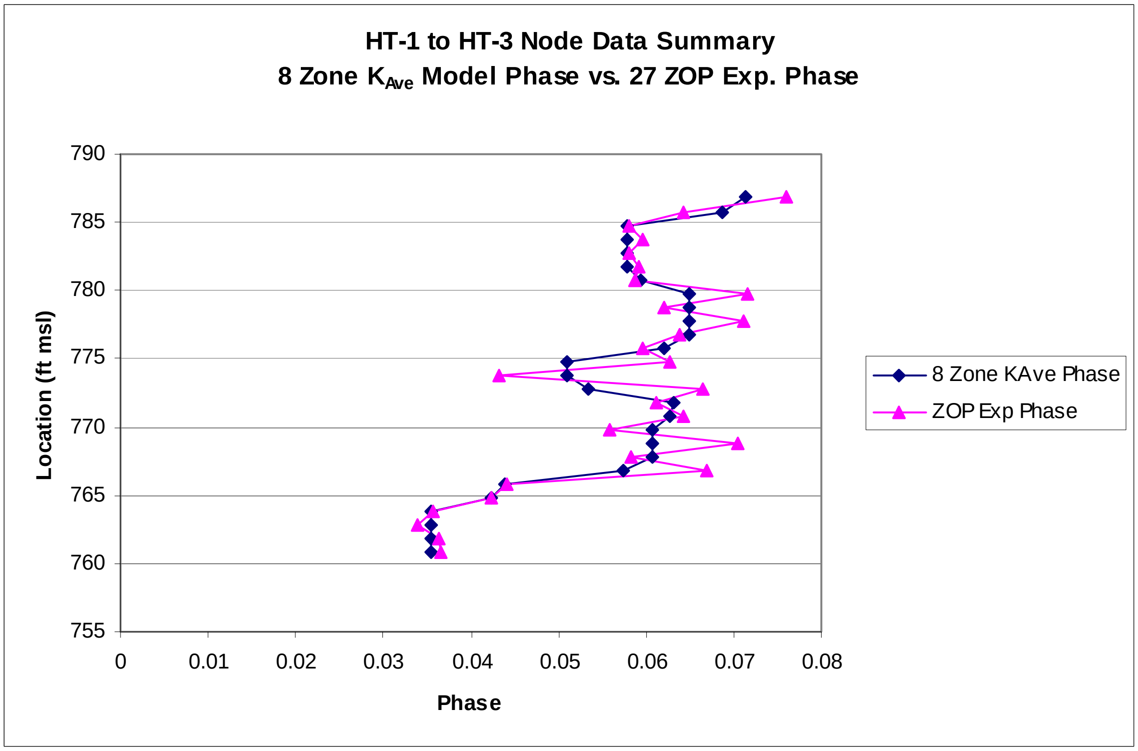
HT-1 to HT-3 Node Data Summary
8 Zone K_{Ave} Model Phase vs. 27 ZOP Exp. Phase
790
785
780
775
770
765
760
755
Location (ft msl)
0
0.01
0.02
0.03
0.04
0.05
0.06
0.07
0.08
Phase
8 Zone KAve Phase
ZOP Exp Phase

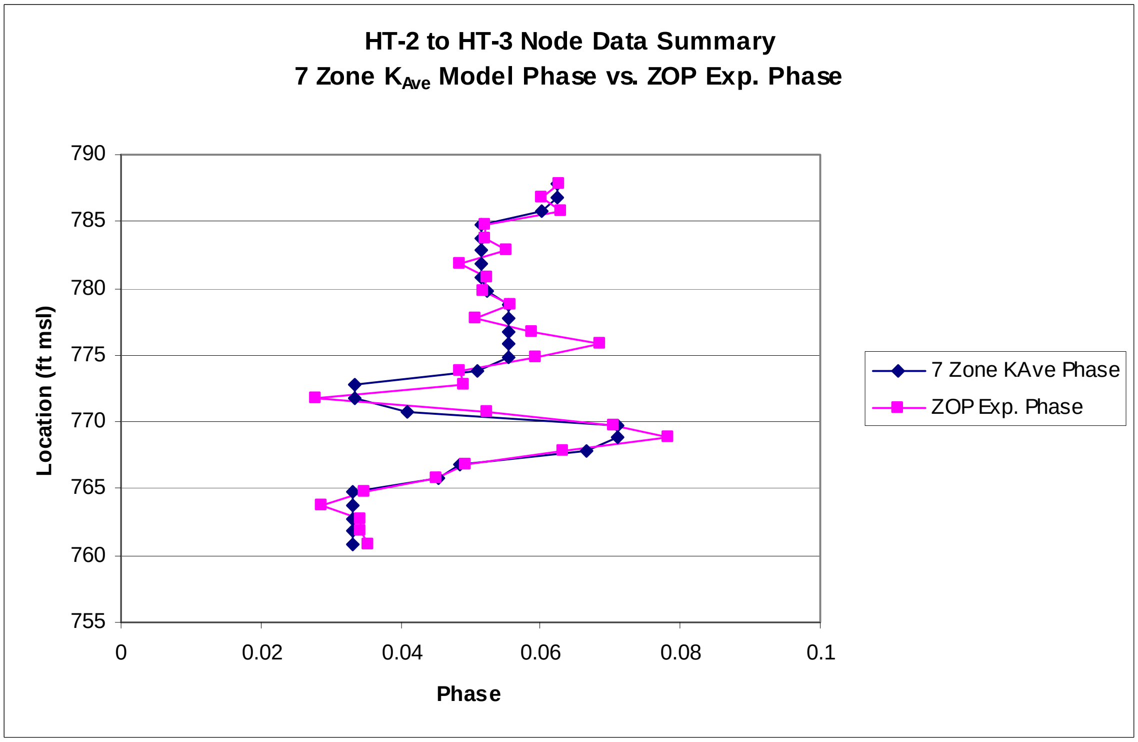
HT-2 to HT-3 Node Data Summary
7 Zone K_{Ave} Model Phase vs. ZOP Exp. Phase
790
785
780
775
770
765
760
755
Location (ft msl)
0
0.02
0.04
0.06
0.08
0.1
Phase
7 Zone KAve Phase
ZOP Exp. Phase

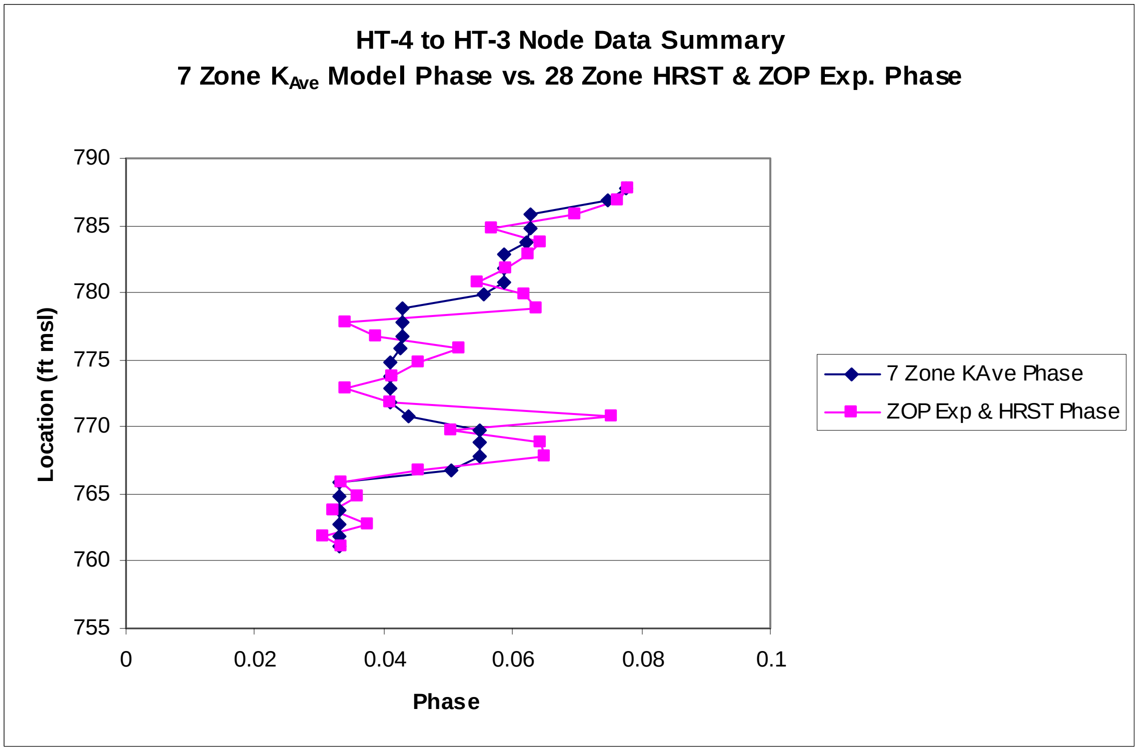
HT-4 to HT-3 Node Data Summary
7 Zone K_{Ave} Model Phase vs. 28 Zone HRST & ZOP Exp. Phase
790
785
780
775
770
765
760
755
Location (ft msl)
0
0.02
0.04
0.06
0.08
0.1
Phase
7 Zone KAve Phase
ZOP Exp & HRST Phase

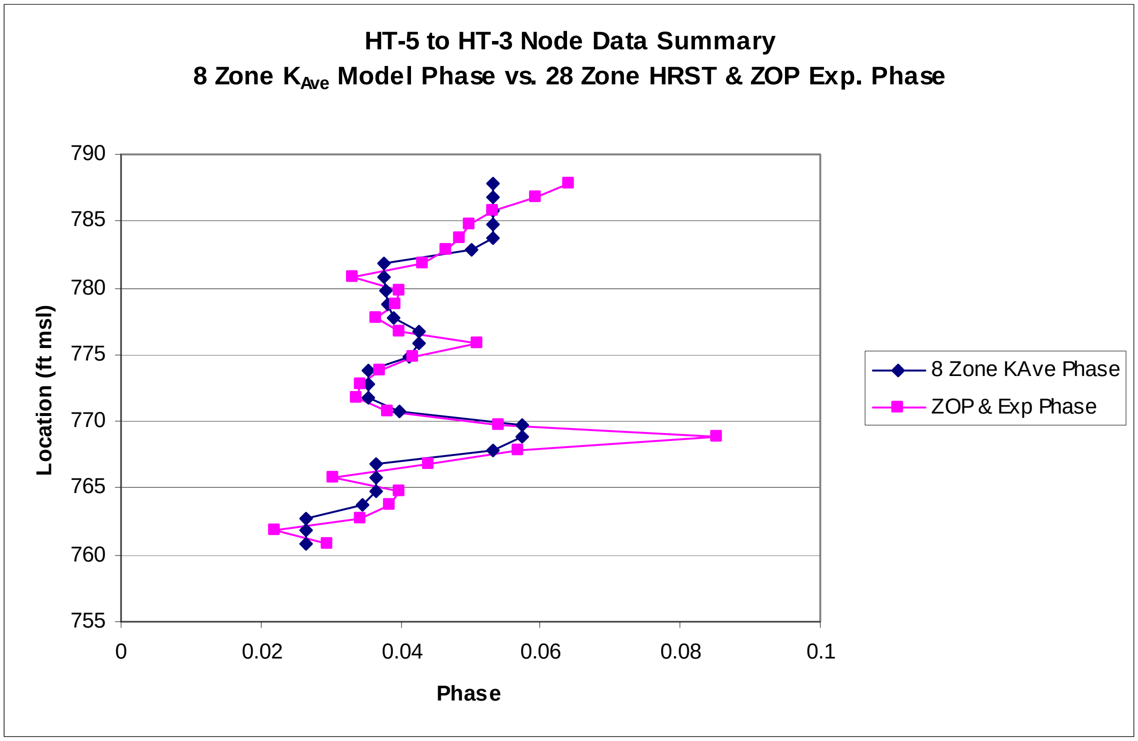
HT-5 to HT-3 Node Data Summary
8 Zone K_{Ave} Model Phase vs. 28 Zone HRST & ZOP Exp. Phase
790
785
780
775
770
765
760
755
Location (ft msl)
0
0.02
0.04
0.06
0.08
0.1
Phase
8 Zone KAve Phase
ZOP & Exp Phase

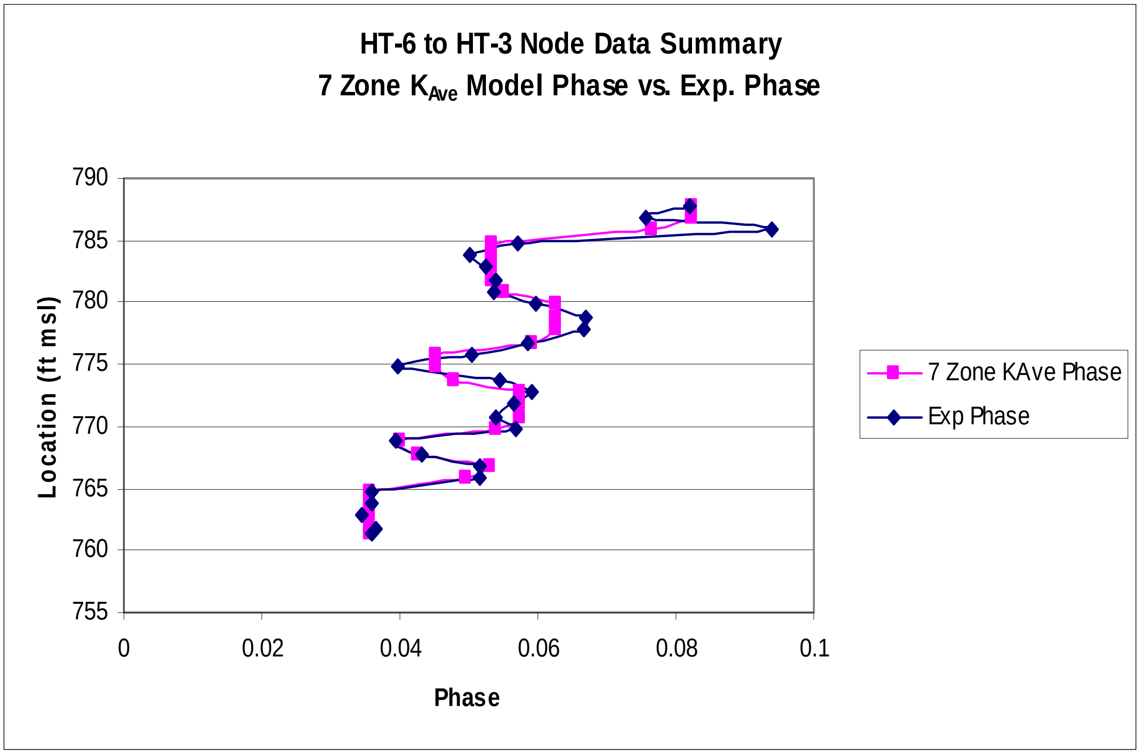
HT-6 to HT-3 Node Data Summary
7 Zone K$_{Ave}$ Model Phase vs. Exp. Phase
790
785
780
775
770
765
760
755
Location (ft msl)
0
0.02
0.04
0.06
0.08
0.1
Phase
7 Zone KAve Phase
Exp Phase

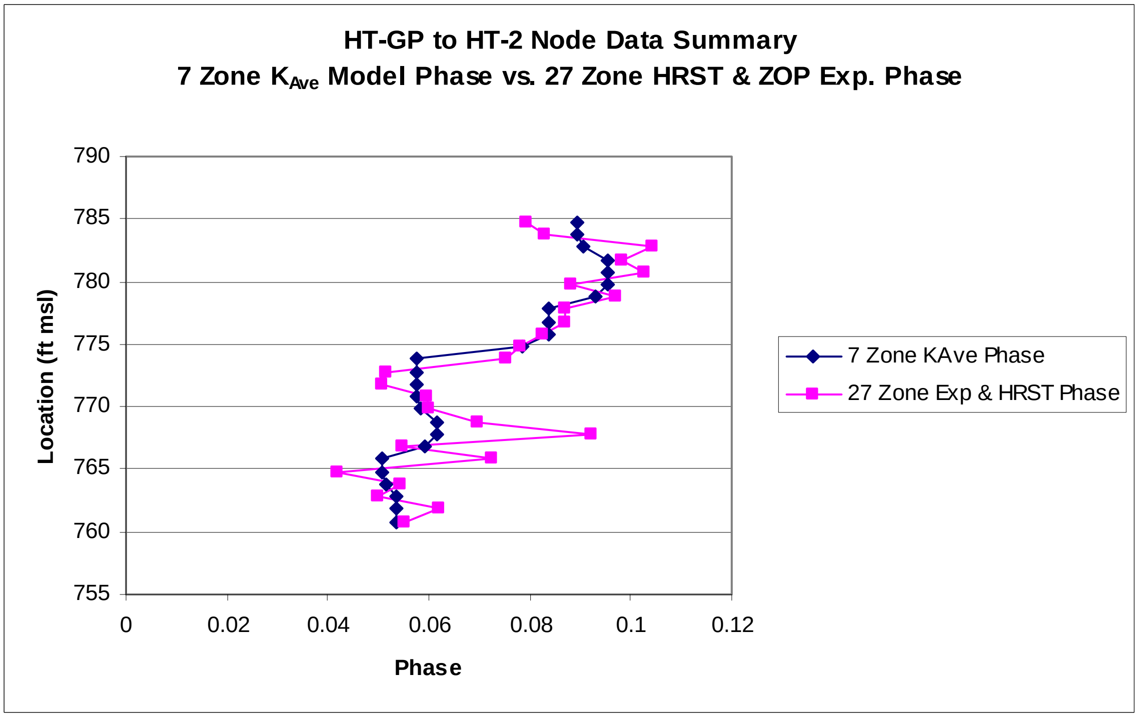
HT-GP to HT-2 Node Data Summary
7 Zone K$_{Ave}$ Model Phase vs. 27 Zone HRST & ZOP Exp. Phase
790
785
780
775
770
765
760
755
Location (ft msl)
0
0.02
0.04
0.06
0.08
0.1
0.12
Phase
7 Zone KAve Phase
27 Zone Exp & HRST Phase

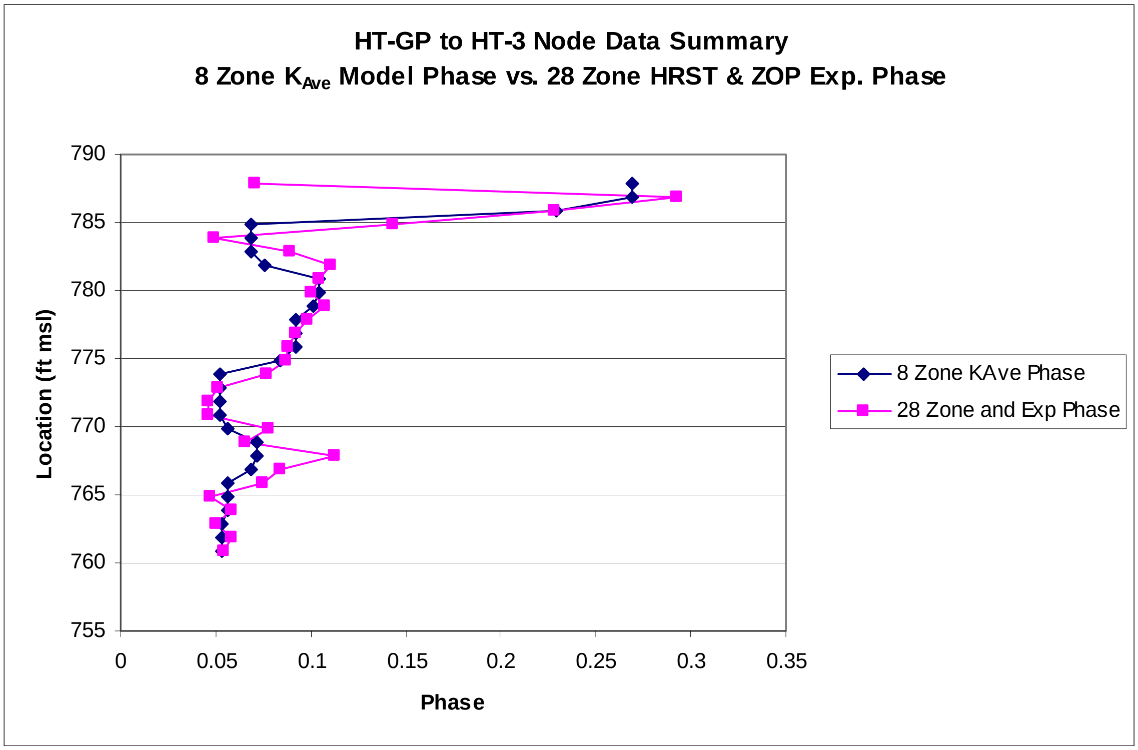
HT-GP to HT-3 Node Data Summary
8 Zone K$_{Ave}$ Model Phase vs. 28 Zone HRST & ZOP Exp. Phase
Location (ft msl)
790
785
780
775
770
765
760
755
0
0.05
0.1
0.15
0.2
0.25
0.3
0.35
Phase
8 Zone KAve Phase
28 Zone and Exp Phase

Appendix D – ZOP K Vertical Profile Charts

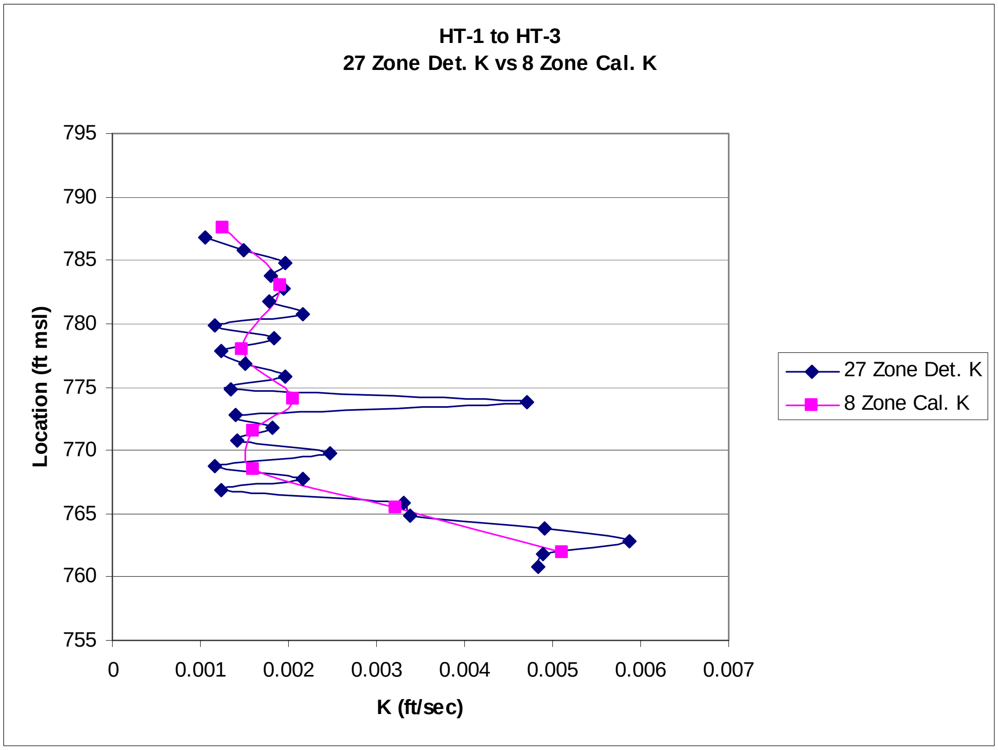
HT-1 to HT-3
27 Zone Det. K vs 8 Zone Cal. K
Location (ft msl)
795
790
785
780
775
770
765
760
755
0
0.001
0.002
0.003
0.004
0.005
0.006
0.007
K (ft/sec)
27 Zone Det. K
8 Zone Cal. K

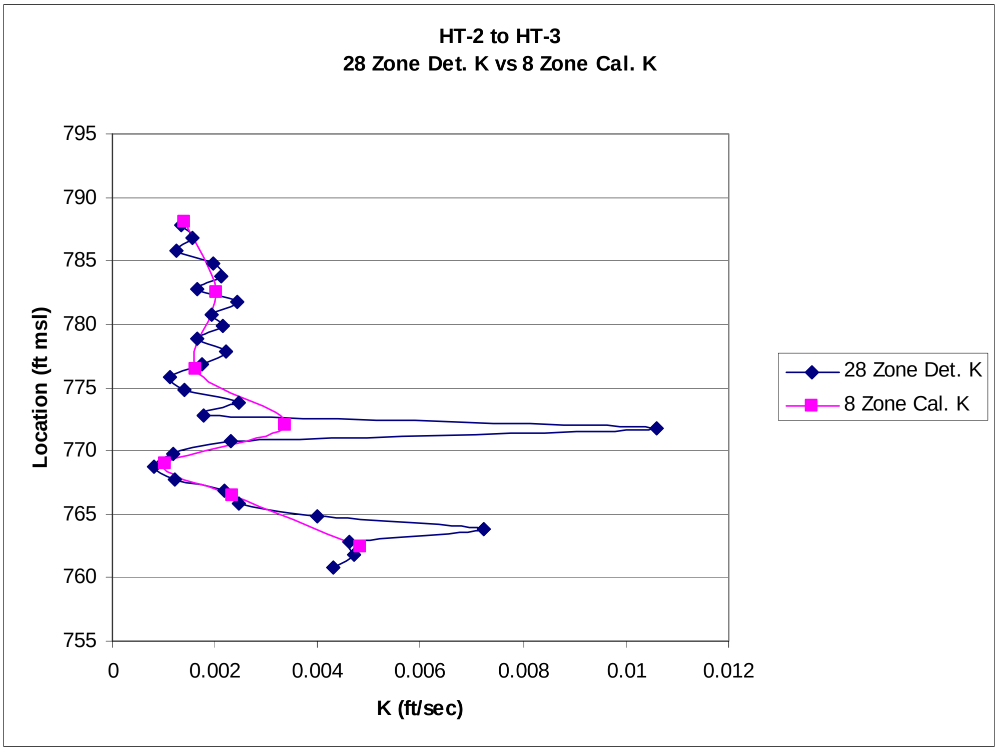
HT-2 to HT-3
28 Zone Det. K vs 8 Zone Cal. K
Location (ft msl)
795
790
785
780
775
770
765
760
755
0
0.002
0.004
0.006
0.008
0.01
0.012
K (ft/sec)
28 Zone Det. K
8 Zone Cal. K

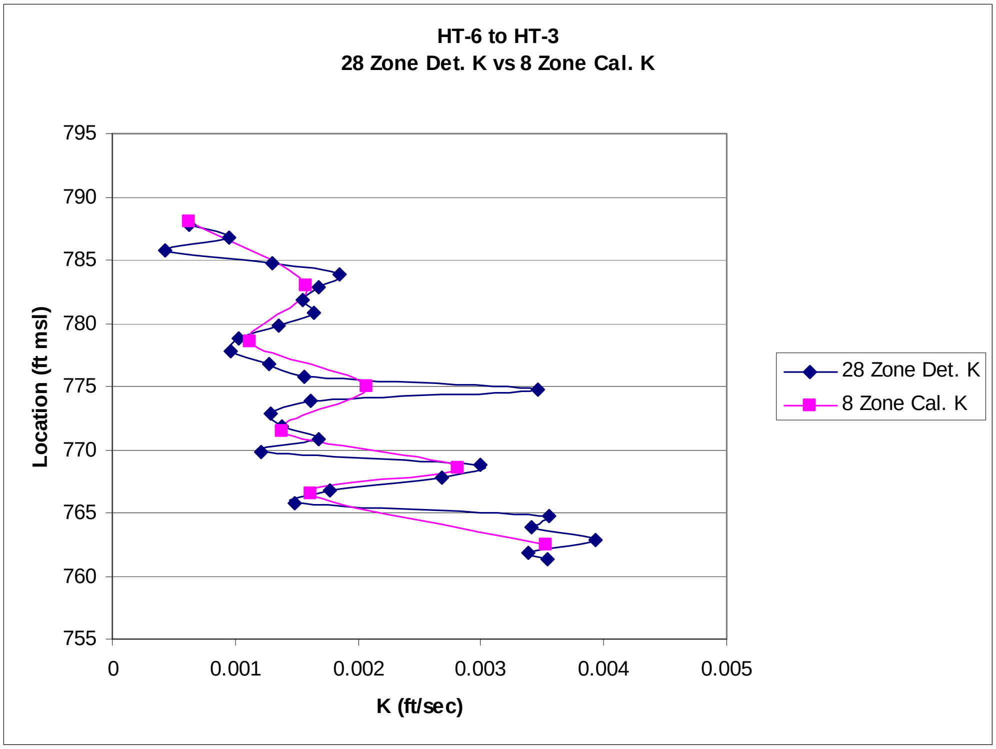
HT-6 to HT-3
28 Zone Det. K vs 8 Zone Cal. K
Location (ft msl)
795
790
785
780
775
770
765
760
755
0
0.001
0.002
0.003
0.004
0.005
K (ft/sec)
28 Zone Det. K
8 Zone Cal. K

Appendix E – Corrected ZOP K Vertical Profile Charts

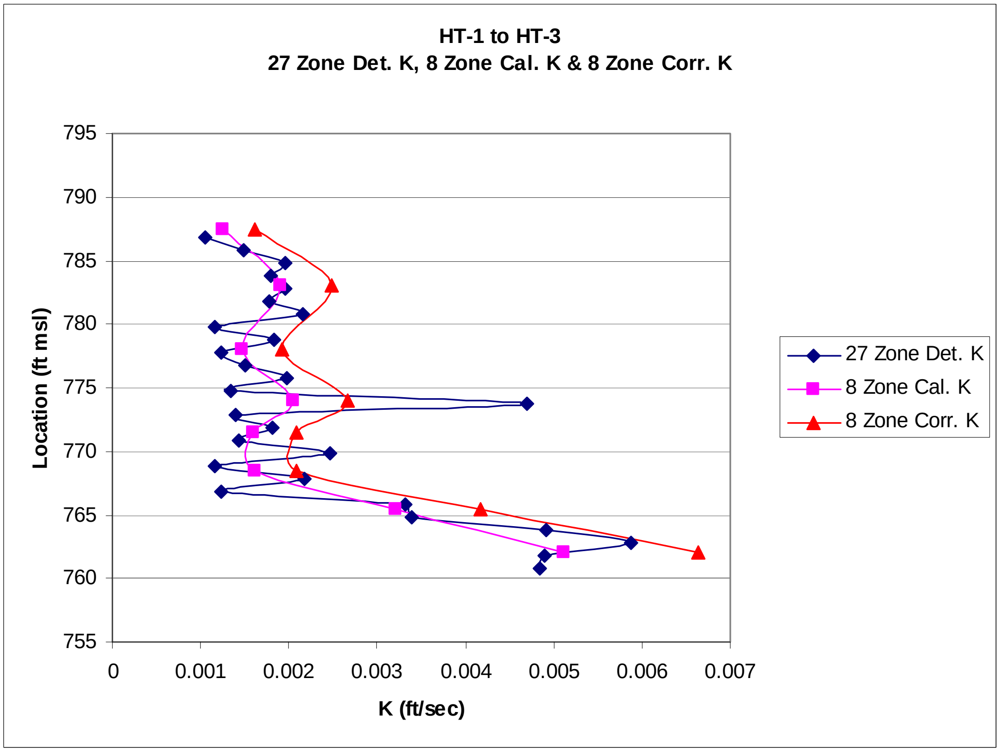
HT-1 to HT-3
27 Zone Det. K, 8 Zone Cal. K & 8 Zone Corr. K
Location (ft msl)
795
790
785
780
775
770
765
760
755
0
0.001
0.002
0.003
0.004
0.005
0.006
0.007
K (ft/sec)
27 Zone Det. K
8 Zone Cal. K
8 Zone Corr. K

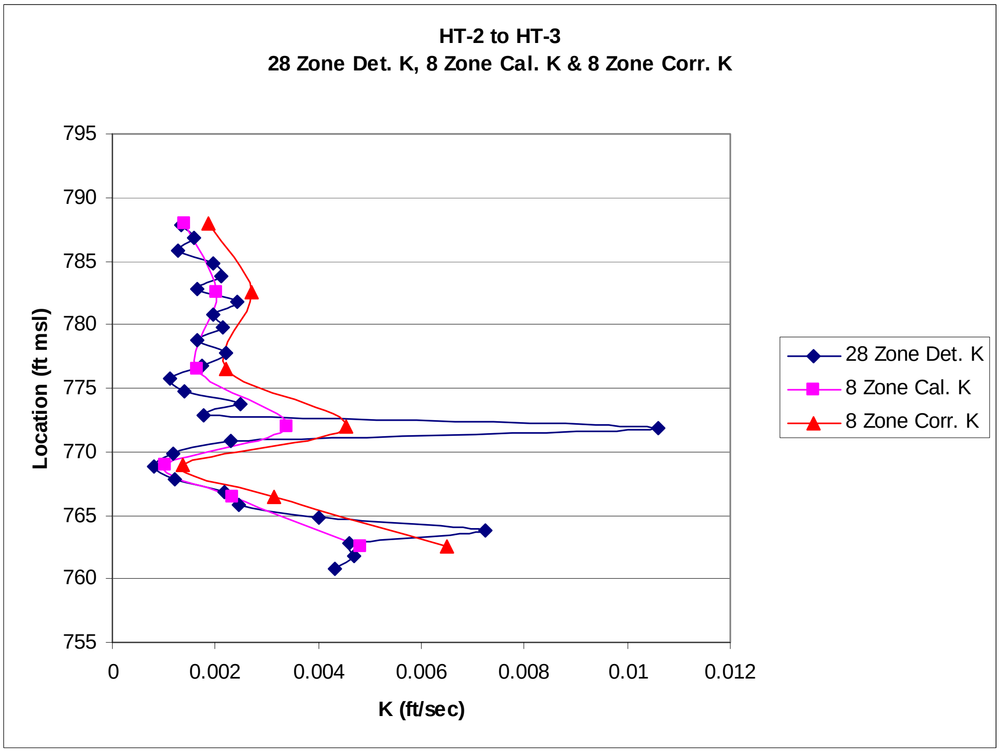
HT-2 to HT-3
28 Zone Det. K, 8 Zone Cal. K & 8 Zone Corr. K
Location (ft msl)
795
790
785
780
775
770
765
760
755
0
0.002
0.004
0.006
0.008
0.01
0.012
K (ft/sec)
28 Zone Det. K
8 Zone Cal. K
8 Zone Corr. K

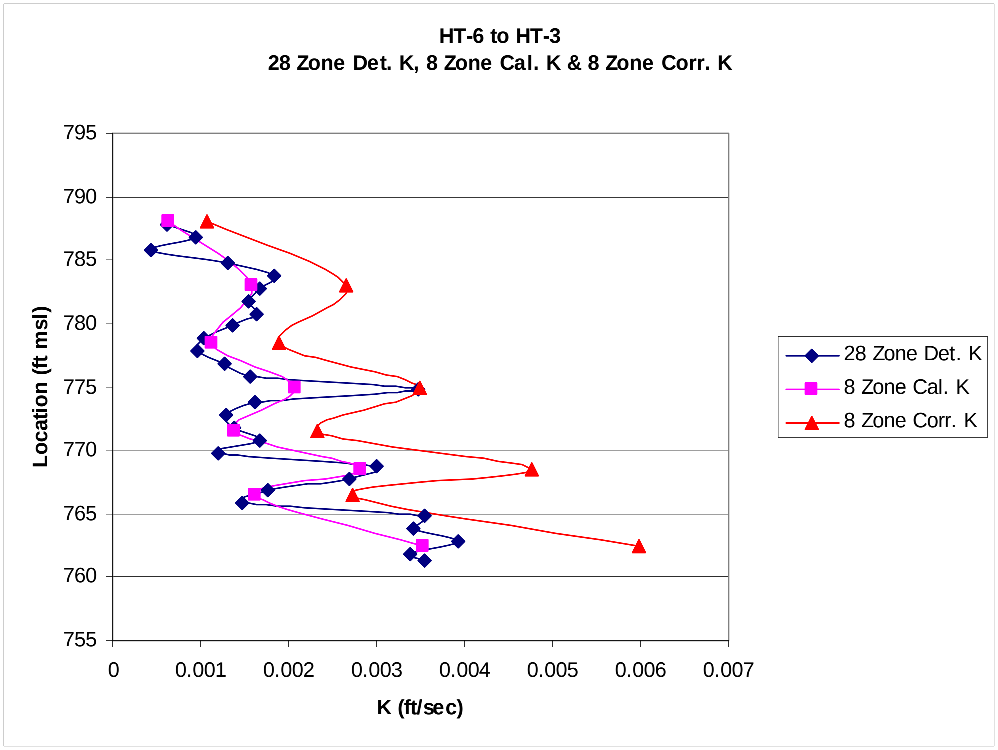
HT-6 to HT-3
28 Zone Det. K, 8 Zone Cal. K & 8 Zone Corr. K
Location (ft msl)
795
790
785
780
775
770
765
760
755
0
0.001
0.002
0.003
0.004
0.005
0.006
0.007
K (ft/sec)
28 Zone Det. K
8 Zone Cal. K
8 Zone Corr. K

Appendix F – % Standard Deviation K For Lateral Heterogeneity Models And The Pumped Hydraulic CPT Source

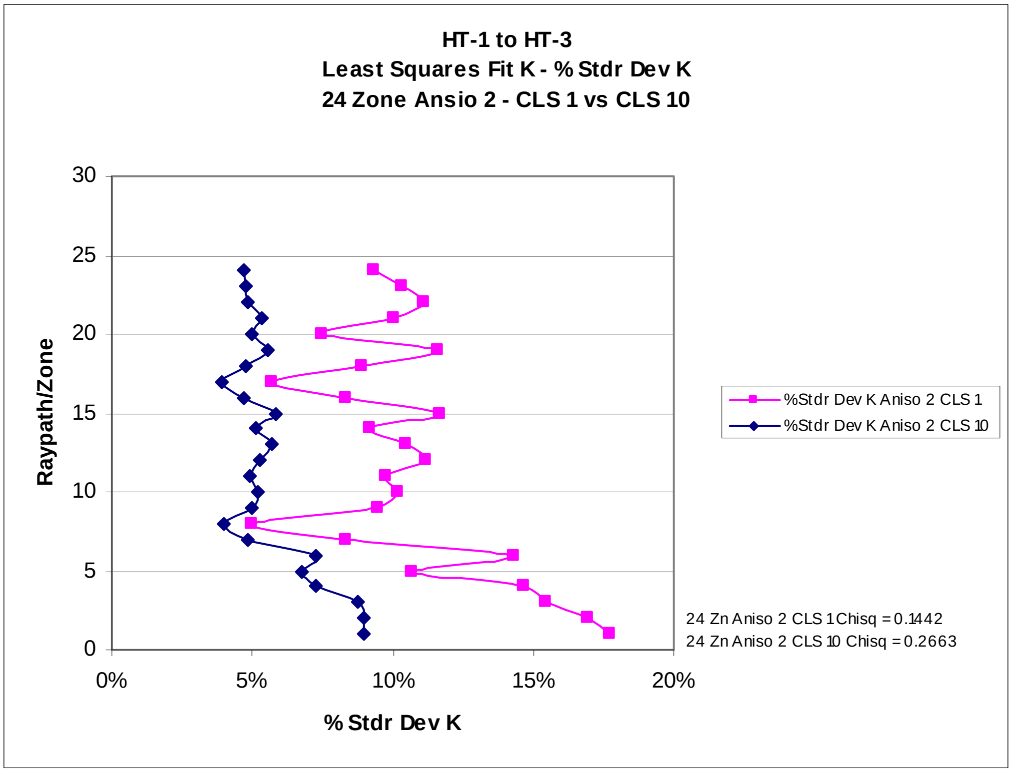
HT-1 to HT-3
Least Squares Fit K - % Stdr Dev K
24 Zone Ansio 2 - CLS 1 vs CLS 10
Raypath/Zone
30
25
20
15
10
5
0
0%
5%
10%
15%
20%
% Stdr Dev K
%Stdr Dev K Aniso 2 CLS 1
%Stdr Dev K Aniso 2 CLS 10
24 Zn Aniso 2 CLS 1 Chisq = 0.1442
24 Zn Aniso 2 CLS 10 Chisq = 0.2663

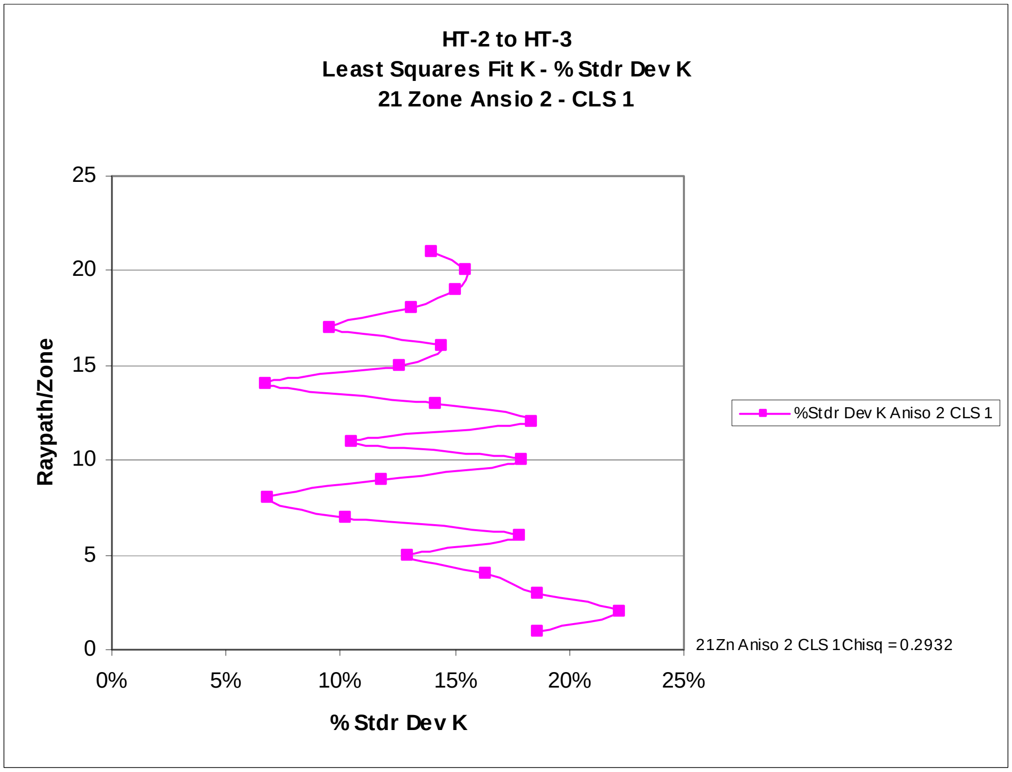
HT-2 to HT-3
Least Squares Fit K - % Stdr Dev K
21 Zone Ansio 2 - CLS 1
Raypath/Zone
25
20
15
10
5
0
0%
5%
10%
15%
20%
25%
% Stdr Dev K
%Stdr Dev K Aniso 2 CLS 1
21 Zn Aniso 2 CLS 1 Chisq = 0.2932

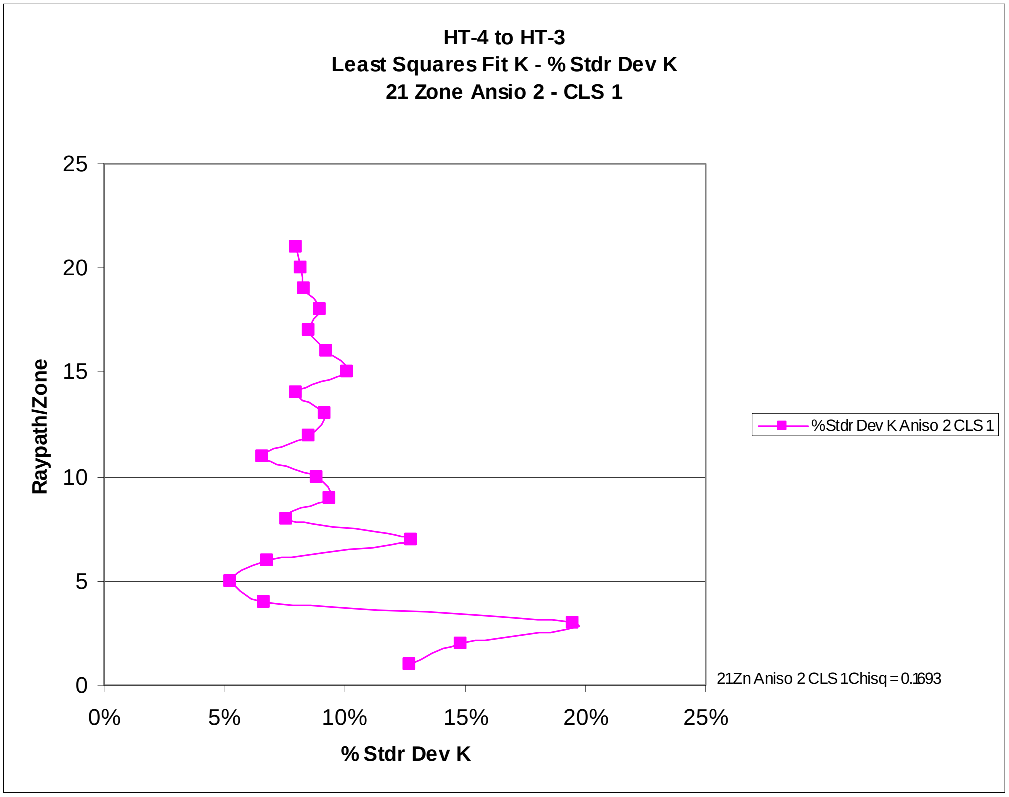
HT-4 to HT-3
Least Squares Fit K - % Stdr Dev K
21 Zone Ansio 2 - CLS 1
Raypath/Zone
25
20
15
10
5
0
0%
5%
10%
15%
20%
25%
% Stdr Dev K
%Stdr Dev K Aniso 2 CLS 1
21Zn Aniso 2 CLS 1Chisq = 0.1693

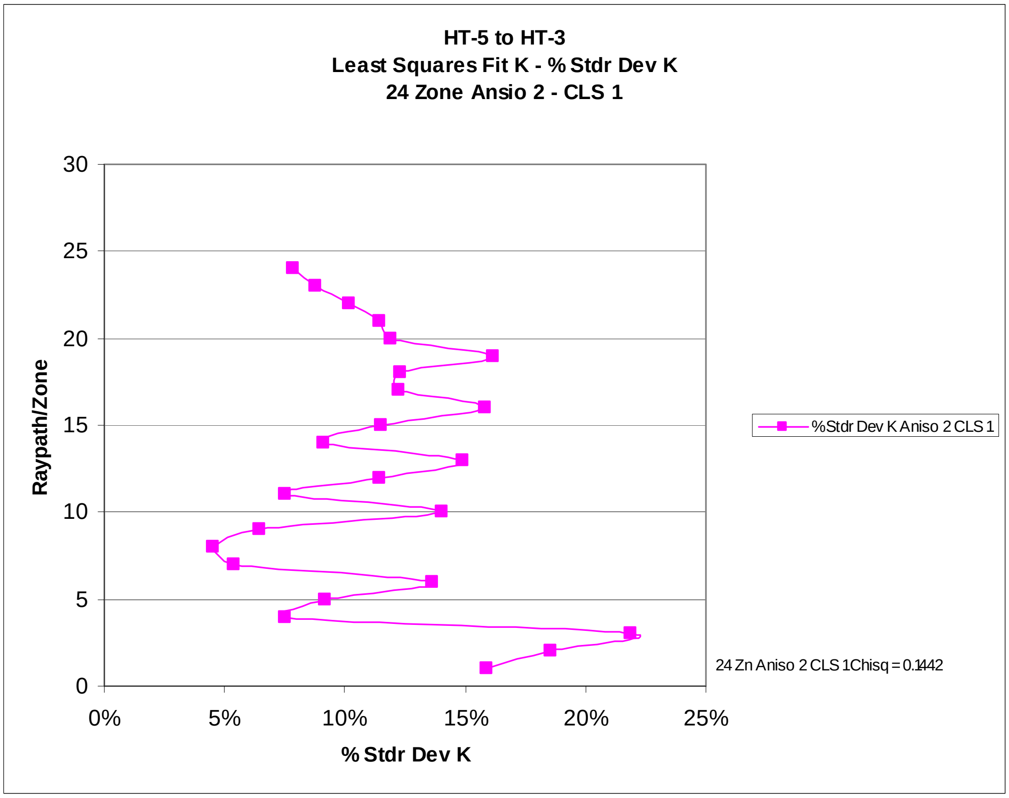
HT-5 to HT-3
Least Squares Fit K - % Stdr Dev K
24 Zone Ansio 2 - CLS 1
Raypath/Zone
30
25
20
15
10
5
0
0%
5%
10%
15%
20%
25%
% Stdr Dev K
%Stdr Dev K Aniso 2 CLS 1
24 Zn Aniso 2 CLS 1Chisq = 0.1442

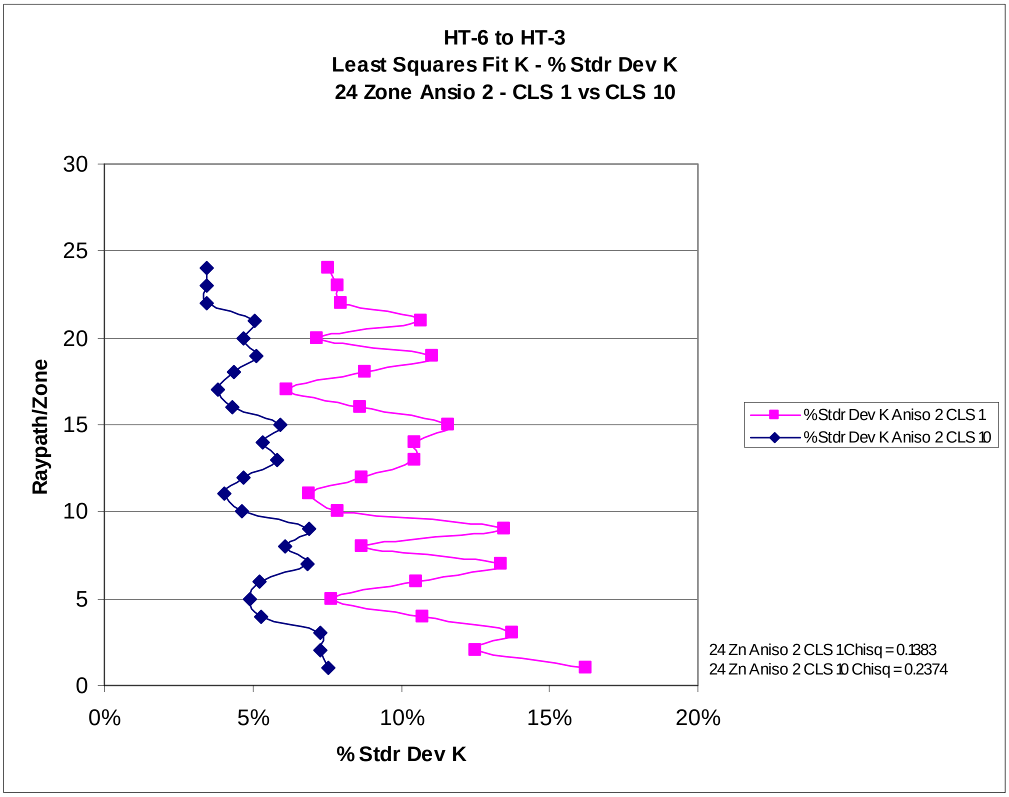HT-6 to HT-3
Least Squares Fit K - % Stdr Dev K
24 Zone Ansio 2 - CLS 1 vs CLS 10
Raypath/Zone
30
25
20
15
10
5
0
0%
5%
10%
15%
20%
% Stdr Dev K
%Stdr Dev K Aniso 2 CLS 1
%Stdr Dev K Aniso 2 CLS 10
24 Zn Aniso 2 CLS 1Chisq = 0.1383
24 Zn Aniso 2 CLS 10 Chisq = 0.2374

Appendix G – % Standard Deviation K For Lateral Heterogeneity Models And The Pneumatic CPT Source

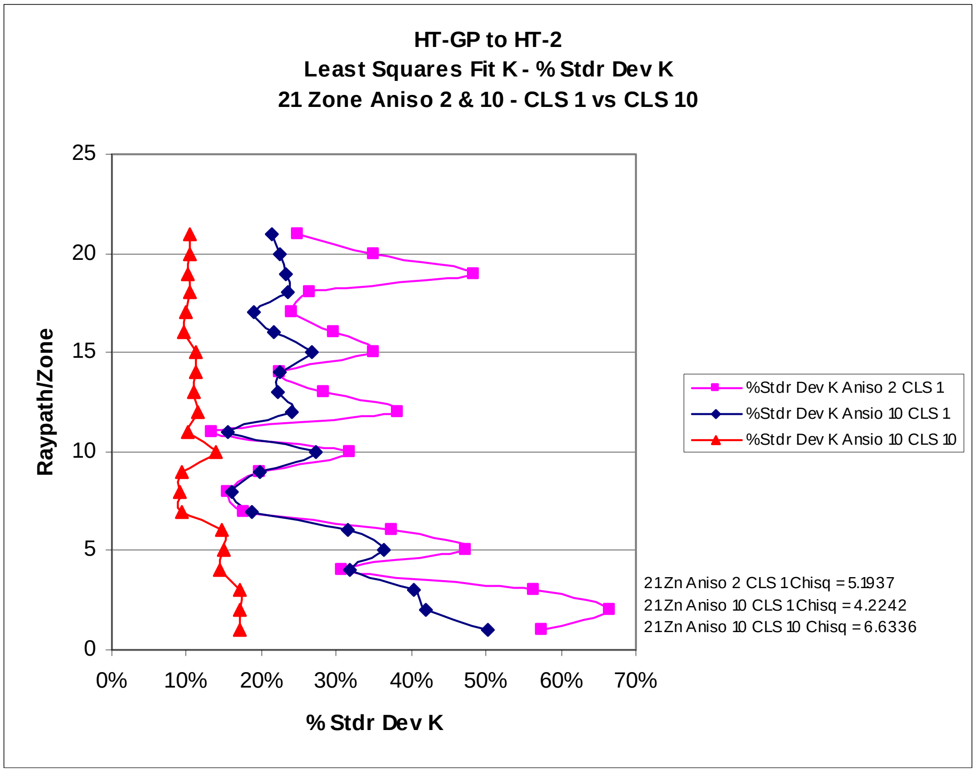
HT-GP to HT-2
Least Squares Fit K - % Stdr Dev K
21 Zone Aniso 2 & 10 - CLS 1 vs CLS 10
Raypath/Zone
25
20
15
10
5
0
0%
10%
20%
30%
40%
50%
60%
70%
% Stdr Dev K
%Stdr Dev K Aniso 2 CLS 1
%Stdr Dev K Ansio 10 CLS 1
%Stdr Dev K Ansio 10 CLS 10
21 Zn Aniso 2 CLS 1 Chisq = 5.1937
21 Zn Aniso 10 CLS 1 Chisq = 4.2242
21 Zn Aniso 10 CLS 10 Chisq = 6.6336

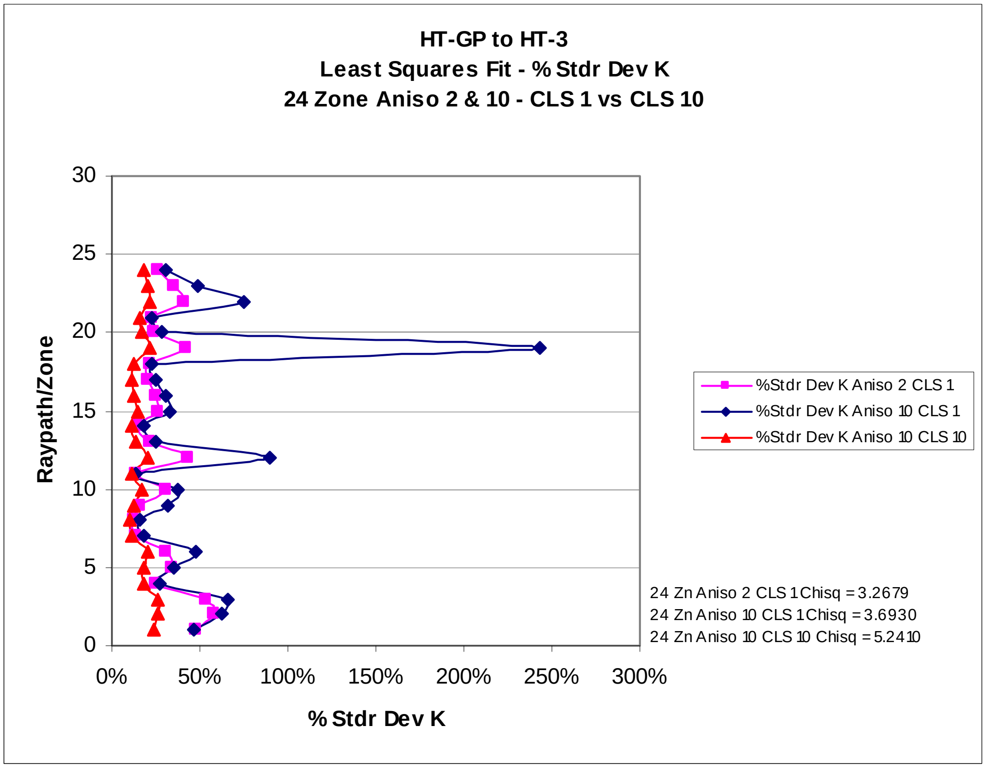
HT-GP to HT-3
Least Squares Fit - % Stdr Dev K
24 Zone Aniso 2 & 10 - CLS 1 vs CLS 10
Raypath/Zone
30
25
20
15
10
5
0
0%
50%
100%
150%
200%
250%
300%
% Stdr Dev K
%Stdr Dev K Aniso 2 CLS 1
%Stdr Dev K Aniso 10 CLS 1
%Stdr Dev K Aniso 10 CLS 10
24 Zn Aniso 2 CLS 1 Chisq = 3.2679
24 Zn Aniso 10 CLS 1 Chisq = 3.6930
24 Zn Aniso 10 CLS 10 Chisq = 5.2410